Kinetic and Mechanistic Study of CO and Hydrocarbon Oxidation, and NO_X Oxidation and Reduction over Pt-Pd Catalysts

A Dissertation

Presented to

the Faculty of the Department of Chemical and Biomolecular Engineering

University of Houston

In Partial Fulfillment

of the Requirements for the Degree

Doctor of Philosophy

in Chemical Engineering

by

Melanie Jane Hazlett

December 2016

Kinetic and Mechanistic Study of CO and Hydrocarbon Oxidation, and NO_X Oxidation and Reduction over Pt-Pd Catalysts

____
Melanie Jane Hazlett

Approved:

____
Chair of the Committee
Lars C. Grabow, Assistant Professor,
Chemical and Biomolecular Engineering

Committee Members:

____
William S. Epling, Professor,
Chemical and Biomolecular Engineering

____
Michael P. Harold, Professor,
Chemical and Biomolecular Engineering

____
Stacey Louie, Assistant Professor,
Civil and Environmental Engineering

____
Tracy J. Benson, Associate Professor,
Chemical Engineering, Lamar University

____
Suresh K. Khator, Associate Dean,
Cullen College of Engineering

____
Michael P. Harold, Professor and Chair,
Chemical and Biomolecular Engineering

Acknowledgements

First and foremost I would like to express my utmost gratitude to my advisor, Dr. William Epling, for providing me with much support, patience, and good humor.

Second, I would like to thank all my lab mates in the Epling group over the years, and other peers at UH, for their help and kindness. Specifically I would like to thank Dr. Tayebeh Hamzehlouyan, Dr. Di Wang, John Pierce, Dr. Justin Dodson, Dr. Sung Bong Kang, Monique Wilburn, Dr. Vencon Easterling, Yasser Jangjoo, Dr. Greg Bugosh, Wendy Lang, and Anh Vu.

Finally, I would not have been able to get this far without the constant love and support of my parents, Janice and Robert Hazlett, and my big brother Mark Hazlett for always being there to play video games with. Lab monkey get up drink coffee, lab monkey write thesis.

Kinetic and Mechanistic Study of CO and Hydrocarbon Oxidation, and NO_X Oxidation and Reduction over Pt-Pd Catalysts

An Abstract

of a

Dissertation

Presented to

the Faculty of the Department of Chemical and Biomolecular Engineering

University of Houston

In Partial Fulfillment

of the Requirements for the Degree

Doctor of Philosphy

in Chemical Engineering

by

Melanie Jane Hazlett

December 2016

Abstract

Increasing vehicle fuel economy is crucial for lowering greenhouse gas emissions. One approach being evaluated is the application of low temperature combustion (LTC) engines, which are more fuel efficient than standard diesel engines. However, current diesel oxidation catalysts (DOCs) are not able to reduce the higher CO and hydrocarbon (HC) levels present in LTC exhaust to the required amount needed to meet environmental regulations.

This dissertation focuses on understanding bimetallic Pt-Pd catalysts with the aim to design catalysts so LTC engines can meet emissions regulations. A series of studies was conducted with Pt:Pd catalysts of varying mole ratio, including bench scale reactor temperature programmed oxidation (TPO) experiments to evaluate catalyst performance and in situ diffuse reflectance infrared Fourier transform spectroscopy (DRIFTS) to evaluate surface species during reaction.

In the first study, CO and C_3H_6 oxidation were characterized. In terms of CO oxidation, the relationship between Pt:Pd ratio and CO oxidation light-off temperatures was related to dicarbonyl species forming on the Pt catalyst leading to CO inhibition, and carbonate species deactivation dominated at high Pd ratios. For propylene oxidation, the Pd-rich catalysts performed poorly, and partial oxidation products deactivated these catalysts. The second study investigated how water addition, a prevalent exhaust component, affects these trends and surface species.

In the third study, spatially resolved Fourier transform infrared spectroscopy (Spaci-FTIR) was used to measure gas-phase concentration profiles during CO and C_3H_6

oxidation reactions over a Pt monolith supported catalyst. Near the catalyst front, due to surface species accumulation on the catalyst surface identified by DRIFTS, two inflection points in the light-off curves were observed and were correlated to accumulation of surface species during reaction.

The final study includes larger HCs, such as dodecane, and investigates how both homogeneous and heterogeneous hydrocarbon oxidation can occur under LTC exhaust conditions. This has implications in the future of catalyst testing for these emission conditions, as well as for the design of these catalysts. Collectively these studies can be used in order to design DOCs to lower light-off temperatures and take advantage of homogeneous hydrocarbon oxidation reactions for downstream catalysts.

Table of Contents

List of Figures

List of Tables

Nomenclature

Al_2O_3	Alumina
BMEP	Brake mean effective pressure
CEM	Controlled evaporator mixer
CO	Carbon monoxide
CO_2	Carbon dioxide
C_3H_6	Propylene
DEE	Diethyl ether
DI	Deionized
DOC	Diesel oxidation catalyst
DOE	Department of Energy
DPF	Diesel particulate filter
DRIFTS	Diffuse reflectance infrared Fourier transform spectroscopy
EDS	Energy dispersive spectroscopy
EPA	Environmental Protection Agency
EXAFS	Extended X-ray absorption fine structure
FTIR	Fourier transform infrared spectroscopy
HC	Hydrocarbon
H_2O	Water
ID	Inner diameter
LNT	Lean NO_X trap
LTC	Low temperature combustion

MFC	Mass flow controller
MS	Mass spectrometer
N_2	Nitrogen
NHTSA	Transportation’s National Highway Traffic Safety Administration
NO	Nitrogen oxide
NO_2	Nitrogen dioxide
NO_X	Nitrogen oxides (inclusing NO, NO_2, N_2O)
N_2O	Nitrous oxide
NMOG	Non-methane organic gases
O_2	Oxygen
PCCI	Premixed charge compression ignition
Pd	Palladium
PEM	Proton exchanged membrane
PROX	Preferential CO oxidation
Pt	Platinum
RCCI	Reactivity controlled compression ignition
Spaci	Spatially resolved capillary inlet
SCR	Selective catalytic reduction
SEA	Electrostatic adsorption
STEM	Scanning transmission electron microscopy
SV	Space velocity
T_{50}	Temperature where 50% conversion is attained (light-off)

TEM	Transmission electron microscopy
TPO	Temperature programmed oxidation
TPD	Temperature programmed desorption
WGS	Water-gas shift
XANES	X-ray absorption near edge structure
XRD	X-ray diffraction

Chapter 1 Introduction

Increasingly stringent environmental policies due to concerns over global warming and climate change, established by agencies such as the Environmental Protection Agency (EPA), are a driving force for increasing engine fuel economy and decreasing their harmful emissions. One approach to increased fuel economies is operating under fuel lean modes, as diesel engines do. Furthermore, new low temperature combustion (LTC) modes being studied are even more fuel efficient.

In order to reduce climate change and strengthen national energy security by minimizing reliance on imported petroleum, fuel economy requirements have been increasing year by year. The EPA and the Department of Transportation's National Highway Traffic Safety Administration (NHTSA) have set rules which increase fuel economy requirements for model year 2017-2025 light-duty and medium-duty passenger cars, and the EPA passed similar rules for heavy-duty vehicles [1]. As mentioned, the LTC engine modes are more fuel efficient, however before engines running in these modes can be commercialized, they have to meet emission regulations. The intrinsic challenge is that as engines get more fuel efficient the exhaust temperatures are lower, which in turn negatively impacts the effectiveness of the catalytic systems necessary to meet the emissions regulations.

The EPA regulates the emissions of nitrogen oxides (NO_X), carbon monoxide (CO), non-methane organic gases (NMOG) or hydrocarbons (HC), formaldehyde and particulate matter [2]. Gasoline engines only require one catalyst to reach the required emissions targets; the three-way catalyst is able to simultaneously oxidize CO and hydrocarbons while reducing NO_X. And currently, there are no particulate regulations impeding gasoline engine use, although those are forthcoming. For diesel engines, and for these newer fuel efficient lean burn engines, it is difficult to reduce NO_X in the high oxygen concentrations present in the exhaust, and particulate is an issue, and so there are multiple catalysts that make up the catalytic aftertreatment system. Firstly, a diesel oxidation catalyst (DOC) is used to oxidize the exhaust gas CO and hydrocarbons to carbon dioxide (CO_2) and water (H_2O), and to oxidize the nitrogen oxide (NO) to nitrogen dioxide (NO_2). Next either a diesel particulate filter (DPF) or a NO_X reduction catalyst is placed. The DPF filters out and oxidizes the particulate matter/soot from the engine exhaust. The NO_X reduction catalyst is either a selective catalytic reduction catalyst (SCR) or lean NO_X trap (LNT). These three catalysts have been optimized to reduce emissions from conventional diesel engines to meet the EPA’s environmental targets, however the LTC engine emissions pose a challenge.

Not only is the exhaust temperature from LTC engines lower than a conventional diesel engine, the composition of the emissions also varies greatly. Comparing conventional (or standard) diesel engine emissions to two different LTC technologies, reactivity controlled compression ignition (RCCI) and premixed charge compression ignition (PCCI), show that the emissions from these LTC engines have much lower NO_X concentrations and less particulate matter when compared to a standard diesel engine [3]. However, there are much higher CO and HC concentrations, as shown in Figure 1-1 comparing standard diesel engine exhaust to RCCI engine exhaust as a function of brake mean effective pressure (BMEP). The higher CO and HC emissions, coupled with the lower engine exhaust temperatures, means that increasing attention needs to be paid to the CO and HC oxidation performance of the oxidation catalysts in the catalytic aftertreatment systems. For commercial Pt and Pt:Pd/Al_2O_3 DOCs, the low levels of CO and HCs emitted under the conventional mode can reach full conversion by 190°C, while the higher concentrations emitted with the RCCI engine resulted in full conversion near 300°C [4].

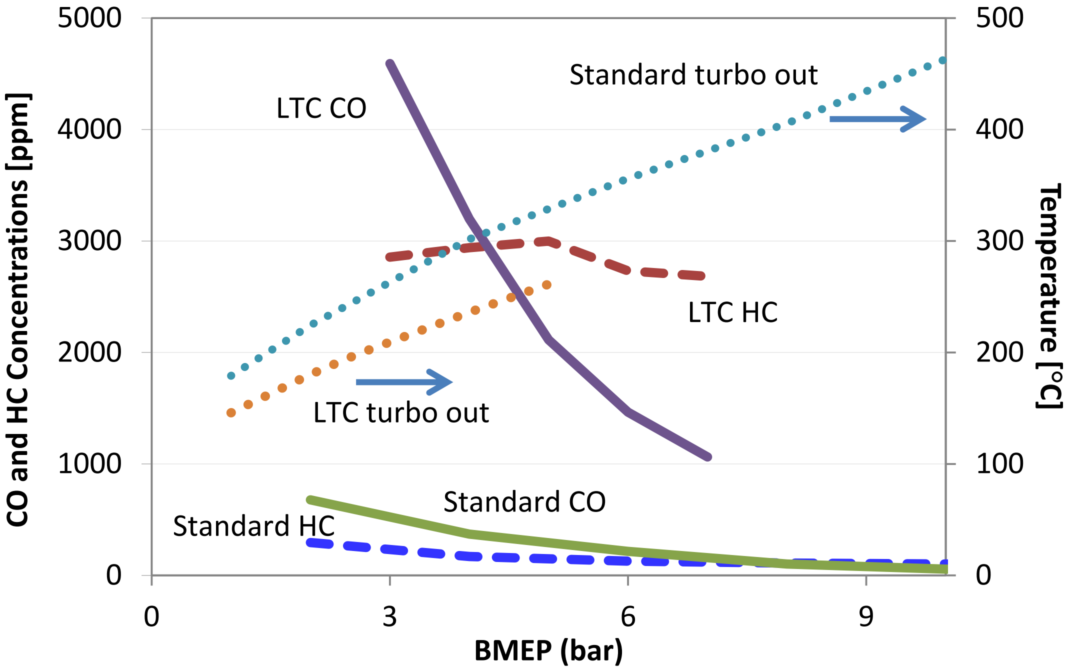

Figure 1-1 CO and HC emissions from standard diesel and LTC RCCI engines, data provided by Oak Ridge National Laboratories

In order to move forward with LTC engines, the oxidation catalysts need to be able to oxidize these high CO and HC emissions at lower temperatures. The Department of Energy (DOE) issued a 150°C Challenge, establishing a goal that CO and HC conversions over the DOCs reach > 90% by 150°C exhaust temperatures [1].

DOCs typically contain platinum (Pt) and/or palladium (Pd) as the precious metal component in order to oxidize CO and HCs. A non-linear relationship between the oxidation performance and Pt or Pd content has been observed, where different Pt:Pd molar ratios achieve the lowest light-off temperatures for different compounds [5], shown in Figure 1-2. Here the light-off temperature is the temperature where 50% of the reactant is converted to products (T_{50}).

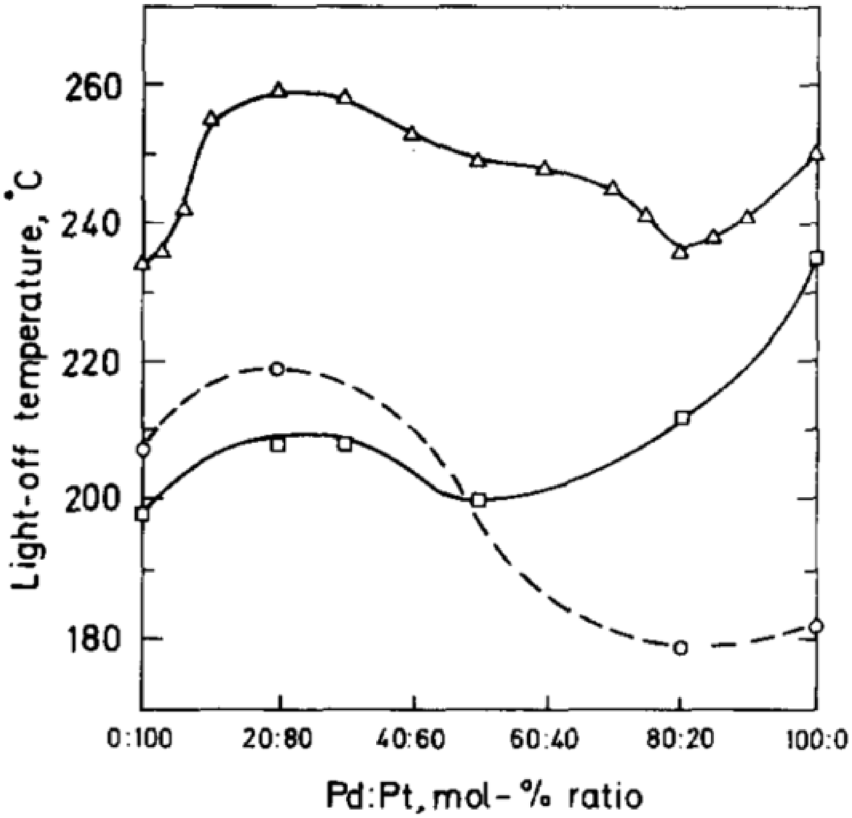

Figure 1-2 T_{50} for xylene (triangles), propylene (squares) as squares, and CO (circles) oxidation as a function of Pd:Pt mole ratio; experimental conditions 220 ppm xylene, 900 ppm C_3H_6, or 4600 ppm CO in air.

In a study of heavy-duty DOC performance, it was shown that a higher Pt content in the bimetallic catalysts improves alkane oxidation, NO oxidation, and alkene oxidation, while catalysts with a higher Pd content showed improved CO oxidation performance [6]. Understanding and predicting this bimetallic behavior has been found difficult as there is no apparent relationship between the metal properties and the catalyst performance [7].

1.1 Research Objective and Outline

The objective of this dissertation is to understand the CO and hydrocarbon oxidation performance characteristics of bimetallic Pt-Pd/Al_2O_3 catalysts, and with this understanding to guide performance optimization, all in the context of the DOE 150°C Challenge. To characterize the reactions, I tested several monometallic and bimetallic Pt/Pd catalysts on different scale benchtop reactors, used diffuse reflectance infrared Fourier transform spectroscopy (DRIFTS) to identify key surface species formed during reaction, and spatially resolved reactant and product distributions in a monolith honeycomb reactor. The chapters contained within this dissertation represent different studies related to these objectives, exploring different facets pertaining to LTC emissions reduction. The content in these chapters are not presented chronologically. The chapters are instead presented in increasing reactor scale and reactant complexity, starting from small reactor scales investigating surface species during reactions to pilot-scale monolith testing with more complex reaction mixtures.

Chapter 2 contains a literature review focused on Pt-Pd catalyst characterization, surface species observable by DRIFTS, and a brief history of studies that involved spatially resolving reactions and what information can be gained from them. This chapter is intended to give a foundation for the studies within the following chapters.

Chapter 3 details the various scales of experimental setups used, providing the schematics and procedures used for catalyst synthesis, packed bed reactor testing, monolith reactor testing, spatial resolution experiments, and DRIFTS experiments. This chapter can be referred to for detailed experimental information for the studies in the later chapters.

Chapter 4 is a kinetic and mechanistic study of CO and propylene oxidation over a range of bimetallic Pt:Pd molar ratio catalysts. Packed bed reactor testing and DRIFTS experiments were conducted for CO and propylene oxidation individually, as well as their co-oxidation. In this study, surface species during reactions were investigated as a function of Pt:Pd molar ratio in order to gain insight into the performance observed in the reactor testing; specifically why certain Pt:Pd ratios resulted in better performance.

As water is ubiquitous in exhaust emissions, it is important to evaluate the effect of water on the Pt-Pd catalysts and Chapter 5 builds on the knowledge from the previous chapter, and focuses on changes in the CO and C_3H_6 oxidation mechanisms on the Pt, Pd and Pt-Pd catalysts with the addition of water. In this study the reactor tests are at the monolith reactor scale, and also include DRIFTS experiments using the catalyst washcoat. The effect of water in both the reaction mixture and pretreatment conditions are investigated.

Chapter 6 moves to a more complex reaction mixture at the monolith reactor scale, this time focusing on a Pt catalyst, in order to evaluate the CO, HC, and NO oxidation reactions as a function of axial location in a monolith channel. Using this spatial resolution technique, reaction zones along the catalyst are identified showing that first CO oxidation occurs, then C_3H_6 oxidation, and finally NO oxidation. The identification of these reaction zones may lead to improved catalyst design.

Chapter 7 contains results of added reaction mixture complexity, and these demonstrate that when higher chain length hydrocarbons are used, both gas-phase reactions and catalytic surface reactions become important. These larger hydrocarbons are more representative of diesel emissions, and it is shown that particularly for RCCI exhaust conditions these gas-phase reactions can occur and as a consequence lead to NO oxidation which may be important for the DPF or SCR catalysts downstream of the DOC.

In Chapter 8 conclusions are drawn from the studies in previous chapters, and recommendations for future research are given.

Chapter 2 Literature Review

For vehicle exhaust aftertreatment catalysts, low pressure drop is preferred to maintain good engine performance and so typically a cordierite honeycomb monolith is used. A high surface area washcoat (also called support) is deposited onto this monolith and the precious metals are impregnated on this washcoat. For diesel oxidation catalysts (DOCs), the washcoat is typically alumina (Al_2O_3), with silica, zirconia, or zeolites occasionally used instead [8]. The precious metals are most commonly Pt and Pd, with Rh sometimes used. For this study, Pt and Pd and Pt-Pd catalysts supported on γ-Al_2O_3 were studied, and so the literature review and subsequent chapters focus on those catalyst formulations. Diffuse reflectance infrared Fourier transform spectroscopy (DRIFTS) was also extensively used for surface species identification in many of the chapters and so a review of the anticipated surface species during CO and C_3H_6 oxidation has been provided. Finally, there is a brief outline of the history and usefulness of spatially revolved experimental techniques.

2.1 Platinum and Palladium Bimetallic Catalysts

In general, a catalyst with both Pt and Pd present as bimetallic particles results in improved oxidation relative to the monometallic catalysts [9], [10]. The bimetallic nature of these catalysts is important as adding Pt to the particles can influence the Pd oxidation state. In one study it was found that a monometallic Pd catalyst was completely oxidized after calcination and in the zero valent state after reduction, however for a bimetallic catalyst both metallic and oxidized forms were present after calcination and reduction [11].

Catalyst characterization techniques are useful to understand the bimetallic particle structure and surface composition, which is important as the available surface area is where the catalytic reactions occur. A multitude of characterization techniques have been used to understand the Pt-Pd particle structures supported on a variety of materials (SiO_2, Al_2O_3, zeolites, carbon); such as extended X-ray absorption fine structure (EXAFS) [9], [11]–[14], X-ray absorption near edge structure (XANES) [12], transmission electron microscopy (TEM) [9], [12], [13], X-ray diffraction (XRD) [11], and DRIFTS [10], [12]. All these techniques have shown that Pd segregates to the particle surfaces which leads to a Pt-rich core surrounded by metallic Pd, or small Pd particles dispersed on the Pt core.

Increasing particle size, which can happen from catalyst sintering or be manipulated during catalyst synthesis, has been shown to increase the amount of Pd that segregates to the surface [15]. With small particle sizes, Pt is also present at the surface. It is also possible for the metallic Pd in the bimetallic particles to be oxidized into PdO clusters under high temperature oxidizing conditions [16]. In another study it was found that surface segregation of Pt-Pd/Al_2O_3 catalysts under oxidizing conditions did not occur, and the particles were present as alloys with PdO dispersed on the support [17]. As such, the enhanced catalytic performance of these bimetallic catalysts was attributed to the co-existence of metallic Pt and Pd on the catalyst surface. In yet another study with Pt-Pd supported on silica no surface enrichment in either metal was observed [18].

It was found that adding Pd to Pt-based catalysts leads to less Pt sintering relative to monometallic catalysts [7], [11], [19], [20]. The sintering of catalysts can be studied by TEM in situ [21]. Using scanning transmission electron microscopy (STEM), it was found that when a physical mixture of Pt/Al_2O_3 and Pd/Al_2O_3 are put together and aged at high temperature of 650°C in air, bimetallic particles actually form [22]. Pt sintering is caused by the formation of volatile PtO_2, whereas PdO is stable up to 810°C [23]; it was found the PdO is able to trap the volatile PtO_2 and lead to bimetallic Pt-Pd particle formation [22]. This helps explain why adding Pd helps protect against sintering, as it stops PtO_2 from sintering to large particles or being lost in the vapor phase.

The effect of synthesis methods of Pt-Pd catalysts has been studied as well. Two catalyst synthesis methods, dry impregnation which is commercially used to make DOCs, and electrostatic adsorption (SEA) which can make very uniform sized particles, were studied [24]. While the SEA method initially leads to good dispersion and well alloyed particles, it was found that after ageing the catalyst performance converges to the same performance as the catalysts prepared by dry impregnation [25].

The support of the catalyst, and addition of promoters, also has an effect on the oxidation performance. A study comparing CO oxidation performance of Pd supported on γ-Al_2O_3 versus La-Al_2O_3 found that the La-Al_2O_3 enhanced CO oxidation performance by affecting how the CO adsorbs to the Pd [26]. With γ-Al_2O_3, CO displaces O from 3-fold hollow sites while with La the O is able to displace CO from these sites. This leads to improved oxygen coverage and a higher CO oxidation rate, due to less CO poisoning.

It was found that the La actually intermingles with the Pd and leads to stabilization of atomically dispersed Pd particles, leading to high CO oxidation activity [27]. The addition of basic additives to Pt/Al_2O_3 catalysts has been studied for CO and propylene oxidation [28]. For three-way catalysts used to treat gasoline exhaust, CeO_2 is a helpful additive to improve the oxygen storage. Two other additives, Na_2O and K_2O, were studied and it was found that these three additives improve CO oxidation performance by enhancing the water gas shift reaction.

In yet another study of $Pd/\gamma\text{-}Al_2O_3$ the authors concluded that under oxidizing conditions and with large CO concentrations in the gas phase, oxidized Pd was not the active site for CO oxidation as is often suggested, but instead the active site was metallic Pd [29]. This was also observed in a methane oxidation study on $Pd/\Theta\text{-}Al_2O_3$ [30], and $Pd/\gamma\text{-}Al_2O_3$ [31]. These studies support the notion that the enhanced catalytic activity in the bimetallic catalysts comes from the Pd being present in the metallic state at the surface of the particle, instead of PdO.

There are a myriad of catalyst properties that are functions of Pt:Pd ratio: for example, particle size, metal oxidation state, and surface composition. There is some debate within the scientific community what the active sites for reaction are and what the surface composition of these particles are, and these seem to change as a function of reaction conditions.

2.2 Surface Species on Pt-Pd Catalysts

This section will provide a review of the various surface species mentioned in the chapters containing surface characterization results; DRIFTS was used to characterize surface species in Chapters 4, 5, and 6. As a quick background, infrared spectroscopy is used to probe the molecular vibrations, and functional groups can be associated with characteristic infrared absorption bands occurring at certain wavenumbers [32]. A molecular vibration is infrared active if there is a change in the dipole moment of the molecule, as such symmetric vibrations cannot be detected. In the mid-infrared region (4,000- 1,000 cm^{-1}) there are two main types of vibrations, stretching vibrations (ν) and bending vibrations (δ in plane, π out of plane). Stretching vibrations occur along the chemical bond, leading to changes in the length of the bond; bending vibrations involve changes in bond angles. For CO and C_3H_6 anticipated oxidation products, these bands are given in Table A-1-1 in the Appendix.

2.2.1 CO Oxidation

CO adsorbs on the metal sites as carbonyls, either linearly or in bridged forms [33]. The linear configurations occurs in the 2110-2050 cm^{-1} wavenumber range, and the bridged configurations occur in the 2000-1800 cm^{-1} wavenumber range. Focusing first on the linear forms, the carbonyl can adsorb linearly to the metal site individually, or can co-adsorb to the metal site with another carbonyl or atomic oxygen [34]. Descriptions of these are shown in Figure 2-1. The bridged configurations can either be doubly or triply adsorbed to the metal sites, also shown in Figure 2-1.

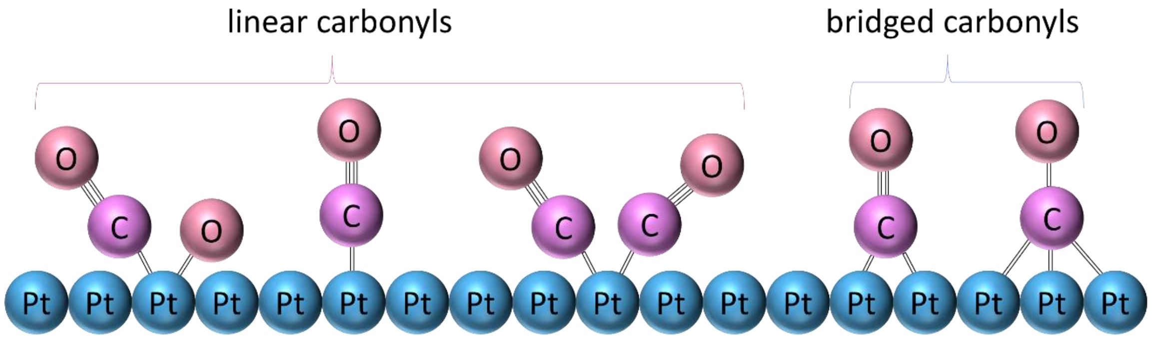

Figure 2-1 Configuration of linear and bridged carbonyls

These adsorbed carbonyls can react with oxygen, hydrogen, or hydroxyl (OH) on the surface to form a number of intermediates; carbonates (either monodentate or bidentate), formate, carboxylate, formyl, carboxyl, and bicarbonate. The bands for these species (shown in A-1-1) are generally all in the 1800-1000 cm^{-1} range for the C-O and C=O vibrations; the formyl and formate will also have C-H stretches in the 3000-2700 cm^{-1} region. The structure of these species are shown in Figure 2-2. The bidentate carbonate can either be attached to one atom or two atoms [35], and carboxylate is attached through the carbon to the metal site [36], [37]. Carboxyl (COH) generally has the carbon triply bound to the metals in a hollow site, much like the triply bridged CO, while formyl (HCO) is generally on an atop site [38]. These intermediates are depicted as adsorbed onto metal sites, however it is possible that these intermediates are present on the alumina support at the particle/support interface.

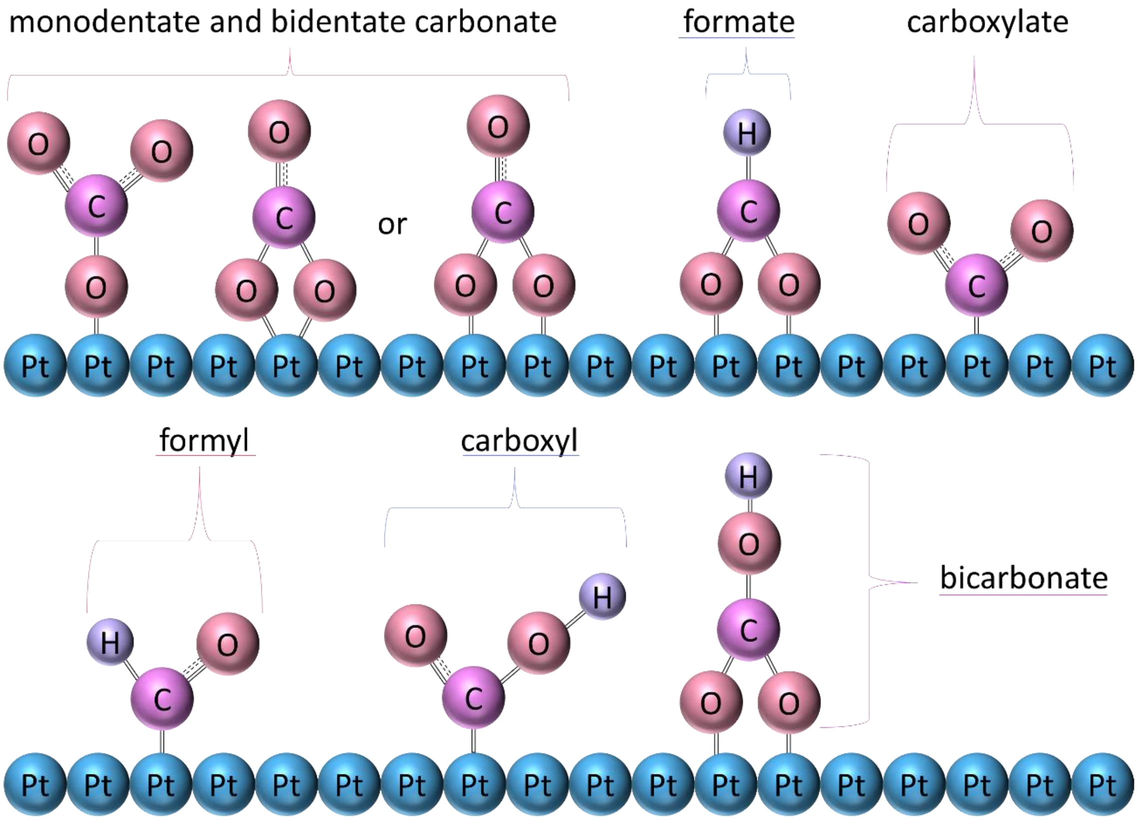

Figure 2-2 Configurations of CO oxidation intermediates

2.2.2 C_3H_6 Oxidation

Propylene can adsorb to the surface in numerous ways, Figure 2-3 shows some possibilities. The π-propylene, di-σ-propylene, and propylidyne configurations are shown [39]. In situations where there are high surface coverages of propylene, the propylidyne will be the most prevalent since it is perpendicular to the surface and takes up the least surface area [40]. Ethylene was observed as a partial oxidation product, the three configurations of ethylene on the surface are shown in Figure 2-4 [41].

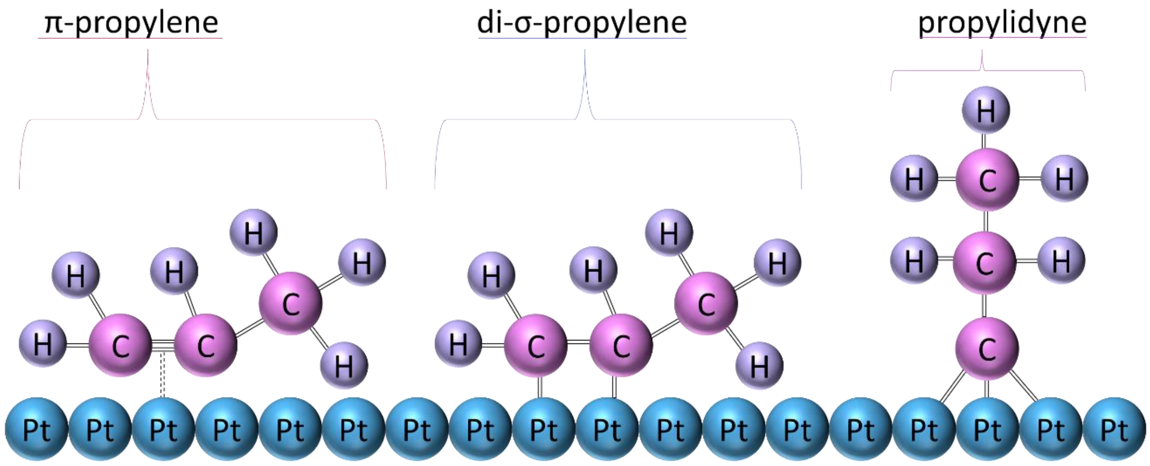

Figure 2-3 Configurations of propylene

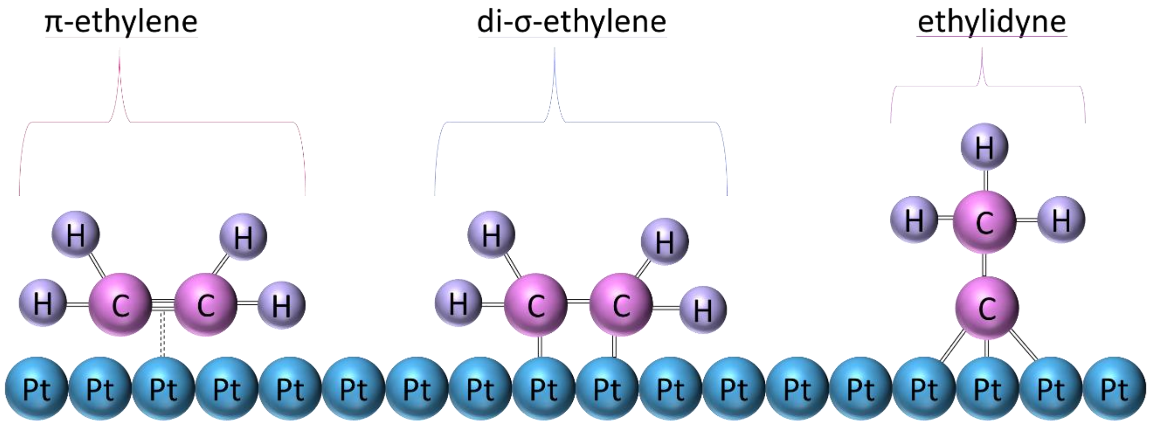

Figure 2-4 Configurations of ethylene

Other partial oxidation intermediates observed are acetone, acetaldehyde, acetate, acetic acid and formaldehyde. Of these, the ones observed on the surface with DRIFTS were acetone and acetate, which are shown in Figure 2-5 along with 1-methylvinyl which is a surface species that has been linked to the formation of acetone on Pt [40], but was not observed in the IR data. Acetone adsorbed onto Pt is considered to be bonded through the oxygen [42], [43].

.

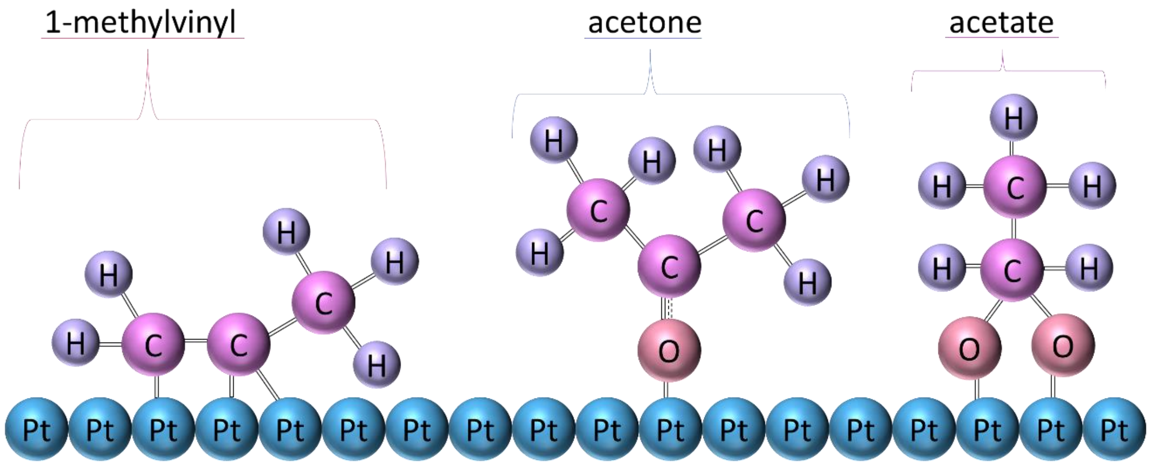

Figure 2-5 Propylene partial oxidation products observed in DRIFTS

CO was also seen as a propylene partial oxidation product, and so the species associated with CO oxidation would also be expected in the DRIFTS study of propylene oxidation.

2.3 Spatial Resolution Experiments

Both mass spectrometry (MS) and Fourier transform infrared spectroscopy (FTIR) have been used for analysis of gas-phase concentrations along diesel oxidation catalysts, as well as other aftertreatment catalysts [44]–[48]. Regardless of the analyzer used, the concept of these experiments remains the same. A small capillary is inserted into one of the channels of the monolith such that some of the flow in the channel travels through the capillary and into a gas analyzer, thereby allowing the study of axial concentration profiles of gas species along the length of the catalyst as that capillary is moved along the channel. This technique is generally termed spatially resolved capillary inlet (Spaci), either Spaci-MS or Spaci-FTIR depending on the gas analyzer used in the particular study.

Spaci-MS was first used in aftertreatment catalysis for the evaluation LNTs, in 1997 [48]. During normal engine operation engine emissions are transient due to varying engine loads and exhaust-gas-recirculation. Furthermore the LNT systems are inherently dynamic even during steady-state engine operation, and at the time the conventional analyzers for exhaust emissions were not able to adequately capture the transient emissions accurately. And so the first capillary inlet MS study focused on comparing the readings from the Spaci-MS to a chemiluminescence-based analyzer, one of the conventional exhaust analyzers, in resolving transient emissions coming from LNT as a proof of concept [49]. The Spaci-MS was demonstrated to provide high-speed diagnostic capability to more accurately measure these transient emissions than the chemiluminescence measurements. Once the Spaci-MS was developed, this technique was further extended to testing multiple sample locations so as to measure both the engine exhaust as well as measuring within the LNT catalysts in order to understand the chemistry occurring, the apparatus schematic is shown in Figure 2-6 [50].

In other bench scale reactor studies using simulated exhaust, the Spaci-MS was used to measure the axial gradients occurring over the catalysts, either by moving the capillary axially along one monolith channel or by placing multiple capillaries at different axial locations of different channels [51]–[55]. The experimental apparatus was also updated with intra-channel temperature measurement using small optical fiber tipped with a thermographic phosphor [52]. The capillary is able to be translated by a stepper-motor-driven translation stage, the measurement being made at increments as small as 3 mm [55]. The Spaci-MS technique was useful in order to evaluate these LNT catalysts, and identify where NO_X storage and reduction occurred over the catalyst as shown in Figure 2-7, with storage gas concentrations of 250 ppm NO, 8 % O_2, 5% H_2O, in balance N_2 and regeneration gas concentrations of 4% CO, 1% O_2, 5% H_2O, in balance N_2 [52]. From this study it was observed that only the front half of the catalyst was being used for NO_X storage and no NO_X was stored in the back half.

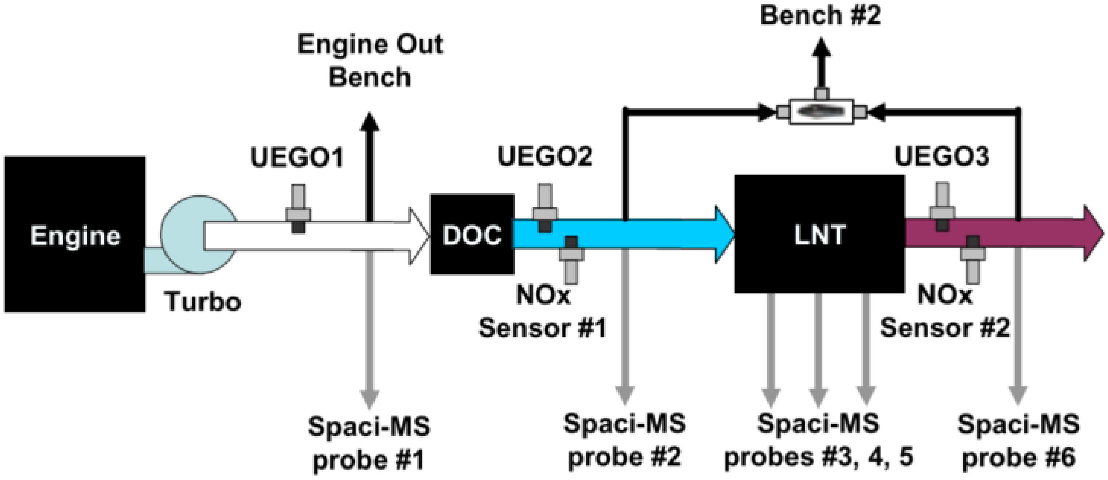

Figure 2-6 Exhaust sampling locations engine testing [50]

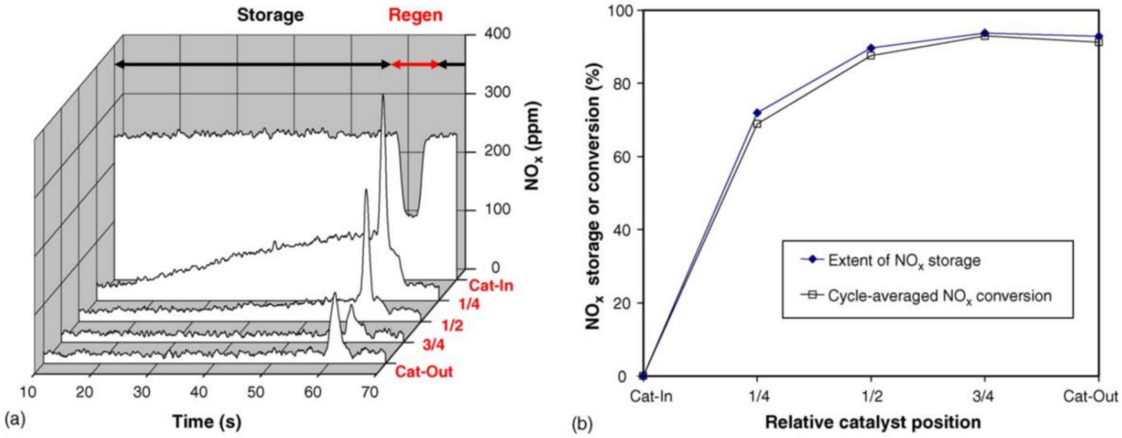

Figure 2-7 Pt/K/Al2O2 monolith during 54 s storage 4 s regeneration cycling; (a) NO_X breakthrough profiles, (b) cycle averaged NO_X storage and conversion [52]

Spaci-MS has also been utilized to measure axial concentration gradients in monolith reactors for hydrocarbon partial oxidation of methane and ethane [56]. In this work a rapid scanning MS and capillary were used to measure the axial concentration profiles and a thin thermocouple was inserted inside this capillary to get axial temperature profiles at very high resolution (< 0.3 mm). In a later study this apparatus was slightly updated to include two capillaries with the effluent of one going to an MS, and the other to a gas chromatograph, and an optical pyrometer was added into the capillary as well [57]. The thermocouple was taken as representative of the gas temperature while the pyrometer readings were taken as representative of the catalyst surface temperatures. This apparatus continues to be used to provide valuable insights into the partial oxidation of methane, ethane and dimethyl ether respectively [58]–[60]. For instance it was found that dry reforming reactions were playing a role in dimethyl ether partial oxidation, while not playing an important role in methane partial oxidation.

Spaci-MS has also been used to study the reactions over a DOC. The effect of propylene concentration on NO oxidation was studied [61], and the reactions of CO, propylene, dodecane and NO oxidation were monitored [45]. In the later study significant NO oxidation was observed right at the dodecane light-off, which is likely related to the homogenous oxidation reactions discussed in Chapter 7. It was also observed that under those experimental conditions, particular reactants light-off in a certain order along the length of the catalyst, which is similar to what was observed in Chapter 6 using Spaci-FTIR experiments over a Pt/Al_2O_3 catalyst with RCCI exhaust conditions. Other recent studies regarding lean burn engine exhaust emissions control with LNT and SCR catalysts have been done using Spaci-MS [62]–[64]. There have also been Spaci-MS experiments on Pt/Pd/Al_2O_3 monolith for methane oxidation for use in treating emissions from natural gas vehicles [65]. The use of the FTIR in Spaci experiments was first used to probe SCR reactions over Fe/zeolite and Cu/zeolite catalysts [46], [66]. The intrusiveness of Spaci techniques have been studied [47], [48], [67]; however with careful implementation it remains a useful technique to get axially qualitative information about the concentration and temperature profiles in the monolith reactor.

Chapter 3 Experimental Methods

3.1 Catalyst Synthesis and Characterization

3.1.1 Powder Catalysts

Powder catalysts were prepared using the incipient wetness method, where the pore volume of the support is filled with a metal salt and water solution to reach a desired catalyst loading. Pt, Pd, and various bimetallic Pt:Pd ratio catalysts were prepared on γ-Al_2O_3 (alumina). The metal salts that were used for Pt and Pd catalysts were $Pt(NH_3)_4(NO_3)_2$ and $Pd(NO_3)_2$ dihydrate, and were purchased from Sigma Aldrich.

The alumina used as the support was provided by SASOL. The surface area is given as 137 m^2/g, with a loose bulk density of 0.38 g/mL and pore volume size of 1.07 mL/g. The particle size distribution given was 35.7% < 25 micron, 64.8% < 45 micron, and 95.3% < 90 micron. This pore volume was validated by experimental measurement, putting deionized (DI) water into known mass of alumina and weighing again after water filled the pore volume.

All catalysts prepared were based on 1 wt% Pt catalyst loading, and molar ratios of Pd added; monometallic Pd catalysts were 0.548 wt% (same mole amount as 1 wt% Pt). The Pt and Pd precursors were weighed using a Mettler AC100 analytical scale, and mixed into the correct volume of water to get desired concentrations. The solutions were then added dropwise to 2 g of alumina. Catalysts were dried overnight and calcined for 4 hours at 550°C in a Neytech Vulcan 3-550 muffle furnace with a ramp rate of 10°C/min. For each catalyst the 2 g sample was prepared to have approximately 1.04×10^{-4} moles of precious metals.

3.1.2 Monolith Catalysts

The monolith catalysts were prepared also by incipient wetness. In this case the monolith cores were provided by Johnson Matthey pre-washcoated with γ-Al_2O_3, and small cylindrical samples were core-drilled out. The pore volume was measured experimentally, and afterwards the appropriate metal salt solutions were made. The difference in this case was that sufficient solution to dip the entire sample was made, and the concentration was made such that the water taken up by the pore volume contains the correct amount of precious metal. Pt and Pd precursors were dissolved in the water solution at the same time and were therefore impregnated on the support at the same time. The catalysts were then dried and calcined in a Neytech Vulcan 3-550 muffle furnace for 4 hours at 550°C, then aged at 700°C in situ under flowing 14% O_2, 5% H_2O in balance N_2.

3.1.3 Particle Size Measurements

Temperature programmed desorption (TPD) after CO adsorption was used to measure metal dispersion [68]. These TPD experiments were done on a bench reactor setup; the total flow rate was 200 mL/min and the CO concentration in the initial adsorption stage was 7000 ppm in N_2 at 30°C for 1 hour, followed by only N_2 for 80 minutes to desorb the physically adsorbed CO, and then a 28°C/min temperature ramp up to 835°C to desorb all the chemically adsorbed CO. The desorbed CO was measured and used to calculate particle size.

CO pulse chemisorption experiments were used in order to measure metal dispersion and particle size for the catalysts studied in Chapter 5. The washcoat was scraped off from the cordierite monolith and pretreated in 10% H_2/Ar at 500°C for 1 h then the temperature was lowered to 35°C in Ar flow. CO pulses (1.12×10^{-6} mol) were injected until no more CO uptake was observed. A stoichiometry of 1 was assumed to calculate particle sizes. For the bimetallic catalysts, a weighted average based on the molar ratios was used to calculate the density and molecular weights. The site density for Pt and Pd were taken as 0.0800 and 0.0787 nm^2/atom respectively [69].

3.2 Bench Scale Powder Packed Bed Reactor

The schematic of the bench scale reactor setup used to test the powder catalysts is shown in Figure 3-1. A series of MKS mass flow controllers (MFCs) was used to control the flow of the various gases used for testing. For the catalyst testing, the gases used were CO, C_3H_6 and O_2 with N_2 serving as the carrier gas. Inlet and outlet lines were primarily 1/8" and 1/4" stainless steel Swagelok tubing and fittings, which were heated above 100°C to avoid any water condensation.

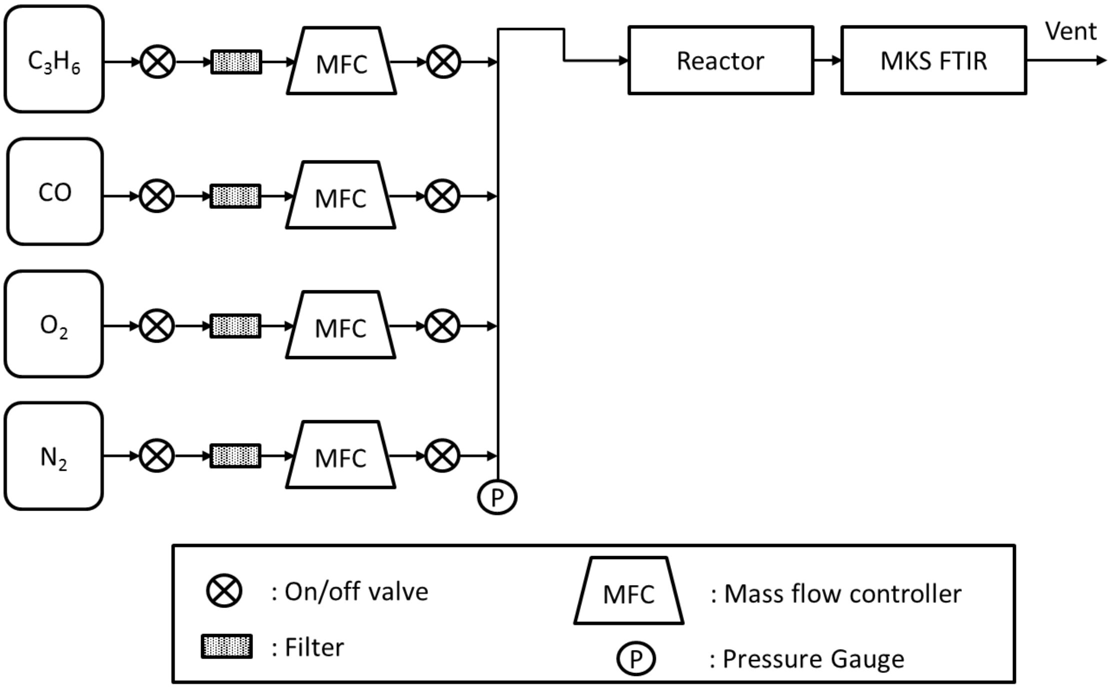

Figure 3-1 Bench scale packed bed reactor experimental setup.

3.2.1 Gas Flow Specifications

A total flow rate of 400 mL/min was used, corresponding to a monolith space velocity of 100,000 hr^{-1} for a typical monolith washcoat loading of 2 g/in^3. The CO concentrations tested increased in 1000 ppm increments from 1000 – 4000 ppm, the C_3H_6 concentrations in 500 ppm increments from 500 – 2000 ppm, and O_2 concentrations in 2% increments from 6-10%. The gas cylinder concentrations and MFC sizing for these tests are provided below in Table 3-1.

Table 3-1 Gas cylinder and mass flow controller specifications for packed bed reactor setup.

Gas	Description	Purity [%]
N_2	Carrier for reactor feed gas	99.999
O_2	Pure	99.993
CO	Balanced with N_2	10
C_3H_6	Balanced with N_2	25

3.2.2 Packed Bed Reactor

For the packed bed reactor testing, the prepared catalyst powder was pressed and sieved to 60-40 US mesh (240-425 µm) sized catalyst particles. This size of particle was selected in order to avoid reactor bypass in the quartz tube reactor with a 4 mm inner diameter (ID). If $D_{reactor}/D_{particle} > 10$ reactor bypass in a packed bed reactor can be neglected. A 29.3 mg catalyst sample was then mixed SiO_2 pellets purchased from Sigma Aldrich, which were sieved to the same size. The SiO_2 pellets were added at 10x dilution by mass in order to reduce temperature gradients in the packed bed reactor. Quartz wool was added to either side of the catalyst bed in a quartz tube in order to keep the catalyst bed stationary. The schematic of the packed bed reactor as described is shown in Figure 3-2.

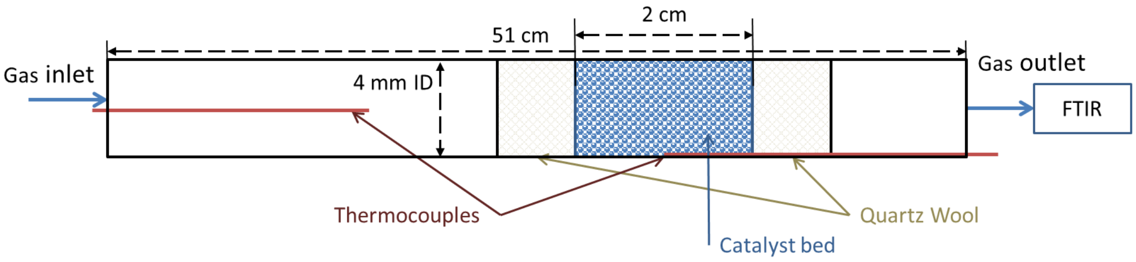

Figure 3-2 Packed bed reactor schematic.

The reactor shown in Figure 3-1 houses the packed bed reactor shown in Figure 3-2 which is heated using a Thermo Scientific Lindberg Blue M Mini-Mite tube furnace. Temperature programmed oxidation (TPO) experiments were conducted using the various reaction feed mixtures described earlier and heating the furnace from 100-300°C at a ramp rate of 5°C/min, then in 10% oxygen and nitrogen only from 300-500°C with a ramp rate of 10°C/min and a 30 min hold. Prior to the temperature ramp, the reactor was held at 100°C for 30 minutes in order to ensure a stable inlet concentration reading.

3.2.3 Analysis and Data Acquisition

Outlet concentrations were measured with an MKS MultiGas2030 FTIR gas analyzer, using the Diesel 1Hz R3 method calibrations to detect concentration levels of CO, C_3H_6, CO_2, ethylene, ethane, methane, formaldehyde, acetaldehyde, acrolein, and acetic acid. Temperatures from the thermocouples, placements shown in Figure 3-2, were recorded using National Instruments LabVIEW software and FieldPoint units. Both the concentration and temperature data were analyzed in Microsoft Excel. Conversion calculations were done with respect to the average inlet concentration measured over the 500 seconds prior to the temperature ramp, and plotted versus the inlet gas temperatures. The results of these experiments are presented in Chapter 4.

3.3 Bench Scale Monolith Reactor

The bench scale monolith reactor setup schematic is shown below in Figure 3-3. This set up features more gas species, now including NO and NO_2, as well as liquid species (DI water and liquid HC). Also for the spatial resolution experiments, which will be highlighted more in section 3.3.4, a capillary is placed into the reactor and the needle valve at the outlet of the reactor is closed slightly to increase the pressure of the reactor and cause flow through the capillary.

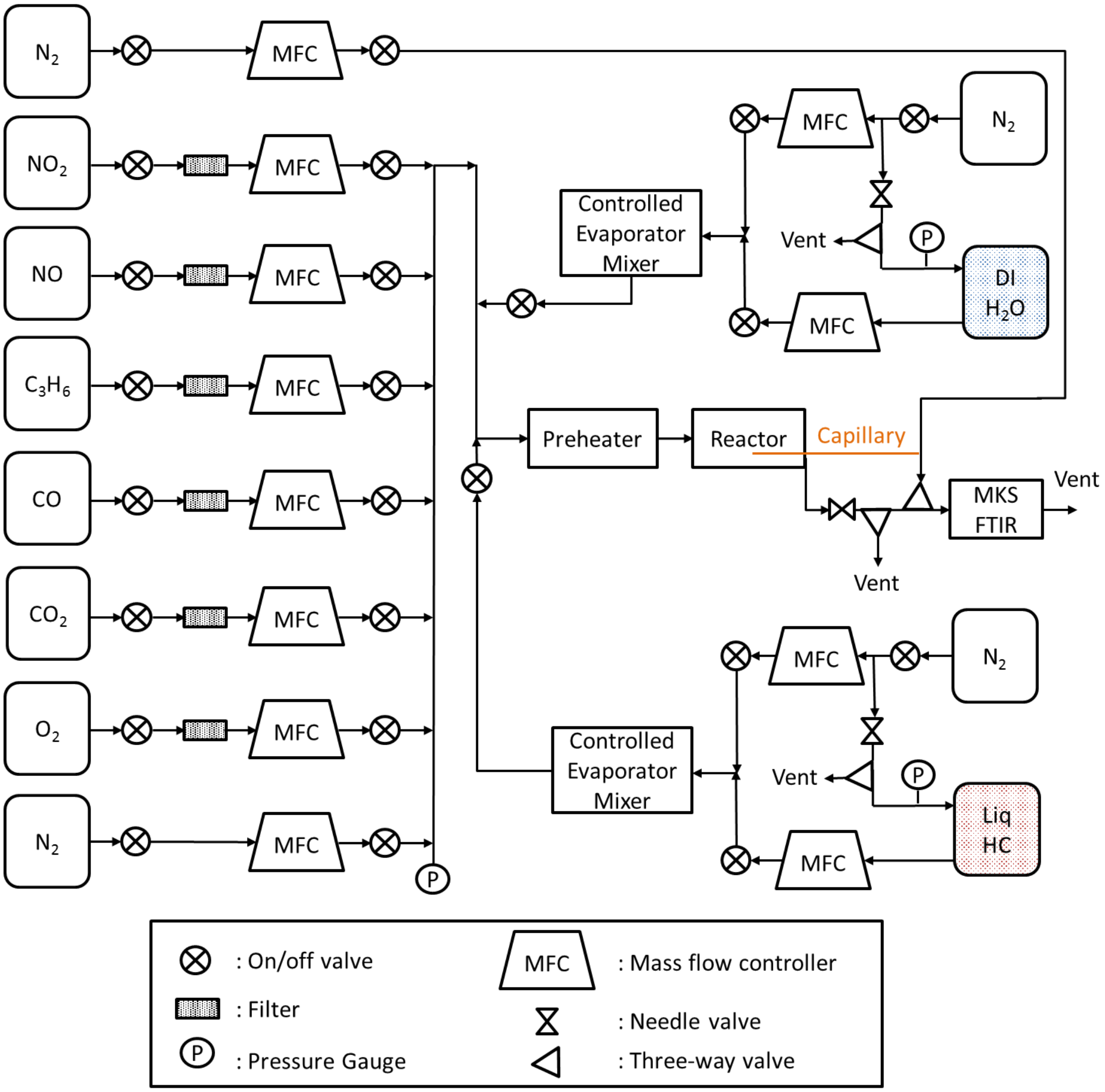

Figure 3-3 Bench scale monolith reactor experimental setup.

3.3.1 Gas Flow Specifications

Bronkhorst mass flow controllers were used to control the flow of the various gases shown in Table 3-2.

Table 3-2 Gas cylinder and mass flow controller specifications for monolith reactor setup.

Gas	Description	Purity [%]
N_2	Carrier for reactor feed gas, capillary nitrogen diluent	99.999
O_2	Pure	99.993
CO_2	Pure	99.995

Table 3-2 (continued)

CO	Balanced with N_2	10
C_3H_6	Balanced with N_2	25
NO	Balanced with N_2	0.4923
NO_2	Balanced with N_2	0.5049

3.3.2 Liquid Flow Controller Specifications

The monolith reactor has two liquid systems, one water system and one hydrocarbon system. The layout of these systems is laid out in the schematic provided earlier in Figure 3-3. A variety of liquid hydrocarbons were used for experiments in Chapter 7. These hydrocarbons were purchased from Sigma Aldrich. A stainless steel container was used to house the hydrocarbons, and after each hydrocarbon was tested a rinse of the next hydrocarbon was flushed through the system to get out the previously tested hydrocarbon.

3.3.3 Monolith Reactor

For the experiments presented in Chapters 5 and 7, the monolith reactor shown in Figure 3-4 was used. The cylindrical catalyst was cut to 2 inches in length, or 5 cm, and approximately 165 channels for testing (0.64 in or 1.62 cm diameter). The monoliths tested had a cell density of 400 cells per square inch. The end caps were custom made from stainless steel parts, and graphite ferrules were used to seal between the end caps and the quartz tube, as well as to seal the thermocouples and the 1/16” caps holding them.

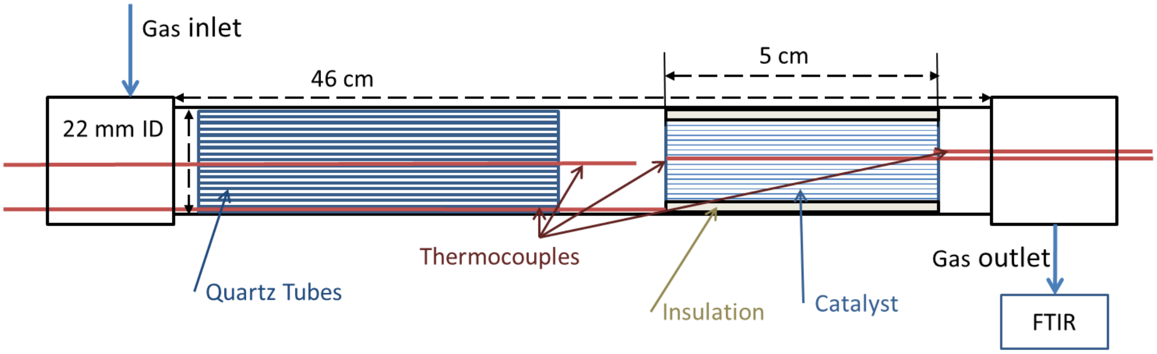

Figure 3-4 Monolith reactor schematic.

3.3.4 Spatial Resolution Monolith Reactor

For the experiments presented in Chapter 6, the spatial resolution monolith reactor shown in Figure 3-5 was used. The cylindrical catalyst was cut to 2 inches in length, or 5 cm, and 132 channels for testing (0.64 in or 1.62 cm diameter). The Pt/γ-Al_2O_3 monolith catalyst tested had a cell density of 325 cells per square inch, with a platinum loading of 50 g/ft^3, an Al_2O_3 loading of 1.59 g/in^3.

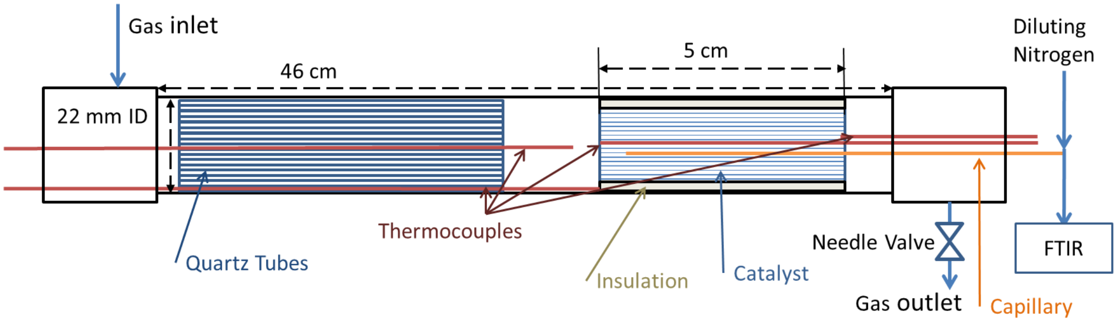

Figure 3-5 Spatial resolution monolith reactor schematic.

3.3.5 Data Acquisition and Analysis

Outlet concentrations were measured with an MKS MultiGas 2030 FTIR gas analyzer, using the Diesel 1Hz R3 method calibrations to detect concentration levels of CO, C_3H_6, CO_2, ethylene, ethane, methane, formaldehyde, acetaldehyde, and other hydrocarbons depending on the study. Temperatures from the thermocouples, placements shown in Figure 3-4, were recorded using National Instruments LabVIEW software and FieldPoint units. Both the concentration and temperature data were analyzed in Microsoft Excel. Conversion calculations were done with respect to the average inlet concentration measured over the 500 seconds prior to the temperature ramp, and plotted versus the inlet gas temperatures.

3.4 Diffuse Reflectance Infrared Fourier Transform Spectroscopy

3.4.1 Gas Flow Controller Specifications

MKS flow controllers were used to control the gas flow. A total flow rate of 50 mL/min was maintained with these controllers. The specifications for the gas cylinders used are provided in Table 3-3. All the gas lines were 1/8" stainless steel tubes, and the inlet lines were heated to 150°C using insulated heating tapes.

Table 3-3 Gas cylinder and mass flow controller specifications for DRIFTS reactor setup.

Gas	Description	Purity [%]
He	Carrier for reactor feed gas/ carrier water/carrier water	99.999
O_2	Pure	99.993
CO	Balanced with N_2	0.5
C_3H_6	Balanced with N_2	10

3.4.2 Water Injection Systems

Two water systems were used for the DRIFTS experiments. For the experiments in Chapter 5, a Bronkhorst controlled evaporator mixer (CEM) system similar to what is shown in Figure 3-3 was used to control He and water flows to get up to a desired 5% H_2O in the feed gas. In Chapter 6, a much simpler water adsorption column was used. A container at ambient temperature filled with glass beads and water had a steady flow of He passed through it; based off of FTIR measurements it was operated such that the feed gas contained 1% H_2O.

3.4.3 Reactor Cell

A small catalyst sample on the order of 30-60 mg depending on the study was placed in the High Temperature Reaction Chamber (HVC) reactor cell shown in Figure 3-6, which is in turn placed in a Harrick Scientific Praying Mantis accessory. The Harrick Scientific Praying Mantis setup is purged with 9 L/min N_2 to remove atmospheric H_2O and CO_2.

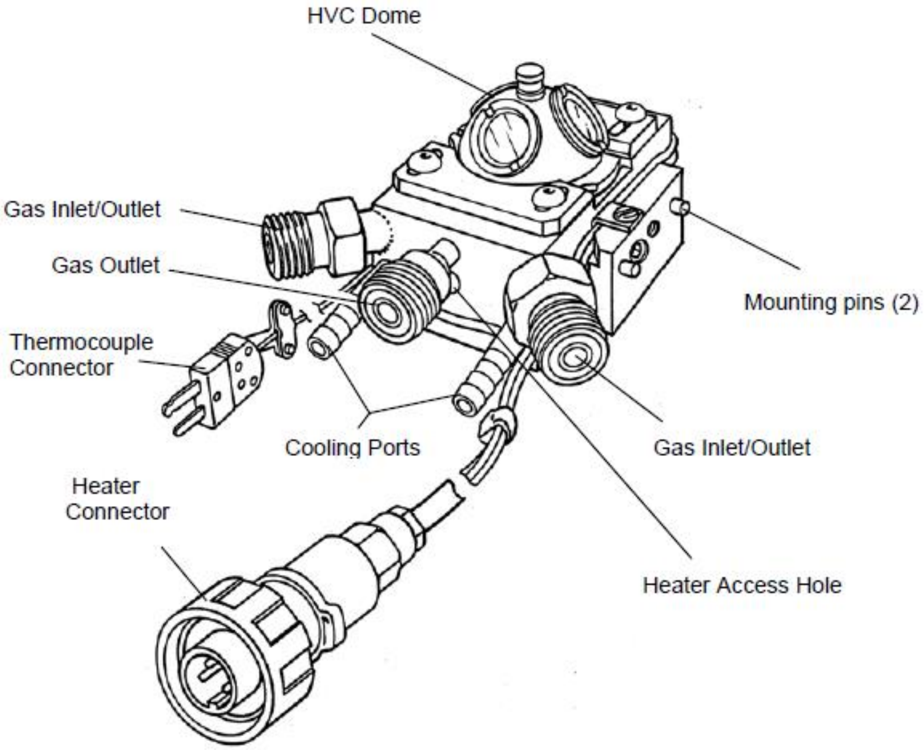

Figure 3-6 The High Temperature Reaction Chamber (HVC) [70]

The inlet gases are passed through the gas inlet port, flow over the catalyst and down through the catalyst, and out the gas outlet. The catalyst sample was either a free powder or pressed to a pellet for the testing into a sample cup of 6.5 mm diameter. A porous screen and quartz beads are placed at the bottom of the sample cup to allow the gas to uniformly pass through the catalyst from top to bottom. The HVC dome houses two optical ZnSe windows sealed with O-ring seals.

For the experiments in Chapter 4, the catalyst samples were diluted with KBr to enhance the strength of signal. For the experiments in Chapters 5 and 6 this was not necessary, and not favorable as the feed gas contained high water concentrations. A heating stage sits under the catalyst sample, and the temperature was controlled by a cartridge heater and a K-type thermocouple connected to a Harrick Scientific temperature controller. The thermocouple measures the temperature of the stage, and so the temperature of the gas stream in He during the temperature ramp was measured separately and the data presented are all plotted as a function of the gas temperature, not the temperature of the heating stage. DI water was pumped through the cooling ports shown.

3.4.4 Data Acquisition and Analysis

A Thermo Scientific Nicolet 6700 spectrometer equipped with an MCT detecter was used in the DRIFTS experiments. Thermo Scientific OMNIC software was used to record spectral data and Watlow EZ-Zone Configurator software was used to control the temperature. The DRIFTS spectra were collected in the 4000-600 cm^{-1} range. Background spectra were taken while flowing He at the starting temperature before each temperature ramp. However there was also a blank background temperature ramp conducted and subtracted from the corresponding temperature point in each temperature ramp. The ramp rate of the TPO experiments varied depending on desired temperature resolution and matching to the TPO experiments of the corresponding bench scale reactor runs, and are reported in those chapters. The reflectance spectrum is taken and converted to KM units using the OMNIC software and stored as a separate .CSV file for each temperature point. MATLAB software is used to load the .CSV files for each temperature, subtract the corresponding temperature background spectra, and save an excel file for each experiment. The number of scans taken for each spectra, unless otherwise specified, is 98 scans, giving a total scanning time of 1 minute. The resolution was 4 cm^{-1}. The temperature reported is the gas-phase temperature at the end of each 1 minute increment, or after each spectra has been taken.

An example spectrum is shown in Figure 3-7. The height of each peak is related to the surface concentration, and so many of the DRIFTS data presented in the following chapters show the peak height of a certain wavenumber as a function of temperature. In order to calculate these peak heights, a baseline between two wavenumbers is calculated for each spectrum and the value of that line at the desired wavenumber is subtracted from the reflectance to get the peak height. This is done for each spectrum at every temperature, in order to get the peak height each wavenumber of interest as a function of temperature. The baseline wavenumbers selected may vary from peak to peak, but are the same for each peak across all the experiments and all catalysts.

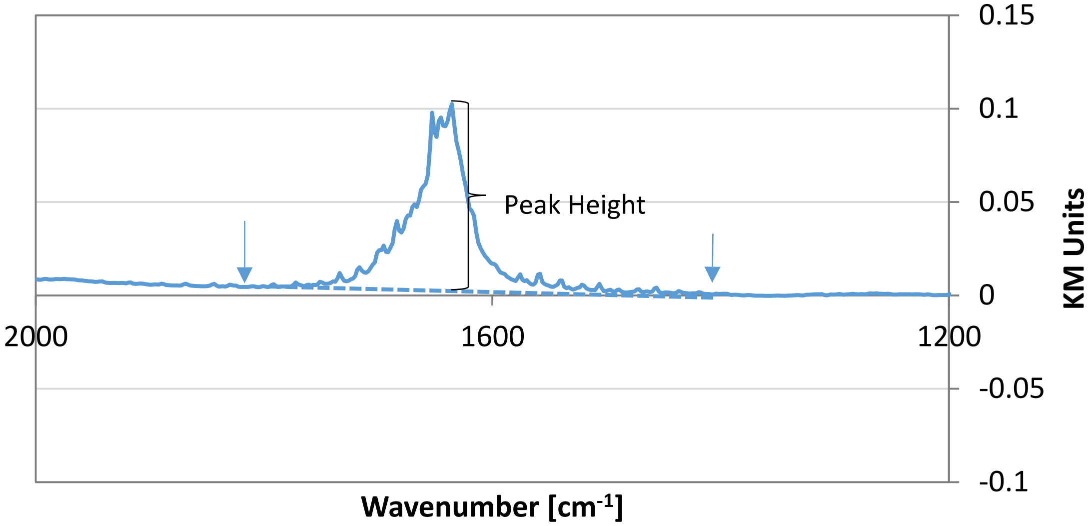

Figure 3-7 Peak height calculation example

Chapter 4 Kinetic and Mechanistic Study of Bimetallic Pt-Pd/Al_2O_3 Catalysts for CO and C_3H_6 Oxidation

Note: The material in this section has been accepted for publication in Applied Catalysis B: Environmental. Reference and figure numbers have changed for dissertation consistency.

4.1 Introduction

Increasingly stringent environmental policies due to concerns over global warming and climate change, established by agencies such as the Environmental Protection Agency (EPA), are a driving force for increasing engine fuel economy and decreasing their harmful emissions. One approach to increased fuel economies is operating under fuel lean modes, as diesel engines do, which are typically more fuel efficient than their gasoline counterparts. Furthermore, new low temperature combustion (LTC) modes being studied for diesels are even more fuel efficient.

In comparing conventional diesel combustion and two LTC technologies, reactivity controlled compression ignition (RCCI) and premixed charge compression ignition (PCCI)[3], the LTC engine emissions have much lower NO_X and particulate matter concentrations when compared to those when running the diesel engine under a normal combustion mode; however the LTC engines emitted higher concentrations of hydrocarbons and CO. This coupled with lower engine exhaust temperatures, by about 40-70°C (since the LTC modes are more fuel efficient), puts increasing emphasis on the oxidation catalyst in the exhaust aftertreatment system to oxidize CO and hydrocarbons.

With regard to how these higher concentrations affect catalyst performance, for commercial Pt and Pt-Pd/Al_2O_3 diesel oxidation catalysts (DOCs), the low CO and hydrocarbon concentrations emitted under the conventional mode reach full conversion by 190°C, while the higher concentrations emitted with the RCCI engine resulted in full conversion near 300°C [4].

Typical CO and hydrocarbon (HC) oxidation catalysts contain Pt and Pd; it is favorable to replace some Pt with Pd for economic reasons, and adding Pd to Pt-based catalysts leads to less Pt sintering relative to monometallic catalysts [7], [11], [19], [20]. It has also been shown that Pd is less sensitive to CO poisoning than Pt [71]. There is a non-linear relationship between oxidation performance and Pt or Pd content, with different Pt:Pd molar ratios achieving the lowest light-off temperatures for different compounds [5]. As an example, in a previous DOC study it was shown that a higher Pt content in bimetallic Pt/Pd catalysts led to better (lower temperature) NO, decane and propylene oxidation, while catalysts with a higher Pd content led to improved CO oxidation performance [6]. Understanding and predicting this bimetallic behavior has proven challenging as to date no apparent relationship exists between the metal properties and catalyst performance [7]. Due to the high CO and HC concentrations in LTC engine exhaust discussed above, more emphasis needs to be placed on understanding the Pt and Pd activity in the DOC.

In general, a catalyst containing a Pt and Pd blend results in improved oxidation relative to the monometallic catalysts and this has been attributed to metal alloying and bimetallic particle formation [9], [10]. The bimetallic interactions are important as Pt influences the Pd oxidation state. For example, in the monometallic case Pd is completely oxidized after calcination and in the zero valent state after reduction, whereas in bimetallic catalysts both metallic and oxidized forms are present after calcination and reduction [11].

Multiple characterization techniques have been used to understand the Pt:Pd bimetallic particle structures supported on a variety of materials (SiO_2, Al_2O_3, zeolites, carbon); such as extended X-ray absorption fine structure (EXAFS) [9], [12]–[14], X-ray absorption near edge structure (XANES) [12], transmission electron microscopy (TEM) [9], [12], [13], and diffuse reflectance infrared Fourier transform spectroscopy (DRIFTS) [10]. All these techniques show that Pd segregates to the particle surfaces, leading to a Pt core surrounded by metallic Pd, or small Pd particles dispersed on the Pt core. It has also been shown that Pd surface segregation increased with particle size, and with small particle sizes Pt was also present at the surface [15]. Also, under high temperature oxidizing conditions, some metallic Pd in these bimetallic particles was oxidized into PdO clusters [16]. However, another study found that surface segregation under oxidizing conditions did not occur, and the particles appeared as alloys with PdO dispersed on the support [17]. In yet another study the authors concluded that under oxidizing conditions and with large CO concentrations in the gas phase, oxidized Pd was not the active site for CO oxidation as is often suggested, but instead the active site was metallic Pd [29].

Thus, not only does changing the Pt:Pd ratio change particle size, metal oxidation state and which metal is present at the particle surface; these properties in turn can vary as a function of reaction conditions, adding to the complexity. In this study we used chemisorption, microscopy, diffuse reflectance infrared Fourier transform spectroscopy (DRIFTS), and CO and C_3H_6 oxidation reactor studies to better understand the catalytic activity and CO and C_3H_6 oxidation reaction mechanisms as a function of Pt:Pd ratio.

4.2 Experimental

4.2.1 Catalyst Synthesis

Monometallic Pt and Pd, and different Pt:Pd ratio bimetallic catalysts were prepared by incipient wetness impregnation on Al_2O_3, using $Pt(NH_3)_4(NO_3)_2$ and $Pd(NO_3)_2$ precursors. The Al_2O_3 was supplied by SASOL Germany, the $Pd(NO_3)_2$ and $Pt(NH_3)_4(NO_3)_2$ were both purchased from Sigma Aldrich. All catalysts prepared were based on the metal molar concentration of a 1 wt% Pt catalyst loading, i.e. the monometallic Pd catalyst contained 0.55 wt% Pd. Catalysts were dried overnight and the heated to 550°C at a 5°C/min ramp rate, and held at 550°C for 4 hours as the calcination step.

4.2.2 CO Chemisorption

Temperature programmed desorption (TPD) after CO adsorption was used to measure dispersion [68]. These TPD experiments were done on a bench reactor setup; the total flow rate was 200 mL/min and the CO concentration in the initial adsorption stage was 7000 ppm in N_2 at 30°C for 1 hour, followed by only N_2 for 80 minutes to desorb the physically adsorbed CO, and then a 28°C/min temperature ramp up to 835°C to desorb all the chemically adsorbed CO. The desorbed CO was measured and used to calculate particle size. For CO a stoichiometry of 1 was assumed to calculate particle sizes. The site density for Pt and Pd were taken as 0.0800 and 0.0787 nm^2/atom respectively [69].

4.2.3 Microscopy

High-angle annular dark-field and bright-field STEM images were recorded using a JEOL 2200FS FEG (S)TEM equipped with a CEOS GmbH (Heidelberg, Ger) hexapole aberration-corrector on the probe-forming lenses. Energy-dispersive x-ray spectroscopy (EDS) results were acquired from a Bruker-AXS X-Flash silicon-drift detector (SDD) mounted on the column; the 30-mm^2 detector provided a collection angle of <0.1 sr.

Because of the limitations of the collection efficiency for the available SDD system, spectra were recorded using a probe current of ~290 pA (i.e. using AMAG mode spot size 4C with a 26.5 mrad semi-angle probe convergence) to provide a reasonable count rate for best statistics. The Objects mode of the Bruker Esprit software was used to select a scan area to cover the entire area of e.g. a 2-5 nm catalyst particle, and a spectrum was collected for 10-30 seconds, a time after which the alumina support became too damaged by beam effects to reliably retain the catalyst particle. On some occasions, “hypermaps” were acquired over a larger area containing a number of catalyst particles, from which EDS quantification values could be obtained by post-processing within the Bruker ESPRIT software, using the Cliff-Lorimer method. Frequency distributions were calculated from these results. The Pt/Pd ratios for ≥10 particles in the 2-5 nm range were sorted into 5% Pt bins ranging from 27.5-77.5% Pt for each bimetallic catalyst. The EDS ratios were sorted into bins that were less than or equal to the bin value (i.e. ≤27.5%, >27.5% but ≤32.5%, etc.). Frequencies were calculated based on the total number of particle ratios measured for each catalyst.

4.2.4 Catalyst Bench Reactor Testing

In reactor tests, 29.3 mg of catalyst was used. The powder material was pressed and sieved to 40-60 US sieve mesh along with SiO_2 particles, and placed in a 4 mm ID quartz tube reactor. The SiO_2 particles were purchased from Sigma Aldrich and were added, at 10x dilution by mass, to minimize temperature gradients. Quartz wool was placed on both sides of the catalyst to keep the catalyst bed stationary.

Temperature programmed oxidation (TPO) experiments were conducted with 3000 ppm CO, and/or 1500 ppm C_3H_6 with excess O_2 (6 or 8 vol%) in order to approximate LTC exhaust conditions. Note that no H_2O and CO_2 were used in these tests; while the CO_2 is not expected to affect the kinetics, H_2O has a known effect on CO and hydrocarbon oxidation. We started with a simple kinetic study without H_2O, so as to decouple any H_2O effect as a function of Pt:Pd ratio on CO and hydrocarbon oxidation, and avoid water gas shift and reforming reactions complicating interpretation as well. MKS mass flow controllers were used to control the gas flow rates to create the desired inlet gas concentrations. Inlet and outlet gas lines were heated above 100°C, in order to avoid product water condensation on the lines. Outlet gas concentrations were measured with a MKS MultiGas 2030 FTIR gas analyzer with built in calibrations.

TPO experiments were conducted from 100-300°C with a 5°C/min ramp rate, and then the CO and/or C_3H_6 were shut off and the ramp continued to 500°C and held for 30 min in 10% O_2 and N_2 only, to pretreat the catalyst for the next experiment. A Thermo Scientific Lindberg Blue Minimite tube furnace was used. Prior to the temperature ramp, the reactor was held at 100°C in order to ensure a stable inlet concentration measurement.

One thermocouple was placed ~2 cm upstream of the catalyst to measure gas inlet temperature, and one thermocouple was placed in the catalyst bed center. A 400 mL/min total flow rate was used, which corresponds to a 100,000 hr^{-1} monolith space velocity for a 2 g/in^3 monolith washcoat loading (292k hr^{-1} on a powder basis). The temperature and concentration data were averaged every 2 seconds, and conversion calculations were done with respect to the average inlet concentration measured over the 500 seconds prior to the temperature ramp. Turnover frequencies were calculated using the dispersion determined from the CO TPD experiments, and a particle molecular weight corresponding to the Pt:Pd ratio on the catalyst.

4.2.5 Diffuse Reflectance Infrared Fourier Transform Spectroscopy (DRIFTS)

In order to identify adsorbed species and possible differences in the oxidation states of the monometallic versus bimetallic samples, in situ DRIFTS experiments were performed using a Nicolet 6700 spectrometer equipped with a MCT detector and a high temperature Harrick Scientific Praying Mantis reaction chamber with ZnSe windows. 30 mg of catalyst was mixed with an equal amount of KBr to form the sample. The DRIFTS spectra were collected in the 4000-650 cm^{-1} wavenumber range, accumulating 98 scans at 4 cm^{-1} resolution.

TPO experiments were performed as part of the DRIFTS experiments. The sample was heated at 5°C/min from 100 to 365°C, and run such that a spectrum was obtained every 5°C. As measured by a thermocouple placed in the gas stream, this corresponded to a 4.2°C/min temperature ramp from 80 to 300°C. A background spectrum was taken at the beginning of the temperature ramp in flowing He, and then the reactant gases were added and the samples were exposed to the feed gas for at least 1 hour before the temperature ramp was started.

The concentrations in the DRIFTS experiments were 0 or 3000 ppm CO, 0 or 1500 ppm C_3H_6, with 8% O_2 in balance He. A 50 mL/min total flow rate was maintained using MKS mass flow controllers. TPO experiments were also performed with O_2 and He only so the spectral data obtained could be subtracted from the spectra obtained during the TPOs with CO, C_3H_6, and both CO and C_3H_6. This was done in order to remove any background shift due to temperature and any other temperature effects. A pretreatment before the experiments and between each TPO experiment at 500°C with 10% O_2 for 30 minutes was used, similar to the pretreatment for the bench reactor testing.

4.3 Results

4.3.1 Catalyst Characterization

The chemisorption results translated to particle sizes are listed in Table 4-1. These catalysts have comparable average particle sizes, all in the 1.6-3.6 nm range. The bimetallic particle compositional morphology was measured by energy-dispersive X-ray spectroscopy (EDS), and these results are shown in Figure 4-1. The x-axis represents the mid-point of the frequency bin used to sort Pt/Pd atomic ratios measured by EDS. Low collection times were required to prevent beam-induced morphology changes to the metal particles resulting in low EDS counts, therefore the frequencies were sorted into ranges to provide more of a qualitative comparison between the different Pt:Pd catalysts.

Table 4-1 Average particle size as a function of Pt:Pd ratio as determined by CO chemisorption using 1:1 adsorption stoichiometry

Ratio (Pt:Pd)	1:0	3:1	1:1	1:3	0:1
Particle Size [nm]	1.9	1.6	2.7	3.6	2.5

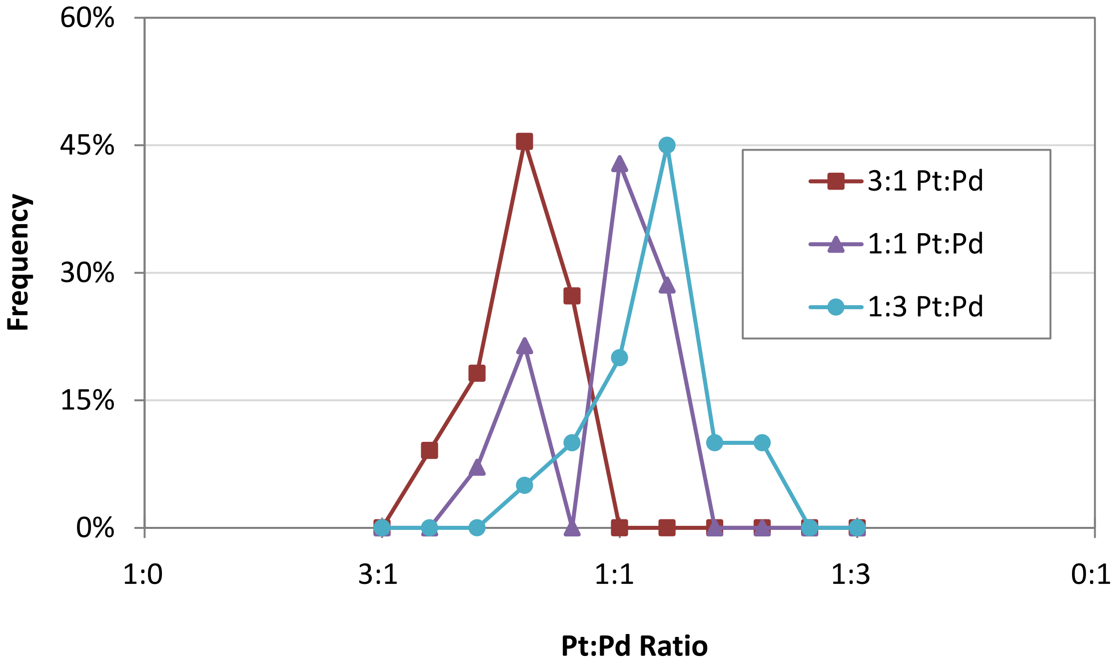

Figure 4-1 Compositional morphology determined using EDS data

Sample loading of the TEM grids often resulted in clumping of the alumina support particles resulting in micrographs which showed both particles in the 2-5 nm range and what resemble agglomerations of particles. Many of these larger agglomerates were the result of the alumina support particles overlapping and do not represent large connected Pt:Pd particles. Therefore, to better represent the catalytically available environments only isolated particles in the 2-5 nm range were evaluated for the graph in Figure 4-1. The EDS data from the 3:1 Pt-Pd catalyst particles suggests Pt-rich Pt-Pd particles; however the frequency distribution of the particles are centered slightly lower, more in the 3:2 Pt:Pd range. High resolution ACEM imaging of the 3:1 catalyst consistently shows rafts < 1 nm. Platinum rafts consisting of 10-20 Pt atoms have been previously observed by ACEM on alumina supported catalysts and likely make-up the remainder of the Pt loading [72]. The 1:1 Pt-Pd catalyst appears to form predominately 1:1 Pt-Pd particles. A high frequency of the Pt-Pd particles on the 1:3 catalyst also fall in the 1:1 Pt-Pd range rather than the anticipated Pd-rich composition. This may suggest that the 1:1 Pt-Pd particles are favored over Pd-rich bimetallic particles during synthesis. The remaining Pd loading is likely present as smaller PdO particles.

Longer EDS collection times over larger areas show that the overall quantification of the Pt:Pd ratios more closely match those used during synthesis, supporting the presence of Pt-only and Pd-only particles to make up the loading imbalances on the 3:1 and 1:3 catalysts. Note, these data clearly show non-uniformity in particle sizes and to some extent composition (with 2 seemingly evident for the 1:3 and 3:1 samples). Such will influence the analysis of the characterization of surface species and where they reside, and admittedly leave questions. However, the synthesis approach used is quite common/typical and thus in the simplest of context the results are meaningful from a practical viewpoint. But also, the results discussed below can be used to distinguish reaction and mechanisms, even with multiple particle types, as will be shown.

4.3.2 CO Oxidation Results

4.3.2.1 Reactor Testing

The CO oxidation conversion data are shown in Figure 4-2 (a). The conversion versus temperature profiles for the Pt, 3:1 and 1:1 Pt:Pd catalysts have a much steeper slope above 20% conversion than the Pd and 1:3 Pt:Pd catalysts. Also, the light-off temperatures for the bimetallic catalysts are generally lower than those for the monometallic catalysts. In evaluating the turnover frequencies, shown in Figure 4-2 (b), no differences in trends are observed. Full CO conversion over the 1:3 Pt:Pd and the monometallic Pd catalyst was not attained, even at high temperature.

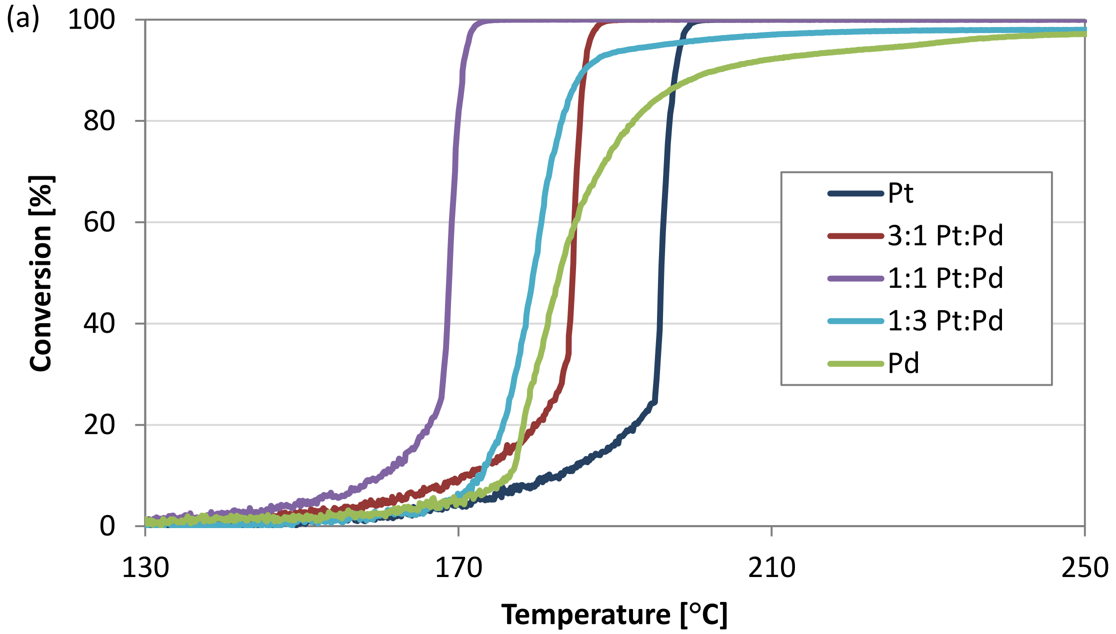

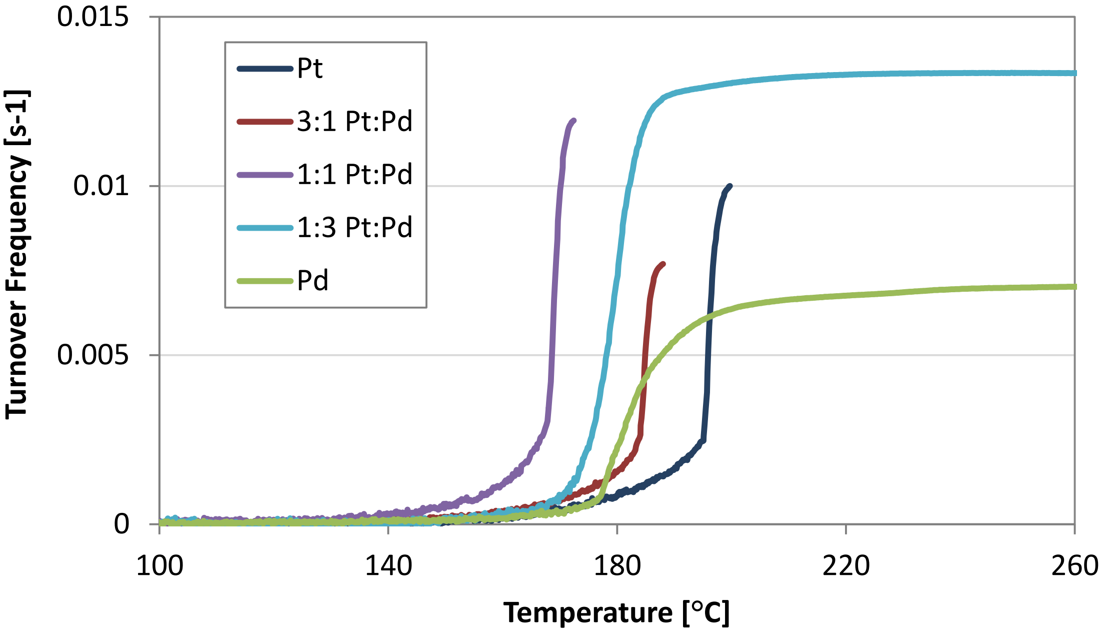

Figure 4-2 (a) CO conversion and (b) turnover frequency as a function of temperature during TPO; 3000 ppm CO, 8% O_2 *in balance* N_2

The temperatures corresponding to 50% CO conversion, T_{50}, where 4 different CO inlet concentrations were used in the inlet gas are shown in Figure 4-3. The difference in CO oxidation performance between the monometallic Pt and Pd samples increased as the CO concentration increased; the monometallic Pt catalyst performance was nearly identical to that of the Pd for 1000 ppm CO, but the successive increase to 2000, 3000 and 4000 ppm CO led to 5°C, 13°C, and 19°C differences between the Pt and Pd catalyst T_{50} values. For the bimetallic samples, there were also some differences in T_{50} with CO concentration increase. If a performance ranking in terms of T_{50} is used, it changes as a function of CO concentration. For all concentrations, the 1:1 and 1:3 Pt:Pd catalysts result in the best and second best performance in terms of T_{50}, respectively. The 3:1 and monometallic Pt catalyst T_{50} values are lower than that of the Pd catalyst at low CO concentrations, but then their performance falls below the monometallic Pd catalyst at 2000 ppm for the Pt catalyst and 3000 ppm for the 3:1 Pt:Pd catalyst.

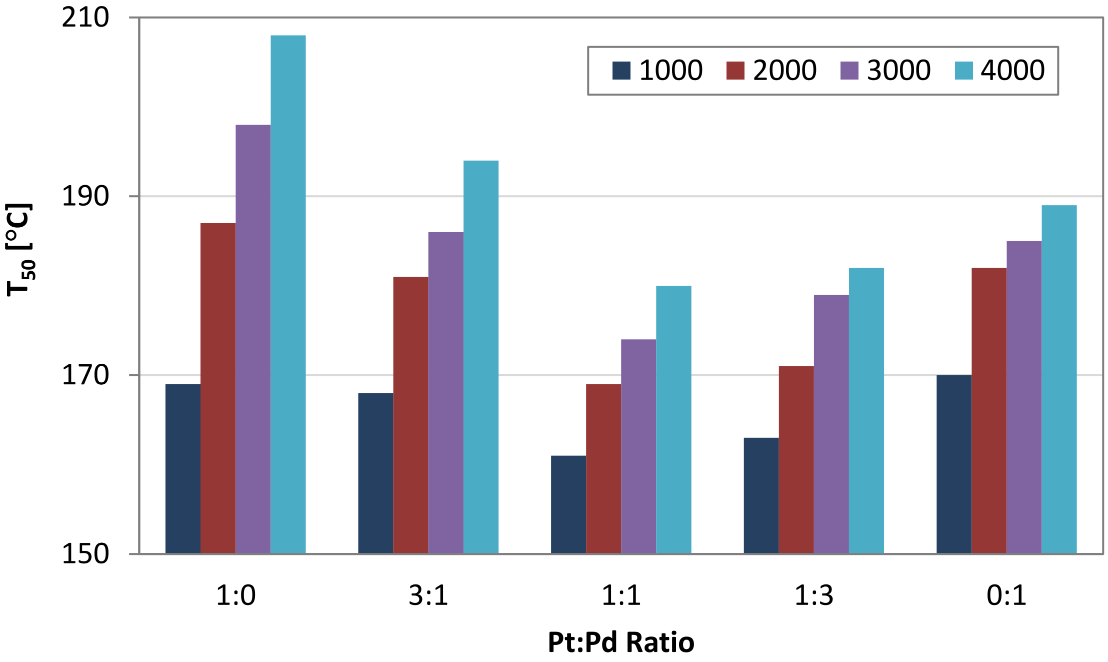

Figure 4-3 CO Oxidation performance with different CO concentrations [ppm] in terms of T_{50}, the temperature where 50% of the inlet CO is oxidized; 1000-4000 ppm CO, 6% O_2, balance N_2

4.3.2.2 DRIFTS Testing

DRIFTS was used to characterize CO interactions with the catalyst surfaces during adsorption and TPO experiments, using a similar approach to that taken with a monometallic Pt catalyst [73]. The DRIFTS spectra obtained after sample exposure to CO and O_2 at 80°C for 1 hour are shown in Figure 4-4 (a) and at 200°C in Figure 4-4 (b), and the species represented by the spectral features are labeled based on literature results. The small feature at ~2200 cm^{-1} corresponds to CO on Lewis acid sites 2190-2200 cm^{-1} [74], and is not considered catalytically important. In comparing the Pt catalyst to the Pd catalyst, there were large differences in the amounts of linear bound carbonyl and triply bound CO between the two.

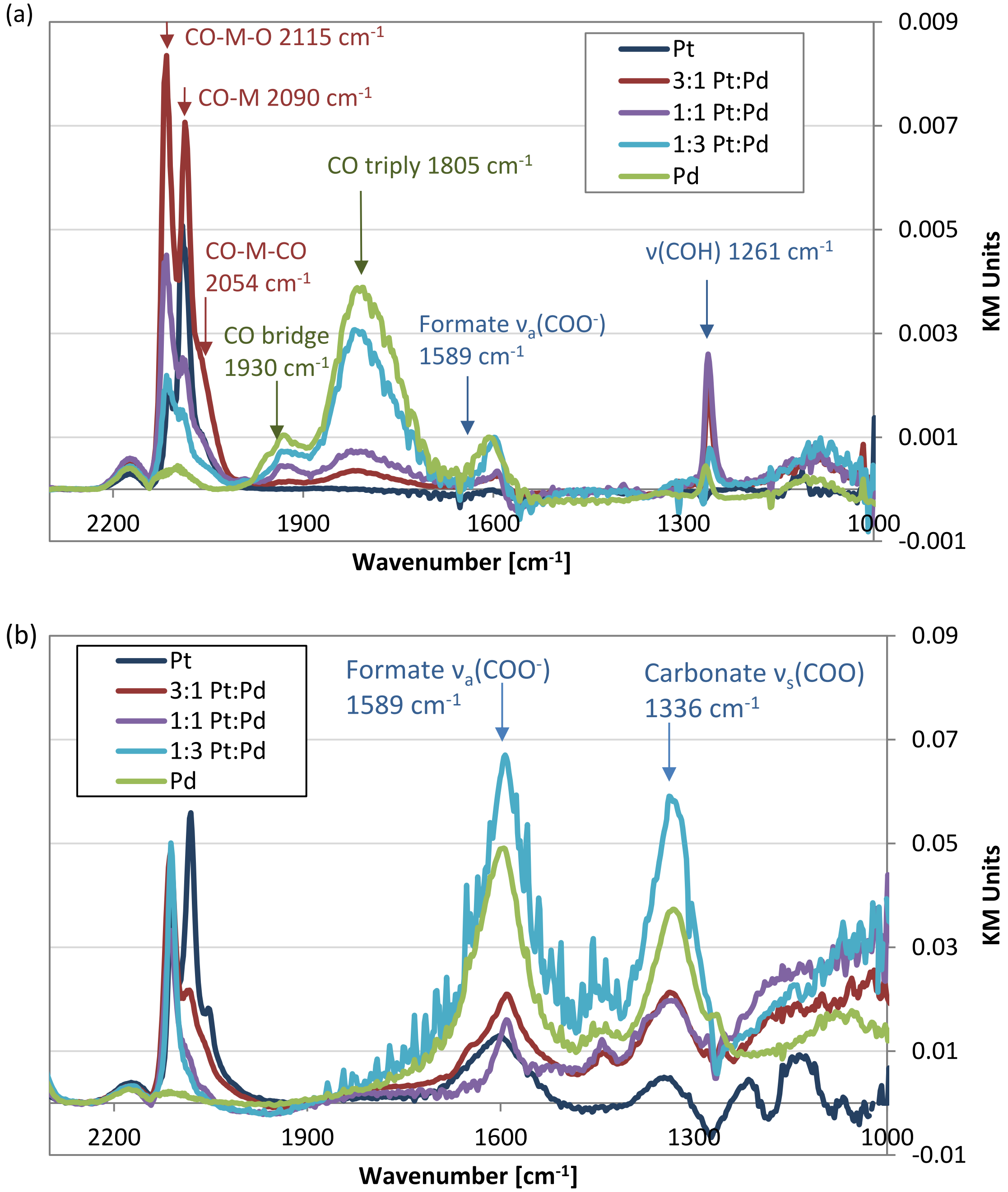

Figure 4-4 DRIFTS spectra during catalyst exposure to CO and O_2 at (a) 80°C and (b) 200°C, with 98 scans at 4 cm^{-1} resolution in 2300-1000 cm^{-1} region; 3000 pm CO, 8% O_2, balance He

The Pd contained less linearly bound and more triply bound, with also some bridge bound carbonyls (at 1930 cm^{-1}). This is consistent with the Pd(111) crystal structure, where Pd(100) would favor linearly bound carbonyls, and Pd(111) favors triply bound CO in the three fold hollow sites [29], [71], [75]. Both of these linearly bound CO features commonly appear with high CO concentrations and the resulting high CO coverages. The lower wavenumber linear carbonyl peak, around 2090 cm^{-1}, is assigned as a single linear carbonyl (labeled as CO-M in subsequent figures, where M represents Pd or Pt), and the higher wavenumber feature at 2111 cm^{-1} (labeled as CO-M-O in subsequent figures) indicates either a dicarbonyl [76]–[79], which has been observed on small particles or atomic Pt, or a linear carbonyl attached to a Pt that is also attached to atomic oxygen [34], [72], [80], [81]. If the 2111 cm^{-1} peak corresponded to a dicarbonyl, another dicarbonyl feature should be observed at 2050 cm^{-1}.

Calculated relative CO-associated peak heights indicate that the 2050 cm^{-1} peak (hereafter labeled as CO-M-CO) is not large enough in comparison to the 2111 cm^{-1} peak for this peak to correspond to only the dicarbonyl species. For instance, in comparing the Pt catalyst to the 1:1 Pt:Pd catalyst, the relative height of the CO-M-O was 230% larger, while the relative height of the CO-M-CO peak was 25% smaller, which clearly indicates that the 2111 cm^{-1} corresponds to something other than only dicarbonyl. Therefore the 2111 cm^{-1} peak has been interpreted as CO-M-O where the carbonyl is adsorbed with atomic oxygen on a metal site, either Pt or Pd. Both the 3:1 Pt:Pd and monometallic Pt catalysts had large linear carbonyl features, but they differed in type. The monometallic sample formed the most CO-M, whereas the 3:1 formed the most CO-

M-O. The 1:1 catalyst formed a large amount of both linear carbonyl in CO-M-O configuration and bridged carbonyl species.

The carbonate and carboxylate peak assignments in the 1800-1000 cm^{-1} range are as follows. The anticipated species for CO oxidation include formate, free carbonate ions, monodentate carbonate, bidentate carbonate, bicarbonate, and COH species. For the formate species, the peaks identified from literature are ν(C-H) at 2962, $\nu_a(COO^-)$ at 1600, and $\nu_s(COO^-)$ at 1394 or 1363 cm^{-1} [35], [74], [82], [83]. For the free carbonate ion, the peaks are $\nu_a(CO_3^{2-})$ at 1450-1420 and $\nu_s(CO_3^{2-})$ at 1090-1020 cm^{-1} [35], [84]. For the moodentate carbonate, the peaks are ν_a(COO) at 1530-1470, ν_s(COO) at 1300-1370, and ν(C-O) at 1080-1040 cm^{-1} [35], [85]. For the bidentate carbonate, the peaks are ν(C=O) at 1530-1620 or 1620-1670, ν_a(COO) at 1270-1250 or 1220-1270, and ν_s(COO) at 1030-1020 or 980-1020 cm^{-1} [35], [85]. For bicarbonate, the peaks are ν(C=O) at 1640-1650, ν_a(COO) at 1430-1470, ν_s(COO) at 1304, and ν(COH) at 1230 cm^{-1} [74], [86]–[88]. For COH, the peak for ν(COH) is at 1270 cm^{-1}; and for HCOH, a bending mode occurs at 1200 cm^{-1} [89]. Many of these peaks for the species mentioned overlap, however using some process of elimination and considering the results in Figure 4-4 (a) allows distinctions to be made. The observed peaks at 1601-1589 cm^{-1}, together with that at 2962 cm^{-1} and a broad peak around 1370-1320 cm^{-1} indicate that there may be formate present. For monodentate carbonate, while there were peaks in the 1300-1370 and 1080-1040 regions, there was not a peak at 1530-1470 cm^{-1} and so this species can be eliminated. For bidentate carbonate, the ν(C=O) of the bidentate was close to the $\nu_a(COO^-)$ of formate, and if present we would expect to see peaks at 1270-1220 and

1080-1040 cm^{-1}, both of which were observed at 80°C and so this surface species is also possible. For the bicarbonate, the peaks anticipated are similar to bidentate carbonate, with the exception of ν_a(COO) at 1430-1470, and ν_s(COO) at 1304. There were no peaks in the 1430-1470 region, and so this bicarbonate species can be eliminated. This leaves formate and bidentate carbonate as possible species that were observed at the beginning of the temperature ramp. These species changed in amount, and other surface species formed, during the temperature ramp, with the spectra obtained at 200°C shown in Figure 4-4 (b). A small peak at 1456 cm^{-1} appeared, and the peaks already discussed increased in intensity. The peak at 1456 cm^{-1} may indicate either free carbonate ions, monodentate carbonates, or bicarbonate. Due to the absence of peaks in the 1220-1270 cm^{-1} range it should not be bicarbonate species; this peak disappeared quickly during the temperature ramp and so this also allows us to identify the 1600 cm^{-1} feature that was at first assigned to either formate or bidentate carbonate to formate only. With the peak at 1456 cm^{-1}, the peak at 1327-1336 cm^{-1} is assigned to the monodentate carbonate species; the expected peaks for formate in this region would be at a slightly higher wavenumber, and in addition we will see that the trends with temperature of these two peaks vary and so we can differentiate them as being related to the different species. Thus the only two peaks in the carbonate/carboxylate region discussed further are the peak at 1589-1601 cm^{-1} associated with formate's ν_a(COO$^-$) and the peak at 1327-1336 cm^{-1} associated with monodentate carbonate's ν_s(COO).

The key feature heights identified above were measured and used to track relative amounts on the surface as a function of temperature, with these results shown in Figure 4-5. In comparing the results of the monometallic samples in Figure 4-5 (a) and (e), formate and carbonate species were formed in greater quantity on the Pd sample relative to the Pt sample. For the bimetallic catalysts in Figure 4-5 (b)-(d), with increasing Pd content, the formate and carbonate peak heights increased. For the Pt, 3:1 Pt:Pd, and 1:1 Pt:Pd catalysts there is a much stronger formate feature relative to carbonate. The height of the various carbonyl species on the catalysts all have maxima at different temperatures; the maxima of the linearly adsorbed species are at higher temperatures than the triply adsorbed species. As the Pd content increases, less CO-M-CO was detected and more triply bound CO was present. The CO-M-O was the largest peak for the 1:1 Pt:Pd catalyst at elevated temperatures, while the same sample had the smallest carbonate peak height through the temperature ramp.

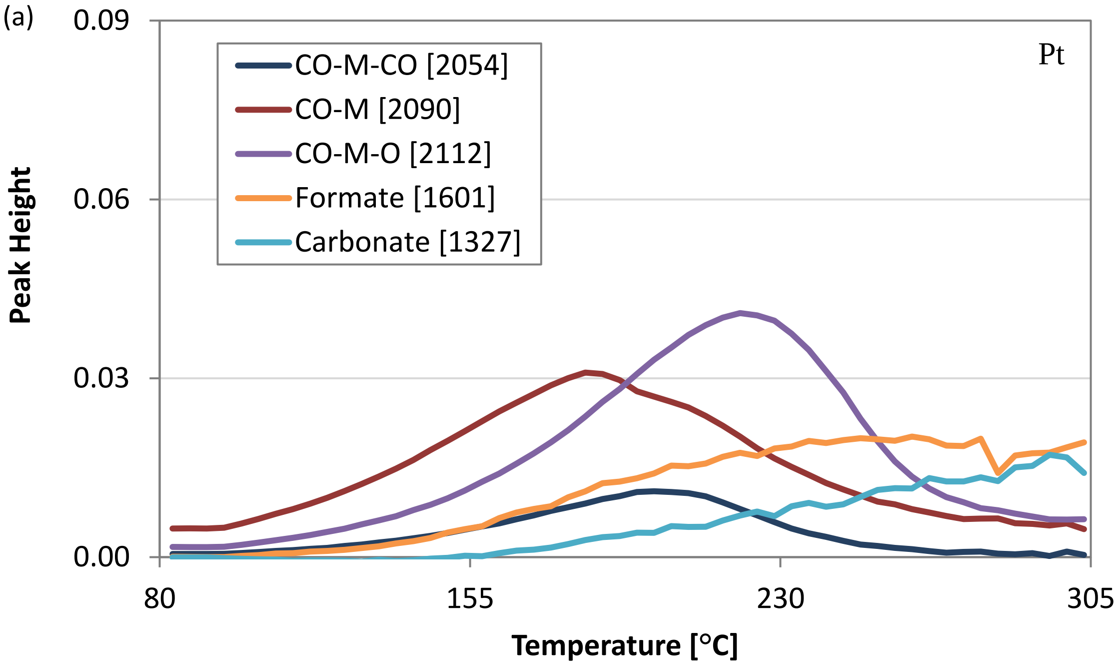

(b)

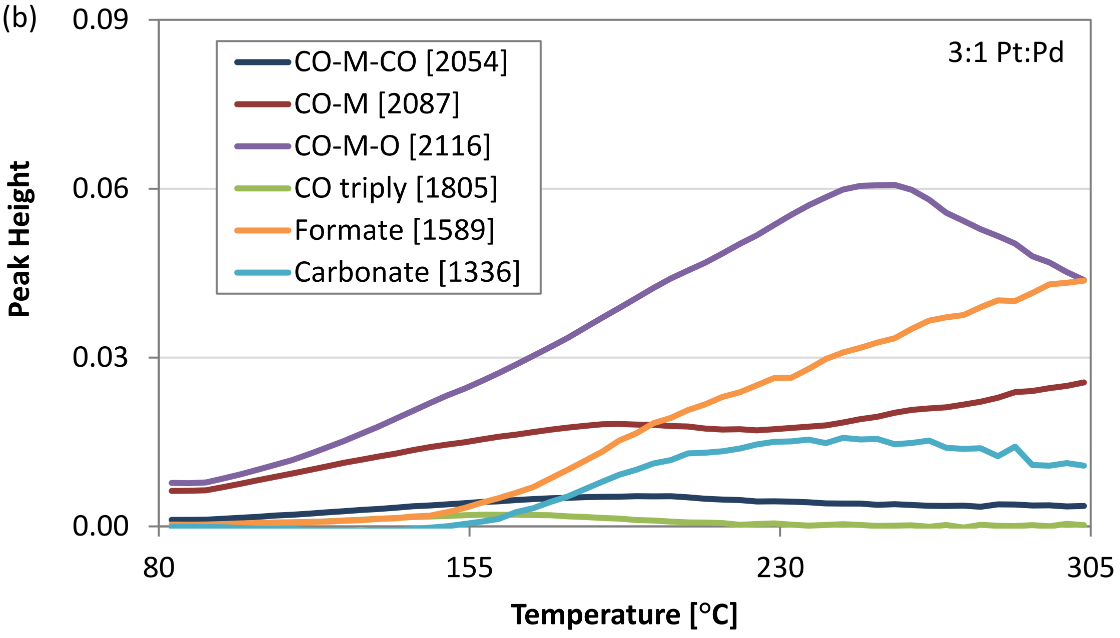

Peak Height
0.09
0.06
0.03
0.00
80
155
230
305
Temperature [°C]
CO-M-CO [2054]
CO-M [2087]
CO-M-O [2116]
CO triply [1805]
Formate [1589]
Carbonate [1336]
3:1 Pt:Pd

(c)

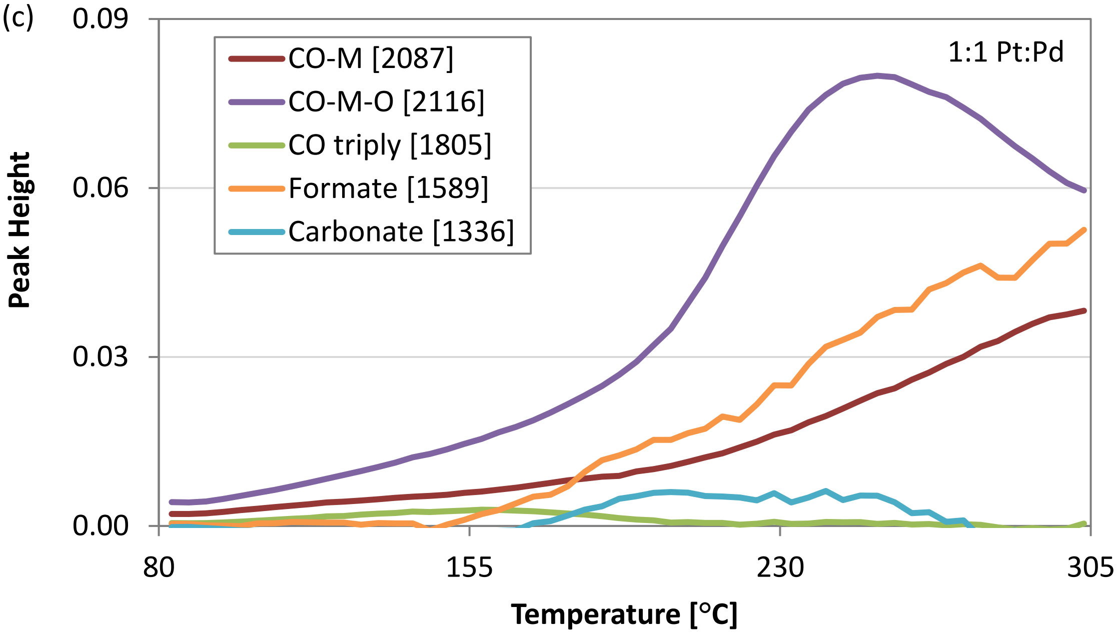

Peak Height
0.09
0.06
0.03
0.00
80
155
230
305
Temperature [°C]
CO-M [2087]
CO-M-O [2116]
CO triply [1805]
Formate [1589]
Carbonate [1336]
1:1 Pt:Pd

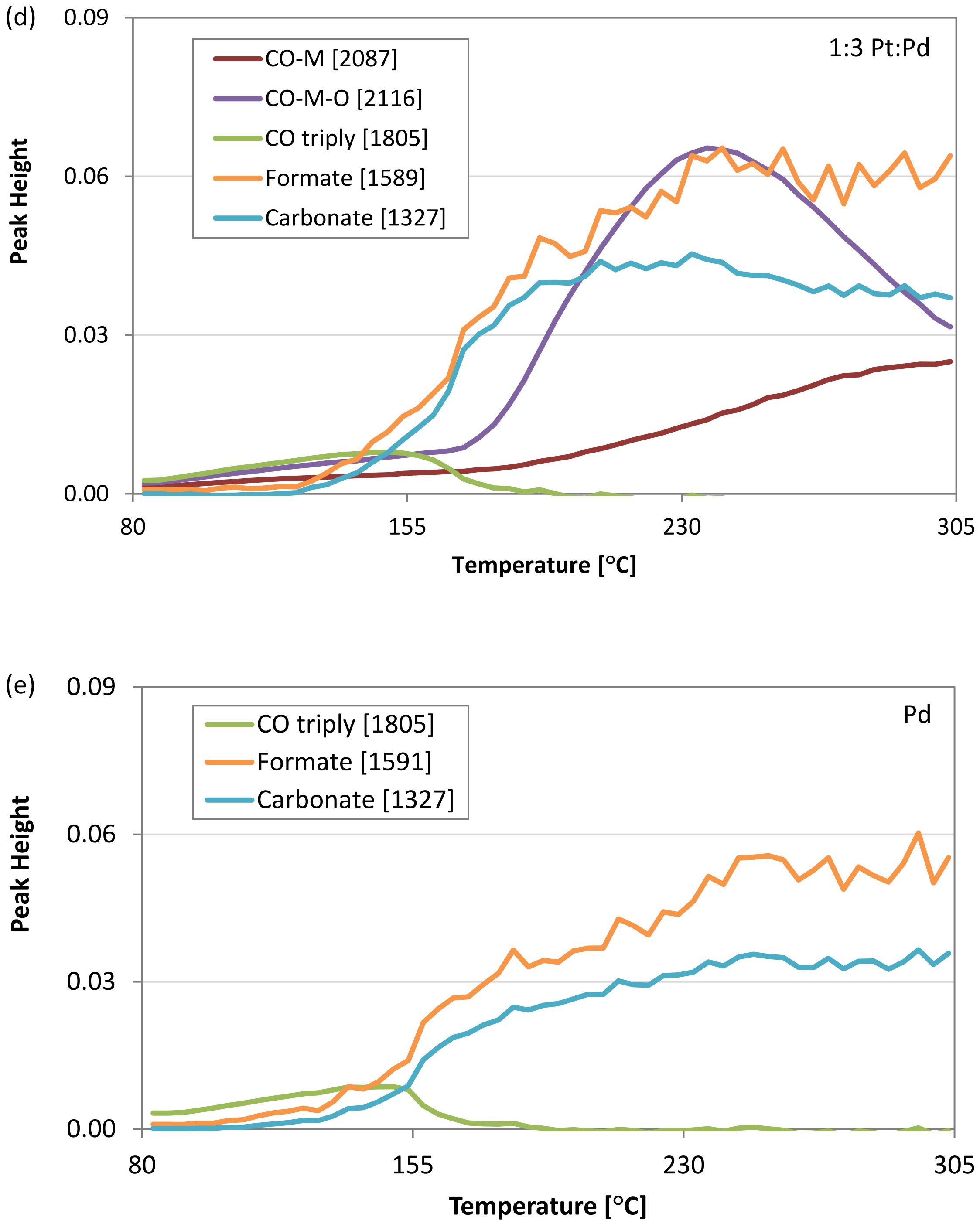

Figure 4-5 Peak height as a function of temperature for peaks of interest in CO oxidation [wavenumber in cm^{-1}] (a) Pt, (b) 3:1 Pt:Pd, (c) 1:1 Pt:Pd, (d) 1:3 Pt:Pd, (e) Pd

4.3.3 C_3H_6 Oxidation Results

4.3.3.1 Reactor Testing

Propylene oxidation performance as a function of temperature and the different Pt:Pd ratios is shown in Figure 4-6 (a) for one C_3H_6 concentration level. The oxidation performance follows a similar trend as observed for CO oxidation in that the bimetallic catalysts showed better performance relative to the monometallic samples. Here though, the Pt catalyst was better than Pd, which was expected as Pt is generally a better alkene hydrocarbon oxidation catalyst than Pd [5]. Oxidation light off occurred at a lower temperature with the 1:1 Pt:Pd than the 3:1 Pt:Pd catalyst, however the 3:1 Pt:Pd catalyst reached full conversion at a lower temperature. The 1:3 Pt:Pd catalyst performance was similar to the Pd catalyst with just a slightly lower light off temperature and it reached a point where the conversion plateaued and did not improve any further as the temperature was increased.

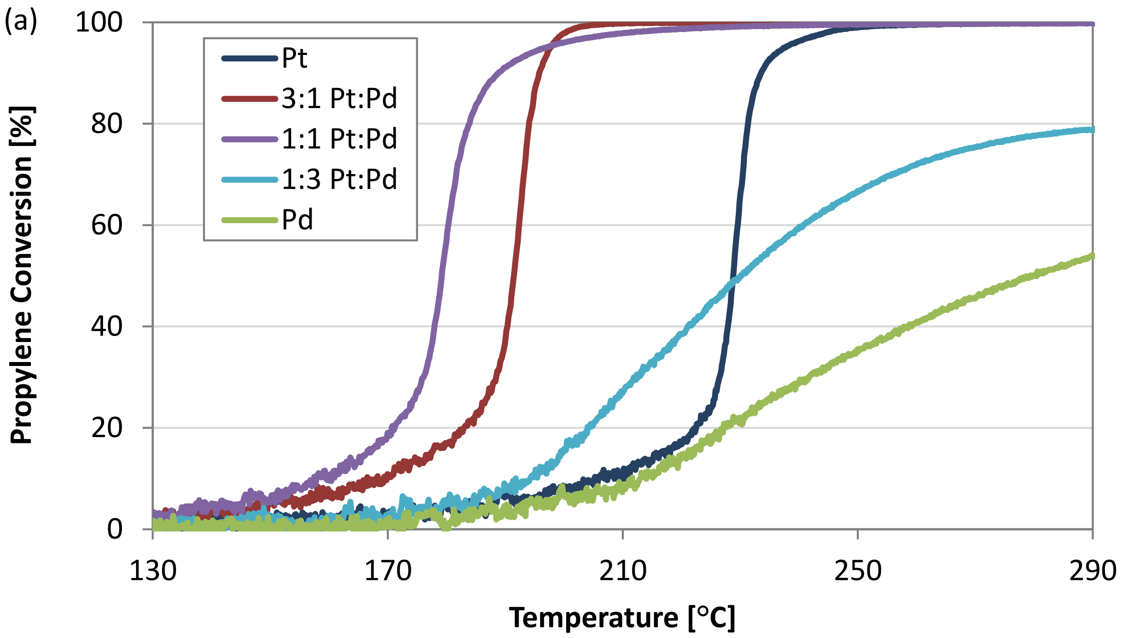

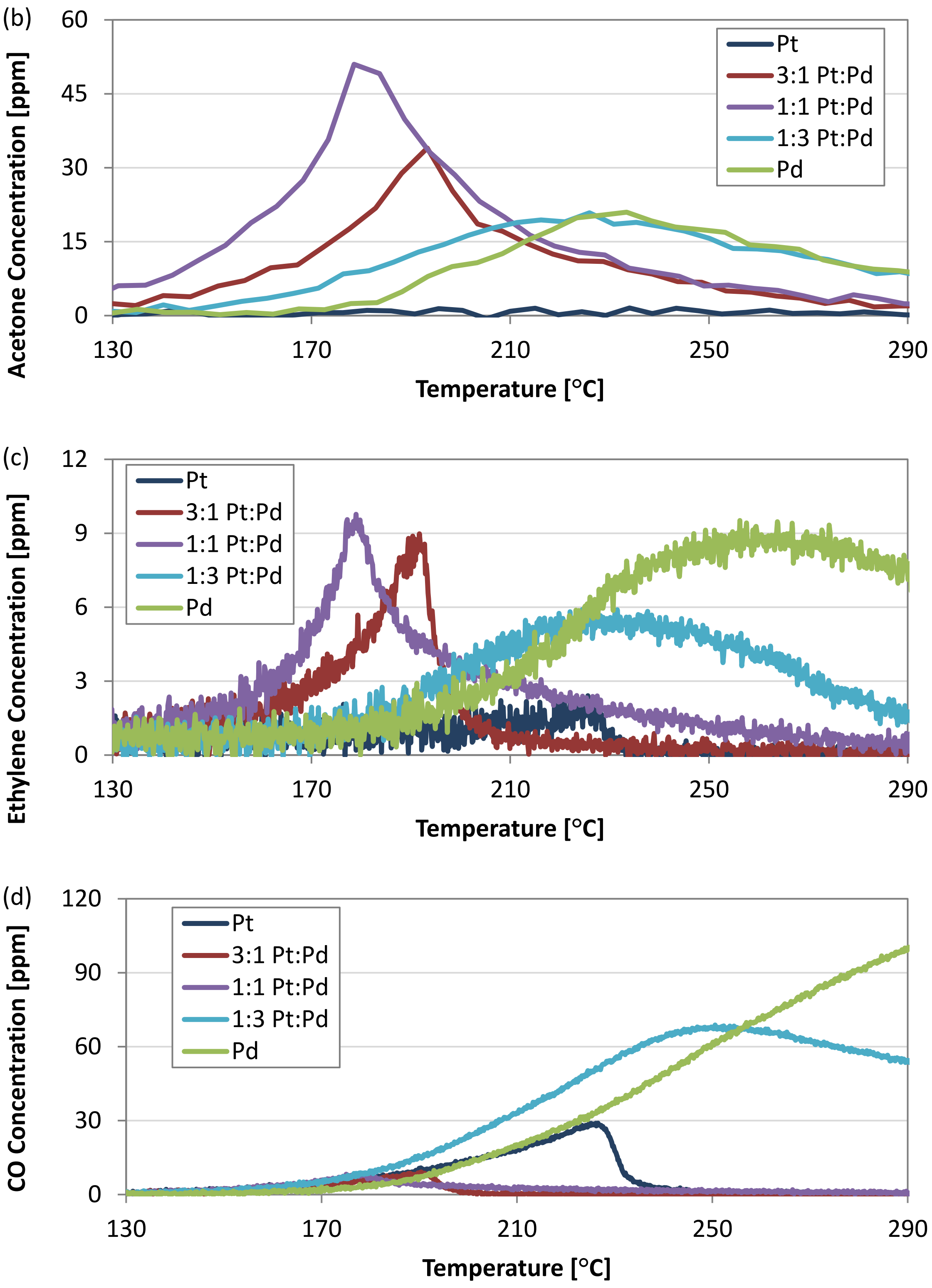

Figure 4-6 (a) C_3H_6 conversion, (b) acetone concentration, (c) ethylene concentration, and (d) CO concentration as a function of temperature during TPO; 1500 ppm C_3H_6, 8% O_2 in balance N_2

In comparing the T_{50} values for different propylene concentrations, Figure 4-7, a clear trend exists where an increase in concentration impacts the T_{50} monotonically for each sample. Over this concentration range, the catalyst performance ranking did not change as it did for CO oxidation, and in all cases the 1:1 Pt:Pd ratio catalyst performed the best. The performance ranking for propylene oxidation for all concentrations is 1:1 > 3:1 > 1:0 > 1:3 > 0:1 Pt:Pd.

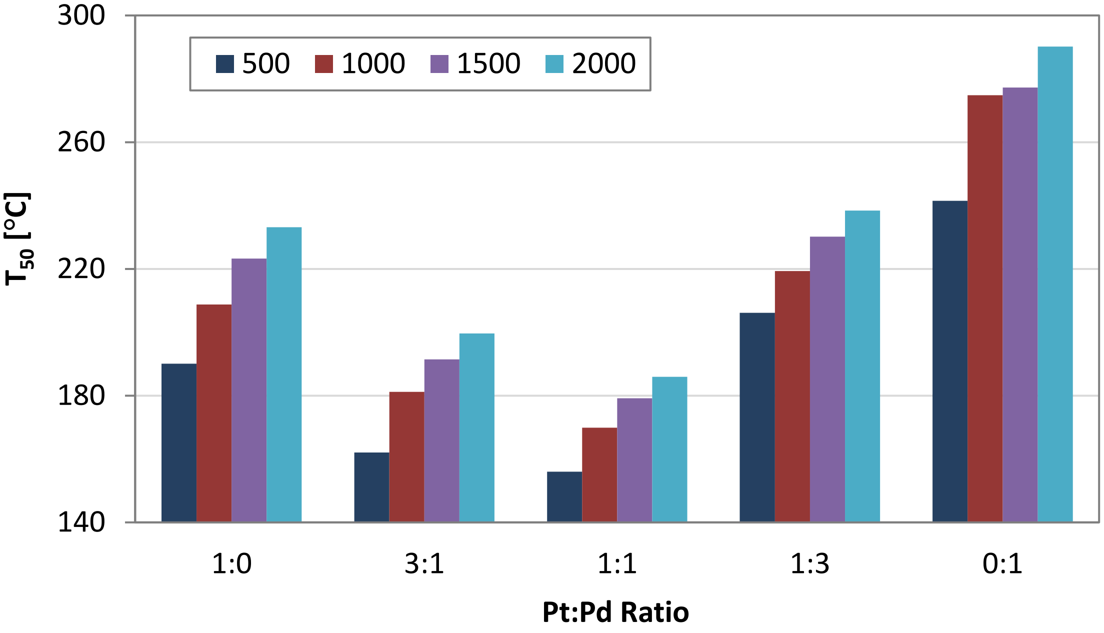

Figure 4-7 C_3H_6 oxidation performance at different C_3H_6 concentrations [ppm] in terms of T_{50}; 500-2000 ppm C_3H_6, 8% O_2, balance N_2

Propylene partial oxidation products vary depending on the catalyst used; for Pt and Pd supported on silica catalysts, partial oxidation products include acetaldehyde, acetic acid, acrolein, acetone and various C_3 acids [90]. However the support is important; as one example acrolein was an abundant product from gold supported on silica catalyst, while with Au on an α-Al_2O_3 support much lower acrolein concentrations were observed [91]. In this study, although acrolein was not observed, there was evidence of ethylene, acetaldehyde, formaldehyde, acetic acid, and acetone. In evaluating partial oxidation product formation as a function of Pt:Pd ratio the most abundant products were acetone, ethylene and CO, presented in Figures 4-6 (b), (c) and (d) respectively. The acetaldehyde formation and acetic acid formation data are shown in Figures 4-8 (a) and (b), respectively. Acetaldehyde formation over each catalyst was around 5-10 ppm with no discernable trend with Pt:Pd ratio. Acetic acid formation was less than 4 ppm, and the 1:3 Pt:Pd catalyst produced the most while the monometallic Pt sample did not catalyze formation of any. CO and ethylene formation increased as the Pd content increased; the 1:3 and monometallic Pd samples catalyzed some formaldehyde formation as an additional partial oxidation product at higher temperatures but at very low concentrations, 1-2 ppm.

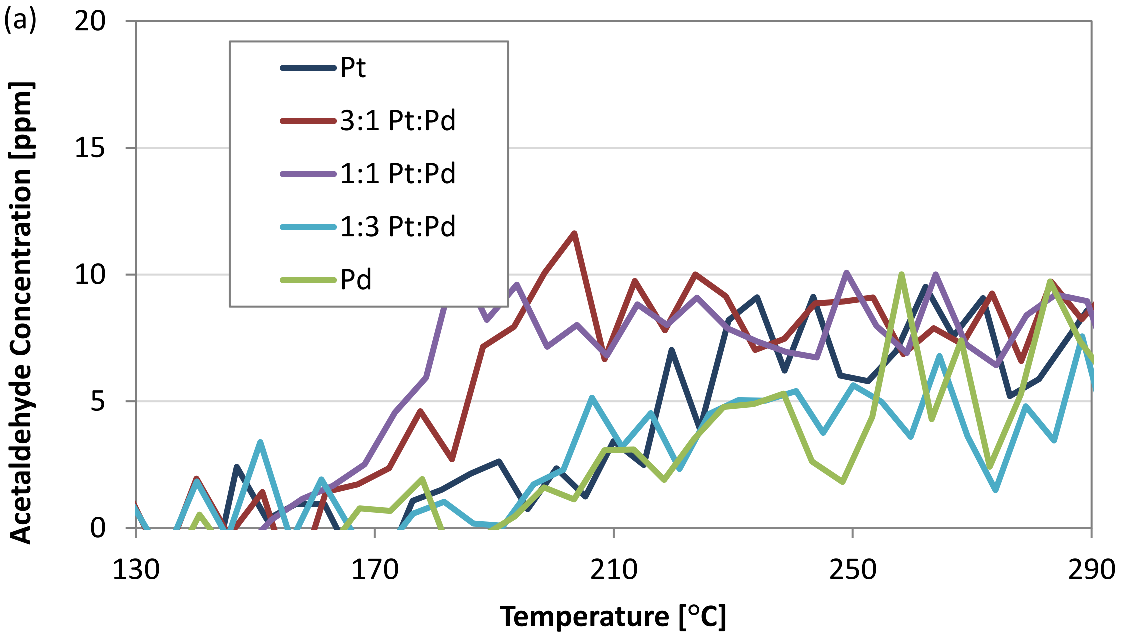

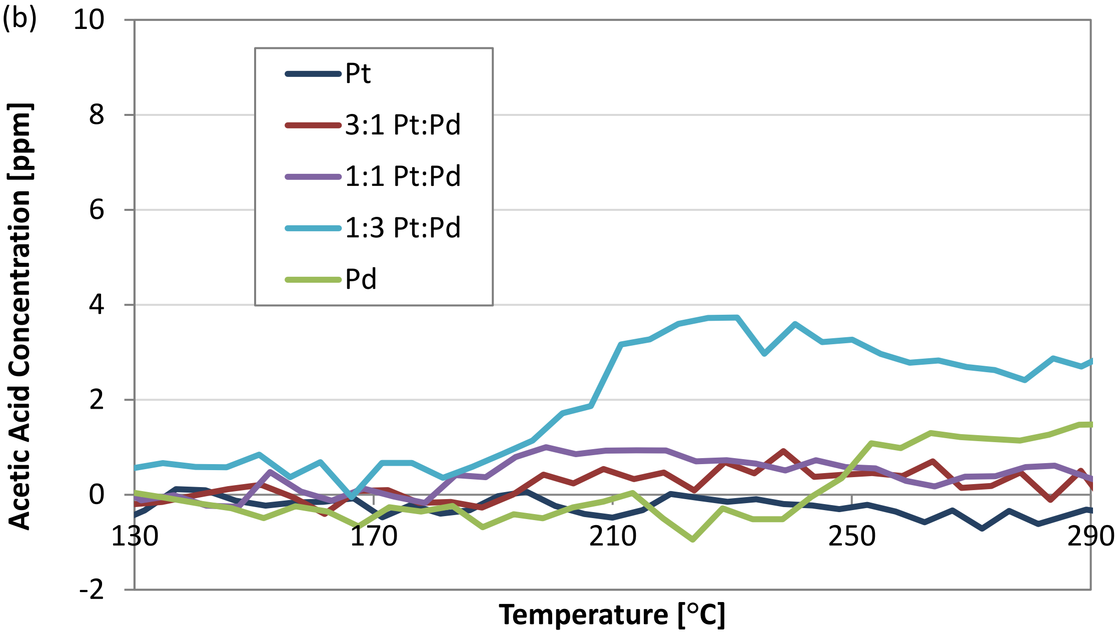

Figure 4-8 C_3H_6 partial oxidation products (a) acetaldehyde and (b) acetic acid as a function of temperature during TPO; 1500 ppm C_3H_6, 8% O_2 in balance N_2

4.3.3.2 DRIFTS Testing

In order to identify which partial oxidation products formed on the catalyst surface we needed to distinguish the reactant propylene from possible partial oxidation products, i.e. acrolein, acetone, acetic acid, ethylene and acetaldehyde. The complete set of peak assignments for the various surface species anticipated are compiled in Appendix 1, Table A-1. Focusing first on propylene, there are three configurations by which propylene can adsorb to the surface; π-propylene, di-σ-propylene, and propylidyne [39]. The various CH stretching peaks in the 2800-3100 cm^{-1} range can be used to distinguish which configuration adsorbed. The spectra obtained at 80°C are shown in Figure 4-9 (a). There were peaks at 2962 and 2906 cm^{-1}; from Table A-1 these correspond to the $\nu_a(CH_3)$ and $\nu_s(CH_3)$ of propylidyne, respectively. Another peak at

1124 cm^{-1} was present, but not shown in the spectra, which corresponds to ν(C-C) of propylidyne. The peaks expected above 3000 cm^{-1} for π-propylene were not present; which is consistent with the absence of acrolein byproduct, since mechanistically it is formed through π-allylic complexes [92].

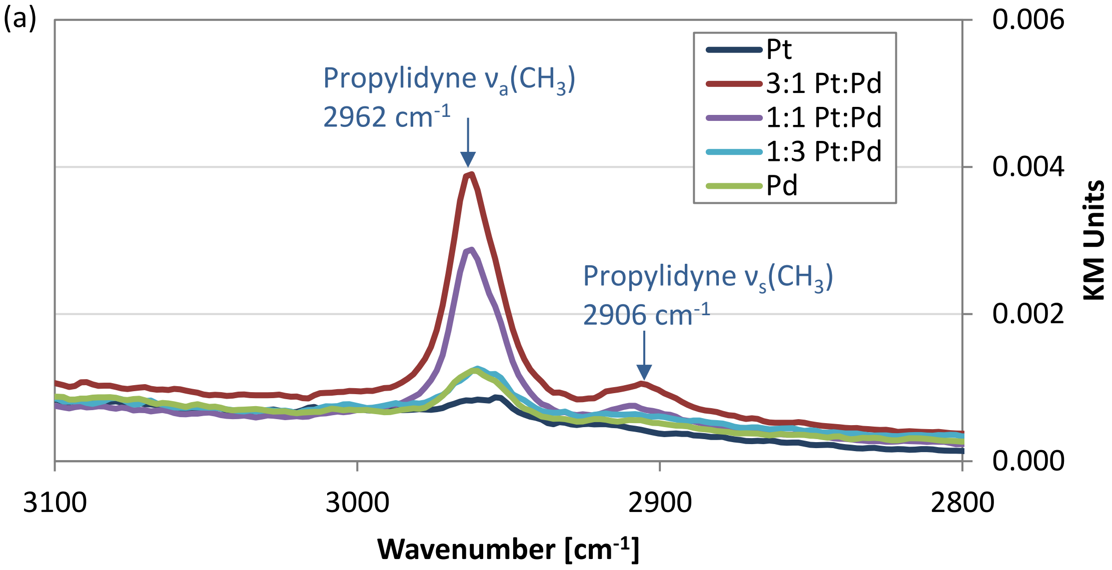

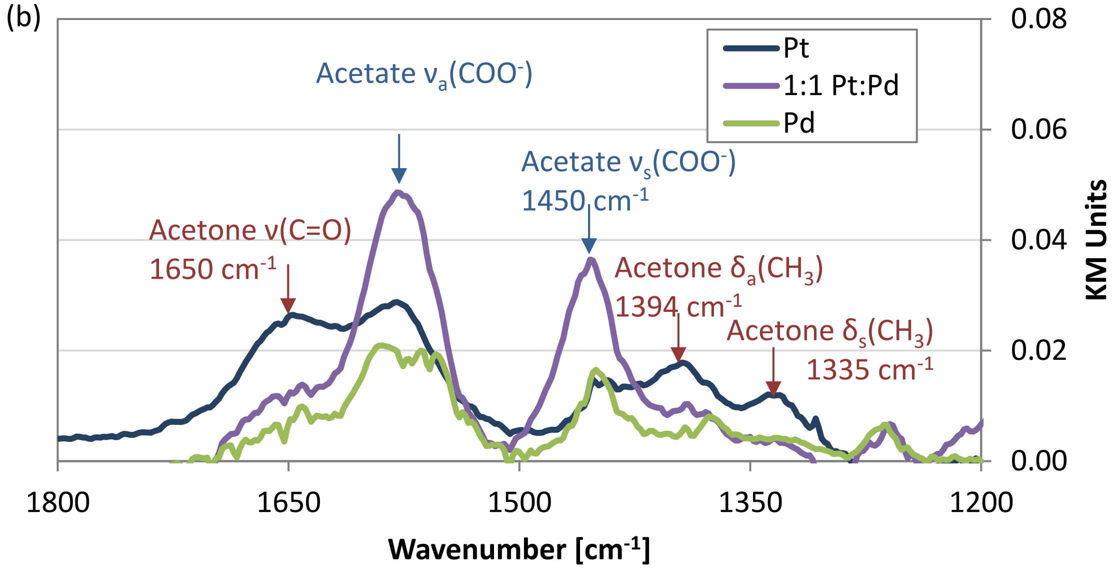

Figure 4-9 DRIFTS spectra obtained during catalyst exposure at (a) 80°C and (b) 229°C, with 98 scans at 4 cm^{-1} resolution; 1500 ppm C_3H_6, 8% O_2, balance He

The peak assignments for acetone, acrolein, acetate, and the various configurations of ethylene are listed in Table A-1. Peaks in the 1200-1800 cm^{-1} range were used to distinguish which oxidation products evolved at higher temperatures, and spectra obtained at 229°C as examples are shown in Figure 4-9 (b). For clarity only the spectra for the monometallic Pt and Pd catalysts and 1:1 Pt:Pd are shown. Peaks at 1649, 1574, 1450, 1394, 1335, 1267 cm^{-1} were observed. The peaks at 1574 and 1450 cm^{-1} were evident with the 1:1 Pt:Pd and Pd samples, at similar ratios and correspond to the $\nu_a(COO^-)$, and $\nu_s(COO^-)$ modes of the acetate species, respectively [93], [94]. The remaining peaks at 1649, 1394, and 1335 could be the $\nu(C=O)$, $\delta_a(CH_3)$ and $\delta_s(CH_3)$ acetone bands, respectfully [42]. While there are several similar IR features between acrolein and acetone, the characteristic $\nu(C=O)$ at 1700 cm^{-1} for acrolein was not observed [95]. Since we observed ethylene as a partial oxidation product, the peaks for the three configurations of ethylene are also listed in Table A-1; π-ethylene, di-σ-ethylene, and ethylidyne [96]. None of the peaks in the DRIFTS results are attributed to the first two configurations of ethylene, however the peaks associated with propylidyne are common to ethylidyne and so the increase in intensity of these peaks with temperature could be associated with ethylidyne as well. The presence of the $\nu(COH)$ is at 1267 cm^{-1} on the 1:1 and Pd sample at 229°C, with the acetate peaks, may also indicate the formation of acetic acid, which is consistent with observations from the reactor testing.

Summarized DRIFTS data obtained from the propylene oxidation experiments are shown in Figure 4-10 (a)-(c), where the acetone $\nu(C=O)$ 1649 cm^{-1} peak, the acetate

$\nu_s(COO^-)$ 1450 cm^{-1} peak, the linear carbonyl 2111 cm^{-1} peak are plotted as a function of inlet gas temperature. The $\nu_s(COO^-)$ peak at 1450 cm^{-1} for acetate was chosen, since the 1574 cm^{-1} feature is near that of a formate peak (1587-1600cm^{-1}) that was observed during CO oxidation, and thus difficult to assign during co-oxidation experiments discussed below. The propylidyne or ethylidyne 1124 cm^{-1} ν(C-C) mode as a function of temperature is plotted in Figure 4-10 (d), and increased with temperature for the Pt catalyst but did not increase significantly on the other catalysts. The acetic acid ν(COH) mode at 1267 cm^{-1} is not plotted as a function of temperature; this peak was observed and increased with temperature for the 3:1 and 1:1 Pt:Pd catalysts, however there was a maxima which did not follow the acetate peak. This may indicate that on the 1:1 and 3:1 Pt:Pd catalysts there was an intermediate temperature range where acetic acid was formed, which is consistent with the reactor testing. The CO-M-CO peak at 2050 cm^{-1} was not observed, and so the 2111 cm^{-1} peak has been attributed to CO-M-O species. Relating these data to the reactor testing, the oxidation onset can be identified by CO formation on the surface, based on the observation from the reactor tests where CO was observed once propylene oxidation commenced. With this indicator, surface CO formation occurred just prior to the temperature where the acetone and acetate related peaks started to increase in intensity. This confirms the association of these peaks with partial oxidation intermediates and not from propylene adsorption on the active sites via π or σ bonding.

(a)

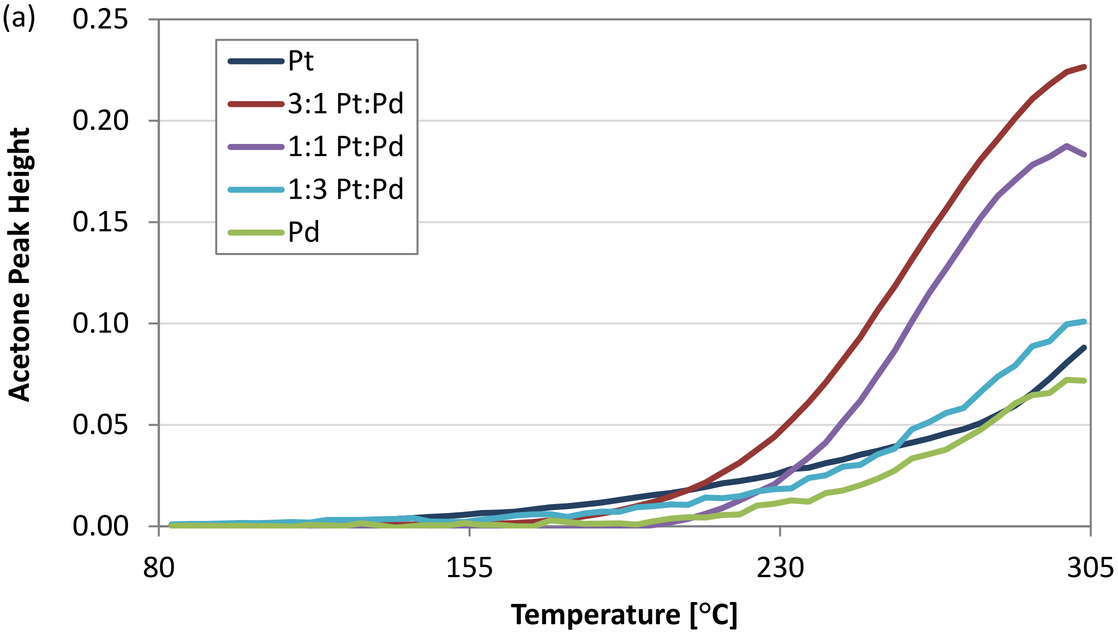

0.25
0.20
0.15
0.10
0.05
0.00
Acetone Peak Height
80
155
230
305
Temperature [°C]
Pt
3:1 Pt:Pd
1:1 Pt:Pd
1:3 Pt:Pd
Pd

(b)

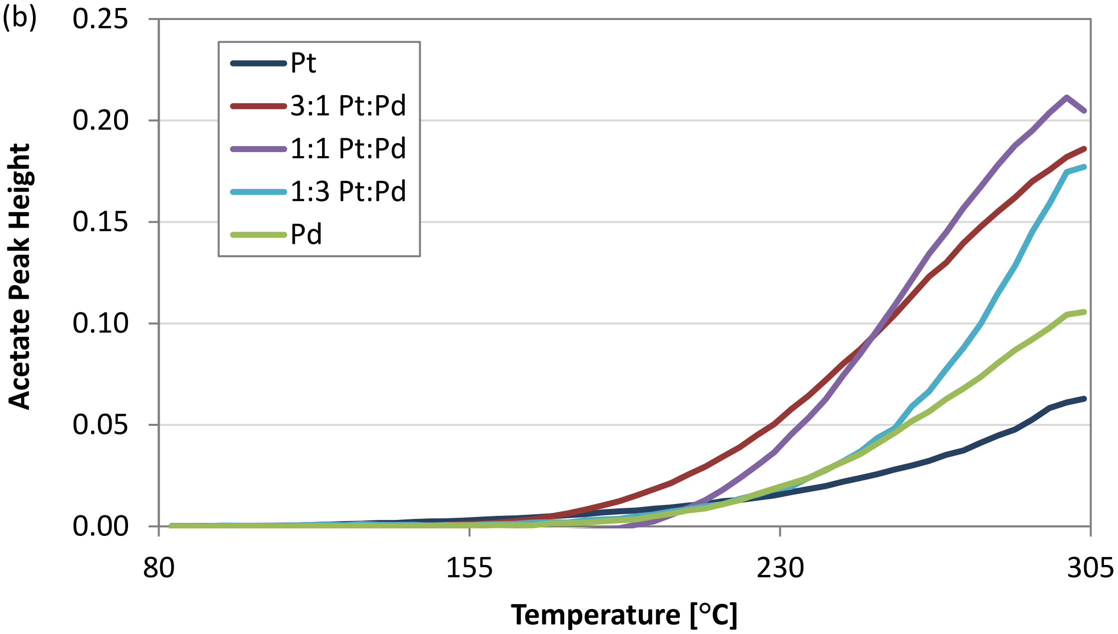

0.25
0.20
0.15
0.10
0.05
0.00
Acetate Peak Height
80
155
230
305
Temperature [°C]
Pt
3:1 Pt:Pd
1:1 Pt:Pd
1:3 Pt:Pd
Pd

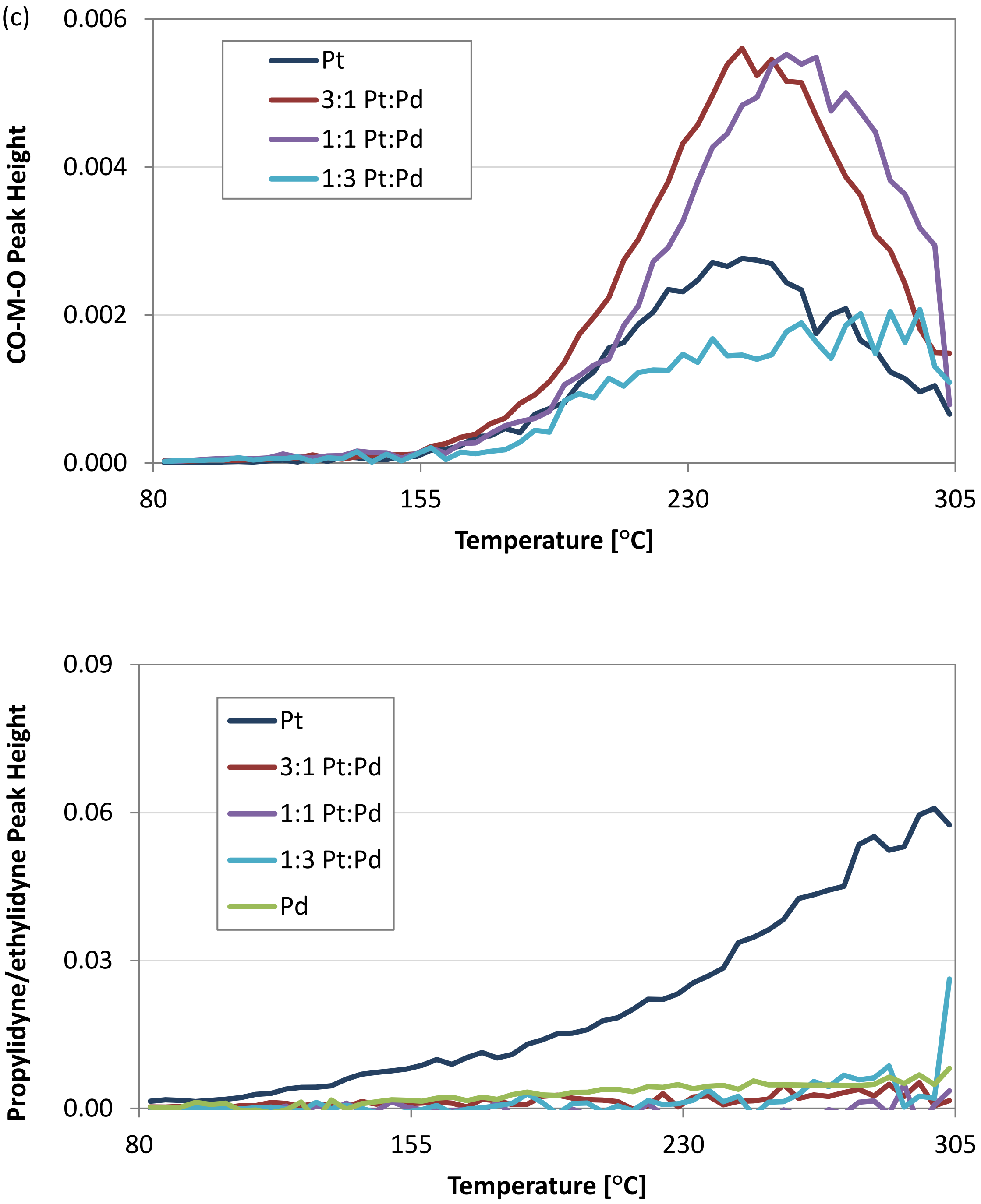

Figure 4-10 Peak height as a function of temperature for (a) acetone [1649 cm^{-1}], (b) acetate [1450 cm^{-1}], (c) linear carbonyl [2111 cm^{-1}], (d) propylidyne/ethylidyne [1124 cm^{-1}] during C_3H_6 oxidation; 1500 ppm C_3H_6 8% O_2, balance He

The partial oxidation products from the reactor testing and DRIFTS tests correlate quite well. From the reactor testing, Figure 4-6 (b), all the samples led to acetone formation, with the formed over the 1:1 Pt:Pd catalyst. Surface acetone formation, in Figure 4-10 (a), followed a similar trend; acetone formation was observed to the largest extent on the 3:1 and 1:1 catalysts. Acetone formation was observed on the surface of the Pt catalyst, but was not present in the gas phase products. From the reactor testing, the Pd-containing catalysts formed the most ethylene, as shown in Figure 4-6 (c). Ethylene formation could be related to the ethylidyne species, which did not increase as a function of temperature for the Pd catalyst, or the acetate species observed on the surface, shown in Figure 4-10 (b), where more formed occurred on the catalysts with a high Pd content, which agrees with reactor results. The CO concentrations from the reactor testing are shown in Figure 4-6 (d), and were the lowest from the 1:1 Pd:Pd and 3:1 Pt:Pd catalysts. The trends observed in the DRIFTS, Figure 4-10 (c), demonstrate that the CO-M-O peak heights during C_3H_6 oxidation go through a maximum for Pt, 3:1 Pt:Pd and 1:1 Pt:Pd catalysts, which was also observed in reactor testing. The highest amount of CO formed on the 3:1 and 1:1 Pt:Pd catalyst surfaces, which also catalyzed the lowest effluent CO concentrations during reactor testing.

4.3.4 CO and C_3H_6 Co-oxidation Results

4.3.4.1 Reactor Testing

CO and propylene co-oxidation performance was also evaluated and representative data are shown in Figure 4-10. The monometallic Pd catalyst performance is not presented, as stable performance between TPO experiments was not attained under these conditions; loss in performance was continuously noted when running repeat experiments to verify reproducibility. All other catalyst resulted in repeatable data, as did the monometallic Pd sample in CO or C_3H_6 oxidation testing. From the conversion data shown in Figure 10, the 1:1 Pt:Pd catalyst was again the best sample, with low temperature light off and rapid acceleration to high conversion for both CO and propylene. The ignition slope for the 3:1 Pt:Pd catalyst was steeper, and the 1:3 Pt:Pd sample resulted in a lower CO light off temperature required compared to the 3:1 sample, but the ignition slope was much shallower and propylene oxidation occurred at a much higher temperature.

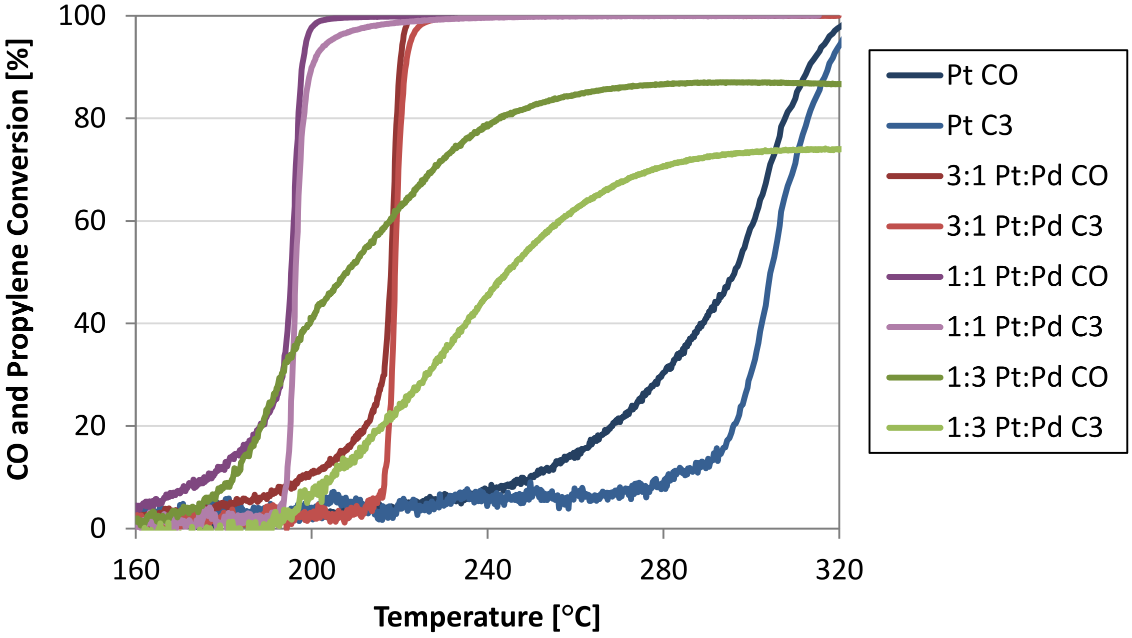

Figure 4-11 CO and C_3H_6 conversion as a function of temperature during TPO; 3000 ppm CO, 1500 ppm C_3H_6, 8% O_2 in balance N_2

For comparison purposes, the T_{50} for CO and C_3H_6 during co-oxidation and individual component oxidation for the catalysts are tabulated in Table 4-2. The 1:3

sample had the largest difference between the CO T_{50} and the propylene T_{50} during co-oxidation. The catalyst performance ranking for co-oxidation in terms of CO T_{50} is 1:1 Pt:Pd > 1:3 Pt:Pd > 3:1 Pt:Pd > 1:0 Pt:Pd, and in terms of propylene T_{50} is 1:1 Pt:Pd > 3:1 Pt:Pd > 1:3 Pt:Pd > 1:0 Pt:Pd.

Table 4-2 T_{50} (temperature at 50% conversion) for CO and C_3H_6 as individual reactants and during co-oxidation; concentrations as labeled with 8% O_2 in balance N_2

Ratio (Pt:Pd)	3000 ppm CO T_{50} [°C]	1500 ppm C_3H_6 T_{50} [°C]	3000 ppm CO and 1500 ppm C_3H_6	
			T_{50} CO [°C]	T_{50} C_3H_6 [°C]
1:0	196	223	296	304
3:1	184	191	218	219
1:1	169	179	196	196
1:3	180	230	208	245
0:1	183	277	--	--

Propylene partial oxidation product formation results are shown in Figure 4-12. With CO present there were in general less partial oxidation products formed. Ethylene formation reached a 4 ppm maximum for the 1:1 and 1:3 Pt:Pd catalysts and acetone formation reached a maximum of 12, 10 and 6 ppm for the 1:1, 1:3, and 3:1 Pt:Pd catalysts, respectively. Acetone and ethylene formation peaked shortly after propylene oxidation onset, while the formation of acetaldehyde, and acetic acid for the 1:3 Pt:Pd catalyst, remained relatively constant with temperature once propylene oxidation began. Much like propylene oxidation in the absence of CO, the lowest concentrations of partial oxidation products were observed from the Pt catalyst. In the presence of CO, only the 1:3 Pt:Pd catalyst yielded acetic acid.

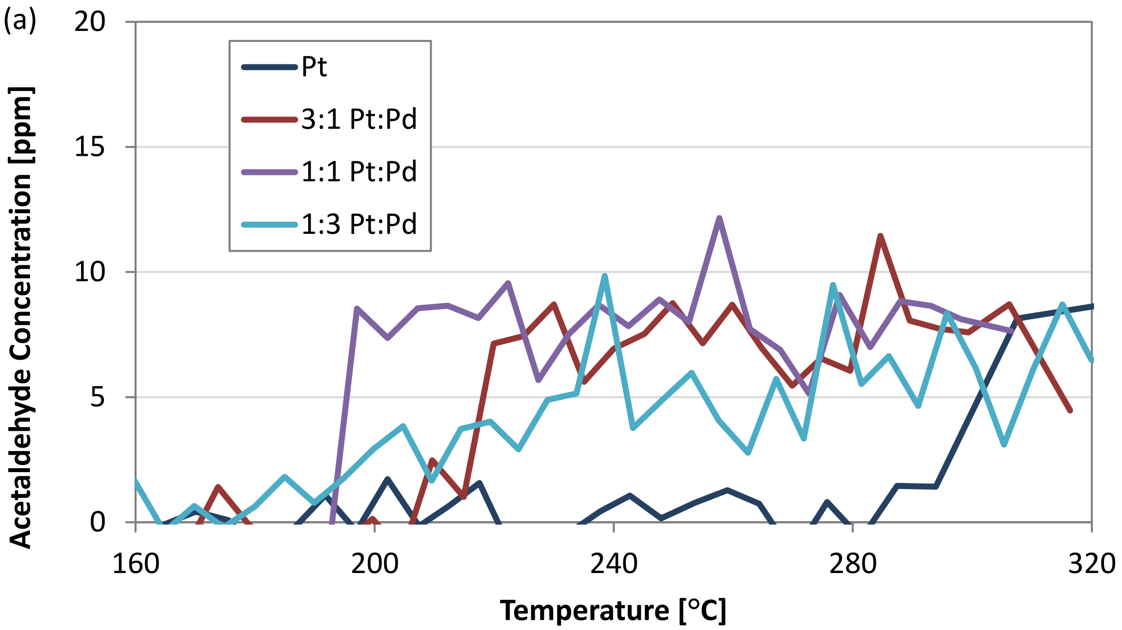
(a)
Acetaldehyde Concentration [ppm]
20
15
10
5
0
160
200
240
280
320
Temperature [°C]
Pt
3:1 Pt:Pd
1:1 Pt:Pd
1:3 Pt:Pd

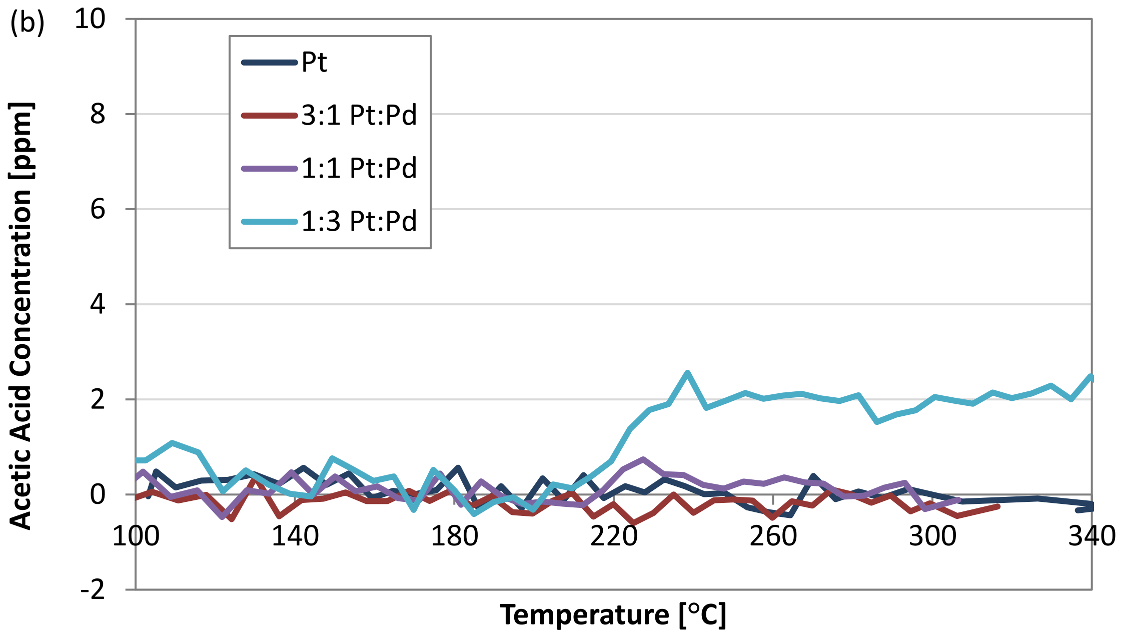
(b)
Acetic Acid Concentration [ppm]
10
8
6
4
2
0
-2
100
140
180
220
260
300
340
Temperature [°C]
Pt
3:1 Pt:Pd
1:1 Pt:Pd
1:3 Pt:Pd

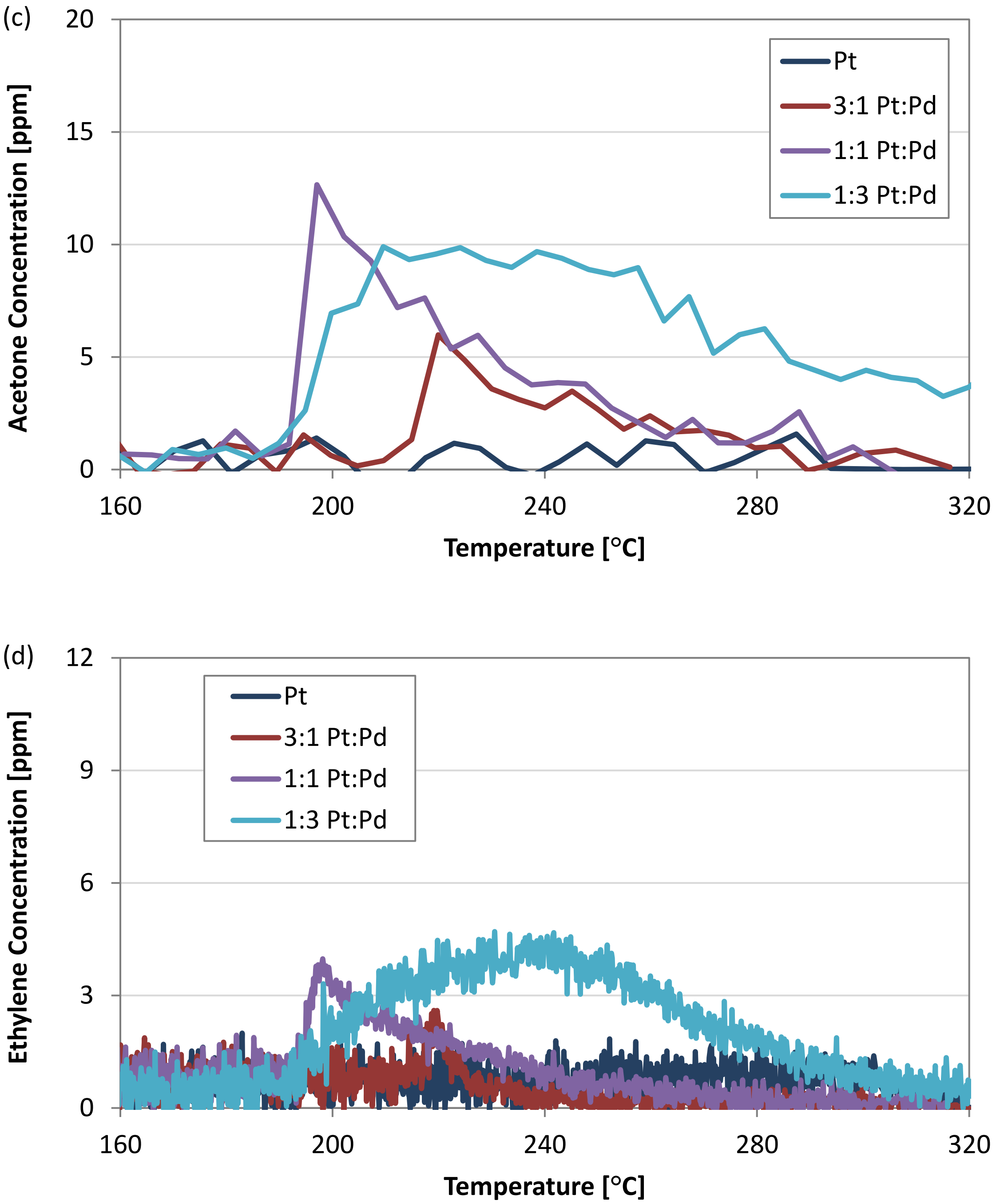

Figure 4-12 (a) Acetaldehyde, (b) acetic acid, (c) acetone, and (d) ethylene concentration during CO and C_3H_6 co-oxidation as a function of temperature during TPO; 3000 ppm CO, 1500 ppm C_3H_6, 8% O_2 in balance N_2

4.3.4.2 DRIFTS Testing

The DRIFTS results for CO and C_3H_6 co-oxidation are summarized in Figure 4-13. The peaks for the CO species occurred at lower wavenumbers, as is expected [80] with propylene in the feed, and therefore peak heights were based on these lower wavenumbers. All the surface species that were observed during the individual CO or propylene oxidation experiments were here again observed. The peaks plotted in Figure 4-13 are the acetone ν(C=O) 1653 cm^{-1}, acetate $\nu_s(COO^-)$ 1450 cm^{-1}, formate $\nu_a(COO^-)$ 1600 cm^{-1}, CO-M-CO 2054 cm^{-1}, CO-M 2084 cm^{-1}, CO-M-O 2112 cm^{-1}, and triply adsorbed CO 1805 cm^{-1} peaks. Note the peak at 1600 cm^{-1} is very close to the 1574 cm^{-1} acetate $\nu_a(COO^-)$ peak; once the peak at 1450 cm^{-1} developed, the peak at 1600 cm^{-1} slowly shifted to the lower wavenumber of acetate and the peak associated with the formate $\nu_s(COO^-)$ at 1342 cm^{-1} disappeared. Also, the peaks at 1390 and 1330 associated with the $\delta_a(CH_3)$ and $\delta_s(CH_3)$ of acetone appeared together with the appearance of ν(C=O) at 1653 cm^{-1}. For this case, the peak at 1329 cm^{-1} associated with monodentate carbonate formation during CO oxidation did not show a trend with Pt:Pd ratio, and also interfered with the acetone $\delta_s(CH_3)$ mode at 1330 cm^{-1}, and so is not plotted in Figure 4-13. The peak at 1267 cm^{-1} was not observed during co-oxidation, and similar to propylene oxidation in the absence of CO, the 1124 cm^{-1} ν(C-C) mode of propylidyne or ethylidyne as a function of temperature increased with the Pt catalyst but did not increase significantly for the other catalysts. The characteristic ν(C=O) at 1700 cm^{-1} for acrolein or other aldehydes was not observed [95], [97].

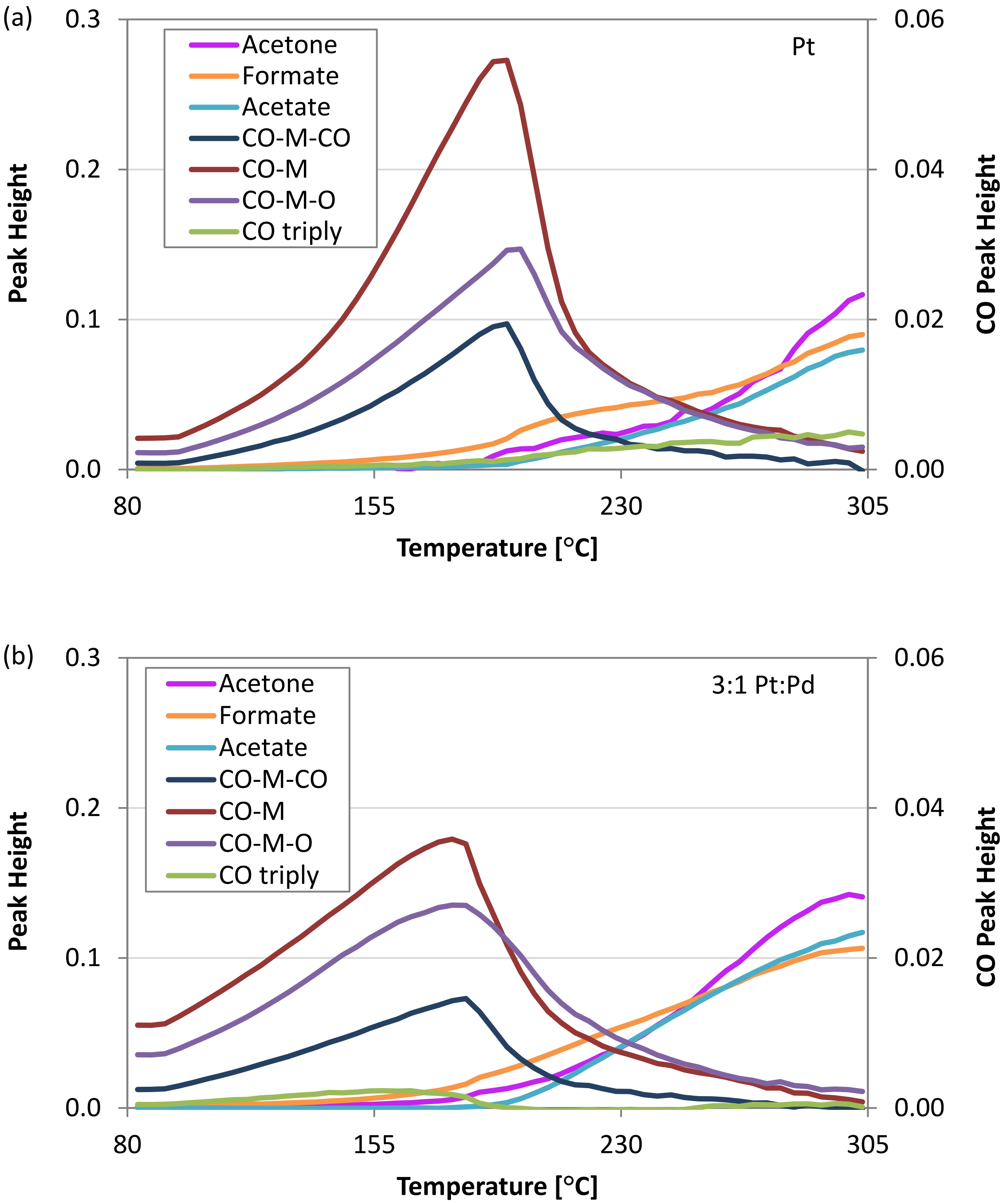
(a)
Pt
Acetone
Formate
Acetate
CO-M-CO
CO-M
CO-M-O
CO triply
Peak Height
0.3
0.2
0.1
0.0
CO Peak Height
0.06
0.04
0.02
0.00
80
155
230
305
Temperature [°C]
(b)
3:1 Pt:Pd
Acetone
Formate
Acetate
CO-M-CO
CO-M
CO-M-O
CO triply
Peak Height
0.3
0.2
0.1
0.0
CO Peak Height
0.06
0.04
0.02
0.00
80
155
230
305
Temperature [°C]

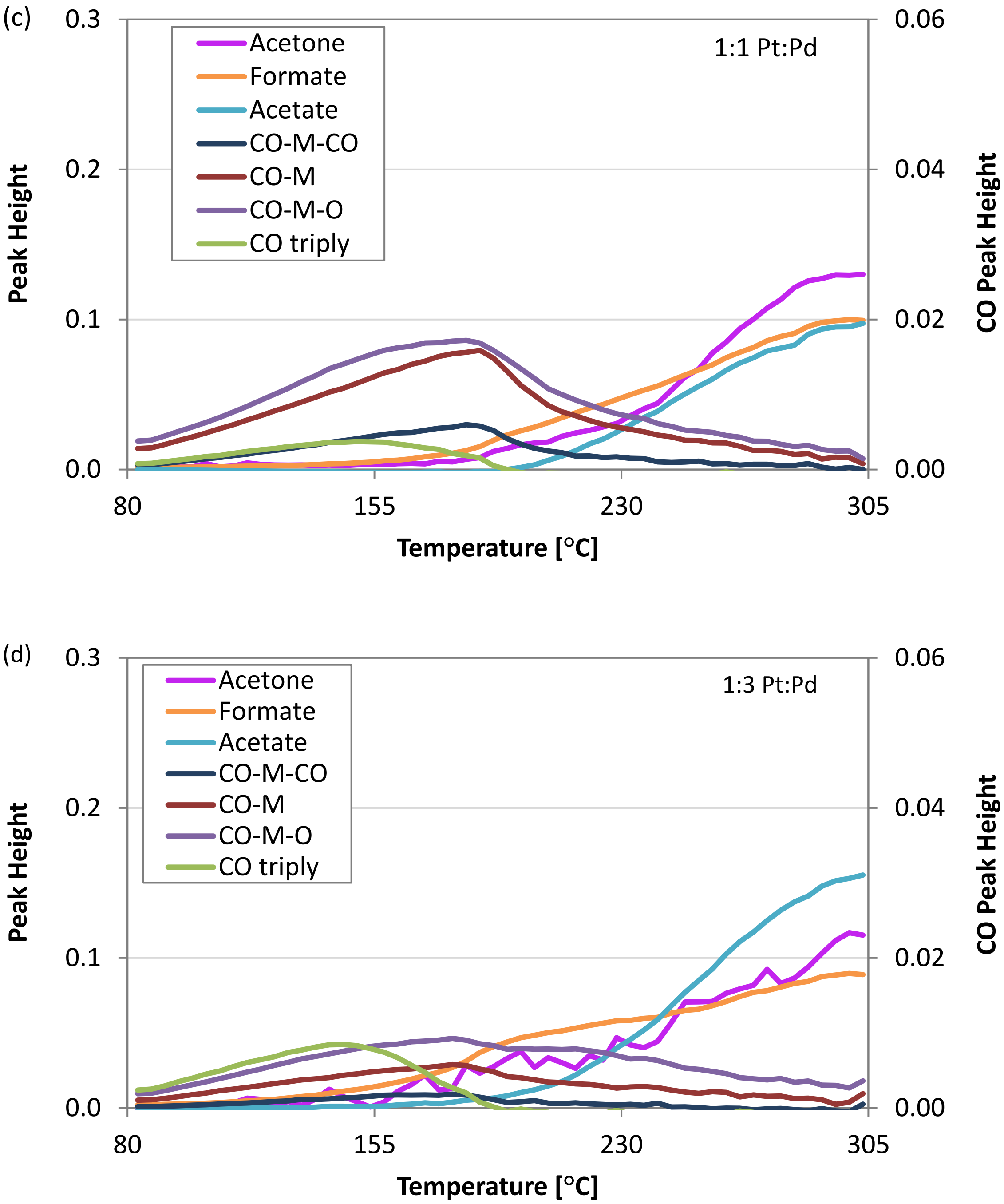

Figure 4-13 DRIFTS peak heights as a function of temperature in CO and C_3H_6 co-oxidation (a) Pt, (b) 3:1 Pt:Pd, (c) 1:1 Pt:Pd, (d) 1:3 Pt:Pd, (e) Pd

4.4 Discussion

4.4.1 Catalyst Characterization

The EDS data, presented in Figure 4-1, suggested that monometallic Pd particles exist on the 1:3 Pt:Pd sample, which is supported by the DRIFTS data where triply bound CO features were observed, Figure 4-4. Based on the DRIFTS results, where the bimetallic catalysts with a higher Pd content had more doubly and triply bound carbonyls, the 1:1 stoichiometry assumed for the CO chemisorption experiments may not be accurate. It is difficult to relate DRIFTS results to surface concentrations, however a rough estimate for bimetallic Pt:Pd catalysts and the differently adsorbed carbonyls has been evaluated in other studies. The extinction coefficient of the linear carbonyl can be 2 to 3 times higher than that of the bridged species [18]. In other studies, this information has been used to calculate surface compositions of Pt-Pd catalysts [12], [18]; however in these studies triply bound species were not observed. Here, we used this information to calculate the relative amounts the observed species, but had to assume that the triply bound species have a similar extinction coefficient to that of the bridged species. If we continue with assumptions, that the oxygen and temperature difference during CO adsorption will not drastically alter the ratios of these species, new values for the CO stoichiometry can be calculated and used to recalculate particle sizes. Using the data obtained at 80°C, and that the extinction coefficient for linearly adsorbed CO is 2.5 times greater than bridged or triply bound CO, the relative amounts of each species, the stoichiometry, and a corrected particle size for each catalyst has been calculated and the results are listed in Table 4-3. The adsorption stoichiometry for each catalyst was calculated to be: 2.60 for Pd, 2.24 for 1:3 Pt:Pd, 1.47 for 1:1Pt:Pd, 1.15 for 3:1 Pt:Pd and 1.20 for Pt. Using these values for the stoichiometry, the following particle sizes were calculated; 1.0 nm for Pd, 1.6 nm for 1:3 Pt:Pd, 1.8 nm for 1:1 Pt:Pd, 1.4 nm for 3:1 Pt:Pd and 1.6 nm for Pt. This estimated correction actually decreases the particle size range, mainly influenced by the stoichiometry correction for Pd rich catalysts since they have the multiply adsorbed CO molecules.

Table 4-3 Fractions of linearly, doubly, and triply bound CO on Pt:Pd catalysts, estimated CO stoichiometry Pt:CO, and revised estimates of average particle sizes

Ratio (Pt:Pd)	1:0	3:1	1:1	1:3	0:1
CO-M-CO [%]	6	7	4	2	0
CO-M [%]	57	38	21	10	4
CO-M-O [%]	14	40	38	15	3
Doubly [%]	23	12	24	22	26
Triply [%]	0	4	12	51	67
Stoichiometry	1.20	1.15	1.47	2.24	2.60
Particle size [nm]	1.6	1.4	1.8	1.6	1.0

4.4.2 CO Oxidation

In terms of CO oxidation, the bimetallic catalysts were superior to the monometallic catalysts. The 1:1 Pt:Pd catalyst resulted in the lowest T_{50} for all concentrations tested and had a steep ignition slope reaching full conversion at the lowest temperatures. While the 1:3 Pt:Pd catalyst reached T_{50} at lower temperatures than the 3:1 Pt:Pd catalyst, it did not reach full conversion. Similarly comparing the Pd and Pt catalyst, the Pd catalyst reached T_{50} at lower temperatures than the Pt catalyst but did not reach full conversion. The decrease in performance ranking for the Pt catalyst observed as the CO concentration increased is consistent with Pt being more sensitive to CO poisoning [71]. By extension this also extrapolated to the Pt-rich samples, which explains why as the CO concentration increased, performance ranking in terms of T_{50} changed.

The differently adsorbed CO species observed via DRIFTS provide some insight into the reason for the performance order change. The 1:1 and 3:1 Pt:Pd catalyst surfaces had a relatively larger amount of CO-M-O species, while the Pt catalyst did for the CO-M species and the Pd and 1:3 Pt:Pd had more triply bound and bridge bound CO. If the triply and bridge bound species were solely responsible for low temperature CO oxidation, the Pd catalyst would be expected to have the lowest temperature oxidation activity. Instead it appears that the CO-M-O species are linked to the low temperature CO oxidation activity. The CO-M-CO species is included in plots where it was significant, which was the case for the monometallic Pt catalyst where the CO-M-CO peak was present during CO light off and reached a maximum before the CO-M-O did. These results also coincide with the reactor data where the Pt catalyzed light off later than the other catalysts, demonstrating more significant CO poisoning. The single carbonyls (CO-M and CO-M-O) formed on the 1:1 catalyst grew in concentration with increasing temperature, and when the CO-M-O peak started to decrease the CO-M continued to increase. In contrast, for the Pt sample the CO-M species peaked at a lower temperature relative to the CO-M-O. The single linearly bound CO trends are manifested in the 3:1 Pt:Pd catalyst as a combination of the two samples, where a maximum was observed, but then an increase at the higher temperatures. This implies that both individual Pt particles must exist in addition to the bimetallic particles, further agreeing with the results from the EDS data, which suggested that the bimetallic particles, while Pt-rich, did not account for all of the Pt loaded on the catalyst. The 1:1 Pt:Pd catalyst had the highest low temperature performance, exceeding that of the 3:1 catalyst even though from the DRIFTS data the 3:1 Pt:Pd catalyst had the highest CO-M-O peak height at low temperatures. This may be due to the higher amount of CO-M observed on the 3:1 Pt:Pd catalyst as well, implying the surface is heavily covered by CO and the availability of oxygen on the surface is low.

The CO-M-O peak was observed on both the 3:1 and 1:1 bimetallic catalysts and Pt-only catalyst. The DRIFTS data from the Pd-only catalyst did not contain peaks for any type of single, linearly bound CO at any temperature studied, but instead had a significant triply bound carbonyl peak at low temperatures. For the 1:3 Pt:Pd catalyst, the more significant triply bound carbonyl peak was also observed, in addition to the linear carbonyls associated with the bimetallics. Previous literature has shown that when CO is adsorbed onto bimetallic Pt:Pd particles, neither bridged nor triply bound carbonyls form, but they do on monometallic Pd samples [98]. The presence of both peaks on the 1:3 Pt:Pd catalyst demonstrates both bimetallic and Pd particles were present on the surface, which was also inferred from the EDS results.

Formate and monodentate carbonate surface species formed during CO oxidation on all catalysts. There was no evidence of bicarbonate. This is not meant to conclude that CO oxidation does not occur through a bicarbonate mechanism, it could be that this species reacts too quickly to be observed. The most carbonate formed on the 1:3 and monometallic Pd catalysts, and formation and accumulation of these species could deactivate active sites and result in full conversion not being reached. This was not a monotonic trend, as there was a higher level of both formate and carbonate on the 1:3 Pt:Pd catalyst than on the Pd catalyst, which would suggest if these intermediates inhibited the reaction then the monometallic Pd sample should have performed better. The 1:3 sample, however, led to a lower CO oxidation light off temperature relative to the monometallic Pd catalyst. This better performance despite the carbonate buildup is attributed to the higher level of CO-M-O, which is apparent on the other more active bimetallic catalysts, suggesting that the alloying promoted formation of highly reactive Pd and Pt oxides. For other Pt-based bimetallic catalysts studied alloying with another metal that easily forms an oxide (Fe, Ni) enabled oxygen dissociation thereby facilitating CO oxidation on Pt [99], similar to what was observed here. For the 1:1 Pt:Pd catalyst, which performed best in the CO oxidation tests, while there was formate production to a similar extent as on the 1:3 Pt:Pd and Pd catalysts, there was less carbonate formation, and the 1:1 Pt:Pd catalyst was more active than the 1:3 Pt:Pd and Pd catalysts. The Pt and 3:1 Pt:Pd catalysts showed evidence of carbonate formation to a higher extent than the 1:1 Pt:Pd catalyst but not as much as the 1:3 Pt:Pd and Pd catalysts. The data support surface carbonates inhibiting CO oxidation. Similar trends have been observed for Au and CoO_X catalysts [100], [101]. It is not clear whether this carbonate was present on the support or on the metal sites themselves from the spectroscopic results, however it at least seems likely that this species is related to the decreased maximum conversion on the Pd-rich catalysts. The Pd catalyst may simply allow the carbonate to spill over to the support and the decreased conversion was due to transport effects. And the nonmonotonic trend discussed above is associated with a combination of inhibition by the carbonates and activity of the CO-M-O species. As water is not being introduced as a reactant, the formation of formate is occurring at the edges of the particles with the Lewis acid sites of alumina [86]. This may be why the carbonate is observed as an inhibitor while the formate is not, as the formate can easily spill over to the support while the carbonate can be formed anywhere on the particle and may have a harder time spilling over.

CO oxidation studied on single Pt atoms suggests a mechanism that goes through a surface carbonate [72]. If the mechanism does go through a carbonate intermediate, then the DRIFTS results suggest that the release of CO_2 through carbonate decomposition in the mechanism may be rate limiting for the 1:3 and Pd samples. For the Pt, 3:1, and 1:1 Pt:Pd catalysts where carbonate did not accumulate to the same extent, the carbonate was either not the primary intermediate in the mechanism or its decomposition to CO_2 is rapid, and thus less was observed. Surface carbonate accumulation leading to a slower ignition rate explains the observed difference in conversion change versus temperature (conversion profile slopes) in the reactor data, its accumulation slows the rate.

To summarize, the lower temperature peak associated with the singly adsorbed carbonyls on the 3:1 Pt:Pd catalyst, Figure 4-5 (b), is related to carbonyls present on the Pt particles, and the higher temperature peak is attributed to the carbonyl on either the Pt or Pd in a bimetallic particle. This altogether indicates that Pd in a bimetallic particle resulted in an increase in the CO adsorbed on the surface as a co-adsorbed carbonyl with oxygen (CO-M-O), which in turn indicates that the improved light off activity could be related to that available oxygen. Changes in rate of conversion as a function of temperature were also related to surface carbonate decomposition. A trade-off occurs when too much Pd is added, where in addition to the co-adsorbed species there is increased inhibition because of formed carbonate species and eventually the bridge and triple bound sites dominate.

4.4.3 C_3H_6 Oxidation

For propylene oxidation, the 1:1 and 3:1 Pt:Pd ratios led to the best observed performance. The partial oxidation products produced during propylene oxidation were not sufficient enough to inhibit propylene oxidation to the same extent as over the more Pd-rich samples, and thus the sharper increase in conversion as a function of temperature and no plateau in conversion was observed. In the reactor testing, the 1:1 and 3:1 Pt:Pd catalysts had the least byproduct CO formation and the most acetone formation; while the Pt catalyst resulted in the least ethylene and no acetone formation. The 1:1 and 3:1 Pt:Pd catalysts had the acetone, ethylene, and CO formation all peak at the same temperature just after catalyst light-off. Conversely, byproducts formed over 1:3 and monometallic Pd catalysts did differentiate with temperature; acetone peaked first, ethylene peaked at a slightly higher temperature, and the CO at a higher temperature still. From the DRIFTS results, the CO-M-O peak was the largest on the 1:1 and 3:1 Pt:Pd catalysts during the CO oxidation experiments, while the CO concentrations during propylene oxidation in the reactor testing were the lowest for these catalysts. These catalysts were able to oxidize the byproduct CO relatively easily. The catalysts which were not able to adsorb the CO through the metal oxide, namely the Pd where the CO-M-O peak was not observed during propylene oxidation, had the highest byproduct CO concentrations.

At the beginning of the propylene oxidation experiments, propylidyne was observed in the DRIFTS spectra, giving the strongest reflectance on the 3:1 Pt:Pd catalyst. In previous propylene adsorption and propylene oxidation mechanistic studies on Pt [39], [40], this propylene configuration was observed at high propylene coverages, and in the absence of co-adsorbed oxygen [40]. At low propylene coverages the expected propylene configuration on Pt was di-σ-propylene. This suggests that in our study the dehydrogenation of propylene to propylidyne occurred readily at the high propylene concentrations used and that oxygen has limited access to the active sites, leading to only the propylidyne configuration. A previous study has shown 1-methylvinyl species forms via oxydehydrogenation of di-σ-propylene [40]. It is this 1-methylvinyl species that has been attributed to the formation of acetone and acetic acid. Formation of acetone is through 1-methylvinyl reacting with oxygen, and acetic acid formation from the removal of the allylic carbon and subsequent oxygen attack on the second carbon. The di-σ-propylene or the 1-methylvinyl species were not observed, however acetone was observed both in the DRIFTS spectra and in the reactor testing; this 1-methylvinyl species may be too short lived on the surface to be observed spectroscopically. Since in this study the propylene adsorbed as propylidyne, it is possible that the propylidyne rearranges to 1-methylvinyl leading to the observed acetone formation.

Oxidation to ethylene and CO in various proportions also occurred at light-off. The CO and ethylene formation quantities do not follow a consistent trend with ratio change; which would at first suggest that this is not as simple as the propylene oxidizing to acetone and then the acetone breaking apart directly into only ethylene and CO fragments. From the same study just mentioned [40], under very HC rich conditions the oxygen was entirely consumed in the formation of acetone and little CO_2 formed, while increasing propylene exposure resulted in increased H_2O and CO production. H_2O and CO formation implies dehydrogenation of propylidyne and subsequent oxygen attack on the first carbon to form the CO, instead of oxygen attack of the vinyl carbon to form acetone. In other words, when there is not enough oxygen around to form acetone, the formation of ethylene and CO may be preferred. This is supported by our observed results; since the bimetallic catalysts and Pd formed oxides more easily than Pt, the higher surface concentration of oxygen on these catalysts leads to more acetone formation but also subsequent oxygenated hydrocarbon formation. On the Pt catalyst, at higher temperatures oxygen could adsorb and the formation of acetone begin. Since there is not much oxygen on the surface, dehydrogenation reactions occurred leading to preferential ethylene formation. This is supported by the DRIFTS data, where the bimetallic catalysts had the highest peak heights for acetone and acetate develop over the temperature ramp and the Pt catalyst had the smallest acetone features and instead had increased ethylidyne formation. During reactor testing, very low ethylene concentrations were observed with the Pt catalyst, however the DRIFTS results demonstrate that the ethylene remains on the surface. Also in the reactor testing the 1:1 and 3:1 Pt:Pd catalysts yielded the most acetone and acetaldehyde. The 1:1 and 3:1 Pt:Pd catalysts formed roughly equal CO and ethylene concentrations once the catalysts lit off, with the CO and ethylene peaking at the same temperatures, supporting a mechanism where the acetone formation occurs in parallel to propylene oxidizing to ethylene and CO.

For the other Pd-rich catalysts, during reactor testing acetone production peaked at lower temperatures than the ethylene, and ethylene production peaked at lower temperatures than CO, and there was also formation of acetic acid. This may indicate that the dehydrogenation reactions to form the ethylene require a higher activation barrier compared to the oxidation mechanism leading to acetone formation. CO formation over the entire temperature ramp and the fact that full conversion of propylene was not achieved over the 1:3 Pt:Pd and Pd catalysts suggests that the availability of oxygen at the surface was not sufficient for complete oxidation. The DRIFTS results for these catalysts do not suggest the surface was completely taken up by partial oxidation intermediates, as the spectra obtained from the more active 1:1 and 3:1 Pt:Pd catalysts contained larger surface species peak heights. However, during reactor testing there was higher cumulative partial oxidation product formation with the 1:3 and Pd catalysts over the temperature ramp, especially CO. The formation of these products could lead to inhibition further down the catalyst bed. This would be in combination with the reaction front propagating through the catalyst where local surface concentrations are rapidly changing between a hydrocarbon covered surface to one that has available sites for O_2 dissociation and reaction [73], [102].

In general, the bimetallic samples appear to have higher affinity for producing the acetone and acetate species. Acetone is observed on the 1:1 and 3:1 Pt:Pd catalyst surfaces at lower temperatures than the others. For the Pt sample, the CO peak intensity increased at a similar temperature as the 1:1 and 3:1 Pt:Pd catalysts, yet in the reactor testing the onset of propylene oxidation for the Pt catalyst was much later. This suggests that CO being initially formed from propylene partial oxidation strongly inhibited the propylene oxidation onset, especially for Pt as would be expected. Furthermore, the differences in the surface CO and acetone amounts support the notion that propylene oxidation occurs by partial oxidation to CO and ethylene. For the 1:1 and 3:1 Pt:Pd catalysts, the temperatures where CO and acetone started increasing were the same (consistent with trends from bench scale reactor testing); for Pt this was not observed.

Based on the overall results, mechanistic trends across the different Pt:Pd ratios exist. For Pd and 1:3 Pt:Pd, the lower quantity of acetone formed in reactor testing and DRIFTS compared to acetate may indicate that the Pd-rich catalysts either have an easier time breaking the first C-C bond so less C_3 products are formed, or as mentioned before there may be less available surface oxygen. Propylene light-off over the Pd catalyst occurred at a higher temperature compared to the other catalysts tested. The ethylene in the outlet peaks before the CO. The ethylene intermediate on the surface should be easier to oxidize than a methyl group remaining from acetone and acetate formation, which may be the culprit for the larger CO production. Based on the CO oxidation results, it is also possible that carbonate from byproduct CO oxidation could inhibit the reaction and deactivate the catalyst much like what was observed during CO oxidation; except with propylene oxidation there are more partial oxidation intermediates that could form monodentate carbonates and also deactivate the sample. This trend is consistent if we consider the 1:1 and 3:1 Pt:Pd samples; from the CO oxidation experiments such carbonates did not form. Unfortunately, the formation of the monodentate carbonate during propylene oxidation is difficult to monitor due to common peak positions with acetone. Mechanistically, the addition of Pd to a Pt catalyst seems to shift the propylene oxidation mechanism from an indirect dehydrogenation mechanism towards a mechanism directly involving oxygen. Past a certain Pd content, the shift towards the direct oxidation mechanism seems to be detrimental as the required oxygen is not able to adsorb or activate on the surface. The presence of both indirect and direct propylene oxidation mechanisms provides the best performance.

4.4.4 CO and C_3H_6 Co-oxidation

In comparing the light off performance ranking under co-oxidation conditions to either CO or propylene oxidation individually, the trend in the ranking more closely resembles that for CO oxidation. This was expected due to strong CO poisoning/adsorption. For instance, in comparing the monometallic Pt sample results, CO oxidation light off occurred at a higher temperature than that of the other samples, as is also the case for the CO and propylene co-oxidation, whereas the Pt sample was not the worst performing for propylene oxidation. The relative amounts of the CO-M-O to CO-M differ between CO oxidation and CO and propylene co-oxidation. During co-oxidation, there was a decreased amount of the CO-M-O and more CO-M and CO-M-CO, compared to the amounts observed during CO oxidation by itself. Since the CO-M-O was associated with high CO oxidation activity, and there was less, lower reactivity would be expected and was indeed observed with the addition of propylene. Since more CO-M and CO-M-CO are observed, this suggests there is less surface O available for formation of CO-M-O, suggesting that propylene inhibited CO oxidation by blocking the oxygen from accessing the active sites via competitive adsorption. Note, the position of the CO-M-O peak also corresponds to that for CO-M-CO, and in this co-oxidation case the CO-M-CO peaks are not trivial. Therefore, the assignment cannot be solely attributed to CO-M-O species but also to CO-M-CO species. This only further highlights the lack of oxygen availability alluded to in the previous discussion. Furthermore, from the DRIFTS peak height as a function of temperature results for co-oxidation, the peak height maximum for the various CO species occurred at a much lower temperature than for CO oxidation alone. This occurred at the same time as formate formation and at slightly higher temperatures the acetone and acetate peak heights increased. Thus some CO is oxidizing through a formate intermediate and making room for propylene adsorption and oxidation to the partial oxidation surface species. This is evidence of competitive adsorption that is leading to the inhibition of both CO and propylene during co-oxidation.

The above comparisons help mechanistically explain how propylene inhibits CO oxidation, and can also describe why there are different rates of conversion change versus temperature. As the Pd content increased, the direct oxidation mechanism became favored, which led to a larger amount of poisoning by inhibiting surface species, consistent with what was observed during propylene oxidation discussed earlier. Similar byproducts were observed during reactor testing, but were lower in comparison to propylene oxidation in the absence of CO. Propylene oxidation is inhibited until the CO desorbs or is oxidized, and therefore lower partial oxidation species concentrations were ultimately observed because the catalyst was at a higher temperature when they form, and was able to more easily oxidize them as they formed. If the direct oxidation mechanism for propylene was indeed the dominant mechanism for the Pd-rich catalysts, this would be consistent with the large offset between the CO and propylene conversion profile and the lower overall conversion for the 1:3 Pt:Pd catalyst seen in co-oxidation compared to oxidation of each component individually. Since there was less available surface oxygen with propylene present due to competitive adsorption, and the direct oxidation mechanism was favored compared to indirect oxidation, more inhibition of the Pd-rich catalyst was observed.

4.5 Conclusions

CO and propylene oxidation, in high reactant concentrations, was studied over Pt-Pd bimetallic catalysts with different Pt:Pd ratios. In evaluating CO oxidation, bimetallic catalysts with a higher Pd content led to lower temperature CO oxidation activity, and this was related to how the CO bound to the bimetallic surface. CO-M-O species, M being the metal, were observed during DRIFTS experiments and were correlated to the most active bimetallic samples. In contrast to the bimetallic samples, CO-M-CO species were observed on the monometallic Pt sample before light off, further demonstrating the greater sensitivity Pt has to CO poisoning. Indeed, with increasing CO concentration, the Pt catalyst was the most affected in terms of increasing inhibition. The Pd-rich catalysts, i.e. the 1:3 Pt:Pd and monometallic Pd samples, appear to be inhibited, or deactivated, through surface carbonate formation. For propylene oxidation, the shift in the T_{50} with increased concentration did not depend on the Pt:Pd ratio; however, there was evidence of partial oxidation product inhibition, due to at least acetone, ethylene, and CO, all observed as surface species/byproducts. The increased rate at which these partial oxidation species accumulate on Pd-rich catalysts coincide with the poorer performance observed during reaction tests. A shift between indirect oxidation on Pt towards direct oxidation on Pd being favored as a function of Pt:Pd ratio was discussed and supported by the observed reaction intermediates. For the 1:1 and 3:1 Pt:Pd catalysts, both mechanisms seem to occur in parallel and a higher surface oxygen availability led to a low temperature light off. For the Pt catalyst, the dehydrogenation mechanism is favored. The available surface oxygen is limiting for both the Pd and Pt catalysts.

In comparison to the single component CO and propylene oxidation, catalyst performance trends during co-oxidation of the two species, indicated by T_{50}, mirror those of CO oxidation by itself. With propylene present in the gas feed, the CO-M-O species was less favored; more triply bound, single carbonyl, and dicarbonyl species were evident. The greater inhibition observed on the monometallic Pt sample was attributed to the greater amount of CO-M-CO species formed, much like in the evaluation of CO oxidation in the absence of propylene. The greater deactivation of the Pd-rich catalyst was attributed to partial oxidation species formation; in this case suffering from both carbonate formation from CO oxidation, as well as partial oxidation products formation from propylene oxidation. The data also indicate that propylene inhibits oxygen availability to the active sites and therefore inhibited CO oxidation light off.

Chapter 5 Mechanistic Effects of Water on CO and C_3H_6 Oxidation on Pt-Pd/Al_2O_3 Bimetallic Catalysts

Note: The material in this section has been submitted for publication. Reference and figure numbers have changed for dissertation consistency.

5.1 Introduction

The role of water in CO and hydrocarbon oxidation mechanisms has implications on a wide range of applications, from automotive exhaust control to proton exchanged membrane (PEM) fuel cells. For instance for natural gas vehicle exhaust, where the exhaust contains large water concentrations from methane combustion, the role of water in the oxidation of methane over Pt and Pd, and Pt-Pd/Al_2O_3 catalysts has been studied and found that water has an inhibiting effect on the oxidation rate [103], [104], and may lead to catalyst deactivation on Pd catalysts [105]. Moreover, hydrothermal treatments on Pt-Pd/Al_2O_3 catalysts may reverse Pd surface segregation that can occur over the catalyst lifetime [103]. For gasoline engine exhaust, the effect of water on a three-way catalyst has been evaluated and it was found that there is some enhancement of CO and propylene oxidation on Pd catalysts [106].

For diesel emissions, adding water to the reaction conditions enhances low temperature CO [107] and propylene catalytic oxidation [108]. Through isotope labeling experiments, it was demonstrated that on a Pd/Al_2O_3 catalyst the low temperature CO and propylene oxidation mechanism involves reactions with species related to water, where oxygen plays a secondary role. This is consistent with findings from CO oxidation on Pt and Pd catalysts for preferential CO oxidation (PROX) for PEM fuel cells. On a Pd/CeO_2-TiO_2 catalyst, low temperature CO oxidation was attributed to reactions with OH from the water present; water has also been seen to suppress some carbonate species formation on the surface which leads to better CO oxidation [109]. Microkinetic modeling of CO oxidation on Pt suggests carboxyl intermediated CO oxidation as in the presence of water [110]. Without water present, the mechanism for CO oxidation on Pt catalysts has been stipulated to be carbonate intermediated [72]. In a recent study it was found that the formation of surface carbonates may be a catalyst poison reducing the activity of Pd and Pd rich Pt-Pd bimetallic catalysts [111]. During co-oxidation of CO and propylene, propylene oxidation is limited until the CO is reacted due to strong CO interaction with the precious metal sites. With this in mind, we narrowed this study to consider separately the effect of water on CO and propylene oxidation.

Recently there has been increasing momentum towards the use of higher efficiency lean combustion modes in the automobile industry due to fuel economy gains. The emissions from these lean combustion modes, or low temperature combustion technologies, are not yet able to meet environmental regulations using the current catalytic aftertreatment systems. These lean combustion fuel modes, specifically reactivity controlled combustion ignition (RCCI), emit much higher CO and hydrocarbon emissions than a conventional diesel engine mode and have a lower exhaust temperature [3]. Therefore oxidation catalysts with higher activity need to be developed and understood before these combustion modes can meet regulations and be implemented commercially. Bimetallic Pt-Pd catalysts have received a lot of attention due to their relatively high oxidation activity that can change as a function of Pt:Pd ratio [5], however the effect of water on these bimetallic catalysts in oxidizing CO and propylene is not as widely studied as on the monometallic catalysts.

In the present study we investigated the effect of water on Pt-Pd/Al_2O_3 catalysts, both when it was present during reaction and also when present in the catalyst pretreatment before reaction. The effect of water on CO and propylene oxidation was measured and surface species on Pt, Pd, and Pt-Pd/Al_2O_3 catalysts were probed using diffuse reflectance infrared Fourier transform spectroscopy (DRIFTS).

5.2 Experimental Methods

5.2.1 Catalyst Synthesis

Honeycomb cordierite monoliths washcoated with γ-Al_2O_3 were supplied by Johnson Matthey, with a 1.59 g/in^3 washcoat loading. Three catalysts were made using incipient wetness impregnation; Pd, 1:1 Pt:Pd, and Pt. The platinum group metal (PGM) precursors were $Pd(NO_3)_2$ and $Pt(NH_3)_4(NO_3)_2$, which were both purchased from Sigma Aldrich. These were weighed and mixed into a DI water solution such that the desired metal loading would fill the alumina pore volume. The loading of the catalysts made were 0.55 wt% PGM for the Pd/Al_2O_3 catalyst, 0.78 wt% PGM for the 1:1 Pt:Pd/Al_2O_3 catalyst, and 1 wt% PGM for the Pt/Al_2O_3 catalyst. These loadings were selected such that the number of moles of PGM on each catalyst were identical. The catalysts were then dried and calcined in a Neytech Vulcan 3-550 muffle furnace for 4 hours at 550°C, then aged at 700°C in situ under flowing 14% O_2, 5% H_2O in balance N_2. The particle sizes as measured by CO pulse experiments for these catalysts were 19.4 nm, 5.2 nm, and 4.3 nm for the Pt, 1:1 Pt:Pd, and Pd catalysts respectively.

5.2.2 Reactor Experiments

The catalysts were placed in a quartz tube which was 1 inch in inner diameter, they were wrapped in insulation to avoid gas bypass, and small hollow quartz tubes were placed upstream to avoid fully developed flow patterns. The gas flow rate used was approximately 11.5 L/min depending on the number of catalyst channels, to maintain a 50,000 hr^{-1} gas hourly space velocity for each experiment. The gas flow was controlled by Bronkhorst mass flow controllers, and the water was evaporated and the flow rate was controlled by a Bronkhorst Controlled Evaporator Mixer system with a liquid flow controller for the water and a carrier nitrogen flow controller upstream of the evaporator.

Temperature programmed oxidation (TPO) experiments were performed with a 7.3°C/min ramp rate of the gas measured upstream of the catalyst, from 80 to 300°C. Upstream of the reactor, the inlet gas stream was heated by a preheater that was ramped in temperature during the experiment in order to keep the temperature gradient along the catalyst length less than 3°C, as measured during an experiment with N_2 only flowing. The outlet gases from each TPO were measured with an MKS MultiGas 2030 FTIR gas analyzer. Based on a repeat experiment the standard deviation of these TPO experiments is 0.4°C.

The gas concentrations during the TPO experiments were selected in order to be representative of the high hydrocarbon and CO concentrations observed in the exhaust from low temperature combustion engines. The concentration levels tested were as follows.

- For CO oxidation experiments 3000 ppm CO, 10% O_2, in balance nitrogen with either 0 or 5% H_2O.
- For a hydrocarbon, propylene was selected, and the concentrations in the inlet gases were 1500 ppm C_3H_6, 10% O_2, 5% H_2O in balance nitrogen with either 0 or 5% H_2O.

In the results presented, the data obtained with 0 and 5% H_2O during the TPO experiments are labeled as RX O2 and RX O2 H2O respectively.

Before each TPO experiment, a pretreatment was performed, lasting 1 hour at 600°C. Different pretreatment conditions were evaluated. For each 0% H_2O or 5% H_2O experiment, a dry or wet pretreatment was conducted with the following concentrations; 14% O_2 and 0 or 5% H_2O in balance N_2. For the TPO with 0% H_2O, the wet pretreatment was followed by an additional 1 hour under dry conditions. In the results presented, the data obtained with 0 and 5% H_2O in the pretreatment are labeled as PT O2 and PT O2 H2O respectively. Note, an experiment labeled as “RX O2 H2O PT O2 H2O” in the legend will have the reaction conditions with CO or propylene, 10% O_2, and 5% H_2O in balance N_2, with a pretreatment of 14% O_2 and 5% H_2O in a balance of N_2 preceding the TPO.

5.2.3 DRIFTS Experiments

In order to evaluate the CO oxidation mechanism over each catalyst, in situ DRIFTS experiments were performed using a Nicolet 6700 spectrometer equipped with an MCT detector and a high temperature Harrick Scientific Praying Mantis reaction chamber with ZnSe windows. The washcoat was scraped off of the cordierite honeycomb monolith and 30 mg was pressed into a pellet and placed into the reaction chamber. The DRIFTS spectra were collected in the 4000 – 650 cm^{-1} wavenumber range, accumulating 98 scans at 4 cm^{-1} resolution.

TPO experiments were performed to mirror the conditions used for the reactor experiments, except the ramp rate of the gas stream was slowed to about 4.2°C/min in order to increase the number of scans acquired during each experiment and the temperature ramp was from 66-300°C. A background spectrum was taken at the beginning of the temperature ramp in flowing He, and then the reactant gases were added and the samples were exposed to the feed gas for at least 1 hour before the temperature ramp was started.

The concentrations during the DRIFTS TPO experiments were identical to the reactor testing; 3000 ppm CO, with 10% O_2 and 5% H_2O in balance He. A 50 mL/min total flow rate was maintained using MKS mass flow controllers. TPO experiments were also performed with O_2 and He (with and without H_2O) only so the spectral data obtained could be subtracted from the spectra obtained during the TPOs with CO. This was done in order to remove background shift due to temperature and any other temperature effects. An analogous pretreatment to the reactor experiments was done before the experiments and between each TPO experiment at 550°C with 14% O_2 with or without H_2O for 1 hour. The various dry and wet reaction and pretreatment conditions are labeled identically in the results as in the reactor experiments.

5.3 Results and Discussion

5.3.1 CO Oxidation Reactor Testing

First the phenomenology of the water effects on conversions will be discussed, followed by characterization to gain insight as to the chemistry changes. As shown in Figure 5-1, CO oxidation over the Pd/Al_2O_3 catalyst depended on both whether 5% water was added to the reaction and/or pretreatment mixtures. In terms of the temperature required to reach 50% CO conversion (T_{50}), when water was added to the reaction T_{50} decreased from 146 to 130°C and water added in the pretreatment decreased T_{50} from 142 to 136°C. Water had a smaller enhancement effect on the reaction when the pretreatment already contained water. In terms of pretreatment effects, when water is in the reaction, the water pretreatment led to a higher T_{50} (130 to 136°C), however when water was not present in the reaction the opposite was observed, the water pretreatment led to a lower T_{50} (146 to 142°C). Furthermore, the light off curve slopes varied with the different conditions; when water was present in the reaction the slope was steeper than the case without water in the reaction mixture.

In contrast, the CO conversion data for the Pt/Al_2O_3 catalyst in Figure 5-2 shows that the pretreatment conditions had very little impact on CO oxidation performance, but with water in the reaction mixture, it had a large inhibiting effect. For example, with the addition of water, the T_{50} values increased by 17 and 19°C respectively in experiments where the pretreatment contained water or did not. Unlike the Pd catalyst where the light off curve slopes varied, the light off curve slopes for the Pt/Al_2O_3 catalyst were similar. The experiments without water in the pretreatment appear to match at low

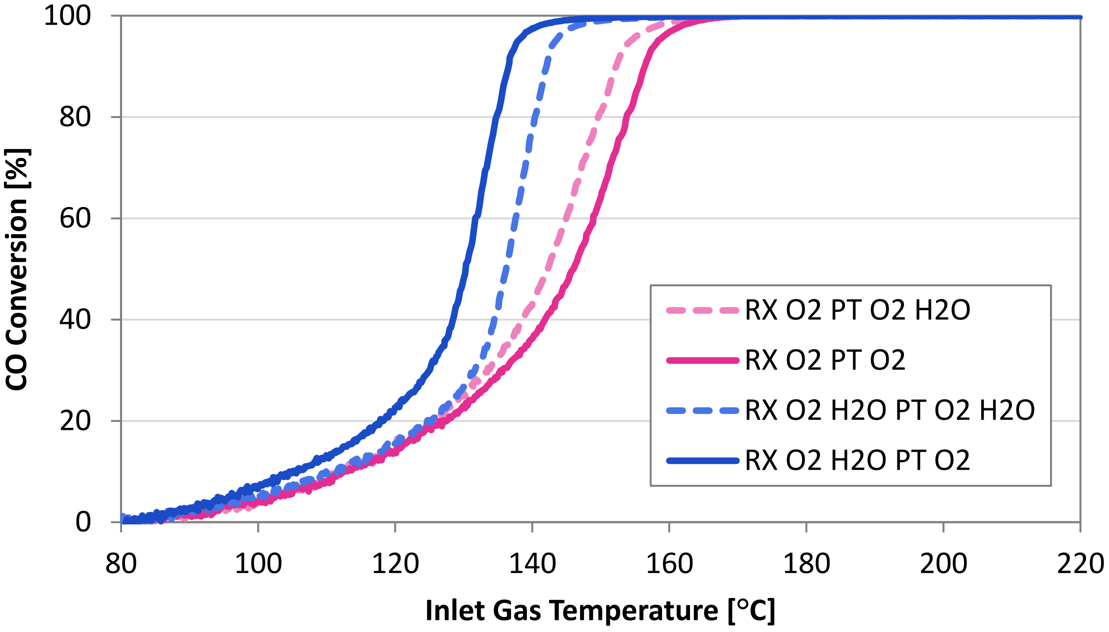

Figure 5-1 Reactor testing Pd/Al_2O_3 catalyst; reaction conditions (RX) 3000 ppm CO, 10% O_2, 0 or 5% H_2O, in balance N_2 and pretreatment conditions (PT) 14% O_2, 0 or 5% H2O, in balance N_2

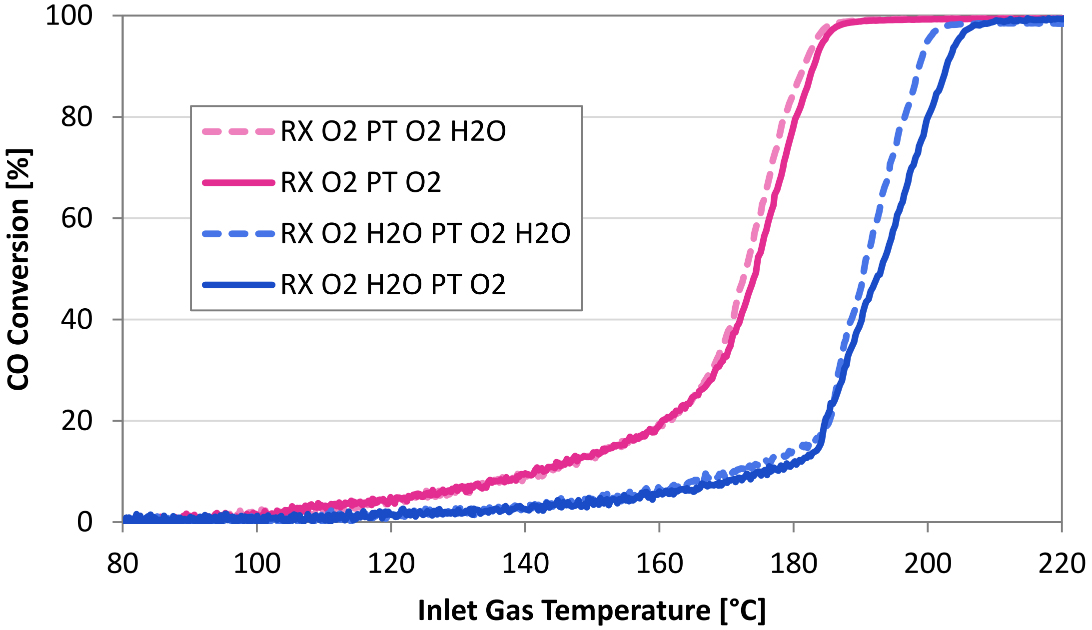

Figure 5-2 Reactor testing Pt/Al_2O_3 catalyst; reaction conditions (RX) 3000 ppm CO, 10% O_2, 0 or 5% H_2O, in balance N_2 and pretreatment conditions (PT) 14% O_2, 0 or 5% H2O, in balance N_2

temperature and then diverge at high temperatures with a smaller slope. Also when there was no water in the reaction mixture there was more low temperature CO oxidation activity.

For the bimetallic Pt-Pd/Al_2O_3 catalyst, the conversion data are presented in Figure 5-3. Here there was an effect of the pretreatment. Without water in the pretreatment, the addition of water to the reaction mixture decreased the T_{50} from 159 to 146°C. With water in the pretreatment, the addition of water to the reaction mixture had no effect on the T_{50} of 156.5°C.

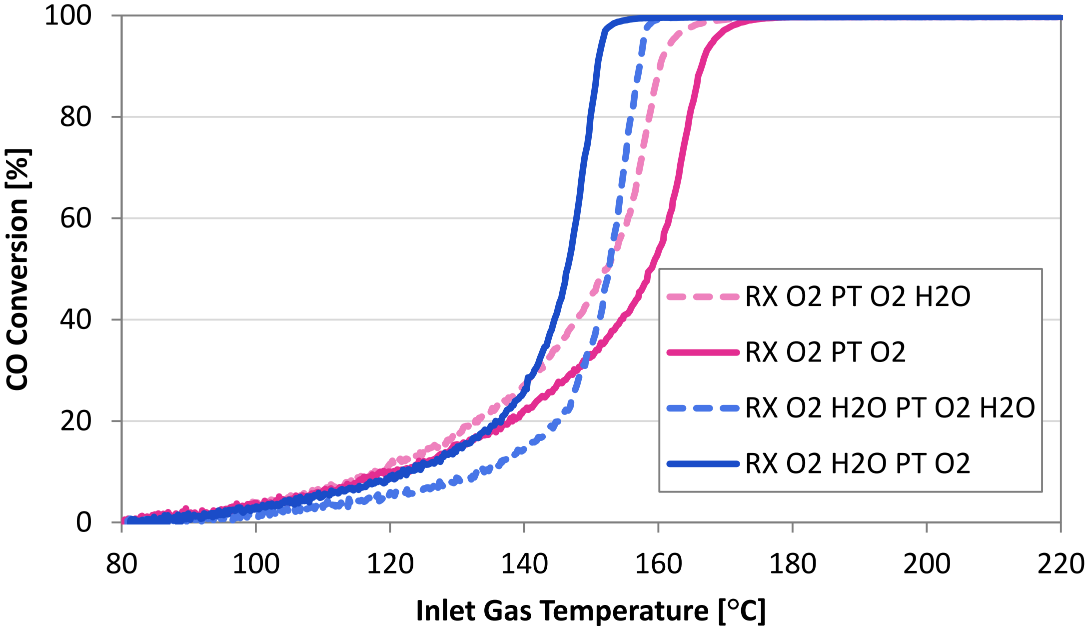

Figure 5-3 Reactor testing 1:1 Pt-Pd/Al_2O_3 catalyst; reaction conditions (RX) 3000 ppm CO, 10% O_2, 0 or 5% H_2O, in balance N_2 and pretreatment conditions (PT) 14% O_2, 0 or 5% H2O, in balance N_2

Although for all experiments the CO oxidation onset occurred at the same temperature, in the absence of water there was a greater increase in the CO oxidation rate below the T_{50} compared to the case with water. However, for the case with water the CO oxidation rate of change accelerated at 145°C such that the light off curves cross at the T_{50} and full conversion was reached at a lower temperature. Qualitatively speaking, the bimetallic catalyst showed aspects of both the monometallic catalysts. When the catalyst was pretreated with water, the low temperature CO oxidation without water associated with Pt was observed *and* the increase in light off curve slopes with water associated with Pd was observed for all pretreatment conditions. DRIFTS experiments were conducted in order to gain mechanistic insights into these water effects.

5.3.2 CO Oxidation DRIFTS Testing

The DRIFTS spectra obtained after exposure to CO and oxygen at 66°C are shown in Figure 5-4. For the Pd/Al_2O_3 spectra, Figure 5-4 (a), linearly bound CO was evident at 2102 cm^{-1}, and some bridged CO formed based on the broad band at 2000-1800 cm^{-1} [89]. Adding water into the reaction mixture increased CO adsorption via both linear and bridged carbonyls. After the water treatment, the broad peak associated with bridged carbonyls diminished and shifted to 1965 cm^{-1}. The shift to higher wavenumber indicates less triply bound and more doubly bound bridged CO. However, the inclusion of water in the pretreatment had opposite impacts on the carbonyl amount depending on whether water was present in the reaction gas mixture. For the Pt/Al_2O_3 spectra, Figure 5-4 (b), the peak at 2094 cm^{-1} is assigned to linearly bound CO and shoulders at 2060 cm^{-1} and 2113 cm^{-1} correspond to co-adsorbed CO and atomic oxygen on a single Pt site, as demonstrated previously [111]. The feature at 1820 cm^{-1} indicates there was

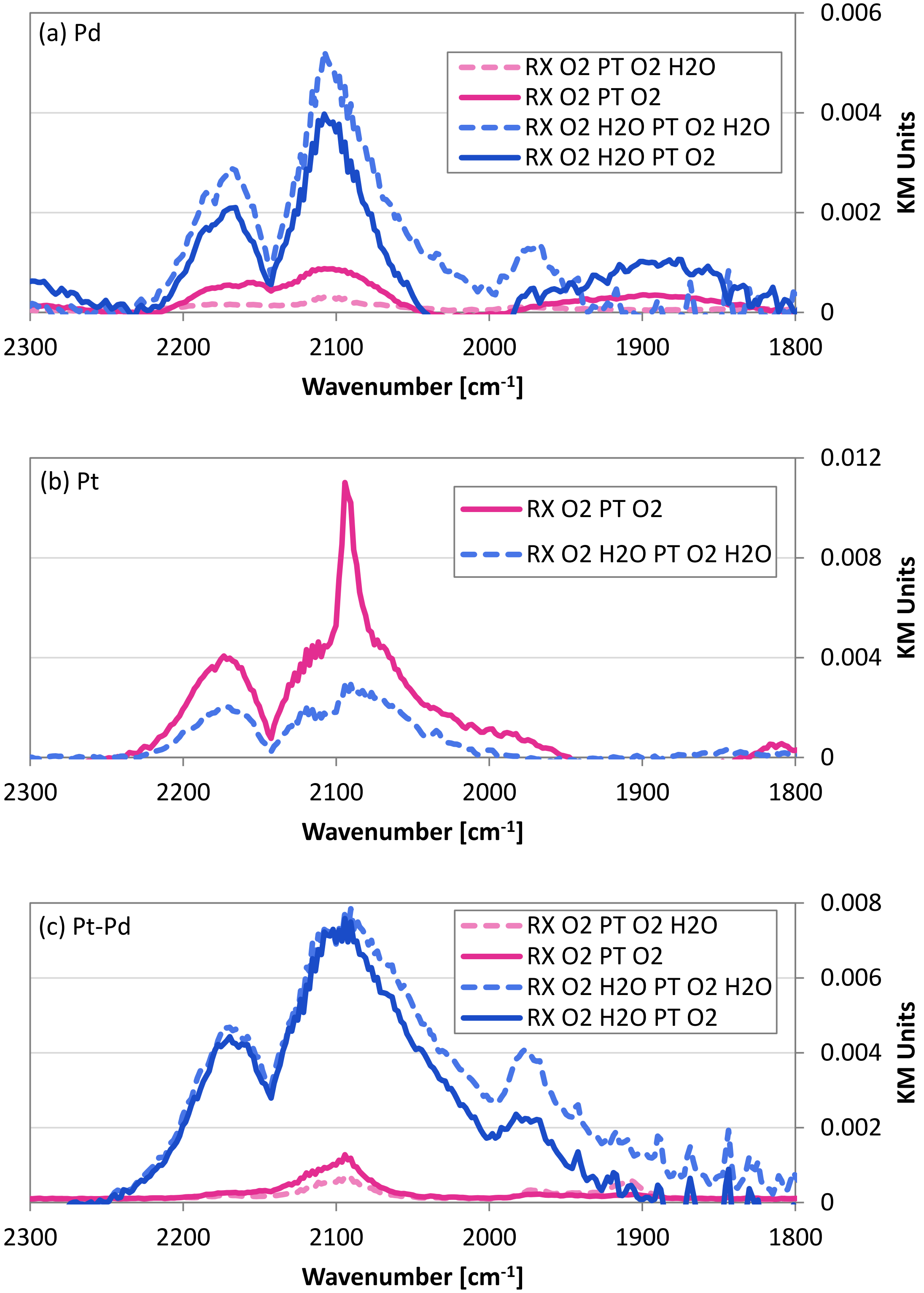

Figure 5-4 DRIFTS spectra at 66°C for a) Pd, b) Pt, c) Pt-Pd catalysts; reaction conditions (RX) 3000 ppm CO, 10% O_2, 0 or 5% H_2O, in balance N_2 and pretreatment conditions (PT) 14% O_2, 0 or 5% H2O, in balance N_2

also triply bound CO, and there is no evidence of the doubly bridged CO [89]. In contrast to what was observed for the Pd catalyst, on the Pt catalyst there was more CO adsorption without water in the reaction mixture, and again in the case of the water pretreatment less bridged CO was observed. The Pt-Pd/Al_2O_3 spectra are shown in Figure 5-4 (c). There was more CO adsorption in the presence of water, but there were no triply bridged carbonyls observed and only the peak at 1965 cm^{-1} for doubly bridged CO observed that was observed on Pd catalyst. The linearly adsorbed carbonyl feature for the bimetallic catalyst seems to be composed of two peaks, encompassing 2102-2090 cm^{-1}, when water was in the reaction mixture. However, when water was absent from the reaction mixture the higher wavenumber peak decreased relative to the lower, indicating that the CO preferentially adsorbed on the Pt in the bimetallic particles when water was absent. When water was in the reaction feed, the CO adsorbed to the Pd as well. Based previous studies, the higher wavenumber peak in the 2170 cm^{-1} range is assigned to CO bound to alumina support Lewis acid sites, expected in the 2200-2186 cm^{-1} range, or CO hydrogen bonded to surface alumina hydroxyl groups, in the 2156-2158 cm^{-1} range [74]. For both the Pd and Pt-Pd catalysts, the presence of water enhanced this peak, while for the Pt the water diminished it. This feature was assigned to CO hydrogen bonded to surface alumina hydroxyl groups, specifically at the particle/support interface, which may later react with alumina OH groups.

CO oxidation mechanisms, with and without water, and the water gas shift (WGS) reaction mechanism, will be discussed briefly in order to aid in the understanding the intermediate species observed spectroscopically in the DRIFTS experiments during CO oxidation. Firstly, for the case without water, the carbonate/carboxylate (CO_3/CO_2) intermediated CO oxidation mechanism is

$$CO + O_2 \rightarrow CO_3, \tag{5-1}$$

$$CO + O \rightarrow CO_2, \tag{5-2}$$

$$CO_3 \rightarrow CO_2 + O, \text{ and} \tag{5-3}$$

$$CO_2 \rightarrow CO_{2(g)}, \tag{5-4}$$

where the reactants, unless otherwise denoted, represent species adsorbed to the surface [36], [37], [72]. This simplifies the list as it allows us to not assign the formed species as monodentate or bidentate, as the carbonate can adsorb in either form, and from the IR spectra we cannot distinguish whether this occurs on the metal sites or on the alumina support. In this abbreviated mechanism, note that the formation of carbonate (reaction 5-1) occurs via the reaction of CO with diatomic oxygen and the formation of carboxylate can occur via either the reaction of CO with atomic oxygen or the decomposition of carbonate (reactions 5-2 and 5-3 respectively).

Secondly, the CO oxidation mechanism with water is

$$CO + OH \rightarrow COOH, \tag{5-5}$$

$$CO + O + OH \rightarrow CO_2OH, \tag{5-6}$$

$$COOH + OH \rightarrow CO_{2(g)} + H_2O_{(g)}, \tag{5-7}$$

$$CO_2OH + OH \rightarrow CO_{2(g)} + H_2O_{(g)} + O, \tag{5-8}$$

$$COOH \rightarrow CO_{2(g)} + H, \tag{5-9}$$

and can either be intermediated by bicarbonate and carboxyl as shown in reactions 5-5 through 5-8 [108], or proceed through the WGS mechanism as captured by reactions 5-5 and 5-9 [112], [113]. The atomic oxygen present in reactions 5-2 and 5-4 could be interpreted as either O_2 dissociative chemisorption on the catalyst, or the reduction of PdO. The water in the gas phase can dissociate to OH and H, and in the presence of so much oxygen the H can react with atomic oxygen from dissociative molecular oxygen adsorption. Bicarbonate is formed as a reaction intermediate in reaction 5-6, and will sit either on the support or metal sites in a bidentate fashion with the OH group positioned perpendicular to the surface. A formate/carboxyl reaction intermediate is formed in reaction 5-5, with direct combination of the OH to the CO. Below, COOH is referred to as carboxyl to distinguish it from the HCOO formate species, however note that the formate species below has also been identified as a WGS intermediate.

The formation of the formate species could come about through the following reactions (reactions 5-10 through 5-12):

$$CO + OH \rightarrow HCOO, \tag{5-10}$$

$$CO + H + O \rightarrow HCOO, \text{ and} \tag{5-11}$$

$$HCOO + OH \rightarrow CO_{2(g)} + H_2O_{(g)}. \tag{5-12}$$

The formate can either form on the support through reactions with OH groups of the alumina, similar to what occurs on ceria [101], [114], or when water is present in the reaction OH from water dissociation on metal sites. The difference between reactions 5-10 and 5-5 is that in reaction 5-10, the OH bond cleaves and the HCOO will be adsorbed in a bidentate configuration with the H sitting perpendicular to the metal site or support [115].

Finally, any hydrogen present that did not react to form an OH group could itself react with CO in the following reactions (reaction 5-13 and 5-14):

$$CO + H \rightarrow HCO \text{ and} \tag{5-13}$$

$$CO + H \rightarrow COH. \tag{5-14}$$

The difference here being whether the H attacks the carbon or the oxygen of the CO. The HCO species represents formyl which was not observed spectroscopically and will not be mentioned further [115]. The COH species may indeed have been present, as the IR peak is common with many of the other species mentioned [89].

In summary there are seven anticipated/possible intermediate species during CO oxidation as follows: monodentate carbonate, bidentate carbonate, carboxylate, bicarbonate, carboxyl, formate, and COH. These intermediates can be distinguished via the DRIFTS spectra, primarily looking in the 1800-1100 cm^{-1} wavenumber range. In order to determine important species, an intermediate oxidation temperature of 162°C was selected, with spectra shown in Figure 5-5 for the three catalyst samples. It should be noted that the water signal was subtracted from these spectra and so while the 1653 cm^{-1} feature is very close to water bending at 1637 cm^{-1} [109], we considered it to be independent from water. The prominent peaks observed in this range appear between 1258-1228 cm^{-1} (referred to as 1240 cm^{-1}), 1443-1432 cm^{-1} (referred to as 1435 cm^{-1}), and 1658-1650 cm^{-1} (referred to as 1653 cm^{-1}). The exact wavenumbers for the maximum peak heights vary slightly as a function of catalyst and experimental conditions. These peaks appear at varying intensities and ratios across the different

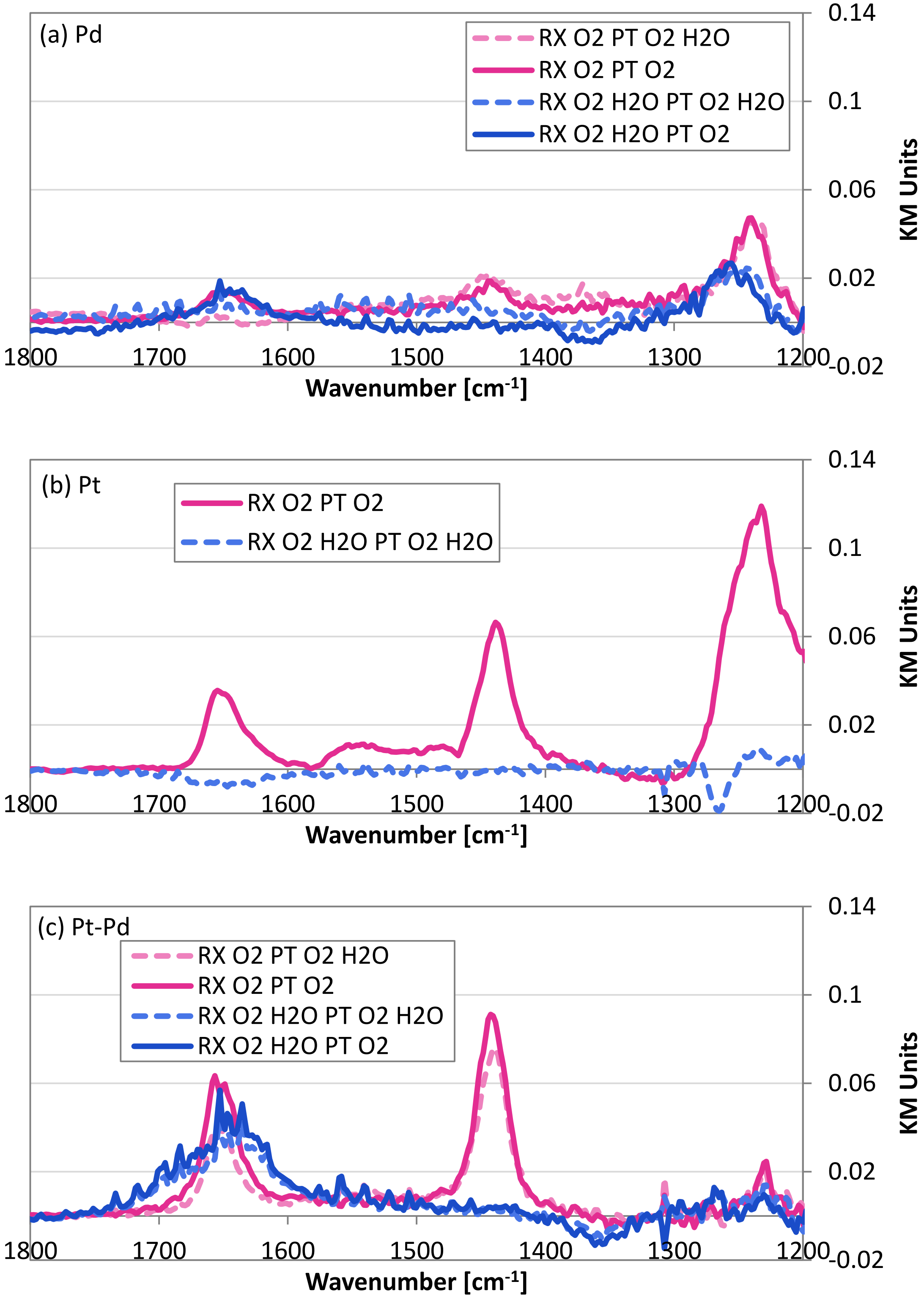

Figure 5-5 DRIFTS spectra at 162°C for a) Pd, b) Pt, c) Pt-Pd catalysts; reaction conditions (RX) 3000 ppm CO, 10% O_2, 0 or 5% H_2O, in balance N_2 and pretreatment conditions (PT) 14% O_2, 0 or 5% H2O, in balance N_2

samples, which aid in assigning them to surface species and the following logic was used based on literature findings.

a) A peak at 1435 cm^{-1} alone indicates either monodentate or free carbonates [35], [84], along with weaker peaks at 1330 cm^{-1} for monodentate and 1090-1020 cm^{-1} for monodentate and free carbonates, which were not observed in this study.
b) Two peaks at 1653 cm^{-1} and 1240 cm^{-1} together indicate bidentate carbonates [35], [85], [116], again a weak peak is expected around 1020 cm^{-1} but not observed.
c) Carboxylate can be identified by 1435 and 1653 cm^{-1} together [35], [85].
d) All three peaks together indicate bicarbonate species [74], with a weak peak around 1300 cm^{-1} that was not observed.
e) A pair of 1240 and 1435 cm^{-1} peaks correspond to carboxyl [84].
f) A peak at 1547 cm^{-1}, which together with a peak at 2960 cm^{-1} and small shoulder at 1392 cm^{-1} indicates formate species [74], [86].
g) Finally the 1240 cm^{-1} peak occurring alone has been assigned to COH; it has been reported on Pt at 1256 cm^{-1} [89].

From this, the carbonate peaks in a) and b) correspond to the carbonate formation in reaction 5-1. The peaks mentioned in c) correspond to carboxylate formation in reaction 5-2. The formation of bicarbonate and carboxyl species mentioned in d) and e) are captured by reactions 5-5 and 5-6. The peaks for formate, reactions 5-10 and 5-11, are given in f). The COH peak given in g) could correspond to CO reacting with H on the surface that has not yet reacted with dissociated oxygen. Many of these peaks overlap, and so distinguishing between these species spectroscopically is a challenge, however there are general trends noted, which will be discussed.

As shown in Figure 5-5 (a), the spectrum obtained during Pd catalyst characterization has both the 1653 and 1240 cm^{-1} peaks when water was or was not added to the reaction mixture, which indicating bidentate carbonate formation. The 1240 cm^{-1} peak height is slightly higher in the absence of water in the reaction feed even though the peak at 1653 cm^{-1} remains constant and the peak at 1435 cm^{-1} appears. This suggests that in addition to the bidentate carbonates, carboxyl species are on the surface. Due to the absence of water in the reaction feed the carboxyl may seem unlikely, however it is possible that OH from the support reacted. Since water was not present in the reaction mixture, the OH on the alumina near the interface of the particle could be depleted via reaction 5-5 and the carboxyl species form on the surface and reaction 5-7 did not occur. Mechanistically this may explain why under conditions with water present in the reaction but not the pretreatment leads to better performance at the lowest temperature while the worst performance was noted when water was not used in reaction or pretreatment conditions. Note that from the mechanism discussed earlier, bidentate carbonate formation implies a reaction with molecular oxygen or two adjacent atomic oxygens. The water pretreatment led to less bridged CO species, as mentioned earlier; if this bridged species were on PdO this would lead to bidentate carbonate formation and the reduction of the PdO to Pd. This may suggest that these bridged CO species might be related to the formation of the bidentate carbonates; indeed the peak at 1653 cm^{-1} was not present when water was used in the pretreatment but not reaction, indicating that there was no bidentate carbonate but only carboxyl. If PdO is reduced, this implies that the 1653 cm^{-1} peak in the case of the water pretreatment and water in the reaction could be related to bicarbonate and not bidentate carbonate.   Together this may suggest that it is not a bidentate carbonate intermediated mechanism, but a monodentate carbonate mechanism associated with the linear carbonyls when the water pretreatment is used. And when water is added to the reaction mixture, the carbonate mechanism is less likely than the carboxyl and bicarbonate intermediated mechanism.

In contrast for the Pt catalyst, shown in Figure 5-5 (b), there was a large peak at 1232 cm^{-1} and also peaks at 1653 and 1437 cm^{-1} when the reaction was run without water in the inlet mixture, the presence of all three peaks suggests bicarbonate. In the absence of water in the reaction, there are peaks associated with formate as described by f). Both formate and bicarbonate would be present on the support or at the metal/support interface as they require reaction with OH groups from the alumina. When water was present in the reaction mixture none of these intermediate peaks were observed, which perhaps indicates the most important barrier for CO oxidation on Pt when water is present is the desorption of CO to allow for oxygen adsorption. The spectrum obtained with the Pt-Pd sample, shown in Figure 5-5 (c), shows large peaks at 1653 and 1443 cm^{-1} and a small peak at 1230 cm^{-1} when water was absent in the reaction mixture, indicating that carboxylate and monodentate carbonate species were present on the surface with a small amount of bicarbonate species present as well. When water was present, the 1435 cm^{-1} peak disappeared, indicating less monodentate carbonate in favor of a carboxyl intermediate, which may be too reactive to observe spectroscopically. There was no evidence of bidentate carbonate on this sample, which is consistent with the small amount of bridged CO species noted earlier on the bimetallic catalyst. For the Pd catalyst, during the experiments without water in the reaction mixture, with the introduction of the CO flow, the H_2O and OH group O-H stretching vibration between 3800-3000 cm^{-1} decreased. This demonstrates that there was consumption the OH on the alumina, and subsequent dissociation and reaction of physisorbed water. For all the catalysts, consumption of OH was observed as a function of temperature. Similar observations were noted for a Pd/CeO_2-TiO_2 catalyst [109]. Since each of these spectra have a spectrum taken during the temperature ramp in oxygen subtracted, the loss of ambient moisture from evaporation should already be accounted for and this extra loss might be from reaction, which is supported by observable carboxyl and bicarbonate species in the absence of water across the different catalyst samples.

From the spectra at one temperature, it seems that the following species are accumulating on the various catalysts:

- Pd: bicarbonate and carboxyl without water to bidentate carbonate when water is present
- Pt: bicarbonate and formate without water, nothing when water is present
- Pt-Pd: carboxylate, monodentate carbonate, bicarbonate without water

In order to differentiate between mechanisms, three characteristic peak heights were chosen to monitor as a function of temperature; 1240, 1435, and 1635 cm^{-1}, plotted in Figure 5-6. The results from the Pd catalyst are shown in Figure 5-6 (a), (d), and (g). When water was not present in the reaction, the peak at 1240 cm^{-1} increased dramatically with temperature, while the peak at 1435 cm^{-1} increased slightly then

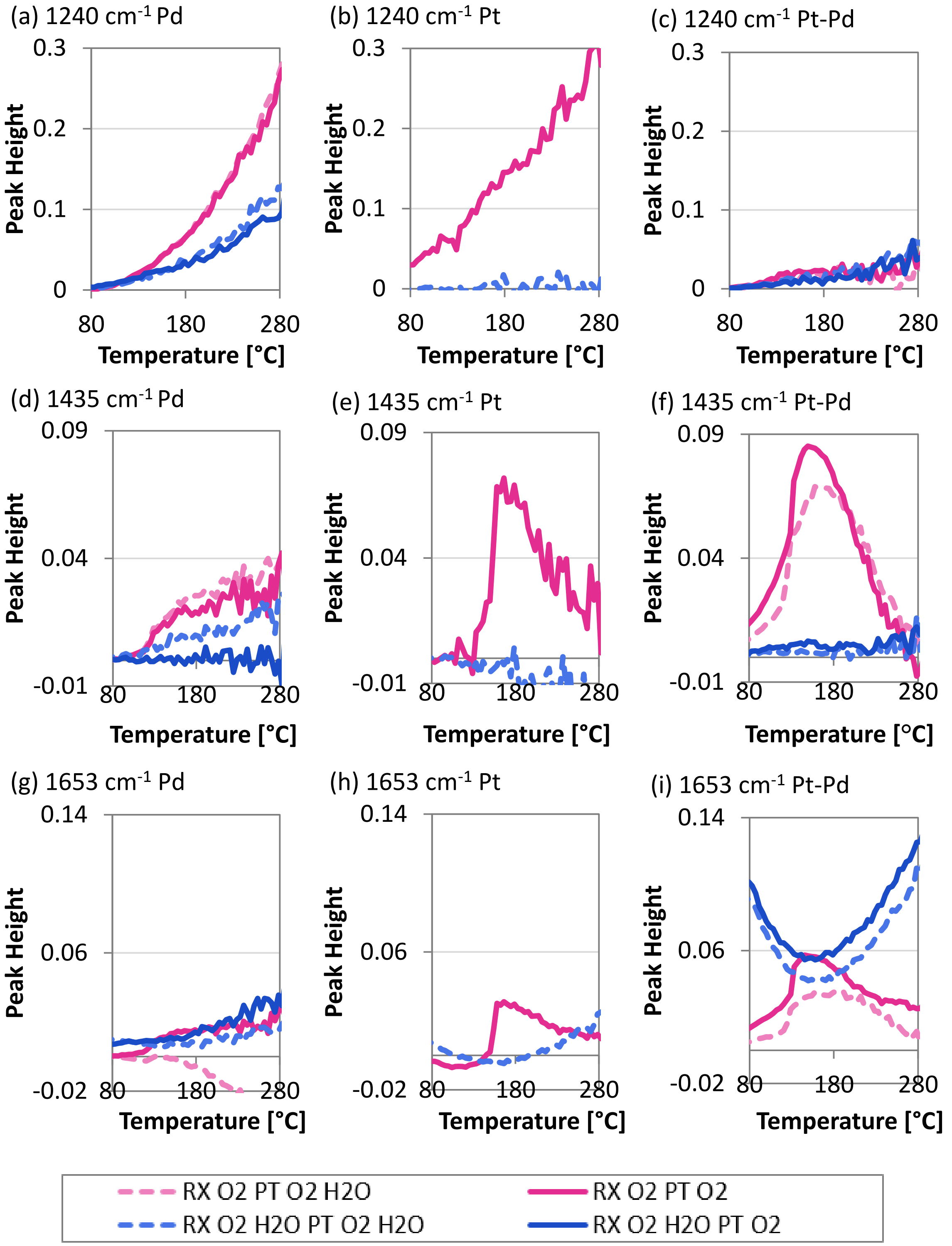

Figure 5-6 DRIFTS spectra peak height for 1240 cm^{-1}, 1435 cm^{-1}, and 1653 cm^{-1} for Pd, Pt, and Pt-Pd/Al_2O_3 catalysts as labeled; various reaction and pretreatment conditions

plateaued and the peak at 1653 increased very slightly then plateaued. This suggests that the bicarbonate species (all three peaks) formed from the OH on the support and then remained on the support, likely at the metal/support interface and did not accumulate further with temperature. The same occurs with the carboxyl formed (1240 cm^{-1} and 1435 cm^{-1}). The more significant increase in the 1240 cm^{-1} feature alone indicates COH species formed. This further suggests that without water in the gas phase, any OH on the support adjacent to the particles reacts with the CO to form these species which remain inactive in the absence of more OH to react with from water dissociation. The build-up of these species may reduce the surface area available for CO oxidation with oxygen and explain why the worst performance for the Pd catalyst was seen without water in the reaction mixture. When water was present, the 1653 cm^{-1} peak does not change much compared to that without water, and there was a marked decrease in the 1435 and 1240 cm^{-1} peaks associated with carboxyl; with water in the reaction mixture the carboxyl was able to react with OH groups from dissociated water.

The peaks at 1240 cm^{-1}, 1435 cm^{-1}, and 1653 cm^{-1} are plotted as a function of inlet gas temperature for the Pt catalyst in Figure 5-6 (b), (e) and (h) respectively. Due to the similarities observed in the reactor testing between pretreatment conditions, the full set of conditions was not tested on this catalyst. Bicarbonate and formate species formed on the Pt catalyst in the absence of water in the reaction. When water was present in the reaction mixture, none of these peaks increased as a function of temperature. When water was not present, there was an intermediate temperature range where the 1435 cm^{-1} and 1653 cm^{-1} peaks increased, much like with the Pd catalyst, except that these peaks reached a maximum and then decreased as a function of temperature. At 166°C the 1435 cm^{-1} was 3.4x greater for the Pt catalyst than the Pd catalyst, while the 1653 cm^{-1} peak was only 2x greater. The 1240 cm^{-1} peak height was also greater at that temperature for the Pt catalyst than the Pd catalyst, by 2.4x. This indicates the higher 1435 cm^{-1} for the Pt catalyst is due to monodentate carbonate rather than carboxyl species, in addition to the bicarbonate or bidentate carbonate species in this intermediate temperature range. At higher temperatures, the 1240 cm^{-1} peak remained while the other two peaks decreased, again suggesting COH accumulation. From these observations, CO oxidation on Pt appears to involve more carbonate intermediates than over the Pd catalyst. Note that on the Pt catalyst, unlike the Pd catalyst, with water in the reaction no bicarbonate formed.

Finally, on the Pt-Pd catalyst, where there was carboxylate and carboxyl intermediates observed with minimal bicarbonate, the peaks at 1240 cm^{-1}, 1435 cm^{-1} and 1653 cm^{-1} are plotted as a function of inlet gas temperature for the Pt-Pd catalyst in Figure 5-6 (c), (f) and (i) respectively. In this case, only small 1240 cm^{-1} features were observed, with no observed difference with or without water. This suggests that bicarbonates, carboxyls, and COH species did not accumulate on the surface of the bimetallic sample with increasing temperature. When water was not present, the 1435 and 1653 cm^{-1} peaks appeared at intermediate temperatures, much like what was observed for the Pt and Pd catalysts except with no accompanying 1240 cm^{-1} peak. In terms of relative peak heights, picking 166°C again, without water in pretreatment or reaction the value of the 1435 cm^{-1} was similar to that of the Pt catalyst and 3.8x that of the Pd catalyst. The 1635 cm^{-1} peak was 3.6x greater than what was observed on the Pd catalyst. This is a similar increase to that noted for the Pd catalyst, and suggests that these two peaks are related to the same species, which further strengthens the assignment to carboxylate.

To summarize these observations, it appears that that the Pd catalyst may have bicarbonate, bidentate carbonate, and carboxyl forming on the surface. On the Pt catalyst some bicarbonate, monodentate carbonate, and formate formed and both of these monometallic catalysts showed evidence of COH formation. For the Pt-Pd catalysts, it appears there were more carboxylate and monodentate carbonates formed, and only a small amount of the bicarbonate. Also the lower 1240 cm^{-1} peak on the Pt-Pd catalyst compared to the monometallic samples suggests the bimetallic suppressed accumulation of COH. This could explain why the Pt-Pd catalyst resulted in the highest light off slope during the bench scale reactor runs, as well as a shifting mechanism when including water into the reaction mixture. A lower activation energy would lead to the higher slope with water. At the same time, the accumulation of the carboxyl and bicarbonate surface species, as well as the COH, in the absence of water would explain the inhibition observed.

For the Pd and Pt-Pd catalysts, a lower light-off was attained when the catalyst was pretreated with oxygen, and water was present in the reaction mixture, whereas on the Pt catalyst this condition gave the lowest light-off performance. For the Pt-Pd and Pd catalysts, the water pretreatment led to better improvement when water was not in the reaction mixture. If this is correlated to the DRIFTS data, over the Pd catalyst, the oxygen pretreatment enhanced the CO adsorption bridged modes while the water pretreatment enhanced linearly adsorbed CO. This, however, was not observed on the Pt-Pd catalyst. This may suggest that the bridged CO species are related to the Pd catalyst's lower temperature light-off when water was present in the reaction and the pretreatment was in oxygen. For the Pt-Pd catalyst, the water did not have as much of a beneficial effect since the bridged CO species was not present. The addition of Pt inhibited CO from binding in a bridged mode when present in a bimetallic particle, which is also supported by the suppression of bidentate carbonate formation during CO oxidation on the Pt-Pd catalyst. However, for the Pt-Pd catalyst, the CO was still able to adsorb on the support/particle interface when water was in the reaction unlike the Pt catalyst, and so the high slope of the light-off curve associated with the bicarbonate/carboxyl mechanism was still attained when water was present in the reaction mixture. The role of the water then appears to be to increase CO adsorption on the support adjacent to the Pd and Pt-Pd particles, replenish OH groups on the support, and also dissociate on the metal sites themselves. For the Pt, the adsorption of water on the metal sites when water was present in the reaction mixture appears to cause inhibition. For the Pd, the higher amount of CO on the support seems to be relevant in the CO oxidation mechanism. These two factors lead to the intermediate behavior seen on the bimetallic catalyst.

5.3.3 C_3H_6 Oxidation Reactor Testing

Propylene oxidation reactions were also run on the bench scale reactor for the three catalyst samples while monitoring changes in oxidation light off and any partial oxidation products formed. From a previous study, the partial oxidation products observed during propylene oxidation over different Pt:Pd catalysts were as follows: CO, formaldehyde, ethylene, acetaldehyde, acetic acid, and acetone. In such high oxygen concentrations, the complete oxidation of propylene to CO_2 and water would be expected as

$$C_3H_{6(g)} + \frac{9}{2}O_{2(g)} \rightarrow 3CO_{2(g)} + 3H_2O_{(g)}. \tag{5-15}$$

As mentioned partial oxidation products, due to high surface concentrations of propylene, do form even in the abundance of oxygen. Previous IR experiments have shown that propylene adsorbed as propylidyne, which may occur through reaction as

$$C_3H_{6(g)} + O \rightarrow \equiv C - CH_2 - CH_3 + OH, \tag{5-16a}$$

$$2C_3H_{6(g)} + O_2 \rightarrow 2(\equiv C - CH_2 - CH_3) + H_2O + O, \text{ or} \tag{5-16b}$$

$$2C_3H_{6(g)} \rightarrow 2(\equiv C - CH_2 - CH_3) + H_2. \tag{5-16c}$$

This configuration, unlike π or σ -bound propylene, allows the propylene to sit perpendicular to the surface and therefore leads to the highest surface coverage, but requires a hydrogen to be abstracted which may react with molecular oxygen to form water or with atomic oxygen to form OH, or alternatively at low oxygen coverages may lead to H_2 formation.

Once higher temperatures are reached, this species likely rearranges to a 1-methylvinyl species (where the central carbon is now doubly bound to the surface) as shown in reaction 5-17 as

$$\equiv C - CH_2 - CH_3 \rightarrow -CH_2 - C - CH_3. \tag{5-17}$$

At low oxygen surface concentrations further dehydrogenation of the alyllic carbon occurs to form water, reactions as

$-CH_2 - C - CH_3 + O \rightarrow -CH - C - CH_3 + OH$ and (5-18a)

$-CH - C - CH_3 + OH \rightarrow -C - C - CH_3 + H_2O.$ (5-18b)

However, the production of acetone is possible via oxygen attack of the vinyl carbon, as shown in reaction 5-19 as

$-CH_2 - C - CH_3 + OH \rightarrow (CH_3)_2C = O.$ (5-19)

Note that the formation of acetone requires regaining the H that was lost during adsorption and so the reaction has been written with OH, indicating dissociative adsorption of the produced water.

Ethylene formation comes from cleavage of a carbon bond, the allylic carbon (the carbon attached to the metal site), to form ethylidyne and CO via another oxygen attack, as shown in reaction 5-20 as

$-C - C - CH_3 + O \rightarrow CO + \equiv C - CH_3.$ (5-20)

This ethylidyne can rearrange and react with H, then desorb to form ethylene.

In the previous IR study, surface acetate was observed as was product acetic acid, which would involve the reaction of ethylidyne with oxygen, and subsequent reactions to acetate and acetic acid, as shown in reactions 5-21 through 5-23 as

$\equiv C - CH_3 + O \rightarrow = CO - CH_3,$ (5-21)

$= CO - CH_3 + O \rightarrow CH_3 - CO_2$, and (5-22)

$= CO - CH_3 + OH \rightarrow CH_3 - COOH.$ (5-23)

Acetaldehyde was observed as a product in the gas phase, but not on the surface. The acetaldehyde may form as shown in reaction 5-24 as

$$\equiv C - CH_3 + OH \rightarrow CH_3 - CHO. \qquad (5\text{-}24)$$

Also in the previous study, acrolein was not observed, likely because in this reaction scheme either the second carbon is attacked first to form acetone, or the oxygen attack of the first carbon results in the cleavage of the first bond. Acrolein was also not observed in this study. Here, product formaldehyde was observed, likely through reactions 5-25 through 5-27 as

$$= CO - CH_3 \rightarrow -CH_3 + CO, \qquad (5\text{-}25)$$

$$-CH_3 + O \rightarrow CH_2 + OH, \text{ and} \qquad (5\text{-}26)$$

$$CH_2 + O \rightarrow CH_2O. \qquad (5\text{-}27)$$

The discussed reaction mechanism was deduced from DRIFTS results that were obtained in the absence of water, and since only small changes in the observed outlet concentrations involving the same intermediates were observed in this study, DRIFTS experiments were not conducted in this study. There was also formation of methane, both with and without water in the reaction, observed over the Pd and Pt-Pd catalysts (shown in supplemental information).

Having gone through the previously reported propylene oxidation reaction mechanism over Pt-Pd catalysts in the absence of water, the effect of adding water is now evaluated. Note that in the above reaction scheme, OH participated in reactions 5-19, 5-23 and 5-24, so one might expect higher concentrations of acetone, acetic acid, and acetaldehyde by adding water due to higher surface OH concentrations. There is also OH or water formation in reactions 5-16 and 5-18, which may imply that water could impact the adsorption and dehydrogenation of propylene.

With the inclusion of water in the reaction mixture steam reforming (SR) reactions could also become important [117]. However SR typically occur at temperatures above 400°C for Pt/Al_2O_3 [28], and are shown below in reaction 5-28 as

$$C_3H_6 + 3H_2O \ \rightarrow \ 3CO + 6H_2. \tag{5-28}$$

Steam reforming reactions are typically neglected during low temperature oxidation, due to high surface oxygen concentrations which may inhibit the water splitting reaction on the surface [107], [117]. The water splitting reaction is

$$H_2O_{(g)} \ \leftrightarrow \ O + H_{2(g)}. \tag{5-29}$$

As shown in Figure 5-9 (a), C_3H_6 oxidation over the Pd/Al_2O_3 depended on both whether 5% water was added to the reaction and/or pretreatment feed mixtures. When water was added to the reaction, the T_{50} increased from 190 to 202°C and water added in the pretreatment increased the T_{50} from 198 to 214°C. This demonstrates that water had an inhibition effect on the reaction when the pretreatment already contained water; the opposite of what was observed for CO oxidation. In terms of pretreatment effects, when water was in the reaction mixture, the water pretreatment leads to a higher T_{50} by 12°C (202 to 212°C) while in the absence of water in the reaction the water pretreatment leads to a higher T_{50} by 8°C (190 to 198°C). The light off curve slopes were similar except for the experiment with water in the reaction but no water in the pretreatment. In this case oxidation started at the lowest temperature but the rate of conversion change with temperature was slower at low temperature; the two cases

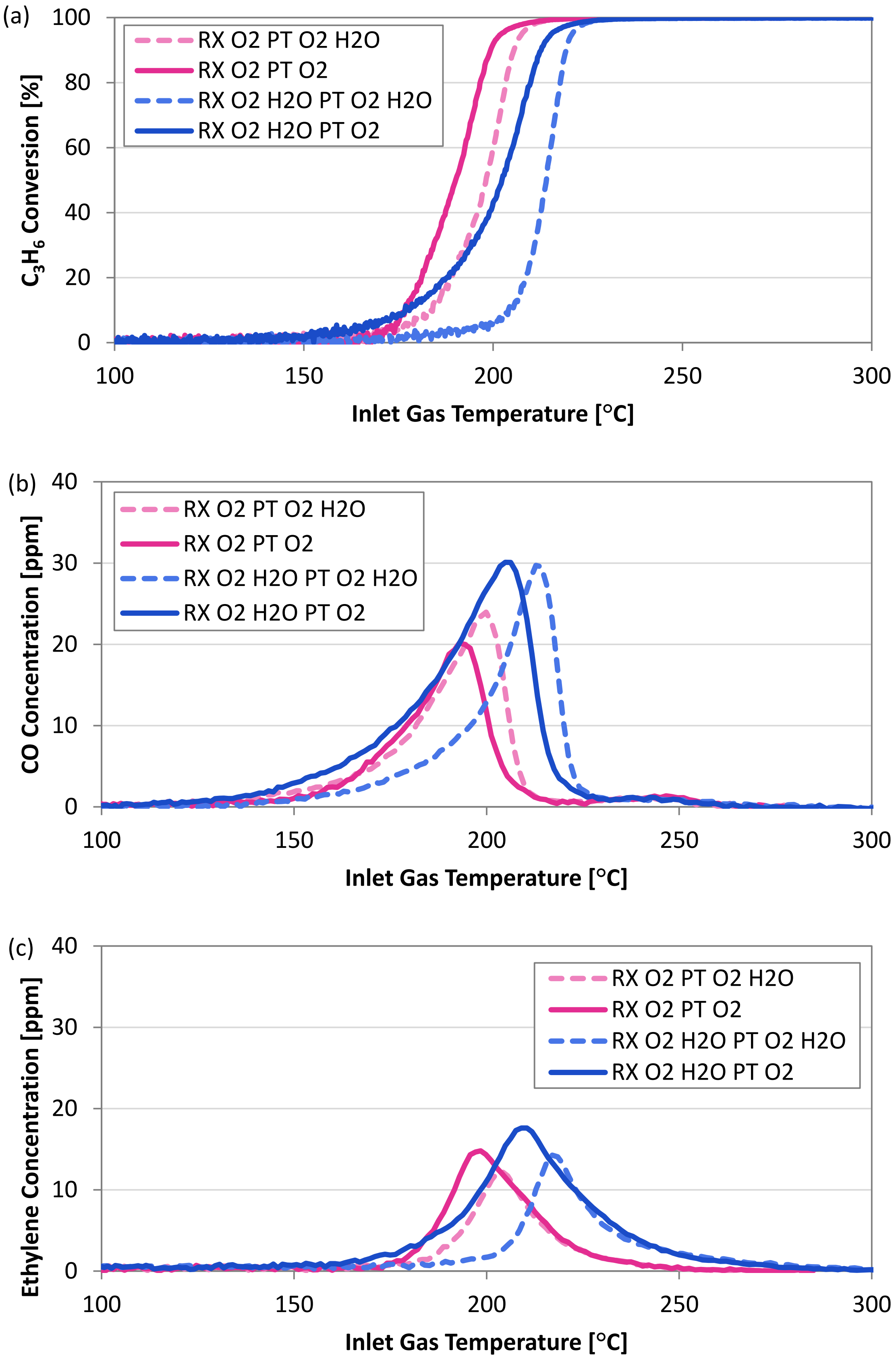
(a)
C_3H_6 Conversion [%]
100
80
60
40
20
0
100
150
200
250
300
Inlet Gas Temperature [°C]
RX O2 PT O2 H2O
RX O2 PT O2
RX O2 H2O PT O2 H2O
RX O2 H2O PT O2
(b)
CO Concentration [ppm]
40
30
20
10
0
100
150
200
250
300
Inlet Gas Temperature [°C]
RX O2 PT O2 H2O
RX O2 PT O2
RX O2 H2O PT O2 H2O
RX O2 H2O PT O2
(c)
Ethylene Concentration [ppm]
40
30
20
10
0
100
150
200
250
300
Inlet Gas Temperature [°C]
RX O2 PT O2 H2O
RX O2 PT O2
RX O2 H2O PT O2 H2O
RX O2 H2O PT O2

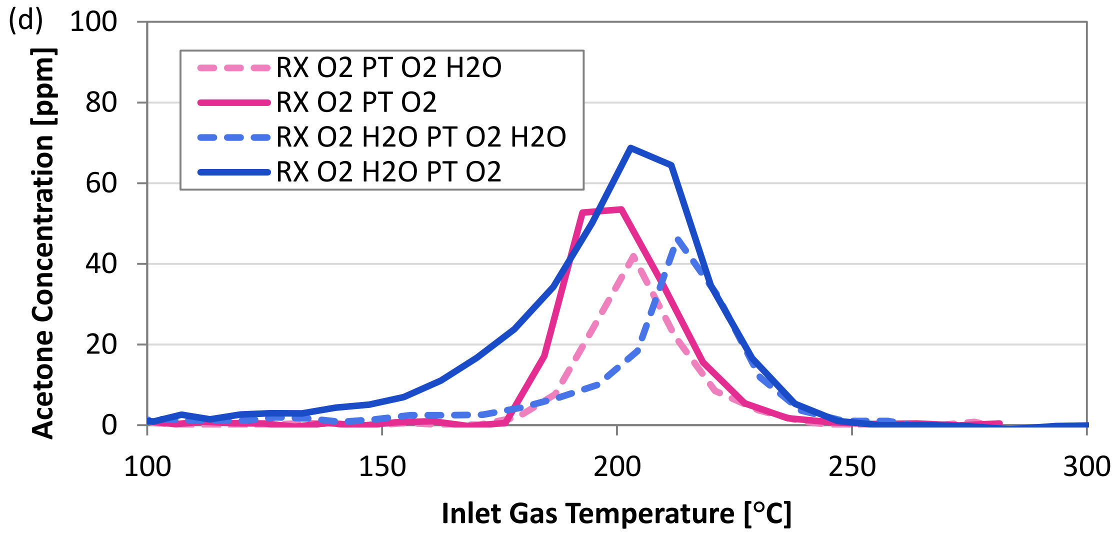

Figure 5-7 Propylene oxidation Pd/Al_2O_3 catalyst; a) propylene conversion, b) CO concentration, c) ethylene concentration, d) acetone concentration

without water in the pretreatment reached T_{10} (temperature at 10% propylene conversion) at the lowest temperature (177°C). This is mirrored in the partial oxidation product formation; CO, ethylene, and acetone as shown in Figure 5-7 (b), (c), and (d), respectively. The most abundant partial oxidation intermediate was acetone, and it and ethylene appeared in the highest concentrations for the experiments where the pretreatment did not include water. On the other hand, the most CO was formed when water was present in the reaction mixture. This is counterintuitive as the Pd catalyst was the better CO oxidation catalyst with water in the reaction mixture, so it is curious that this partial oxidation product was not easily oxidized in the presence of water. The peak partial oxidation product formation coincided with conversion in the range of 45-60% propylene conversion. The peak in CO formation occurred prior to that of ethylene formation. Other partial oxidation products such as formaldehyde, acetaldehyde, acetic acid, and acrolein, usually anticipated from propylene oxidation, were also measured.

Acrolein was not observed and formaldehyde was formed at concentrations below 2 ppm over all catalysts and conditions and its concentrations are therefore not shown. Acetaldehyde and acetic acid formation was on the order of 5 ppm, and is provided in Appendix 3 for all catalysts in Figure A-3-1 through A-3-3, along with methane formation. Acetic acid formation only occurred with water in the reaction mixture, but not on the Pt catalyst, and is also shown in supplemental information. There were no interesting trends with the addition of water on acetaldehyde formation, and the concentrations of these other intermediates were much less than the others chosen for discussion. Methane formation took place at high temperatures above light off on the order of 10 ppm for Pd and Pt-Pd catalysts, and no methane was observed to form for the Pt catalyst.

Relating these results back to the mechanism discussed, there was in increase in concentration of intermediates acetone, ethylene, CO and acetic acid when water was introduced to the reaction mixture, and no effect on the acetaldehyde formation. The increase in ethylene production was much less than the increase in CO production, which indicates that this CO may not originate from the first C-C bond cleavage in reaction 5-20 but from the partial oxidation of C_2 or C_1 partial oxidation products. Acetone production, reaction 5-19, was greater with water added to the reaction mixture, and as this reaction involves OH, increased water dissociation would lead to this product. There was also more acetic acid production when water was in the reaction mixture (reaction 5-23), also consistent with higher OH surface concentrations.

In contrast to the Pd catalyst, the presence of water in the reaction actually reduced the temperature for C_3H_6 light off over Pt/Al_2O_3, with a T_{50} decrease from 273 to 264°C, as shown in Figure 5-8 (a). As with CO oxidation, the pretreatment again had no effect on light-off. In terms of the partial oxidation intermediates ethylene was not observed during any experiments. Acetone was only observed when water was present in the reaction, but only at very low concentrations, < 2 ppm.

In previous work, it was hypothesized that on the Pt surface the indirect oxidation propylene oxidation mechanism is favored (reactions 5-18 and 5-20), where hydrogen is abstracted from the surface to produce ethylene and CO instead of acetone (reaction 5-19), which was formed with Pd catalysts. Here, water impacted the balance between direct and indirect oxidation occurring on the surface. With the addition of water, dissociation into H and OH occurred, and the OH can then react with adsorbed propylene to produce acetone, however still at very low concentrations.

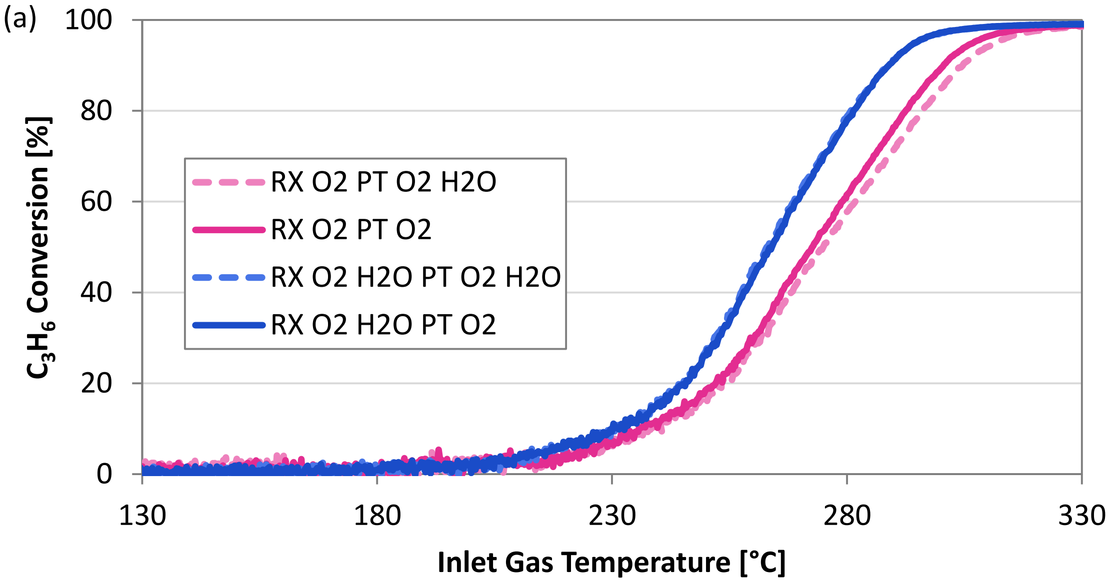

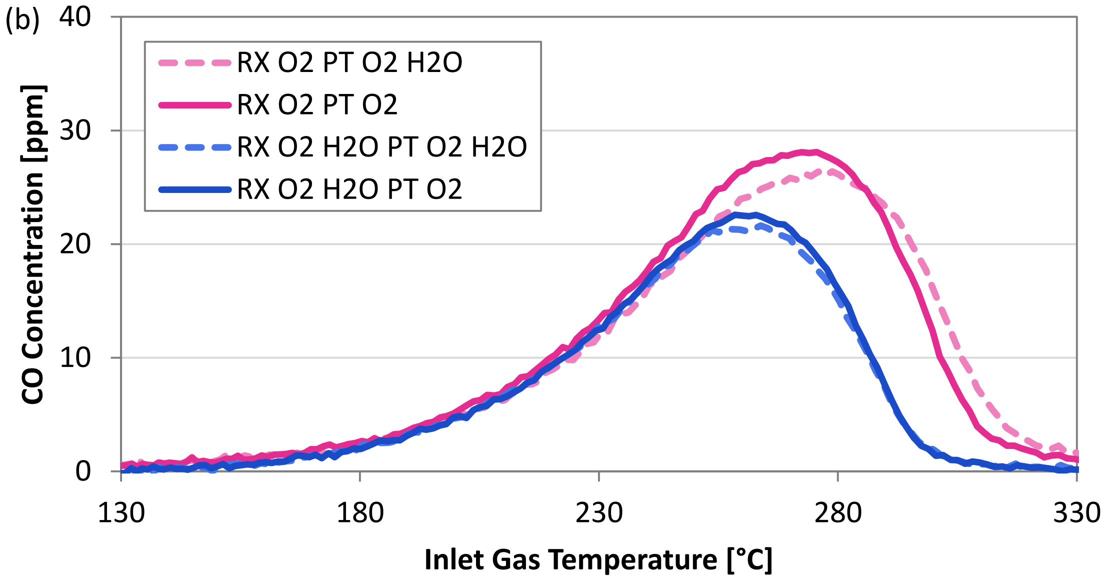

Figure 5-8 Reactor testing Pt/Al_2O_3 catalyst; reaction conditions (RX) 1500 ppm C_3H_6, 10% O_2, 0 or 5% H_2O, in balance N_2 and pretreatment conditions (PT) 14% O_2, 0 or 5% H_2O, in balance N_2. (a) Propylene conversion, (b) CO concentration

Note that the previous study showed acetone on the surface but not in the gas phase, here with water added there were higher surface acetone concentrations formed such that some desorbed from the catalyst surface. CO formation, shown in Figure 5-8 (b), was lower in the presence of water which is further consistent with the shift towards acetone production away from the dehydrogenation reaction 5-18 leading to CO formation in reaction 5-20. The higher prevalence of the mechanism towards acetone in this case led to a lower light off temperature, even though on the Pd catalyst this path inhibited performance. This alludes to a desired balance between these mechanisms. Also the acetaldehyde concentration decreased when water was in the reaction mixture, even though OH is a reactant in reaction 5-24. This may suggest that on the Pt catalyst the OH abstracts hydrogen from ethylidyne, or reaction 5-22 to acetate or complete oxidation is favored. In our previous IR study, there was more ethylidyne on the surface of the Pt catalyst and less acetate, so the reaction of OH with ethylidyne to acetaldehyde may have a higher activation barrier on Pt.

For the bimetallic Pt-Pd/Al_2O_3 catalyst, the presence of water in the reaction mixture inhibited propylene oxidation light off as was observed for the Pd catalyst, as shown in Figure 5-9 (a). With or without water in the pretreatment, the addition of water to the reaction mixture increased T_{50} by ~3°C. In terms of the pretreatment, the addition of water led to 2°C higher T_{50} values. The inhibition by water in both the reaction and the pretreatment follows the Pd catalyst trend, but the inhibition extent is decreased, apparently influenced by Pt. CO, ethylene, and acetone oxidation by-product concentrations are plotted in Figure 5-9 (b), (c) and (d). Overall this catalyst resulted in similar levels of partial oxidation products as the Pd catalyst except CO, along with very little C_3H_6 oxidation inhibition by water in the reaction mixture. CO formation was lower than that observed from either Pt or Pd, and there was more CO formed when water was present in the reaction mixture. The higher CO concentration with the addition of water was also observed on the Pd catalyst. And similar ethylene and acetone formation levels as were obtained with the Pd catalyst were observed. Interestingly even though the T_{50} shifted higher when water was in the reaction mixture, the conversions in all cases up to 20% were very similar. This is similar to what was observed on the Pt catalyst where water had a small effect on the lower conversion. The steeper light off slope for C_3H_6 oxidation on the Pt-Pd catalyst than either the Pt or Pd may be related to the CO formation, as there was less CO formed on the bimetallic catalyst to inhibit oxidation of the propylene.

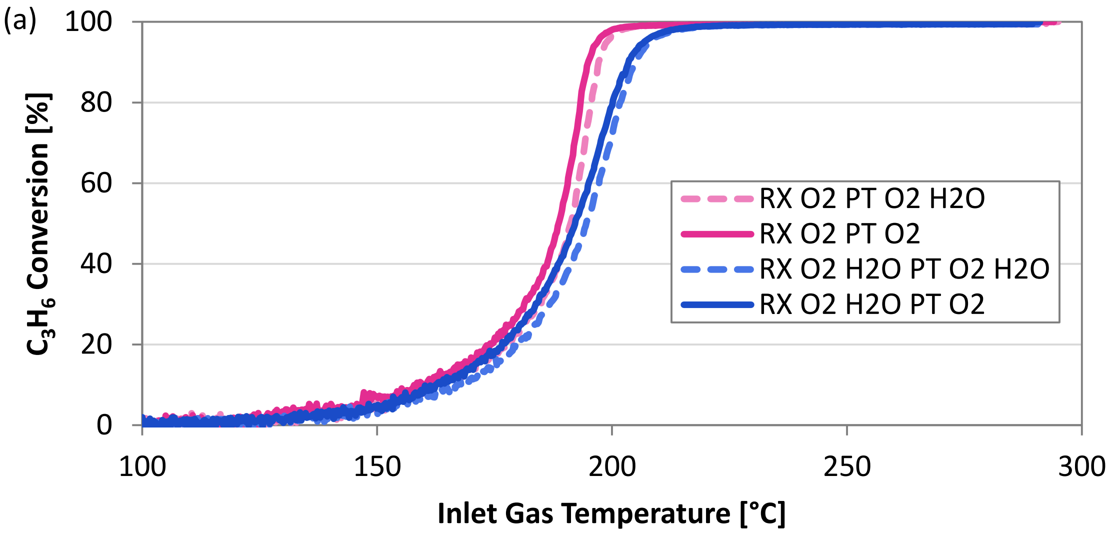
(a)
C_3H_6 Conversion [%]
100
80
60
40
20
0
100
150
200
250
300
Inlet Gas Temperature [°C]
RX O2 PT O2 H2O
RX O2 PT O2
RX O2 H2O PT O2 H2O
RX O2 H2O PT O2

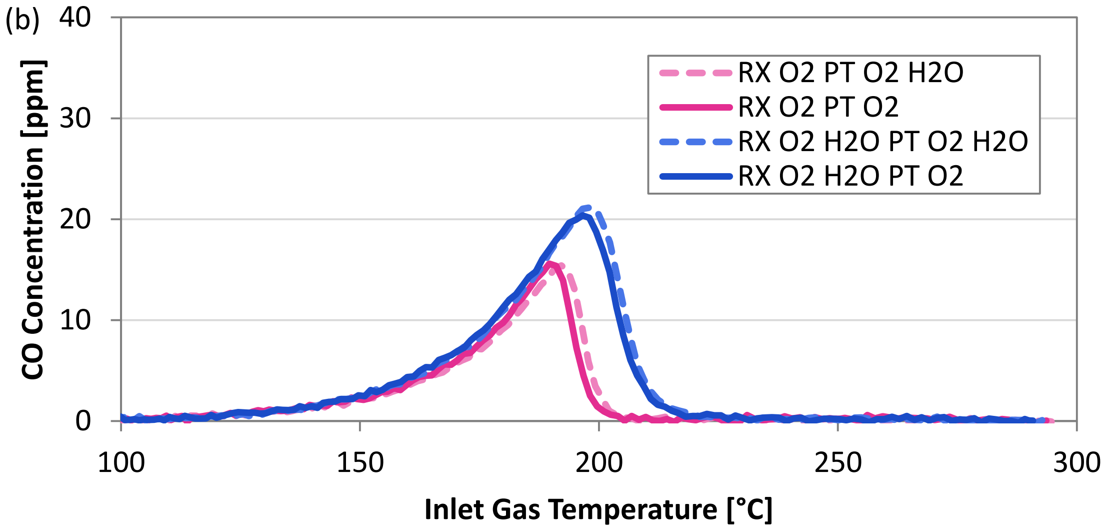
(b)
CO Concentration [ppm]
40
30
20
10
0
100
150
200
250
300
Inlet Gas Temperature [°C]
RX O2 PT O2 H2O
RX O2 PT O2
RX O2 H2O PT O2 H2O
RX O2 H2O PT O2

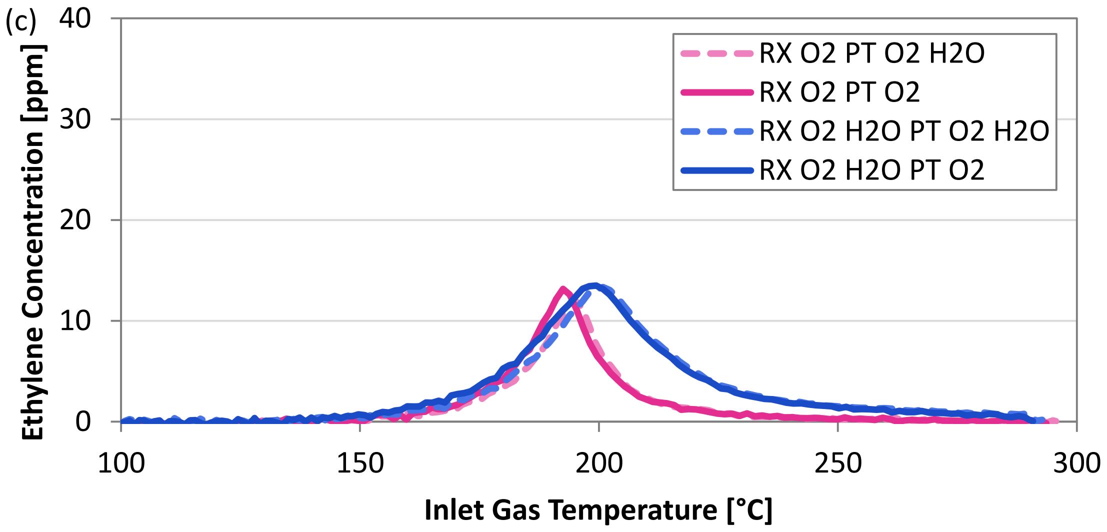
(c)
Ethylene Concentration [ppm]
40
30
20
10
0
100
150
200
250
300
Inlet Gas Temperature [°C]
RX O2 PT O2 H2O
RX O2 PT O2
RX O2 H2O PT O2 H2O
RX O2 H2O PT O2

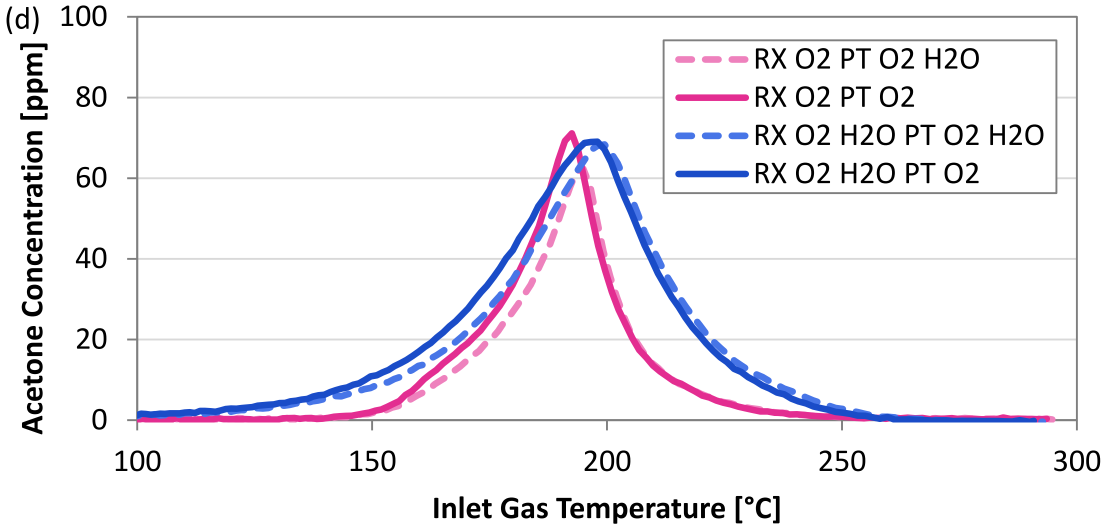

Figure 5-9 Reactor testing 1:1 Pt:Pd/Al_2O_3 catalyst; various reaction and pretreatment conditions (a) propylene conversion, (b) CO concentration, (c) ethylene concentration, (d) acetone concentration

Relating this back to the mechanism, for the Pt-Pd catalyst the higher concentrations of CO with water, like on the Pd sample, may be related to the partial oxidation of C_2 and C_1 products instead of being produced via reaction 20, leading to ethylene and CO formation, however there was still less CO formation than that from the Pd catalyst. When water was in the reaction mixture, there was less acetaldehyde produced and more acetic acid, indicating the increased OH on the surface influenced the ratio of reactions 5-23 and 5-24. This is counterintuitive, as one would expect that an increase in surface OH concentration would lead to more acetaldehyde formation in reaction 5-24 since 5-23 requires the reaction of the same species with atomic oxygen before reaction 5-23 can take place. However, for the Pt catalyst with water in the reaction mixture there was also lower acetaldehyde production. Chemistry associated with both metals are therefore observed; the Pd, more acetic acid production with water in the reaction, as well as Pt, lower acetaldehyde production with water in the reaction.

5.4 Conclusions

The effect of water on CO and propylene oxidation under simulated RCCI exhaust conditions was investigated. The addition of water to both the reaction mixture and the pretreatment was studied. Water in the reaction mixture improved the CO light-off on Pd catalysts, and water in pretreatment had various effects. On the Pt catalyst, water inhibited CO oxidation and the pretreatment had no effect. On the Pt-Pd catalyst, water helped at high temperatures but had either no or negative impact on low temperature CO oxidation. The DRIFTS results showed that there was more CO adsorption on the Pd and Pt-Pd catalysts when water is present in the reaction mixture, especially at the particle/support interface. Surprisingly the opposite effect happened on the Pt catalyst, the water appeared to compete with CO adsorption which may account for the inhibition observed.

Mechanistically, on the Pd catalysts the surface intermediates show more bicarbonate, and carboxyl when water was absent from the reaction mixture, while bidentate carbonate is on the surface when water was present. The buildup of bicarbonate and carboxyl was associated with poor performance when water was not in the reaction, as these built up on the surface with no OH to react with and limited the surface area. On Pt, bicarbonate, formate and monodentate carbonate appear when water is absent in the reaction mixture, and nothing was observed when water was present. This suggests that CO desorption is rate controlling when water is present, and then intermediates can easily react. On the Pt-Pd catalyst, carboxylate, monodentate carbonate, and bicarbonate intermediates were observed without water, and nothing with water. Also the Pt-Pd catalyst showed the least accumulation of COH. The Pt-Pd catalyst has intermediate light-off performance, and intermediates, to that of each monometallic catalyst.

For propylene oxidation, the reaction mechanism was discussed for each of the reaction intermediates observed in the gas phase. The inclusion of water into the reaction mixture had trivial effects on the partial oxidation product distributions; slightly more CO is produced over the Pd and Pt-Pd catalysts when water was in the reaction mixture and slightly less is produced over the Pt catalyst. This is not surprising, as water is a reaction product and so water dissociated on the catalyst surface would be expected. The water did have an impact on the light-off performance. On the Pd catalyst, when water was in the reaction propylene light-off was inhibited. This was also the case when water was in the pretreatment. For Pt, the water in the reaction actually lowers propylene light-off temperature, and the pretreatment has no effect. Water inhibited CO oxidation, so this may suggest water acted directly as propylene oxidant. For the Pt-Pd catalyst, very slight inhibition by water in the reaction and pretreatment was observed.

Chapter 6 Spatially Resolving CO and C_3H_6 Oxidation Reactions in a Pt/Al_2O_3 Model Oxidation Catalyst

Note: The material in this section has been published in Catalysis Today volume 267 p. 157-166, 2016. Reference and figure numbers have changed for dissertation consistency.

6.1 Introduction

Concerns over global warming, climate change and vehicle exhaust impacts on human health have led to the implementation of regulations on vehicle emissions by agencies such as the Environmental Protection Agency (EPA). These policies have acted as a driving force in optimizing engine operation as well as catalytic aftertreatment systems, in order to reduce harmful emissions. New low temperature combustion (LTC) engines have been developed with improved fuel economy, but it is still necessary to understand how their exhaust conditions will affect the performance of catalytic aftertreatment systems, which have been optimized for different exhaust conditions.

LTC technologies include Premixed Charge Compression Ignition (PCCI) and Reactivity Controlled Compression Ignition (RCCI) as two examples. Oak Ridge National Laboratory, in a comparison of conventional, PCCI and RCCI combustion [3], have shown that RCCI combustion produced much larger concentrations of CO and hydrocarbons than either the conventional or PCCI combustion, and the engine out temperature was also lower. The PCCI emissions showed similar hydrocarbon concentrations to conventional combustion and slightly higher CO concentrations, while RCCI showed CO concentrations four times greater and hydrocarbon concentrations ten times greater than conventional combustion. In terms of the NO_X concentrations, both the PCCI and RCCI produced lower emissions than conventional combustion; with PCCI combustion having about a 33% reduction in NO_X and RCCI about 93% reduction compared to the conventional combustion emissions. The diesel oxidation catalyst (DOC) is a standard aftertreatment component and is meant to oxidize the CO and hydrocarbons present in the engine exhaust. However with the lower exhaust temperature, higher DOC space velocity, and higher hydrocarbon levels, the Oak Ridge National Laboratory data also show that the hydrocarbon emissions from the RCCI combustion exhaust after a DOC were high compared to conventional and PCCI exhaust. They showed that compared to conventional combustion, where the lower CO and HC levels allow the DOC to operate at full conversion by 190°C under their test conditions, the high concentrations of CO and HC in RCCI engine exhaust moved 100% conversion over the DOC to 300°C [4].

For LTC engines, with their potentially higher levels of engine out CO and hydrocarbons and lower exhaust temperatures [1], DOCs need to be evaluated and optimized for these conditions. Typically, studies that included the oxidation of CO and hydrocarbon mixtures over DOCs have used lower total concentrations of CO and hydrocarbons; or in situations with high CO concentrations (on the order of 1 vol%) very low hydrocarbon concentrations were used (100 ppm) [102], [118]. On the other hand, where comparable hydrocarbon concentrations were tested, the CO concentrations were nearly an order of magnitude lower than RCCI emissions [45]. Since CO strongly inhibits hydrocarbon oxidation and vice versa, it is important to consider situations where both concentration levels are high in order to select appropriate DOCs to treat LTC emissions.

Both mass spectrometry (MS) and Fourier transform infrared spectroscopy (FTIR) have been used for analysis of gas-phase concentrations along diesel oxidation catalysts, as well as other aftertreatment catalysts [44]–[48]. Regardless of the analyzer used, the concept of these experiments remains the same. A small capillary is inserted into one of the channels of the monolith such that some of the flow in the channel travels through the capillary and into a gas analyzer, thereby allowing the study of axial concentration profiles of gas species along the length of the catalyst as that capillary is moved along the channel. In this study, Spaci-FTIR was used to monitor CO and C_3H_6 oxidation along a Pt/Al_2O_3 catalyst. Diffuse reflectance infrared Fourier transform spectroscopy (DRIFTS) was also used to characterize the surface of the catalyst during reaction.

6.2 Experimental Methods

6.2.1 Catalyst Information and Reactor Testing

The catalyst used in this study was provided by Johnson Matthey. The catalyst is a $Pt/\gamma\text{-}Al_2O_3$ monolith catalyst, with a platinum loading of 50 g/ft^3, an Al_2O_3 loading of 1.59 g/in^3, and a cell density of 325 $channels/in^2$. A monolithic core with a cross section of 132 channels and cut to a length of 2 inches was used in the bench scale reactor experiments. The catalyst was wrapped in insulation and placed in a quartz tube reactor placed inside a Lindberg temperature controlled furnace. Four thermocouples were inserted to monitor the upstream gas temperature, the catalyst front and back temperatures at the radial center, and the catalyst front at the wall. Small glass tubes, with an ID of 2.5 mm and OD of 3 mm, were placed upstream of the sample to ensure good mixing of the inlet flow and avoid a fully developed flow pattern.

For the spatial resolution set-up, a fused silica capillary with an ID of 320 µm and OD of 430 µm was inserted into a channel in the center of the catalyst. The axial location of the capillary was changed by pulling or pushing the capillary through a graphite ferrule seal at the reactor outlet, similar to experiments done by Luo et al [46]. The outlet of the capillary was connected to a stream of N_2 (390 mL/min) to carry the gas mixture to the gas analyzer. The gas analyzer used was an MKS MultiGas 2030 FTIR, with a 200 cm^3 cell. The gas hourly space velocity (GHSV) of each experiment was 55,000 hr^{-1}, with a total flow rate of 12.2 L/min. An estimated 92 mL/min of gas flowed through each channel. The flow through the capillary was maintained at 20 mL/min, using a needle valve placed downstream of the reactor to provide a pressure in the reactor slightly above ambient (about 1.15 bar). The flow through the capillary was found to not vary with the capillary position along the length of the catalyst.

There are studies that have evaluated the extent of the intrusiveness of this technique with regards to the flow patterns and rates and reactions taking place in the channel of the monolith [47], [48]. In this study we recognize that the capillary carrying the flow from the channel, in our case taking about a quarter of the flow in the channel, may impact the reaction, however we believe the technique still provides valuable qualitative information regarding key trends in the reaction profiles along the length of the catalyst.

All the gases except for the balance N_2 were supplied by Praxair, and the balance N_2 was supplied via an On-Site N_2 generator. A Bronkhorst CEM system was used to introduce water to the gas stream. The gas flows were controlled with various Bronkhorst mass flow controllers, and the gases used were CO, C_3H_6, NO, NO_2, and CO_2. All the upstream and downstream lines were heated above 100 °C at all times in order to prevent water condensation.

Temperature programmed oxidation (TPO) experiments were performed with different CO, C_3H_6 and NO concentrations: 0 or 3000 ppm CO, 0 or 1000 ppm C_3H_6, 0 or 50 ppm NO, 0 or 30 ppm NO_2, 14% O_2, 5% H_2O, 5% CO_2 and a N_2 balance. These levels were chosen based on data provided by Oak Ridge National Laboratory, obtained via measurements of the exhaust from a Reactivity Controlled Combustion Ignition (RCCI) engine. Temperature ramps from inlet gas temperatures of 80°C to 300°C at a ramp rate of about 7.3°C/min were used. The inlet gas stream was also heated by a preheater that was ramped in temperature during the TPO in order to keep the temperature gradient under non-reacting conditions along the catalyst length below 3°C. This was tested and verified with only N_2 flowing. The sample was aged at 700°C in 14% O_2 and 5% H_2O for 5 hours prior to testing, and a few TPO experiments with CO and propylene in the gas mixture were done to ensure catalyst stability and repeatability. In between each TPO experiment a pretreatment in the aging gas mixture was done at 500°C for 30 minutes.

The gas concentration data collected were averaged for every 4 seconds for the CO and propylene conversion data, every 20 seconds for NO_2 and N_2O concentration, and every 100 seconds for the NO concentrations due to increased noise in the NO, N_2O and NO_2 signals after the dilution with the N_2 carrier stream. All the conversion data are plotted as a function of the gas inlet temperature, measured from the thermocouple placed 1 cm in front of the catalyst in the middle of the reactor tube. The catalyst exotherm data plotted is the difference of the temperature of the back of the catalyst and the temperature of the inlet gases. Adiabatic temperature rises were calculated assuming the ideal gas law applies. Plots for the experiments in the following sections show total NO_X conversion defined as

$$X_{NO_X} = \frac{(C_{NO}+C_{NO_2}+2C_{N_2O})_{inlet}-(C_{NO}+C_{NO_2}+2C_{N_2O})_{outlet}}{(C_{NO}+C_{NO_2}+2C_{N_2O})_{inlet}} \times 100\% \qquad (6\text{-}1)$$

in other words describing the amount of inlet NO_X that is converted to nitrogen.

6.2.2 DRIFTS Experiments

In order to identify adsorbed species and surface reaction intermediates during reaction, in situ DRIFTS experiments were performed using a Nicolet 6700 spectrometer equipped with a MCT detector and a high temperature reaction chamber (Harrick Scientific Praying Mantis) with ZnSe windows. The catalyst was scraped off the cordierite and pressed to a pellet of 60 mg. The DRIFTS spectra were collected in the 4000-650 cm^{-1} wavenumber range, accumulating 64 or 128 scans at 4 cm^{-1} resolution. Nicolet OMNIC software was used to process the reflectance data into Kubelka-Munk (KM) format.

TPO experiments were performed on the sample with a gas stream temperature ramp from 84 to 210°C at 4.2°C/min, collecting 128 scans or 66 to 175°C with a ramp rate of 1.7°C/min collecting 64 scans for further temperature resolution. In order to obtain a more time resolved data set of the light off behavior on the surface, without compromising the integrity of the measurement by reducing the number of scans, these TPOs were performed with a slower ramp rate than that of the bench reactor testing. A background spectrum was taken at the beginning of the temperature ramp in flowing He, and then the reactant gases were added and the samples were exposed to the feed gas for 1 hour before the temperature ramp was started.

The concentrations used in the DRIFTS experiments were 0 or 3000 ppm CO, 0 or 1000 ppm C_3H_6, 14% O_2, and 1% H_2O in balance He. The absence of CO_2 in the inlet gas is not expected to affect the results. The total flow rate of the inlet stream was maintained at 50 mL/min by MKS mass flow controllers. The water supplied to the DRIFTS was from an absorption/bubbler column with 12 mL/min He flowing.

TPO experiments were also performed with H_2O, O_2, and He only so the spectral data obtained could be subtracted from spectra obtained during the TPOs with CO, C_3H_6, and both CO and C_3H_6. This was done in order to remove the features associated with water during the temperature ramp as well as the background shift due to temperature and any other temperature effects. A pretreatment before the experiments and between each TPO experiment at 500°C with 14% O_2 and 1% H_2O for 30 minutes was used, similar to that of the pretreatment for the bench scale reactor tests.

6.3 Results and Discussion

6.3.1 Spatially Resolved TPO Experiments

6.3.1.1 Spatially Resolved CO and Propylene Oxidation in the Absence of NO_X

The spatially resolved conversion results for the CO only TPO experiment are shown in Figure 6-1 (a), and the normalized reaction rates for the sequential 0.5 inch segments are shown in Figure 6-1 (b). The plot of normalized reaction rates for the sequential 0.5 inch segments is another way of looking at the conversion plots for the spatially resolved data, and is included to provide a different view of the conversion plots. These data demonstrate that back to front light-off was observed, as has been previously shown when relatively slow ramp rates are used [44], [45].

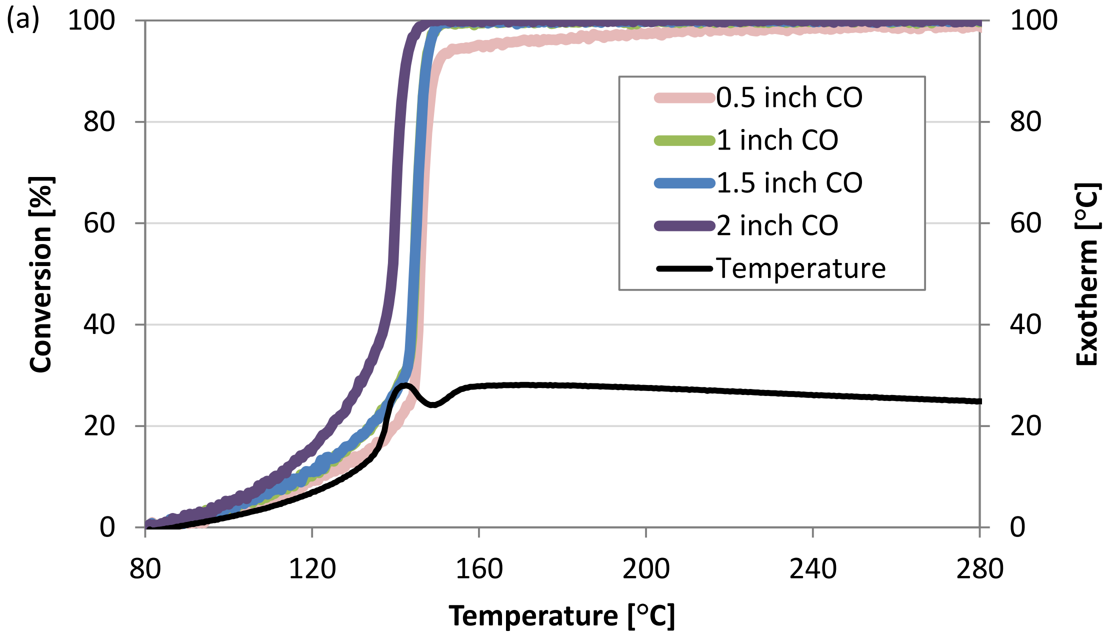

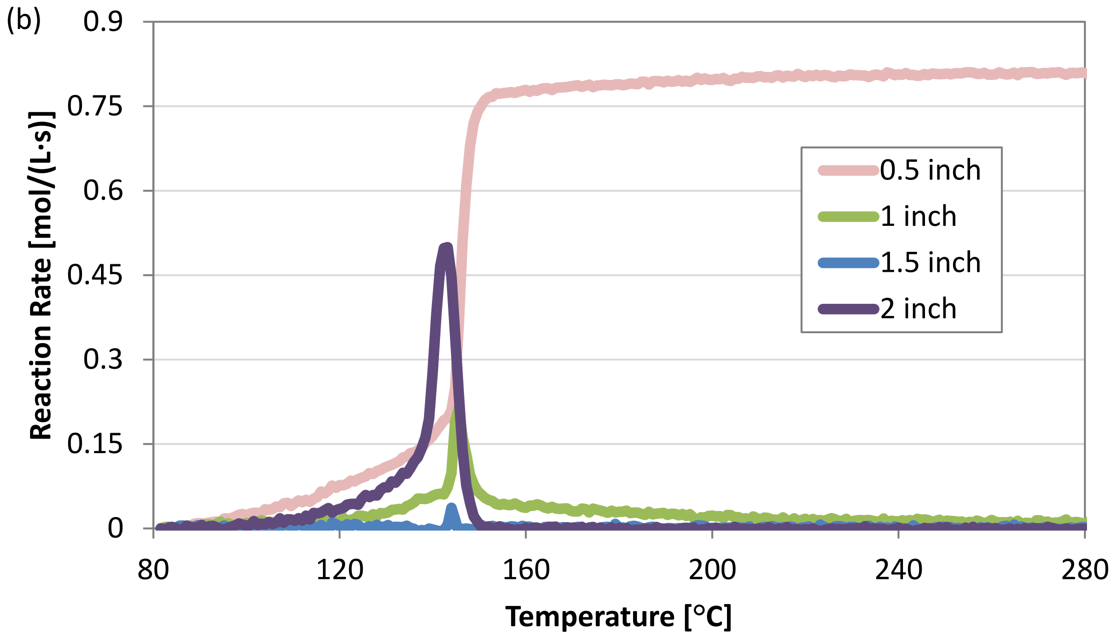

Figure 6-1 (a) CO conversion as a function of upstream gas temperature at four positions along the catalyst length, (b) reaction rate per 0.5 inch segment of catalyst

This back-to-front reaction propagation is due to a combination of the exothermic CO oxidation reaction and some oxidation occurring down the length of the channels, which leads to lower CO self-poisoning at the outlet of the sample. With the lowered self-poisoning more CO oxidation occurs as a function of position from the inlet, and thus more heat is generated, such that the outlet of the sample can be at a higher temperature than the inlet (if the ramp rate is slow, as mentioned). This in turn leads to slow solid heat conduction moving upstream and the back-to-front reaction propagation. The data for conversion as a function of temperature for the middle areas of the catalyst, as well as for the measurement done at 0.5 inches, are quite similar. The onset of oxidation at the back of the catalyst is observed at a slightly lower upstream temperature, about 5°C, before the others. These results suggest that the propagation of the reaction front through the catalyst was quite rapid. Previous experiments at a higher space velocity with only 800 ppm of CO did not show this fast light off behavior, the reaction propagated more slowly over a larger length of catalyst [119]. However, the higher exotherm obtained here resulted in the rapid propagation and the overlapping conversion data through the middle and front of the catalyst. Near the catalyst front, 0.5 inch, 100% conversion was not reached over the temperature range used, likely due to residual CO self-poisoning with the high entering concentrations, as well as mass transport limitations at higher conversions.

A similar trend exists in the propylene TPO results, shown in Figure 2 a) and b), where the light-off curves still indicate back to front light off, yet are more spread out for the different capillary positions when compared to the CO data, which indicates different self-inhibition properties for propylene. The peak reaction rate in each 0.5 inch segment (measured from the back of the catalyst) is approximately equal, again showing a slower and progressive reaction front moving from the back to the front of the catalyst. Also note, there was no evidence of intermediate CO formation or any other partial oxidation intermediate during these experiments. While the temperature rise associated with the oxidation of propylene is higher, a maximum catalyst temperature rise of 28°C was measured during the CO TPO experiment, and 57°C for propylene at light-off (adiabatic temperature rise under these conditions calculated to be 30°C and 66°C respectively), this isn’t sufficient to overcome the activation barrier as quickly along the length of the catalyst as was for the case of CO. These temperature rise data, taken as the difference between the back of the catalyst and the front of the catalyst, are also plotted in Figure 6-1 and Figure 6-2. From these two sets of data, under the conditions tested, nearly all the CO is oxidized by 150°C and propylene is oxidized by 190°C, when these species are oxidized separately.

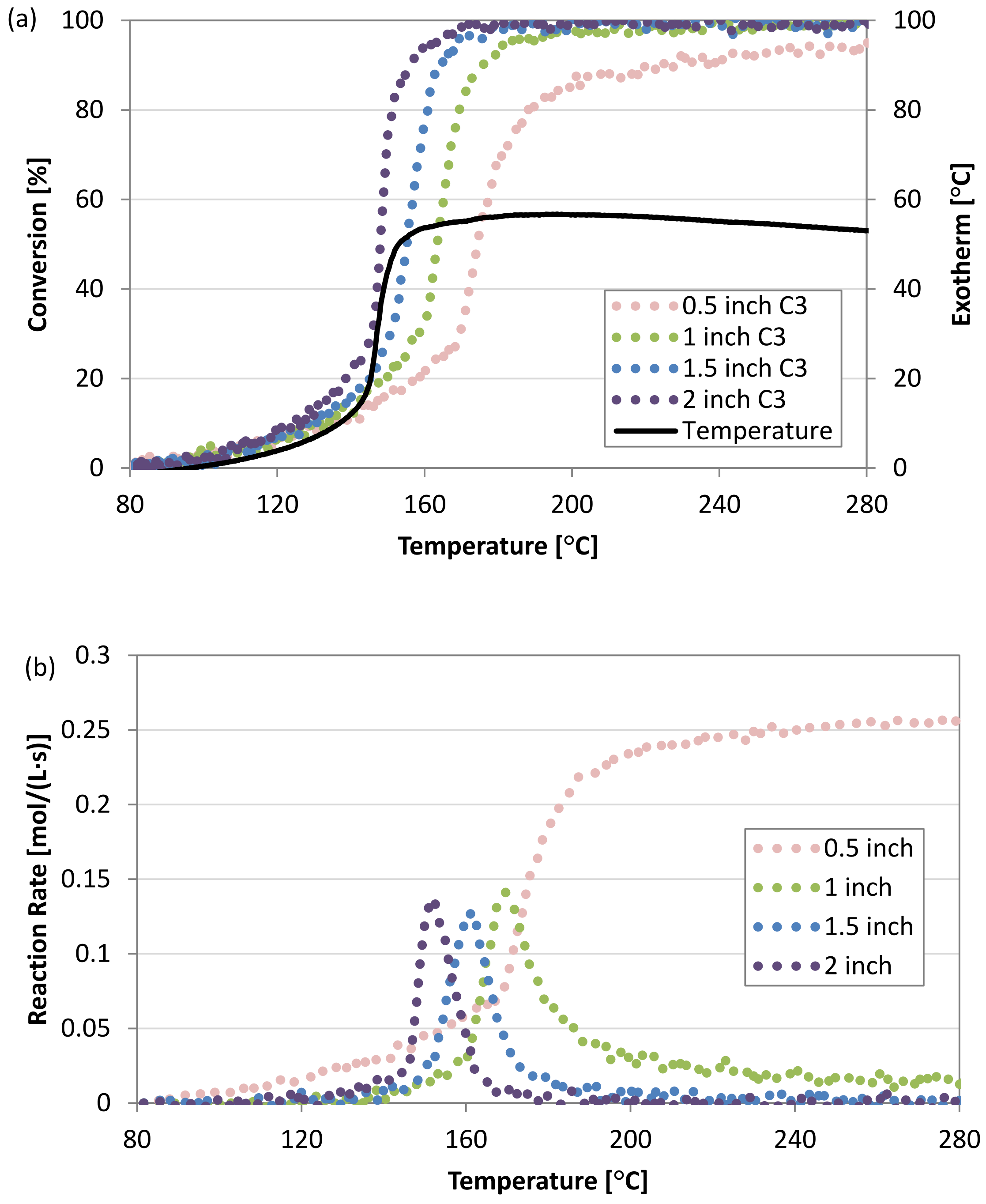

Figure 6-2 (a) Propylene conversion as a function of upstream gas temperature at four positions along the catalyst length, (b) reaction rate per 0.5 inch segment of catalyst

When comparing these to the results obtained from the TPO with the mixture of CO and propylene, shown in Figure 6-3, it is apparent that both the CO and propylene oxidation reactions are inhibited by the presence of the other reactant, as the onsets of conversion are shifted to substantially higher temperatures, and furthermore, the light-off curves at different capillary positions are more spread out. This is consistent with a mechanism that includes C_3H_6 inhibition of CO oxidation and vice versa [118]. In terms of the propylene, the onset of light off is observed once most of the CO is oxidized.

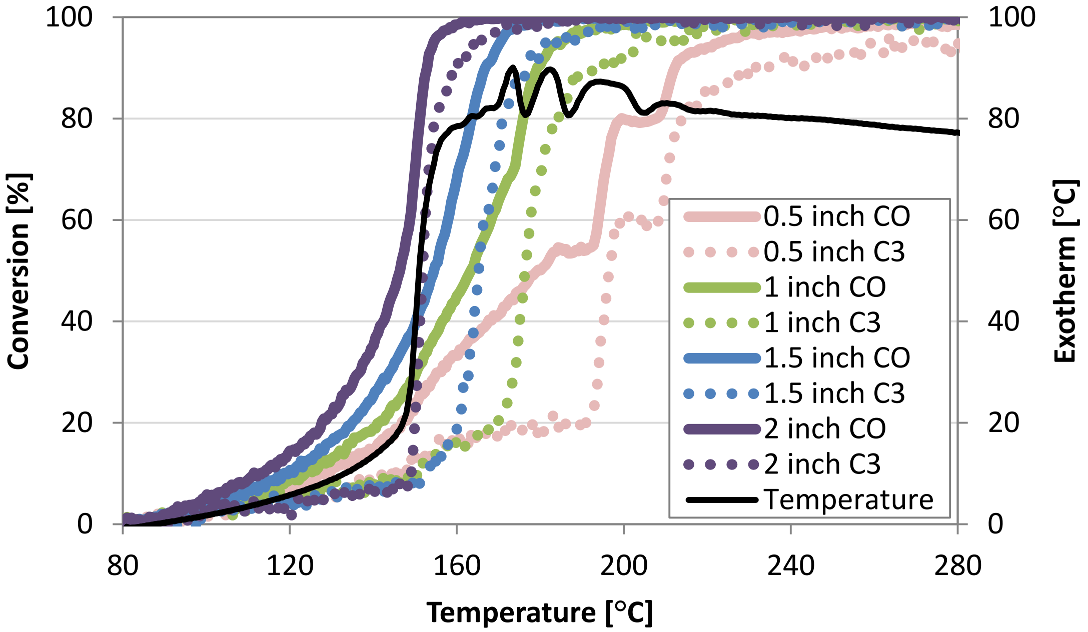

Figure 6-3 CO and propylene conversion as a function of upstream gas temperature at four positions along the catalyst length

The rapid onset of C_3H_6 oxidation after CO oxidation is caused by the availability of active sites for C_3H_6 adsorption and reaction that were not present at lower temperatures due to the strong adsorption of CO on those sites. The spreading of the light-off curves indicate an additional inhibition interaction, where for example in kinetic studies not only inhibition terms for the individual components, CO and propylene, are present to account for competitive adsorption, but an additional term including the concentration of both CO and propylene is applied when there are high concentrations of the two [118]. This additional inhibition term was related to the low concentration of oxygen on the surface relative to high concentrations of CO and propylene, where the surface is crowded by CO and partial oxidation intermediates.

At the 0.5 inch measurement position, two "steps" in the CO and propylene conversion versus temperature curves were observed, the first occurring around 182-192°C and the second occurring around 197-207°C. In an experiment done where the full reactor outlet was measured (i.e. not through the capillary, but all flow went through the FTIR analyzer), some formaldehyde byproduct was observed, Figure 6-4, at concentrations too low to detect through the capillary due to the dilution.

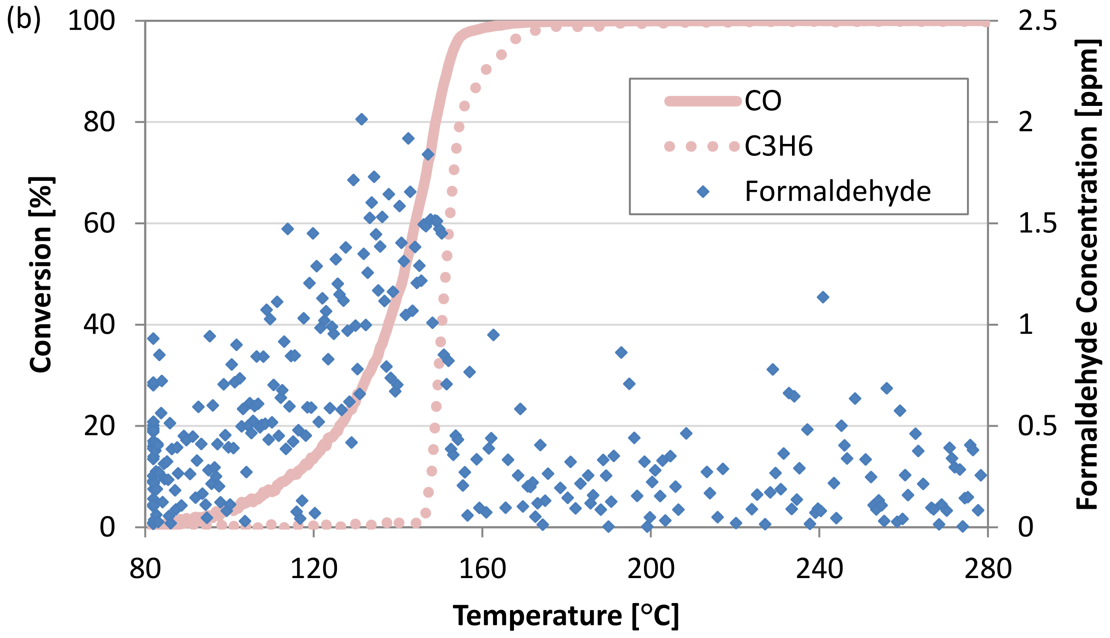

Figure 6-4 CO and propylene conversion and formaldehyde formation at the reactor outlet

Formaldehyde is not anticipated to be a reaction intermediate that leads to the inhibiting steps, as it is very easily oxidized on Pt compared to CO [120]; however the involvement of the formaldehyde in the surface chemistry of the intermediates could contribute to the trends observed. The steps and the formaldehyde byproduct suggest the formation and build-up of some surface intermediate causing the observed inhibition, prompting the DRIFTS experiments, which will be discussed below. These steps dissipate along the length of the catalyst; the steps are clearly visible at the 0.5 inch position, appear as slight inflection points at the 1 inch position, and are not apparent in the data obtained at the 1.5 inch and 2 inch positions. This suggests the heat generated from the oxidation reactions occurring upstream, in combination with the lower concentrations of reactants downstream, was sufficient to cause the surface intermediates to completely oxidize or desorb. The measured catalyst temperature rise with CO and propylene reached a maximum of 90°C, approaching the calculated adiabatic temperature rise of 95°C at light-off conversions, and this large exotherm would lead to rapid CO desorption and oxidation, in turn allowing increased propylene adsorption and oxidation, which leads to the formation of surface intermediates and the inhibition of the oxidation of both CO and propylene. In the plot of the temperature rise along the catalyst as a function of inlet temperature in Figure 6-3, there are distinct local maxima in the temperature difference measured, which can be attributed to a reaction starting and then stopping, and are in line with the “steps” in conversion seen. As will be discussed below, with the DRIFTS data, these local maxima are associated with oxidation of surface intermediate species, which are the causes of the observed inhibition effects.

6.3.1.2 Spatially Resolved CO and Propylene Oxidation, and NO_X Reactions

The results of the NO TPO with both NO and NO_2 present in the feed gas are shown in Figure 6-5. NO oxidation extent builds along the length of the catalyst, plateauing around 180°C, resulting in 88% NO oxidation at the 2 inch position. A back-to-front ignition profile is not observed in this experiment, due to the lack of any significant exotherm due to the low concentration of NO added as well as the smaller heat of reaction.

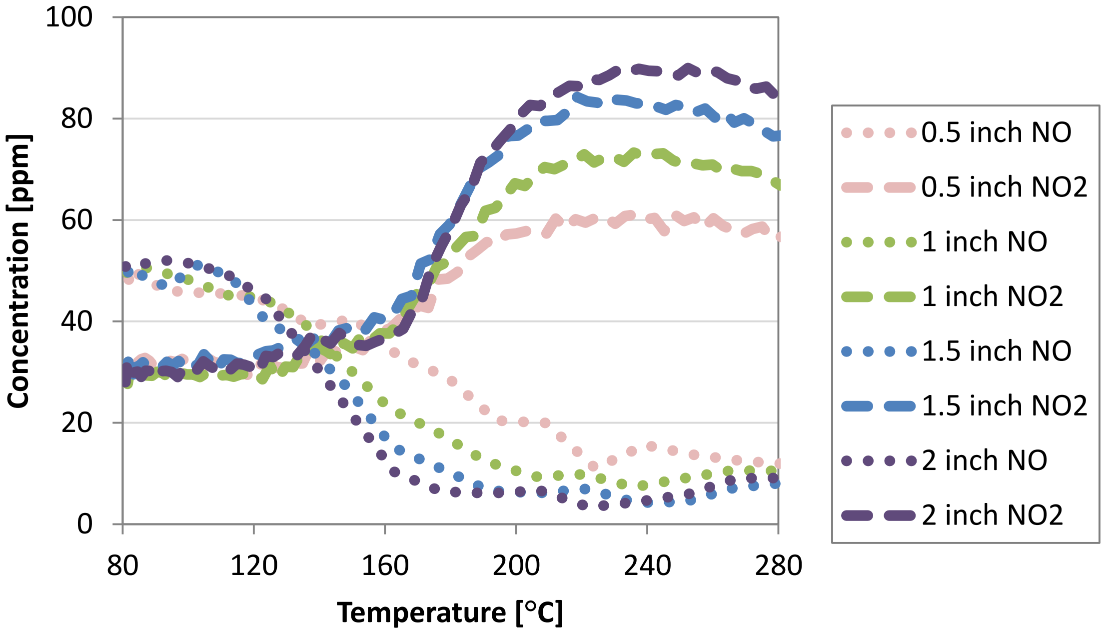

Figure 6-5 NO_X concentrations as a function of catalyst position and upstream gas temperature

In comparing the CO oxidation TPO results in the presence and absence of NO_X, Figure 6-6 (a) and Figure 6-1, the onset of CO oxidation was shifted to higher temperatures in the presence of NO_X. And in comparing the NO oxidation data, Figure 6-6 (b) and Figure 6-5, the apparent onset of oxidation of NO to NO_2 was also shifted to higher temperature, and the extent of reaction at higher temperatures was decreased.

These data demonstrate that CO inhibited NO oxidation as well as NO_X inhibited CO oxidation. The inhibition of CO oxidation is due to competitive adsorption of NO and CO on the active sites [121].

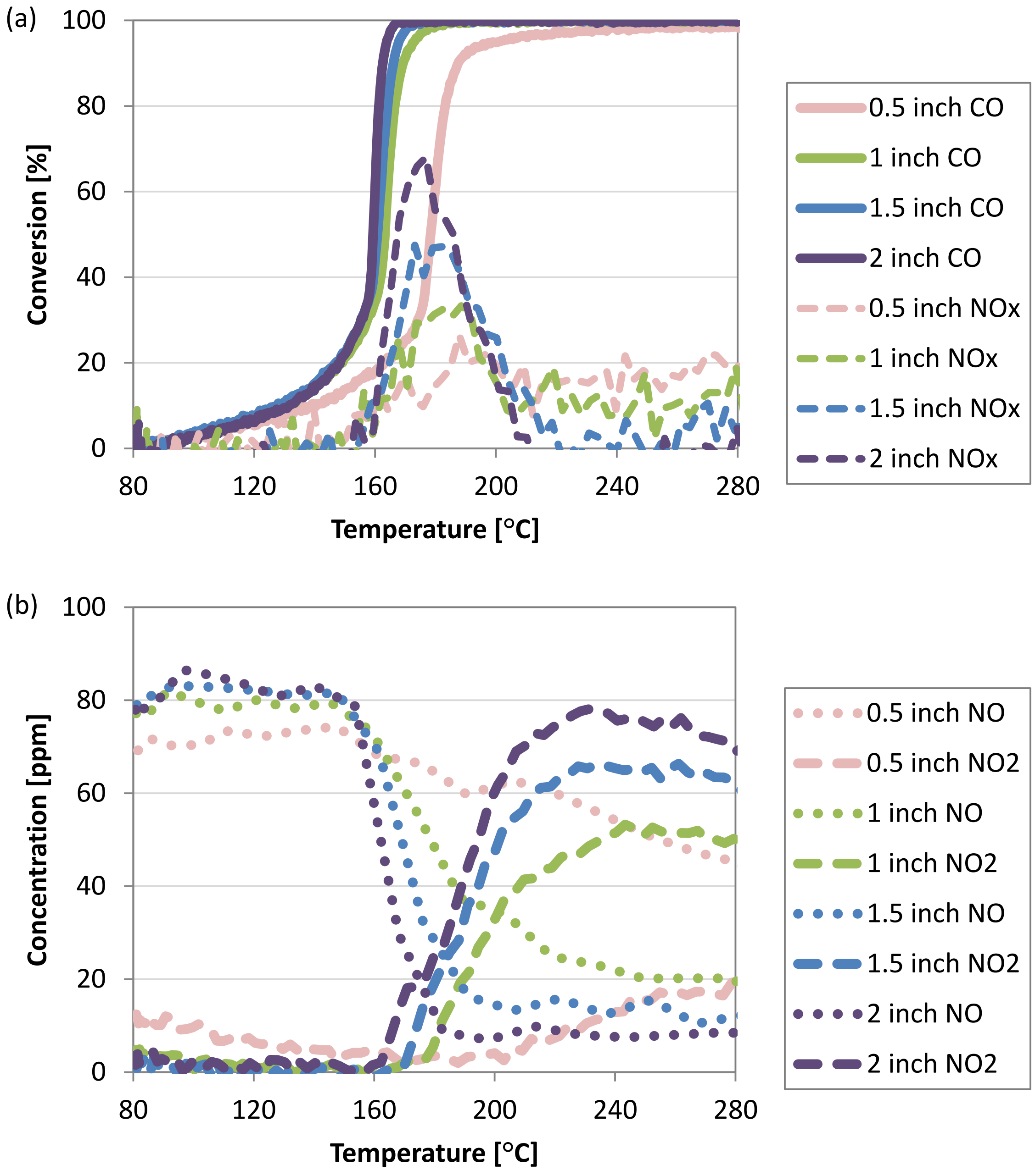

Figure 6-6 (a) CO and NO_X conversion, and (b) NO_X species concentration profiles at different catalyst positions as a function of upstream gas temperature

Between 80 and 150°C, most of the NO_2 present in the feed gas was reduced to NO, with this apparently a relatively easy reaction since most occurred within the first 0.5 in of the catalyst. NO_2 reduction to NO over similar catalysts has been regularly observed, and is also responsible for the observed lack of NO oxidation when substantial amounts of CO are still present [61], [122], [123]. As the temperature increased there was an intermediate temperature region where most of the NO_X was reduced to N_2. Reduction of NO_X to N_2 and N_2O by CO has been discussed in relation to three-way catalysts for the treatment of gasoline exhaust [124], [125], and additionally various hydrocarbons including C_3H_6 have also been found to reduce NO_X to N_2 and N_2O [126], [127]. The difference in these experiments is that no N_2O formation was observed with the reduction of NO_X with CO, and this is likely due to the high CO coverage on the surface. Mechanisms reviewed in reference [124] demonstrate that N_2O formation requires adsorbed NO and possibly atomic N on the surface. With such high concentrations of CO, the Pt is likely in a metallic state facilitating relatively rapid NO decomposition and thus there is a lack of available adsorbed NO once reaction onset begins. At 2 in, almost 70% of the NO_X was reduced to N_2 (no N_2O was observed) at about 180°C, which coincided with complete CO consumption. There was a similar trend for the other positions, and at the 0.5 inch position NO_X reduction was maintained at 20% even at high temperatures. As the temperature increased, more and more of the CO was oxidized by O_2, leaving less on the surface available for NO_X or Pt reduction. However, some remained in the upstream portion, since that was the region that was catalyzing the CO oxidation and thus some selectivity for the reduction reaction was still maintained.

The propylene and NO_X conversion results, with no CO in the feed gas, are shown in Figure 6-7 (a), and the NO_X species concentrations are shown in Figure 6-7 (b). During this experiment, reduction of NO_2 to NO was not observed at low temperature, however as the temperature increased there was complete reduction of NO_2 to NO and N_2, and N_2O was also observed. Note, no N_2O was formed in the previous set of results with CO and NO_X. This reduction behavior of NO_2 with propylene, as well as CO, has been previously observed, and the formation of N_2O over Pt/Al_2O_3 catalysts via hydrocarbon selective catalytic reduction (SCR) of NO_X is expected based on previous studies [122], [128]. At 208°C, peak N_2O formation was observed and the conversion of NO_X to N_2 was 26%. The NO_X conversion reached a peak at 198°C, 40%, before N_2O formation was noted, and both values were much lower than those with CO as the reductant. However, with propylene, the onset of NO_X conversion actually occurred at a lower temperature and increased with propylene conversion, stabilizing to around 25% at high temperature.

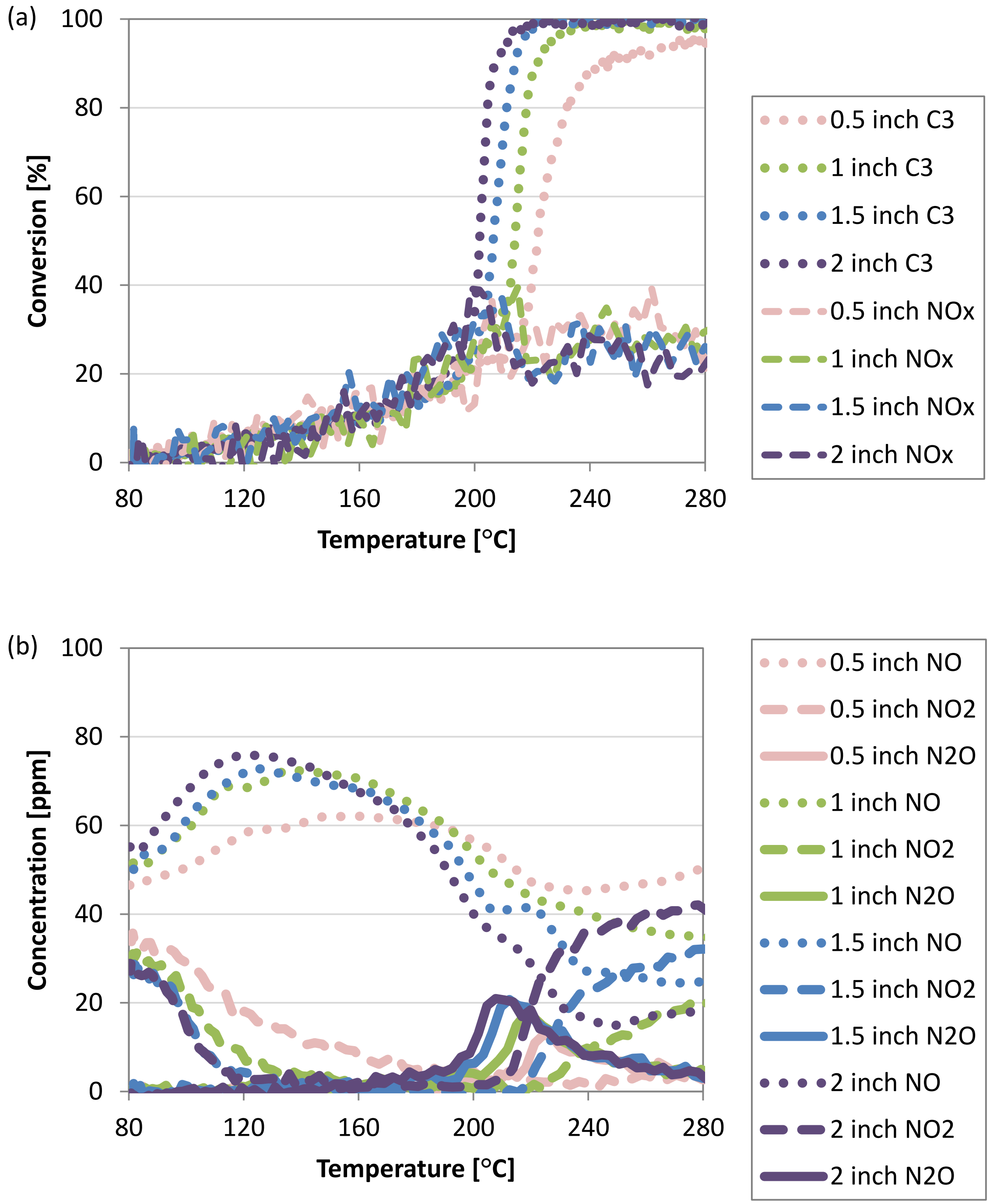

Figure 6-7 (a) Propylene and NOx conversion, and (b) NO$_X$ species concentration profiles at different catalyst positions as a function of upstream gas temperature

In comparing the propylene TPO data in the presence of NO$_X$ to those in the absence, Figure 6-2, where most of the propylene was oxidized by 190°C, again the presence of NO_X inhibited propylene oxidation, here with a 60°C shift in the light-off curve. This inhibition effect is consistent with previous studies, where competitive adsorption onto active sites was cited as the cause [128]. Peak N_2O formation shifted to lower temperatures further along the length of the catalyst, and it always corresponds to roughly the temperature where 50% of the propylene was oxidized. This is consistent with the idea that incomplete combustion products of propylene are reactive with NO_X species [94], [126], [127], as these incomplete combustion products, which may include CO and acetate and formate species, would have high surface concentrations right at light-off.

The conversion data and NO_X concentration profiles obtained when using the full mixture (CO, C_3H_6 and NO_X) are shown in Figure 6-8 (a) and Figure 6-8 (b) respectively. Nearly all of the NO_2 is reduced at low temperatures at the front of the catalyst, as was the case with just CO and NO_X, Figure 6-6 (b), demonstrating that propylene does not inhibit this reduction reaction. One of the inhibition steps observed during the CO and propylene TPO, without NO_X present, in Figure 6-3, was again evident but under these conditions was present throughout the length of the catalyst, shifting slightly to lower temperatures along the catalyst length and over a smaller temperature range. This indicates that NO_X is reacting with a surface species that was responsible for the second inhibition step in the absence of NO_X. Previous work has shown that surface nitrates react with propylene to form surface carboxylic species [129]; specifically it was found that acetate intermediates react with nitrates [94]. Therefore, likely propylene adsorbed and oxidized partially to acetate (evidence to be shown below), which then was immediately oxidized by nitrates on the surface, leading to only one observable inhibition step since the acetate intermediate was no longer stable or long lived on the surface. Formation of N_2O was again observed in the temperature range where some but not all of the propylene was oxidized. The peak in N_2O production seems to correspond to a temperature where most of the propylene is oxidized. The formation of N_2O in the presence of propylene has been related to a shift in the ratio of adsorbed propylene and surface NO_X, where the less surface NO_X leads to an incomplete reduction of nitrates to N_2O [128].

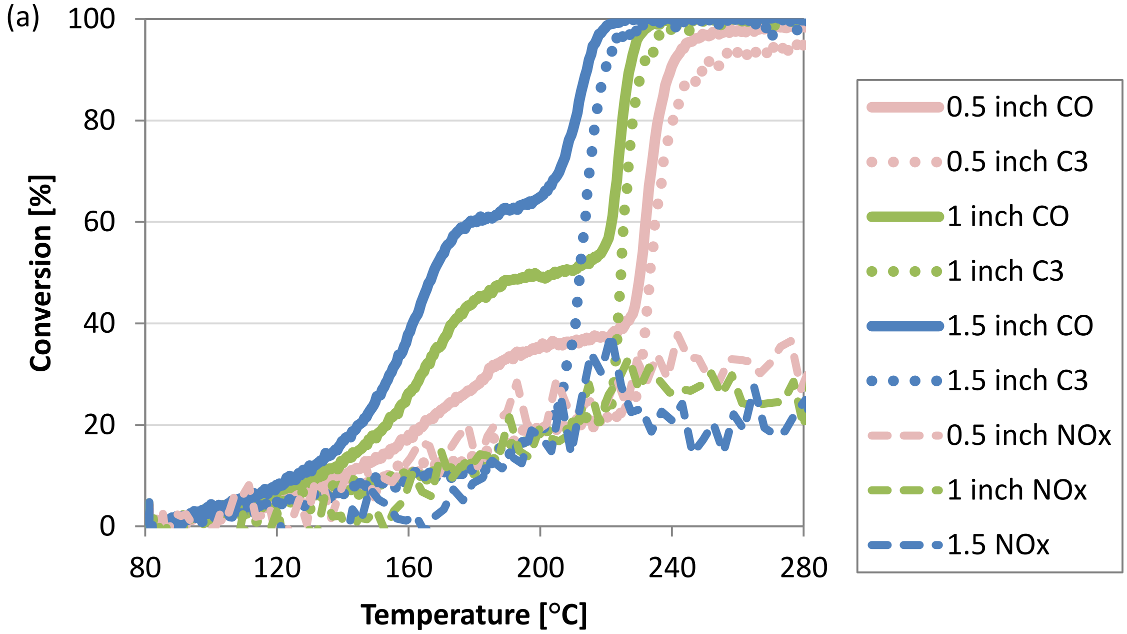

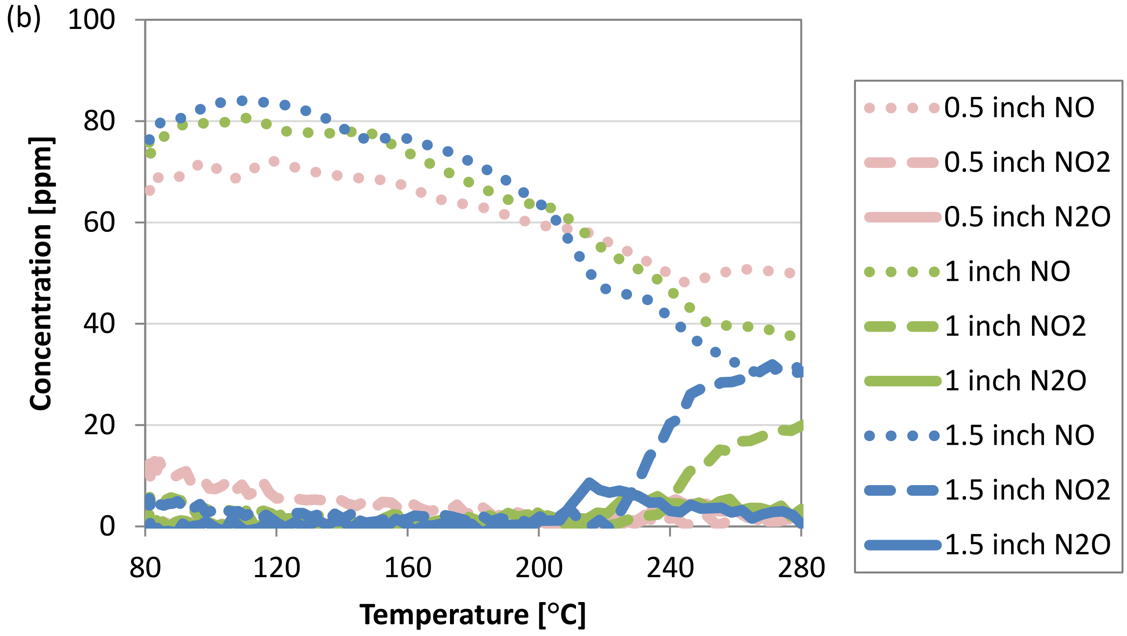

Figure 6-8 (a) CO, Propylene and NOx conversion, and (b) NO_X species concentration profiles at different catalyst positions as a function of upstream gas temperature

As shown in Figure 6-8 (a), the NO_X conversion data look more similar to the case of the C_3H_6 and NO_X TPO than that of the CO and NO_X TPO, suggesting that the propylene adsorbed on the surface inhibits the surface CO from acting as an NO reductant in this temperature range, while the CO still acts as an NO_2 reductant to NO at the lower temperatures. These trends can be related to surface overages. At the beginning of each of the CO and NO_X and the CO, C_3H_6 and NO_X TPOs, the CO is able to reduce all the NO_2 to NO because CO or NO is preferentially adsorbed on the surface relative to propylene. In the presence of both CO and propylene, once the CO lights off, the surface would then become covered with propylene and intermediates of propylene, which would effectively block the active sites and stop the reduction of NO by CO. For ease of comparison, Table 6-1 lists the T_{50}'s for all the experiments performed.

Table 6-1 T_{50} for different reaction conditions

	CO	**C_3H_6**	**CO + C_3H_6**		**CO + NO_X**	**C_3H_6 + NO_X**	**CO + C_3H_6 + NO_X**	
Position	T_{50} [°C]	T_{50} [°C]	$T_{50,CO}$ [°C]	T_{50,C_3H_6} [°C]	T_{50} [°C]	T_{50} [°C]	$T_{50,CO}$ [°C]	T_{50,C_3H_6} [°C]
0.5 inch	145.9	174.2	180.8	196.5	178.2	246.7	230.5	233.6
1 inch	144.5	163.2	164.1	176.4	163.2	213.8	211.1	224.5
1.5 inch	144.5	153.9	154.3	165.0	161.0	206.5	167.8	212.4
2 inch	138.8	148.1	146.4	151.7	159.4	201.7	--	--

6.3.2 DRIFTS TPO Experiments

The inflection, or step, in conversion as a function of temperature, where the rate of conversion change slows, during a propylene oxidation light-off experiment has previously been observed experimentally under conditions more relevant to conventional diesel exhaust, i.e. with lower CO and propylene concentrations and higher NO concentrations [130]. As observed in the data shown in Figure 6-3 and Figure 6-8, these steps occurred in both CO and propylene light-off curves, with and without NO_X. To better understand this inhibition effect, the interaction between CO and propylene was characterized using DRIFTS. DRIFTS TPOs were conducted with similar experimental conditions to those of the bench scale reactor tests. The differences between these experiments was that the water concentration was lower, only 1% by volume instead of 5%, there was no CO_2 in the feed gas for these tests, and the ramp rates used were slower. These changes are not expected to influence the nature of the surface intermediates observed, and if anything should exaggerate them. Due to inherent differences in the DRIFTS cell and bench scale reactor, particularly the space velocity; the temperatures at which the CO and C_3H_6 light off were expected, and were observed, to be much lower in the DRIFTS data compared to the bench scale reactor.

6.3.2.1 CO TPO

Representative DRIFTS spectra obtained during the CO TPO experiment are shown in Figure 6-9. There was a shift from high coverage at low temperature of linearly bound CO, 2090 cm^{-1}, to bridged CO at low coverages and high temperatures, 1800 and 1730 cm^{-1}, consistent with previous observations [84]. Bands at 1455, 1330, and 1540 cm^{-1} increased with temperature over the course of the TPO, and these have been assigned to absorbed carbonate species, either in the monodentate or bidentate adsorption mode[84]. A band at 1650 cm^{-1} also increased slightly over the span of the temperature ramp, and this is attributed to the bending of water adsorbed on Pt [84]. Bands at 1300 and 1500 cm^{-1} are assigned to surface carboxyl groups [84].

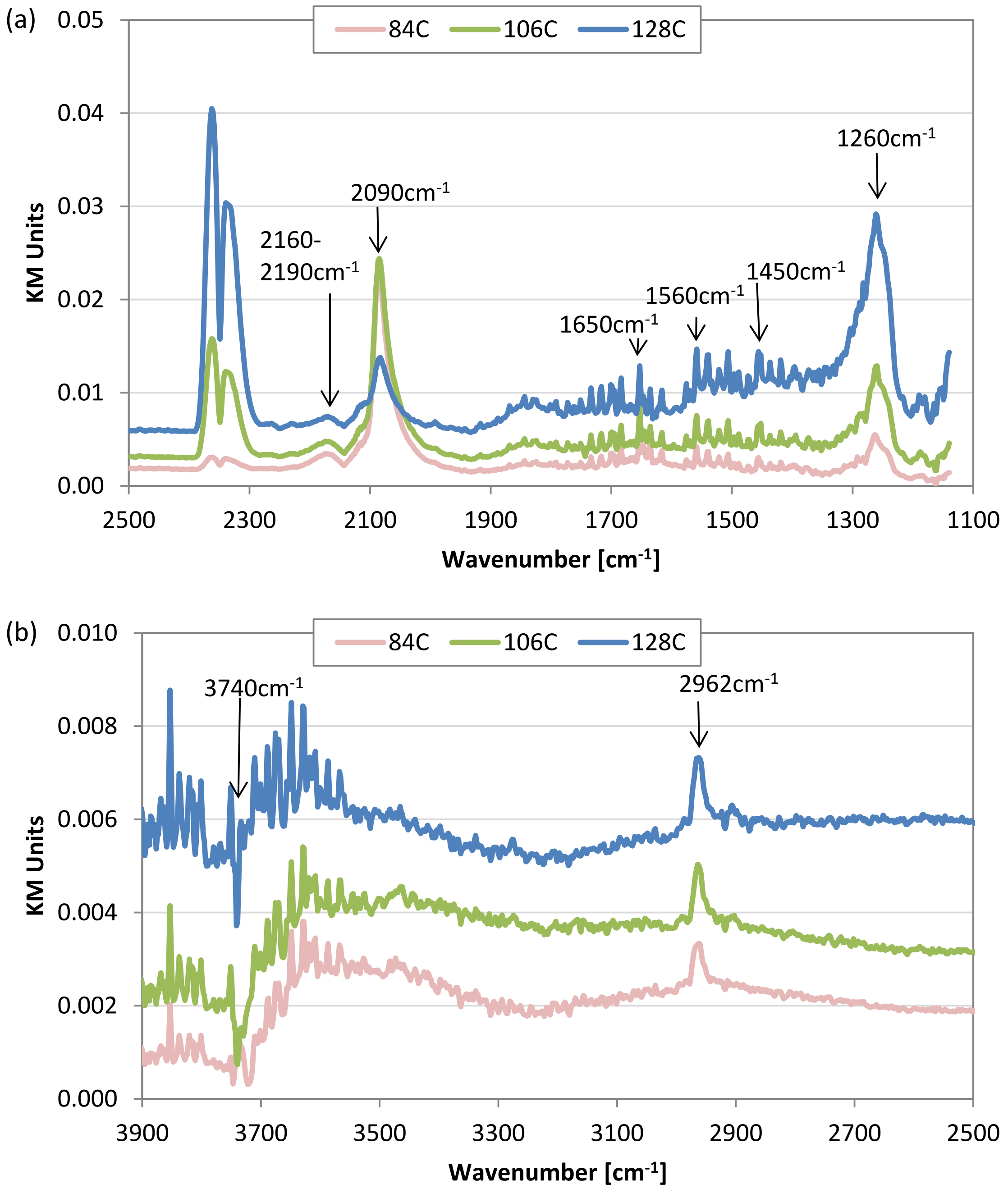

Figure 6-9 DRIFTS spectra obtained during the CO TPO; (a) 1100-2500cm^{-1} wavenumber region, (b) 2500-3900cm^{-1} wavenumber region

Over the course of the temperature ramp a large broad peak between 1200-1260 cm^{-1} developed, and can be attributed to -COH and other species with more hydrogen content [38], [89], [131]. From these results, and the observed depletion of the -OH feature at 3740 cm^{-1}, it is inferred that some CO adsorbed and reacted with the Lewis acid sites on the alumina support to form surface formate species [132]. vCH features at 2962 cm^{-1} increased over the temperature ramp, further substantiating the formation of surface formate species on the alumina [82], [133]. Other peaks related to the formate species can be observed at 1332, 1370, 1395 and 1665 cm^{-1} [128], [129], [134], [135]. There is also evidence of bands at lower temperatures, 2185-2190 cm^{-1}, corresponding to CO on alumina's Lewis acid sites, as well as H-bonded CO on hydroxyl sites on the alumina at 2160 cm^{-1} [74].

6.3.2.2 C_3H_6 TPO

The formation of formates on Pt/Al_2O_3 during propylene oxidation has been reported in the literature, with bands associated with said formates at 1332, 1370, 1395 and 1665 cm^{-1}, all of which were observed during the propylene TPO, Figure 6-10 a). Peaks that have been associated with an acetate species at 1457 cm^{-1}, and carboxylate species at 1580, 1642 and 1672 cm^{-1} [128], [129], [134], [135] are also evident. Again the feature at 2962 cm^{-1} was observed (Figure 6-10 b)), and this time was present over the entire temperature range. The initial spectrum before the temperature ramp shows a broad peak in the range of 1680-1560 cm^{-1}, which increased with temperature and has been attributed to π-bonded ethylene on Pt/SBA-15 catalysts [41]. This seems reasonable as the adsorption of propylene on Pt could be activated to form formate and ethylene intermediates, substantiated by the observed ethylene and formate peaks at the beginning of the ramp and their increase as the temperature increased.

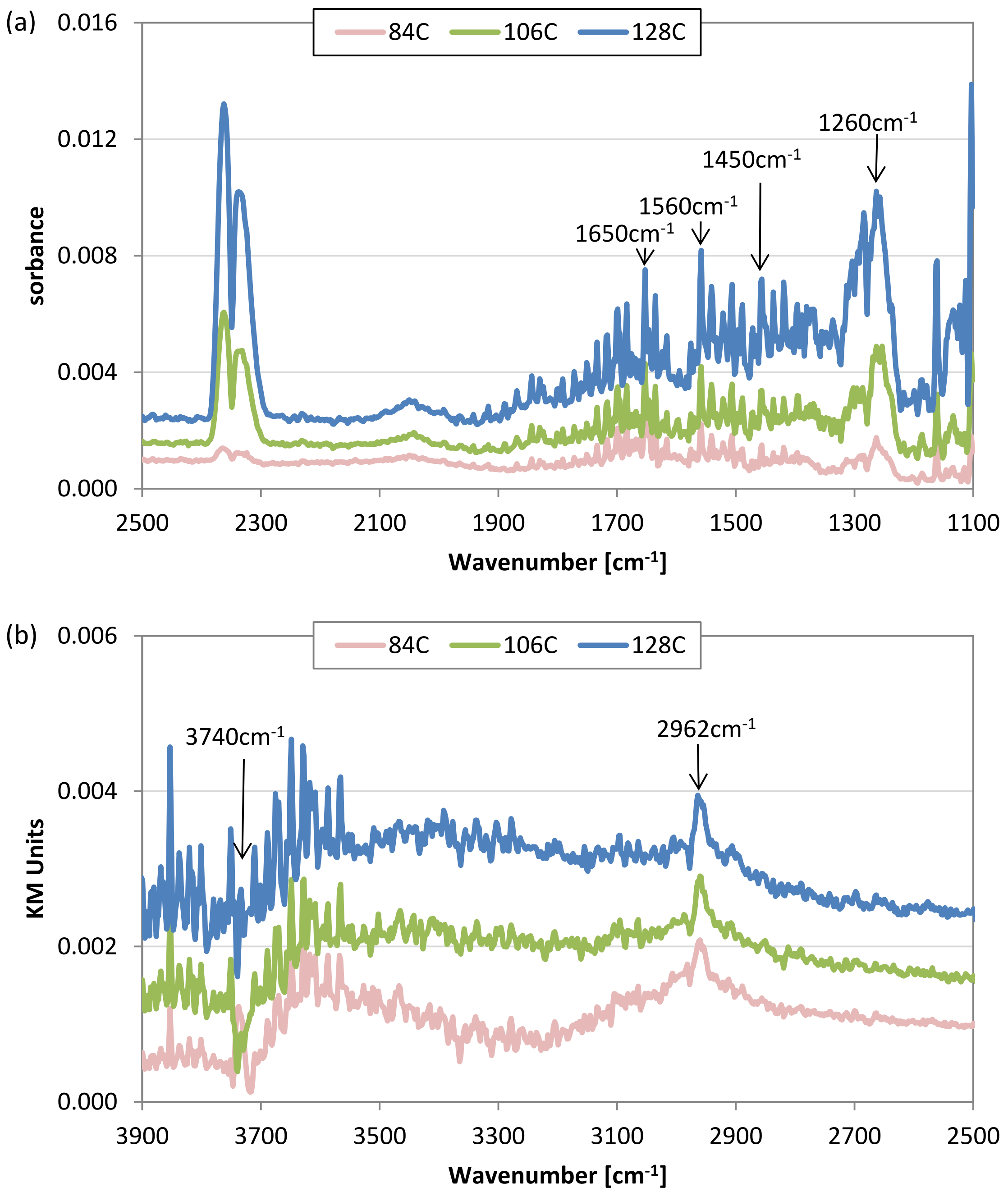

Figure 6-10 DRIFTS spectra obtained during the C_3H_6 TPO; (a) 1100-2500cm^{-1} wavenumber region, (b) 2500-3900cm^{-1} wavenumber region

6.3.2.3 CO and C_3H_6 TPO

The IR spectral features observed during CO and propylene (co-added) oxidation are largely the same as those noted during the oxidation of the single components. As with CO oxidation, the peaks for linearly- and bridge-bound CO are observed. If the CO peak height is plotted as a function of temperature for both the CO TPO and the CO/C_3H_6 TPO, shown in Figure 6-11 (a), a step in the surface concentration of CO is present when C_3H_6 was part of the mixture, similar to the step in the conversion vs temperature data obtained during the TPO in the bench reactor, and is absent when C_3H_6 was not part of the mixture. There is also a region at higher temperatures, after this step where the surface CO rate loss appears to slow, which may correspond to the second inhibition step observed in the bench reactor data.

(a)

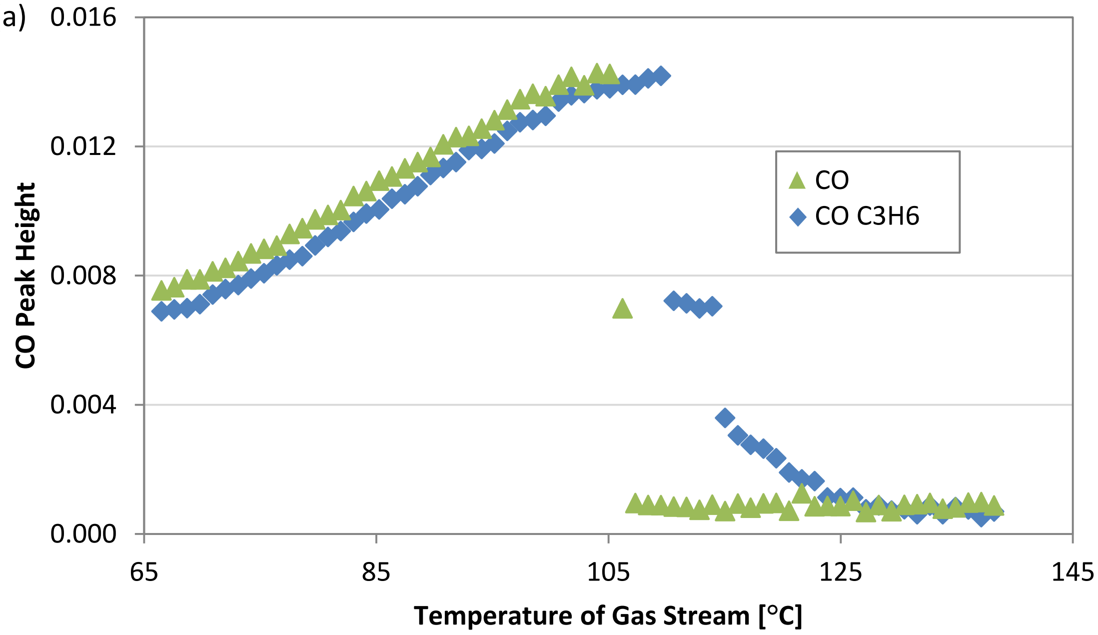

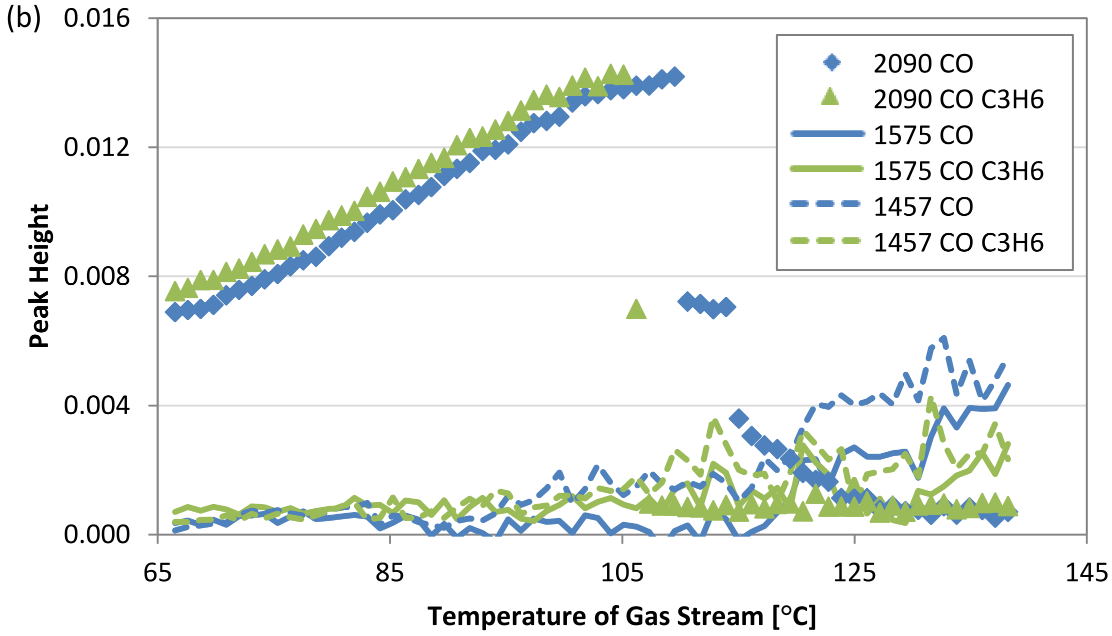

Figure 6-11 (a) CO [2090cm^{-1}], and (b) ν_sRCOO$^-$ [1457cm^{-1}] ν_sRCOO$^-$, ν_{as}COO$^-$ [1575cm^{-1}] peak heights as function of temperature during the DRIFTS TPO experiment

The peak for linearly bound CO shifted from 2090 to 2073 cm^{-1} in the presence of propylene as temperature increased, shown in Figure 6-12. Part of this shift is solely due to temperature, when only CO is oxidized the shift with temperature is 2090 to 2082 cm^{-1}, with literature suggesting this is the CO moving from terrace sites to edge or kink sites, or represents an electron transfer due to another adsorbed species [84], [136]. The larger CO peak shift in the presence of propylene suggests that the electron transfer is from an intermediate of propylene oxidation; a similar peak shift was noted during co-adsorption of ethylene and CO, due to the π-ethylene species [41], [136], [137]. Since ethylene and propylene can both form this π-species on the surface, it is not immediately clear whether the adsorbed species here is propylene or ethylene. There was an increased amount of formate formed in the presence of propylene which would suggest a scission of the propylene into ethylene and formate species. At the beginning of the temperature ramp, the CO was linearly bound, however as the temperature increased this peak shifted and the peaks for π-bonded propylene or ethylene and formate species began to emerge, suggesting that as some CO was oxidized at the beginning of the temperature ramp, propylene was able to adsorb on the active sites and either co-adsorbed with CO, or went through an activated adsorption to form ethylene and formate.

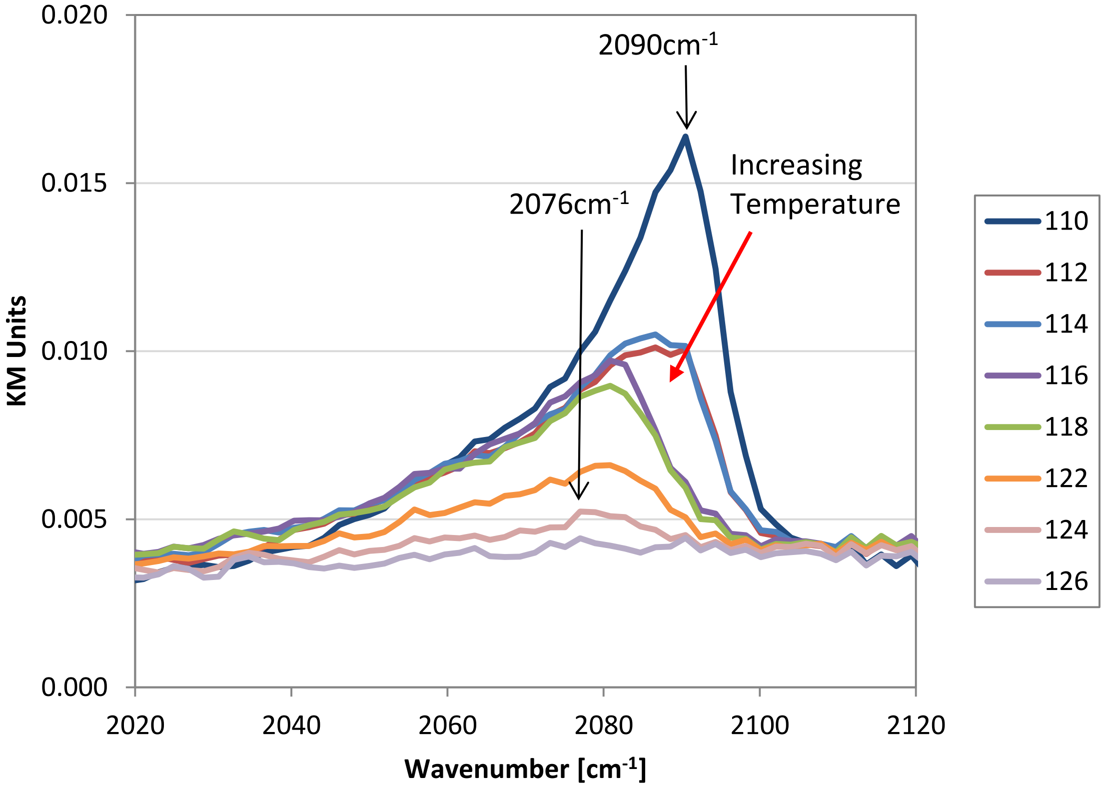

Figure 6-12 DRIFTS CO peak shift during CO and C_3H_6 TPO, temperature in °C

A subtraction of the spectra of the CO TPO at 106°C from the spectra of the CO/C_3H_6 TPO at 110°C yields the results shown in Figure 6-13. The only unique peaks observed are at 1454 cm^{-1} and 2966 cm^{-1}, which are attributed to either π-ethylene or π-propylene [136], as well as the presence of a larger amount of formate, a band shift in the CO-related adsorbed species, and a small peak at 1666 cm^{-1} which has also been attributed to π-ethylene [41]. As mentioned earlier, the increased amount of formate, as well as the emission of formaldehyde during the bench reactor tests, Figure 6-4 (b), suggest that the scission of propylene to ethylene and formates is taking place in one activated adsorption step. These data demonstrate that the adsorbed ethylene is a surface intermediate species during the co-oxidation of CO and propylene and was observed on the surface in the same temperature range as the first inhibition step during the bench reactor experiments.

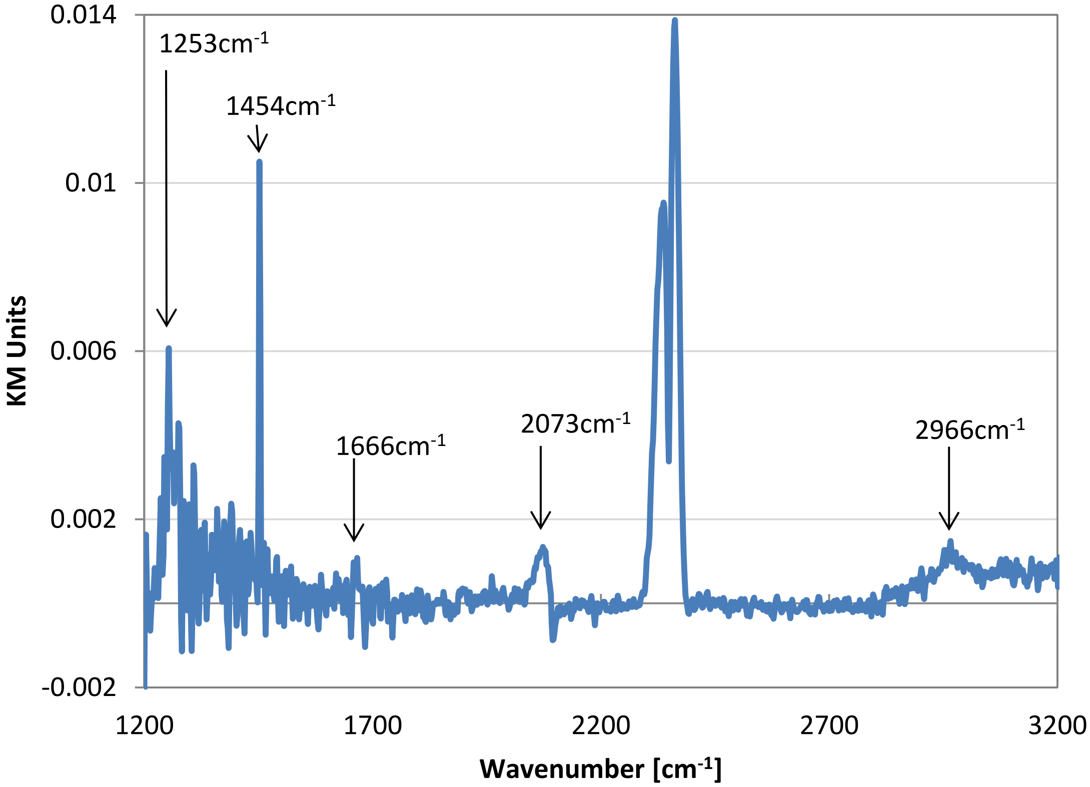

Figure 6-13 Residual spectrum after the subtraction of the CO DRIFTS spectrum obtained at 106°C from the spectrum obtained during the CO + C_3H_6 TPO obtained at 111°C

In terms of the second step, if the carboxylate peaks are plotted as a function of temperature, Figure 6-11 (b), the only increase in peak height observed, compared to the case without propylene, is *after* the surface CO step and still in the region where the CO was present on the surface. Therefore, as the reaction proceeds, the carboxylate peaks increase with temperature, indicating that either the adsorbed propylene or the ethylene can partially oxidize to form the acetate and formate species, which covers the active sites and leads to the second inhibition step. The absence of a second step in the presence of NO_X is related to consumption of the acetate species, i.e. the second inhibition step. This is based on the formation of more significant formate species on a Pt/Al_2O_3 surface in the presence of surface nitrates [128], and in the data shown in Figure 10 b) this coincides with the higher temperature step, which is therefore associated with the acetate species.

In summary, the first step observed in the bench reactor data appears to be caused by propylene adsorbing to the surface and forming ethylene and formate, then as the temperature increases an activation barrier to partially oxidize the ethylene to acetate is overcome to reach the second step where the acetate species and adsorbed CO coexist on the surface causing the second inhibition step.

6.4 Conclusions

During the oxidation of CO and C_3H_6, as well as reactions involving NO_X, CO poisons the catalyst and acts as a strong inhibitor for the oxidation of both NO and C_3H_6. Furthermore, the NO_X reduction capability at the high concentrations of CO used was significant; NO_2 was consistently reduced to NO at low temperatures in the presence of

CO, and at CO light-off, 70% of the NO_x was reduced to N_2. The reduction ability of the propylene was less significant, as not all of the NO_2 was reduced to NO at low temperature, and only about 40% NO_X conversion to N_2 was observed at light-off, where some N_2O was also observed. In the presence of both CO and C_3H_6, low temperature NO_2 reduction again occurred, due to the high CO or NO coverage at low temperature, relative to propylene, thus resulting in a similar trend as the experiment with CO and no propylene. However, low NO_X conversion and N_2O formation at light-off was attained, as was the case with C_3H_6 as the reductant. At CO light-off, the propylene adsorbs to the active sites and thus the NO_x reduction trends then follow those observed when just propylene was added.

In the absence of NO_X, there were two inflections in the CO conversion versus temperature results when propylene was part of the feed mixture, indicating inhibition "steps". DRIFTS results show that ethylene and formaldehyde intermediates formed during the first step, and then acetates in the second step. These partial oxidation products of propylene, in the presence of high CO surface coverages, were able to inhibit the light-off of each species, resulting in the observed inhibition. In the case of CO, C_3H_6 and NO_X all reacting at once, only one of the inhibition effects was observed. This indicates that one of these intermediates was consumed in NO_X reduction, while the other intermediate was not as easily oxidized by surface NO_X species. This is likely due to reaction between partially oxidized intermediate acetate species with surface nitrates leading to the formation of formate, while the ethylene species does not easily react with the surface nitrates and remains an inhibiting species.

Chapter 7 Coupled Heterogeneous and Homogeneous Hydrocarbon Oxidation Reactions in Model Diesel Oxidation Catalysts

Note: The material in this section has been accepted for publication in Emission Control Science and Technology, CLEERS-2016 Special Issue. Reference and figure numbers have changed for dissertation consistency.

7.1 Introduction

Low temperature combustion (LTC) technology for vehicle engine applications is a possible path to achieve improved fuel economy; however the emissions characteristics LTC engines are a challenge. For example, in a recent study comparing engine exhaust from an engine running in conventional, Premixed Charge Compression Ignition (PCCI) and Reactivity Controlled Compression Ignition (RCCI) combustion modes, RCCI produced much higher CO and hydrocarbon concentrations than conventional or PCCI engines [138], and that these were not adequately converted using modern diesel oxidation catalyst (DOC) technology [4]. This is exacerbated by the lower exhaust temperatures, where for example in modeling RCCI drive cycle engine emissions, the RCCI exhaust average temperature is about 200°C [139], posing a challenge for the DOC.

With such high CO and hydrocarbon concentrations, when the oxidation reactions do light off, large exotherms will evolve on the DOC surface. As an example estimate, from reference [138], if we choose dodecane as a representative hydrocarbon and the conditions described for the engine operating at 4.2 bar brake mean effective pressure and 2300 rpm, the adiabatic temperature rise is 24°C for conventional exhaust, 32°C for PCCI exhaust, and 197°C for RCCI exhaust. As reference, the CO concentrations emitted were estimated as 1400, 2200 and 4500 ppm, and dodecane concentrations were estimated as 53, 57 and 688 ppm for conventional, PCCI, and RCCI exhaust, respectively. Dodecane was chosen as the representative hydrocarbon since the majority of hydrocarbons present in conventional diesel engine exhaust are in the C_6-C_{18} range [140], the other gas constituents in this calculation example were assumed to be 10% CO_2, 10% H_2O, 10% O_2 and balance N_2 and heat capacity temperature dependence for gases were considered [141]–[143].

As will be shown, the combination of the large exotherm, high concentrations of large hydrocarbons and low NO_X concentrations can lead to homogeneous oxidation of the larger hydrocarbons within the catalyst channels. The implication, and observation, is that the radicals evolved from gas-phase hydrocarbon oxidation are able to oxidize NO to NO_2 in the gas-phase. There may be advantages in regards to “additional” NO_2 production. NO_2 is an oxidant in hydrocarbon oxidation, and stronger than O_2 itself [61], [122], [134], and could therefore enhance DOC performance. NO_2 can also improve downstream selective catalytic reduction (SCR) via allowing the fast SCR reaction [144] or can oxidize soot on a diesel particulate filter (DPF) [145]. The latter seems most interesting, since NO_2 can passively regenerate the DPF at moderate temperatures, while with O_2 as the oxidant, high temperatures are required, often generated by fuel injection [146]. Thus, if extra NO_2 can be generated via gas-phase NO oxidation as a consequence of the high exotherm over the DOC and the consequential low temperature gas-phase hydrocarbon oxidation, less of these high temperature DPF regeneration events would be required. This would lower the amount of fuel that would need to be injected, improving fuel economy and potentially lowering overall CO_2 emissions.

Increased gas phase NO_2 formation has been observed in previous studies; plasma-enhanced catalysis was investigated for improved NO to NO_2 oxidation such that better NO_X reduction over SCR catalysts could be obtained. Gas-phase NO oxidation was observed in two-step plasma-catalysis treatment [147], where a goal was NO_2 formation to improve NO_X reduction over a zeolite catalyst. However, not only was NO_2 responsible for some enhanced NO_X reduction, the plasma itself contributed as well [148]. This phenomenon was of particular interest for hydrocarbon SCR (HC-SCR) application. Indeed, combining the plasma process with a HC-SCR catalyst led to lower HC-SCR reaction temperatures [149]. The plasma treatments were never implemented, perhaps due to sufficient gains in SCR technology that deemed them unnecessary, however there is similar chemistry at play in this study with regards to gas phase NO oxidation.

In this study, evidence of homogeneous hydrocarbon oxidation within the model DOC used is provided. The impact of purposefully injecting a hydrocarbon to catalyze gas-phase NO oxidation was also studied. After evaluating different hydrocarbons and the correlated NO oxidation, further testing was done with diethyl ether, and with the inclusion of a model DOC. This would be analogous to injecting the hydrocarbon upstream of the DOC, with the intent to take advantage of the catalyst exotherm to produce extra NO_2.

7.2 Experimental Methods

7.2.1 Hydrocarbon Screening Experiments

Hydrocarbon homogeneous oxidation studies were performed in the same reactor as the catalyst testing described below, and with the same total flow rate, 12 L/min. The reactor system is comprised of several Bronkhorst mass flow controllers, and two Bronkhorst Controlled Evaporator Mixer (CEM) systems to control the water and hydrocarbon flow rates. The concentrations used in the hydrocarbon screening tests were as follows: 250 ppm hydrocarbon, 0 or 25 ppm NO, 10% O_2, 5% CO_2, and 5% H_2O in balance N_2. Hydrocarbons tested include n-hexane (C_6H_{14}), 1-hexene (C_6H_{12}), cyclohexane (C_6H_{12}), cyclohexene (C_6H_{10}), dodecane ($C_{12}H_{26}$), hexadecane ($C_{16}H_{34}$), diethyl ether $(C_2H_5)_2O$, tert-amyl ether ($C_6H_{14}O$), butyl acetate ($C_6H_{12}O_2$), hexyl acetate ($C_8H_{16}O_2$), and acetaldehyde (CH_3CHO). All hydrocarbons tested were purchased from Sigma Aldrich. The liquid flow controller flow limits resulted in one exception to the 250 ppm, acetaldehyde, and for this case the lowest possible concentration attainable, 470 ppm, was used.

Reactions were carried out in a quartz tube, which was heated by a Lindbergh Minimite furnace. Temperature programmed oxidation (TPO) experiments were performed with a ramp rate of 7.3°C/min. The inlet gas stream was also heated by a preheater that was ramped in temperature during the experiment. By controlling the heating rates both upstream and in the reactor we ensured hydrocarbons reacted/oxidized in the reactor, not in the upstream tubing. This was confirmed through temperature and gas concentration measurements; the temperature measurements for these experiments were at the same locations as detailed in the catalyst testing. The preheater temperature was kept below the temperature of the reactor. It was ramped from 114 to 300°C as measured from the outside of the tubing resulting in estimated gas temperatures of 70-255°C, below or near temperatures where the hydrocarbons tested oxidize homogeneously. Concentrations were measured using an MKS MultiGas 2030 FTIR; some of the hydrocarbon calibrations were made in house while others were supplied by MKS. Some partial oxidation products were measured; however due to the complexity and large number of reactions occurring, these products are by no means exhaustive and the relative amounts of these are not discussed at length. The reported hydrocarbon conversions were calculated based on the amount of hydrocarbon that disappeared compared to the inlet concentration. A verified NO_2 concentration calibration was used to measure NO conversion, and it was verified that its measurement had no impact on, or interference by, hydrocarbons. However, a complete nitrogen balance was not obtained with the NO, NO_2, N_2O and nitric acid measurements, which indicates N_2 formation or the formation of small concentrations of nitrogen containing hydrocarbon species.

7.2.2 Catalyst Synthesis

A γ-Al_2O_3 washcoated cordierite monolith with 400 cells per square inch was supplied by Johnson Matthey, with an Al_2O_3 loading of 1.59 g/in^3. Cylindrical monolith cores were cut from this piece. Two catalysts were made using incipient wetness impregnation; a 1:1 molar ratio of Pt:Pd and a monometallic Pt catalyst. The precursors used were $Pd(NO_3)_2$ and $Pt(NH_3)_4(NO_3)_2$, both purchased from Sigma Aldrich. The precursors were measured and mixed in a solution such that the desired metal loading would fill the pore volume of the alumina. The loading of the catalysts made were 0.775 wt% precious metal for the 1:1 $Pt:Pd/Al_2O_3$ catalyst and 1 wt% Pt for the Pt/Al_2O_3 catalyst. The catalysts were dried and calcined for 4 hours at 550°C. The cylindrical catalyst was then cut to 2 inches in length, or 5 cm, and approximately 165 channels for testing (0.64 in or 1.62 cm diameter), then aged in the reactor at 700°C for 24 hours in 14% O_2 and 5% H_2O in balance N_2.

7.2.3 Catalyst Testing

Four thermocouples were used to monitor temperatures inside the reactor; one 5 cm upstream of the catalyst, one just inside a radially central channel at the catalyst front, similarly the catalyst back, and one at the reactor tube wall at the catalyst front. The catalyst was wrapped in insulation to avoid gas bypass, and small quartz tubes were placed upstream of the catalyst. The gas hourly space velocity (GHSV) of each experiment was 50,000 hr^{-1}, with a total flow rate of approximately 12 L/min depending on the number of catalyst channels.

The initial gas concentrations tested were representative of the high hydrocarbon and CO concentrations observed in the measurement made in RCCI exhaust, using propylene to represent light hydrocarbons and dodecane to represent large hydrocarbons. For comparison, when in a RCCI mode, engine exhaust operating at 4.2 bar brake mean effective pressure and 2300 rpm contains 7300 ppm hydrocarbons on a C_1 basis, and 4500 ppm CO [1]. The concentrations tested were as follows: 3000 ppm CO, 1500 ppm C_3H_6, 250 ppm $C_{12}H_{26}$, 25 ppm NO, 10% O_2, 5% CO_2, and 5% H_2O in balance N_2. Based on the results of the hydrocarbon screening, a separate set of experiments was run with 250 ppm of diethyl ether, to explore as a possible purposeful additive to the exhaust to enhance gas-phase NO and hydrocarbon oxidation. Different NO concentrations (50 and 250 ppm) were also tested to monitor the effect of NO concentration on the gas-phase NO oxidation to NO_2.

Temperature programmed oxidation experiments were performed with a ramp rate of 7.3°C/min. The inlet gas stream was preheated, also using a temperature ramp in order to minimize the temperature gradient under non-reacting conditions along the catalyst length. With only N_2 flowing the maximum temperature gradient was less than 3°C during a simulated TPO. In between each TPO experiment, the catalyst was pretreated using the same species and concentrations described for the aging gas conditions, except the temperature was held at 600°C for 1 hour. The outlet gases were again measured using the MKS MultiGas 2030 FTIR. Conversion data are plotted using the inlet gas temperatures, the catalyst exotherm reported is the difference between the temperature measured at the catalyst back and the catalyst front.

7.3 Results and Discussion

7.3.1 Homogeneous Hydrocarbon Oxidation

During the course of diesel oxidation catalyst (DOC) testing we observed gas-phase oxidation of dodecane and a significant impact on NO oxidation extent. Also, in most cases adding small concentrations of NO lowered this hydrocarbon homogeneous oxidation onset temperature. Evidence of this is shown in Figure 7-1. Dodecane oxidation began around 330°C in the absence of NO, whereas with NO, dodecane started to oxidize around 305°C. At this same temperature, high NO oxidation conversion was also observed. In order to evaluate the extent of this oxidation, and to maybe identify other hydrocarbon types that might either promote or undergo gas-phase, or homogeneous, oxidation at DOC-relevant temperatures, several other hydrocarbon species were individually added to the simulated mixture.

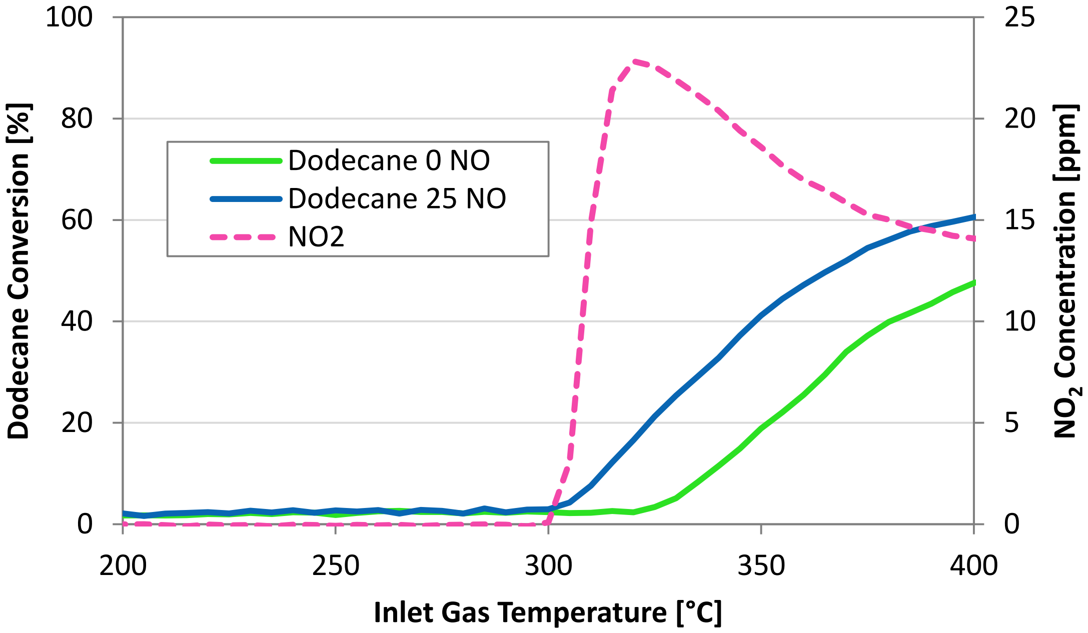

Figure 7-1 Homogeneous dodecane oxidation in an empty quartz tube reactor. Experimental conditions: 250 ppm $C_{12}H_{26}$, 0/25 ppm NO, 5% CO_2, 5% H_2O, and 10% O_2 in balance N_2

Before reviewing those data, the background chemistry will be reviewed as this will be used to explain the observed trends. For the initiation of gas-phase alkane oxidation, the following reaction 7-1 has been accepted as the initiating step, where a hydrogen is abstracted from the hydrocarbon by oxygen [143]:

$$C_nH_{2n+2} + O_2 \rightarrow \cdot\ C_nH_{2n+1} + HO_2\ \cdot. \tag{7-1}$$

Further propagation of the oxidation, based on alkylperoxy radical isomerization theory [143], is as follows:

$$\cdot\ C_nH_{2n+1} + O_2 \rightarrow C_nH_{2n+1}OO\ \cdot, \tag{7-2}$$

$$C_nH_{2n+1}OO\ \cdot \rightarrow C_nH_{2n}OOH, \tag{7-3}$$

$$C_nH_{2n}OOH \rightarrow P + OH\ \cdot\text{, and} \tag{7-4}$$

$$C_nH_{2n+2} + OH\ \cdot \rightarrow \cdot\ C_nH_{2n+1} + H_2O. \tag{7-5}$$

In the above reactions, the hydrocarbon undergoes intramolecular rearrangement to produce highly reactive hydroxyl radicals in reaction 7-4 and products (denoted as P) such as O-heterocycles, carbonyl compounds and alcohols. These hydroxyl radicals are then able to start the chain propagation of hydrocarbon oxidation in reaction 7-5.

However, once NO is added to the reaction mixture, after the hydrocarbon oxidation initiation stage, reactions 7-2 and 7-3 are not the only ones that can produce the reactive hydroxyl radical. NO can participate in the following reactions to also produce the reactive hydroxyl radicals, which propagate hydrocarbon oxidation and result in the formation of large NO_2 concentrations [150], [151]:

$$HO_2\ \cdot +NO \rightarrow OH\ \cdot + NO_2\text{ and} \tag{7-6}$$

$$C_nH_{2n}OO\ \cdot\ + NO \rightarrow C_nH_{2n}O\ \cdot + NO_2. \tag{7-7}$$

The hydrocarbon to NO_X ratio is important, as at high NO_X concentrations the following reactions are preferred, leading to loss of the desired chain propagating radicals and instead nitrous and nitric acid formation [150]:

$OH\cdot + NO \;\rightarrow\; HONO$ and (7-8)

$OH\cdot + NO_2 \;\rightarrow\; HNO_3.$ (7-9)

Reactions 7-6 and 7-7 explain how NO_2 is produced, and reactions 7-5 and 7-6 lead to the propagation of hydrocarbon oxidation in the gas-phase.

Evidence of the NO impact was more pronounced in the gas-phase oxidation of hexane, data shown in Figure 7-2. In the absence of NO, there was little low temperature hexane oxidation suggesting a larger energy barrier in either reaction 7-3 or 7-4, preventing the formation of the hydroxyl radical responsible for chain propagation.

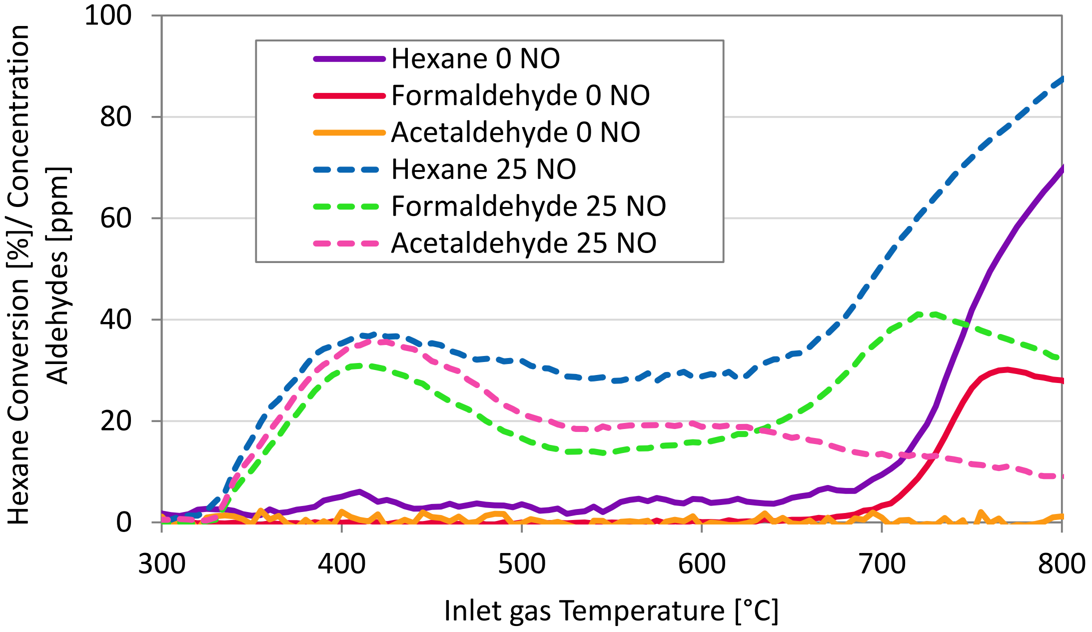

Figure 7-2 Homogeneous hexane oxidation in an empty quartz tube reactor; conversion of hexane (%) and formation aldehydes (ppm). Experimental conditions: 250 ppm C_6H_{14}, 0/25 ppm NO, 5% CO_2, 5% H_2O, and 10% O_2 in balance N_2.

However, with the addition of NO, low temperature hexane oxidation was observed, due to NO participating in reaction 7-6, producing the highly active hydroxyl radicals. In both cases formaldehyde, acetaldehyde and alcohol formation were observed, as also shown in Figure 7-2.

There is an intermediate negative temperature dependence for the gas-phase oxidation reactions, due to a shift between two mechanistic regions, a low temperature oxidation mechanism discussed above, and a high temperature combustion mechanism [143], [152]. The alkylperoxyl radicals formed at low temperatures become unstable at high temperature and will either break apart back into the alkyl and oxygen, or into an alkene and HO_2, which leads to chain termination via production of unreactive H_2O_2 [153]. The high temperature mechanism involves hydrogen abstraction reactions as follows [143]:

$$\cdot C_nH_{2n+1} + O_2 \rightarrow C_nH_{2n} + HO_2 \cdot \text{ and} \tag{7-10}$$

$$C_nH_{2n+2} + HO_2 \cdot \rightarrow \cdot C_nH_{2n+1} + H_2O_2. \tag{7-11}$$

As a consequence of the shift to the high temperature mechanism, there is a change in the nature of the hydrocarbons produced; the oxygenated hydrocarbon products are favored in the low temperature oxidation region while the alkene products are favored in high temperature combustion. This is consistent with the products observed in this study, with alkene, and CO, as measured products plotted in Figure 7-3 (a) with NO and (b) without NO as an example. It is also possible that the NO_2 itself is reacting with the hydrocarbons to form nitrous acid and nitrogen containing hydrocarbons, and such chemistry between NO_2 and light alkanes has been studied [154], [155].

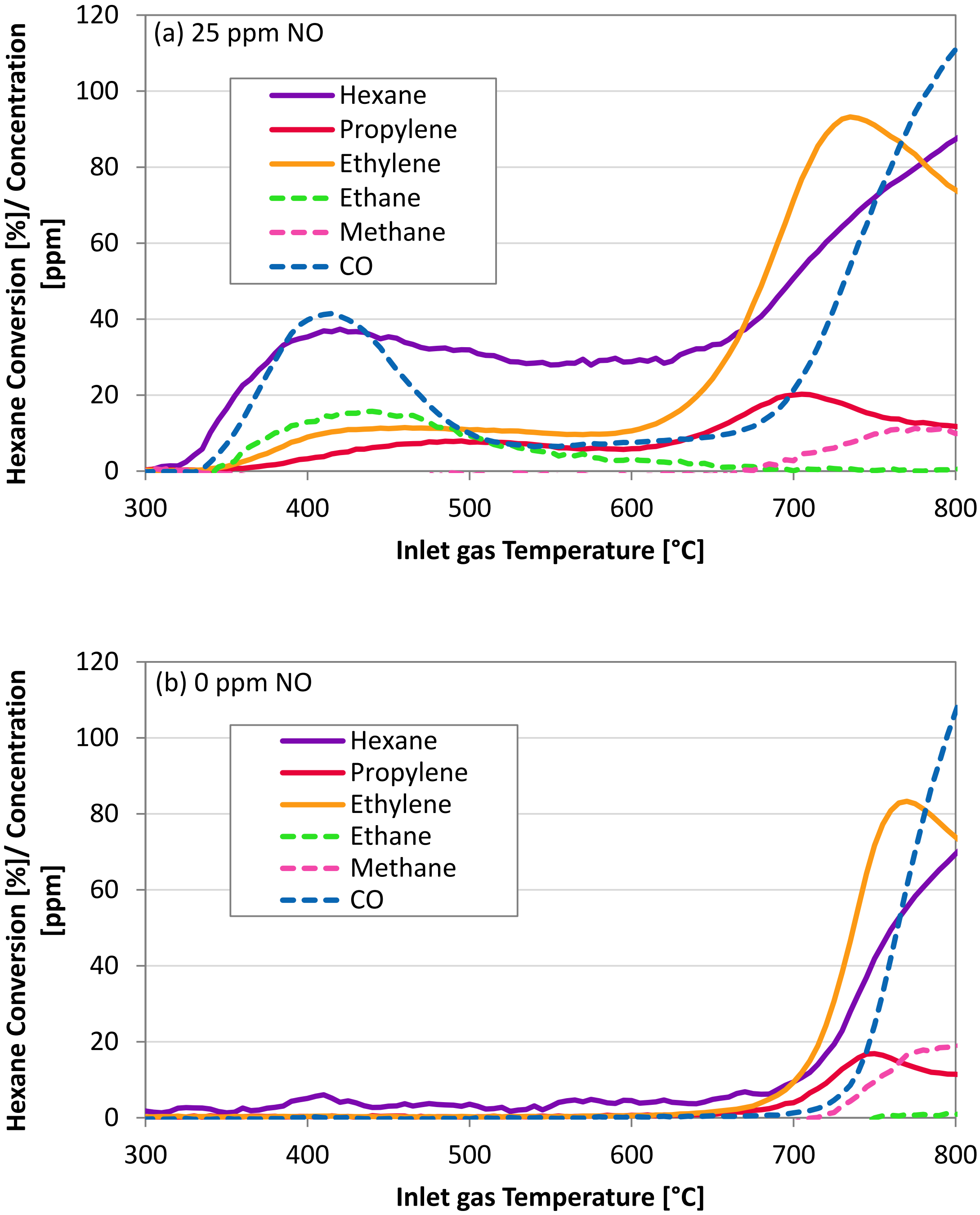

Figure 7-3 Homogeneous hexane oxidation in an empty quartz tube reactor; hexane conversion and formation byproducts. Experimental conditions: 250 ppm C_6H_{14}, 0/25 ppm NO, 5% CO_2, 5% H_2O, and 10% O_2 in balance N_2.

A systematic study using different hydrocarbons was carried out, where alkane size was compared as were some hydrocarbon types, for example alkanes versus alkenes versus cyclic hydrocarbons, with results shown in Figure 7-4 (a). In general for alkanes, as chain length increases, the temperature required for oxidation should decrease and oxidation rate increase, but this change becomes smaller with increasing chain length until no improvement occurs [156], [157]. Such a trend is noted in Figure 7-4 (a), with the required temperature being less for dodecane versus hexane. Increasing the chain length further, to hexadecane, resulted in no improvement. This study focused on straight chain hydrocarbons as branching inhibits low temperature oxidation [157]. In terms of an alkane versus alkene, in comparing hexane to hexene, higher temperatures were required for alkene oxidation onset, likely due to the fact that the hydrogen dissociation energy for alkenes is higher than that for alkanes [152], so the analogous initiation reaction for an alkene requires a higher temperature. Similarly, cyclohexene required a higher temperature than cyclohexane.

In terms of NO_2 formation, with results shown in Fig. 7-4 (b), NO_2 was observed when low temperature hydrocarbon oxidation began and its formation decreased with increasing temperature. This is consistent with the chemistry discussed previously, at the higher temperatures the alkylperoxy radicals are not stable and therefore reaction 7-7 occurred to a lesser extent due to lack of reactant. Once the temperature increases enough for high temperature hydrocarbon combustion, the HO_2 radical required for NO oxidation shown in reaction 7-6 favors reacting with the alkane or water to produce H_2O_2 and OH radicals. The OH radical produced via the reaction with water is good for the continued hydrocarbon oxidation, however would shift the equilibrium of reaction 7-6 away from NO oxidation.

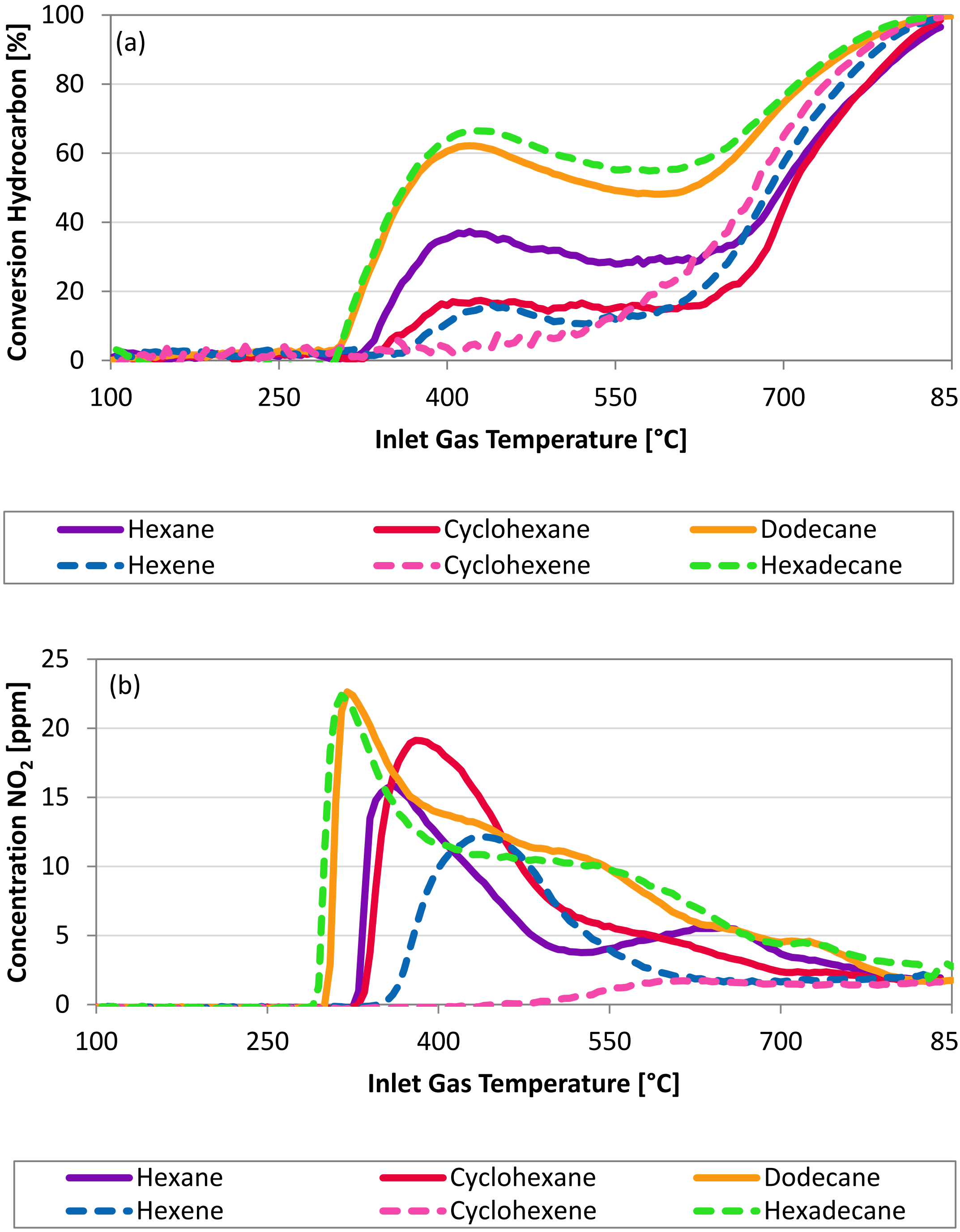

Figure 7-4 Homogeneous oxidation of n-alkanes and alkenes and cyclic alkanes and alkenes; (a) hydrocarbon conversion and (b) NO_2 formation. 250 ppm hydrocarbon, 25 ppm NO, 5% CO_2, 5% H_2O and 10% O_2 in balance N_2.

With a growing diversity of fuel choices and thus possible constituents, there are of course limitless possible hydrocarbons to evaluate. This study focused on possible candidates known to be present in biofuels, but also ones which might help catalyze NO oxidation. For example, as ethers and esters seemed likely to undergo the low temperature oxidation reactions [143], diethyl ether and tert-amyl methyl ether were selected, and butyl acetate and hexyl acetate for evaluation. Although there is some interest in dimethyl ether as an alternative fuel [158], it was not chosen as a candidate since its gas-phase oxidation does not occur until well above 300°C [151], and indeed preliminary tests showed it was not promising for low temperature NO_2 formation. Diethyl ether was instead chosen and is known to undergo gas-phase oxidation at a lower temperature than dimethyl ether [143]. Since aldehydes were observed as low temperature oxidation products, acetaldehyde was also chosen and evaluated.

The oxygenated hydrocarbon gas-phase oxidation results are shown in Figure 7-4 (a). Acetaldehyde does not undergo the low temperature oxidation mechanism, and only reacts at high temperatures. In comparing hexyl acetate and butyl acetate, the larger acetate led to slightly more low temperature oxidation and the onset of high temperature oxidation occurred at a lower temperature. In comparing tert-amyl methyl ether and diethyl ether, both show low temperature conversion, however diethyl ether conversion was more significant. The poorer performance of the tert-amyl methyl ether seems intuitive since one end of the ether is branched tert-amyl, which would be relatively harder to abstract a hydrogen from to initiate oxidation, and the other end is the methyl constituent, which would be more difficult to abstract a hydrogen from than the ethyl. The oxygenated hydrocarbon conversion profiles differ from those above, the negative temperature dependence was still evident, but less significant; however the trend in NO_2 formation was very similar to that observed with the other species gas-phase oxidation.

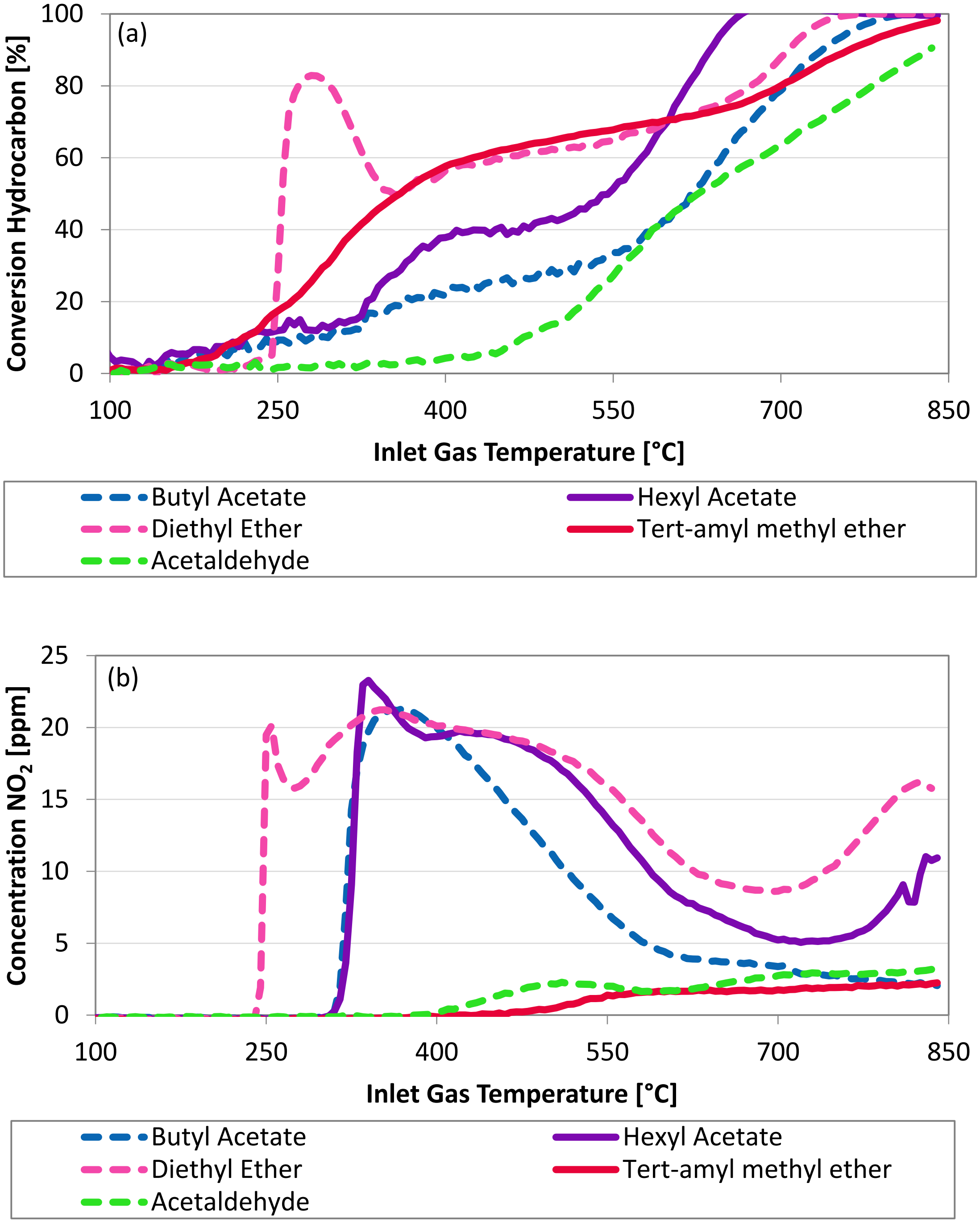

Figure 7-5 Homogeneous oxidation of the various oxygenated hydrocarbons as labeled; (a) hydrocarbon conversion and (b) NO_2 formation. Experimental conditions: 250 ppm hydrocarbon, 25 ppm NO, 5% CO_2, 10% O_2 and 5% H_2O in balance N_2.

In terms of this NO_2 formation, Figure 7-4 (b), the acetates and diethyl ether led to low temperature NO_2 formation with diethyl ether oxidation leading to NO_2 formation at a lower temperature than the alkanes. Unlike the other hydrocarbons tested, the tert-amyl methyl ether did not show NO_2 formation in the low temperature range and hardly any at the high temperature range. In general, with temperature, NO_2 formation initially went through a maximum, again linked to a change from low to high temperature mechanisms. There was also a dip in NO_2 formation in the diethyl ether experiment at low temperature, which was associated with nitric acid formation (data not shown for brevity and due to lack of strong confidence in the accuracy of amount measured).

Diethyl ether seemed to be interesting in terms of low temperature oxidation (60°C lower than the lowest non-oxygenated hydrocarbon dodecane), but also led to significant low temperature NO_2 formation. With the thought that it might be a candidate for purposeful addition into the exhaust to stimulate NO_2 formation for downstream NO_X reduction or particulate filtration systems, it was selected for further testing. Moving to an even larger ether would likely lead to even lower temperature oxidation if desired, however the tradeoff would be larger hydrocarbon fragments as partial oxidation products.

The proposed initiation reaction for diethyl ether, and subsequent peroxide radical formation and decomposition are shown in reactions 7-12 through 7-15 as [143]:

$$CH_3CH_2OCH_2CH_3 + O_2 \rightarrow CH_3\dot{C}HOCH_2CH_3 + HO_2\cdot, \tag{7-12}$$

$$CH_3\dot{C}HOCH_2CH_3 + O_2 \rightarrow CH_3C(OO\cdot)HOCH_2CH_3, \tag{7-13}$$

$$CH_3C(OO\cdot)HOCH_2CH_3 \rightarrow 2CH_3CHO + OH\cdot, \text{ and} \tag{7-14}$$

$$CH_3C(OO\cdot)HOCH_2CH_3 \rightarrow CH_3CH_2O\cdot + OH\cdot + CH_3CHO. \tag{7-15}$$

Interestingly, in evaluating the diethyl ether gas-phase oxidation data shown in Figure 7-6, contrary to the other hydrocarbons studied, the addition of NO to the reaction mixture didn't lower the oxidation temperature. For diethyl ether oxidation, the peroxide radical decomposes to acetaldehyde and OH radicals directly (reactions 7-14 and 7-15), while for alkane oxidation the peroxide first needs to react to an acid which then decomposes to form the OH (reactions 7-3 and 7-4).

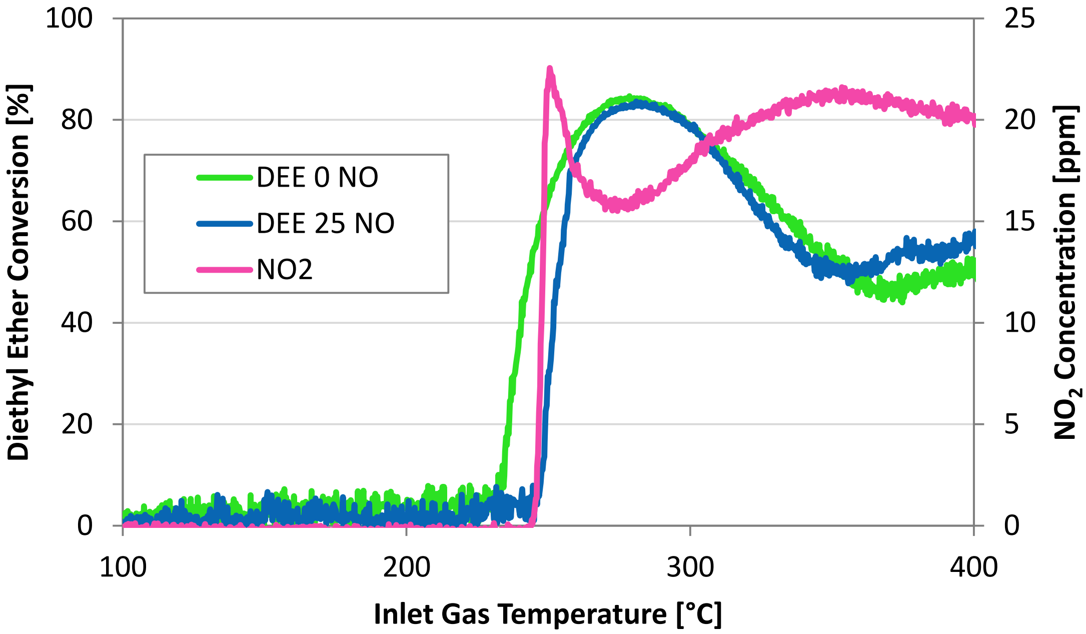

Figure 7-6 Diethyl ether homogeneous oxidation in an empty quartz tube reactor. 250 ppm $(C_2H_5)_2O$, 0/25 ppm NO, 5% CO_2, 5% H_2O, and 10% O_2 in balance N_2.

With the addition of NO, analogous to the mechanism of gas-phase alkane oxidation, the NO_2 formed during the gas-phase diethyl ether oxidation comes from NO reacting with the peroxide radical,

$$CH_3C(OO\cdot)HOCH_2CH_3 + NO \rightarrow CH_3C(O\cdot)HOCH_2CH_3 + NO_2, \tag{7-16}$$

in addition to the HO_2 radicals in reaction 7-6.

The following hydrocarbon partial oxidation products were observed; acetic acid, formic acid, formaldehyde, acetaldehyde, and CO in the low temperature range (starting around 250°C), and then a shift to ethylene, methane, and higher CO concentrations above 600°C. These are consistent with the mechanisms mentioned above [143], as well as in a recent study of dimethyl ether gas-phase oxidation [151].

7.3.2 Coupled Homogeneous and Heterogeneous Hydrocarbon Oxidation

As discussed, a longer chain alkane has a higher rate of low temperature gas-phase oxidation than a smaller alkane. Catalytic alkane oxidation is more complex as the longer chain alkane requires more free catalytic sites to adsorb [8], however the first step in oxidation is breaking the C-H bond, toughest for methane and progressively easier as the chain length increases [159]. Alkene oxidation over an oxidation catalyst is generally easier than alkane oxidation [160], with the opposite true in the gas-phase case. These generalities suggest that homogenous oxidation of a large alkane to smaller alkene fragments could have a substantial effect on catalyst performance, and that if both homogeneous and heterogeneous reactions occur they can impact each other. Automobile exhaust contains a plethora of different hydrocarbons, and so decoupling these chemistries would be rather challenging. This study does not intend to do so, but instead to demonstrate that both homogeneous and heterogeneous reactions are indeed occurring under these test conditions. For previous studies focused on plasma enhanced catalysis, propylene was the representative hydrocarbon used [147]–[149]. It is often used as a model hydrocarbon simulating engine exhaust for catalyst testing, however LTC exhaust also contains larger hydrocarbons closer in size to unburnt diesel fuel. To simulate these, dodecane is often used, however some quantity of cetane (hexadecane) and other fuel constituents would also likely be present in the exhaust [140]. These larger hydrocarbons oxidize more easily in the gas-phase once the DOC gets hot enough without requiring any plasma processing, as demonstrated by the results discussed above. To summarize the catalyst performance under all reaction conditions tested with both catalysts, the T_{50} (temperature where 50% reactant is converted) data are presented in Table 7-1.

Table 7-1 T_{50} (temperature required for 50% conversion) of CO, C_3H_6, $C_{12}H_{26}$ and $(C_2H_5)_2O$ oxidation over with 25 ppm NO, 5% CO_2, 5% H_2O, and 10% O_2 in balance N_2.

Concentrations [ppm]				T_{50} 1:1 Pt:Pd/Al_2O_3 [°C]				T_{50} Pt/Al_2O_3 [°C]			
CO	C_3H_6	$C_{12}H_{26}$	$(C_2H_5)_2O$	CO	C_3H_6	$C_{12}H_{26}$	$(C_2H_5)_2O$	CO	C_3H_6	$C_{12}H_{26}$	$(C_2H_5)_2O$
0	0	0	250	--	--	--	230	--	--	--	172
0	1500	0	250	--	211	--	224	--	276	--	272
3000	1500	0	250	183	190	--	195	283	290	--	282
3000	1500	250	0	192	197	199	--	300	306	312	--
3000	1500	250	250	192	197	199	198	295	301	308	290

This table will be further referred to later, however it is interesting that the DEE T_{50} values over the Pt:Pd and Pt catalysts (230 and 172°C) are much lower than the DEE T_{50} in the quartz tube (253°C), which corresponds to homogeneous oxidation. The DEE T_{50} decreases due to catalytic oxidation of the DEE, however once the temperature limit required to commence homogenous oxidation is reached both catalytic and homogeneous DEE oxidation occurs. The interplay of the catalytic and homogenous reactions is the focus of this section.

As noted, gas-phase NO oxidation could be beneficial for downstream catalyst systems. Two catalyst formulations were evaluated as model DOCs, with the effect of diethyl ether injection on NO oxidation measured, the primary focus of this section, although the impact on the other hydrocarbon species oxidation was also measured to ensure no negative effect on this DOC aspect. NO_2 formation as a function of inlet NO concentration over the 1:1 Pt:Pd/Al_2O_3 catalyst is shown in Fig 7-7. For 25 ppm NO, NO oxidation began at 198°C, quickly reached 80% conversion to NO_2 at 200°C, and reached a maximum at 205°C corresponding to 84% conversion to $NO_{2,}$ before decreasing.

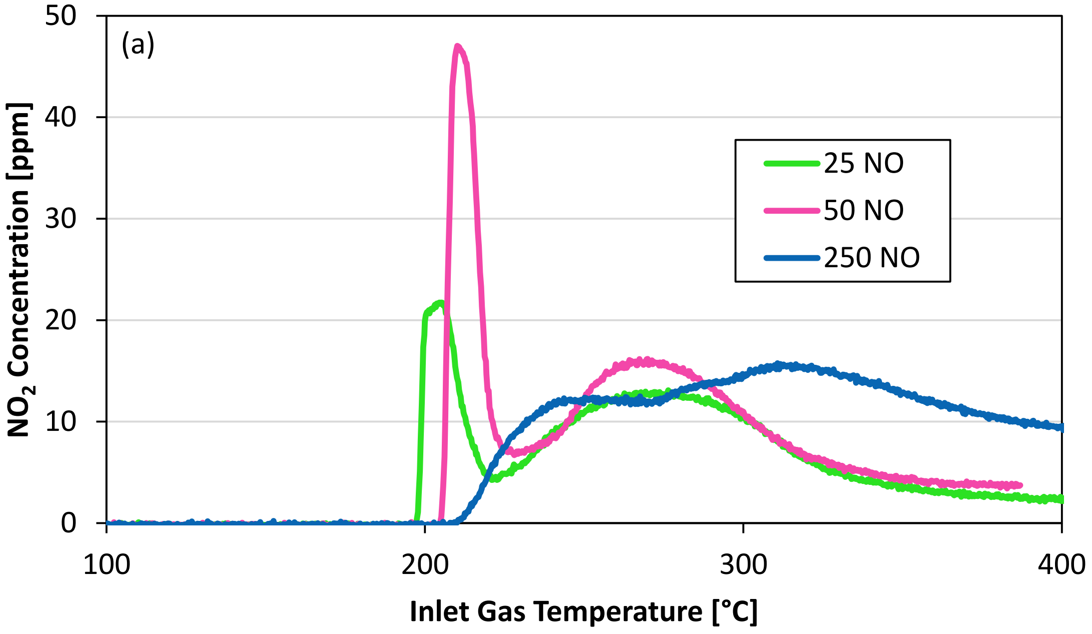

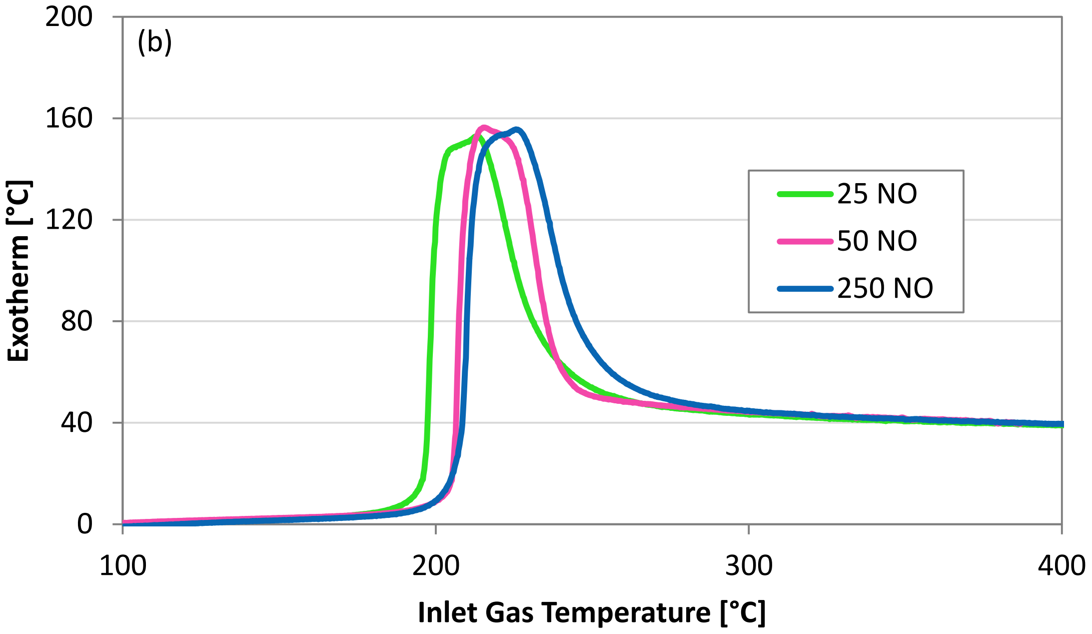

Figure 7-7 (a) NO_2 formation and (b) catalyst exotherm over the 1:1 Pt:Pd/Al_2O_3 catalyst. 3000 ppm CO, 1500 ppm C_3H_6, 250 ppm $C_{12}H_{26}$, 250 ppm $(C_2H_5)_2O$, 25/50/250 ppm NO, 5% CO_2, 5% H_2O, and 10% O_2 in balance N_2.

The NO oxidation onset at 198°C corresponded to a 56°C catalyst exotherm based on the oxidation of the hydrocarbons and CO; the maximum in NO oxidation at 205°C corresponded to 92% diethyl ether conversion with a 148°C reaction exotherm. It is clear that this NO_2 generation originated from homogeneous reactions, as the catalyst exotherm contribution puts the temperature above the 245°C required for DEE homogeneous conversion. As NO concentration increased, from 25 ppm to 50 ppm, NO oxidation onset increased to 205°C, reached 80% conversion at 208°C, and reached a maximum at 210°C corresponding to 89% conversion to NO_2 before decreasing. With 50 ppm NO, NO oxidation onset at 205°C corresponded to a catalyst exotherm of 20°C; the maximum in NO oxidation at 210°C corresponded to 80% diethyl ether conversion with a 136°C catalyst exotherm. The maximum NO oxidation occurred when the CO and hydrocarbon species were almost completely oxidized. The extent of the exotherm that was generated when NO oxidation onset was observed was high enough to provide the required temperature for gas-phase diethyl ether oxidation, which began at 245°C in the empty reactor/quartz tube as shown in Figure 7-6, but not high enough to oxidize dodecane in the gas-phase, which began around 305°C in the empty reactor/quartz tube as shown in Figure 7-1. It was this onset of diethyl ether oxidation which led to NO oxidation. After the sharp peak in NO_2 formation, after CO and propylene oxidation lit off, there was a decline in NO_2 formed, which was caused by a loss in diethyl ether due to its oxidation over the catalyst surface. There was another NO oxidation conversion peak at a higher temperature, which corresponds to the region where dodecane homogeneously oxidized. NO_2 formation occurred at a slightly higher temperature for the case of 50 ppm NO because CO and propylene oxidation lit off at a higher temperature due to NO inhibition. Increasing the NO concentration to 250 ppm led to a lack of NO_2 formed as the consumption of the hydroxyl radicals via reactions 7-8 and 7-9 were preferred with the relatively large NO to hydrocarbon concentration. Also the temperature required for NO_2 formation onset was higher, again due to increased NO inhibition. These results demonstrate that if a hydrocarbon were to be purposefully injected to stimulate NO oxidation, some optimization of the hydrocarbon to NO_X ratio would be required to minimize chain terminating reactions.

The effects of adding propylene and CO to the reaction mixture that included diethyl ether are described by Figure 7-8 (a) and (b), which are plots of the NO_2

formation and catalyst exotherm data. With only diethyl ether and NO, NO_2 formation began at 256°C, and reached a maximum at 322°C with 93% diethyl ether conversion.

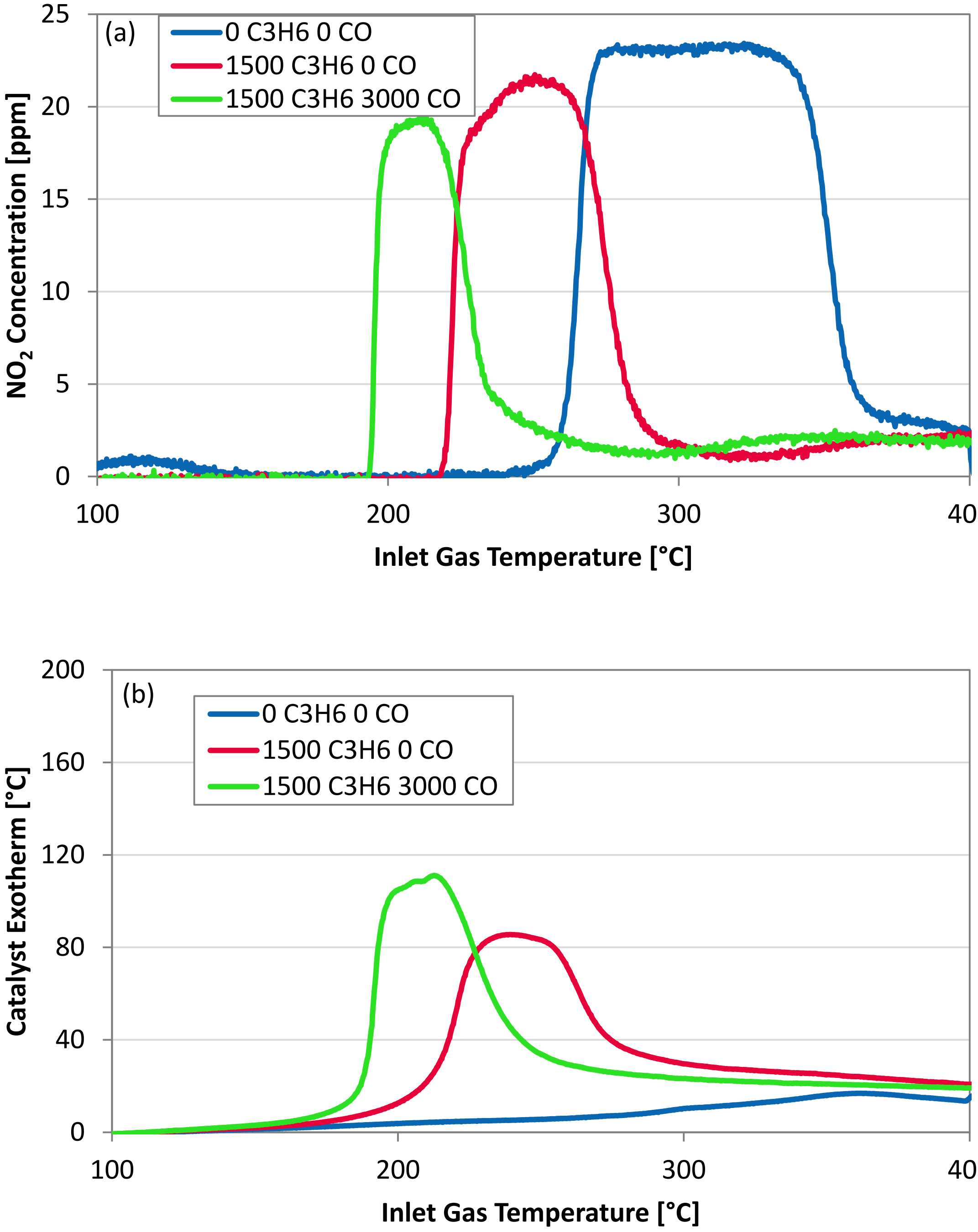

Figure 7-8 (a) NO_2 formation and (b) catalyst exotherm with and without CO or C_3H_6 over 1:1 Pt:Pd/Al_2O_3 catalyst. 0/3000 ppm CO, 0/1500 ppm C_3H_6, 250 ppm $(C_2H_5)_2O$, 25 ppm NO, 5% CO_2, 5% H_2O, and 10% O_2 in balance N_2.

In the absence of the catalyst (the empty quartz tube), NO_2 formation was observed at 245°C, which suggests some NO_2 reduction back to NO over the catalyst via diethyl ether oxidation or oxidation of its decomposition products. With propylene added to the reaction mixture, NO_2 formation onset decreased to 219°C. The reaction exotherm at this point was 48°C, sufficient to cause gas-phase diethyl ether oxidation within the catalyst that then led to gas-phase NO_2 formation. Adding CO to the mixture led to NO_2 formation at 194°C, with a catalyst exotherm of 90°C. Although the increased exotherm allowed for diethyl ether gas-phase oxidation, it also increased the rate at which it oxidized on the catalyst. The more diethyl ether that oxidized on the catalyst, the less gas-phase oxidation occurred such that no NO_2 formation was observed at high temperatures unlike what was observed without the catalyst. Thus, as the exotherm increased, the NO_2 formation temperature range narrowed. Of note, this sequential addition of propylene and CO is a further demonstration that the exotherm generated caused diethyl ether to oxidize homogeneously at what would be considered inlet gas temperatures typically used in oxidation catalyst testing and characterization.

The NO oxidation data shown in Figure 7-9 (a) were obtained with diethyl ether (DEE) added to a more complex inlet gas mixture, with CO, a small alkene (propylene), a large alkane (dodecane) and NO. In the absence of diethyl ether, NO oxidation began at 206°C, with an associated 139°C exotherm, while with diethyl ether NO oxidation was observed at 198°C where there was a 56°C exotherm (exotherm data provided in Figure 7-9 (b)). The temperature range where there are very high NO_2 concentrations was very narrow, indicating the diethyl ether was easily oxidized over the catalyst in this full mixture condition due to the large exotherm. At higher temperature, NO oxidation was enhanced via dodecane homogeneous oxidation. However, diethyl ether addition to the reaction mixture hindered NO_2 formation above 205°C where dodecane gas-phase oxidation could have led to higher conversion. This is likely due to the slightly higher temperature rise via the exotherm caused by diethyl ether oxidation (11°C) at 205°C, leading to a higher rate of dodecane oxidation on the catalyst surface and therefore again less gas-phase oxidation. If diethyl ether were to be used with such a mixture and at the high concentrations examined, it would need to be added during catalyst light off before its catalytic oxidation eclipses homogeneous oxidation. In terms of T_{50} for the 1:1 Pt:Pd catalyst, the addition of diethyl ether had no effect on the T_{50} for the other species present in the reaction mixture. As propylene and CO were consecutively added to the reaction mixture, the DEE T_{50} decreased due to the discussed exotherm effects, in line with NO oxidation.

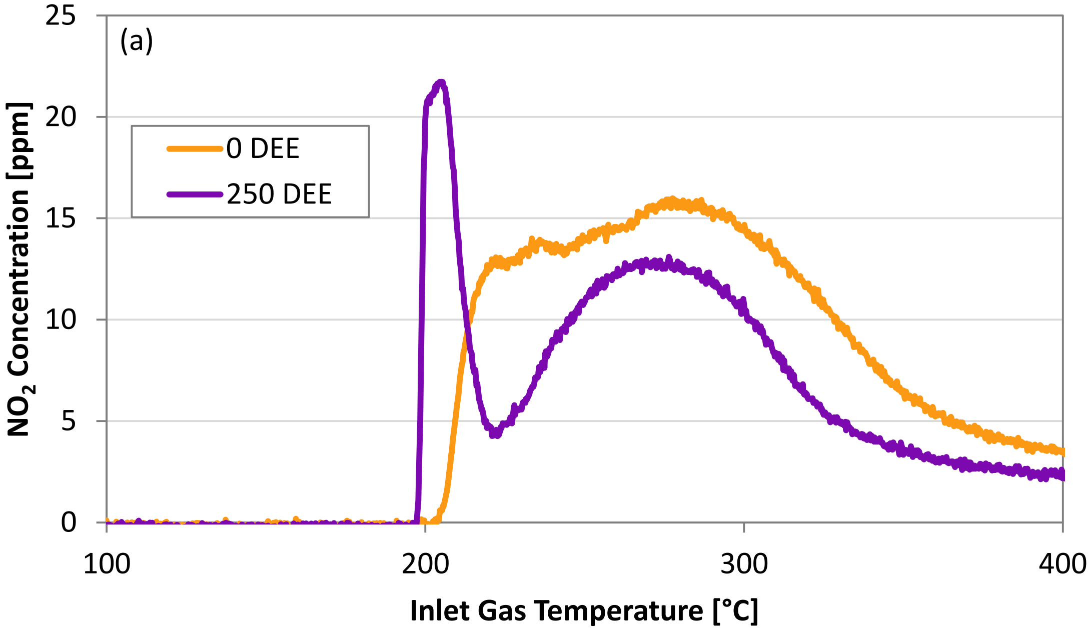

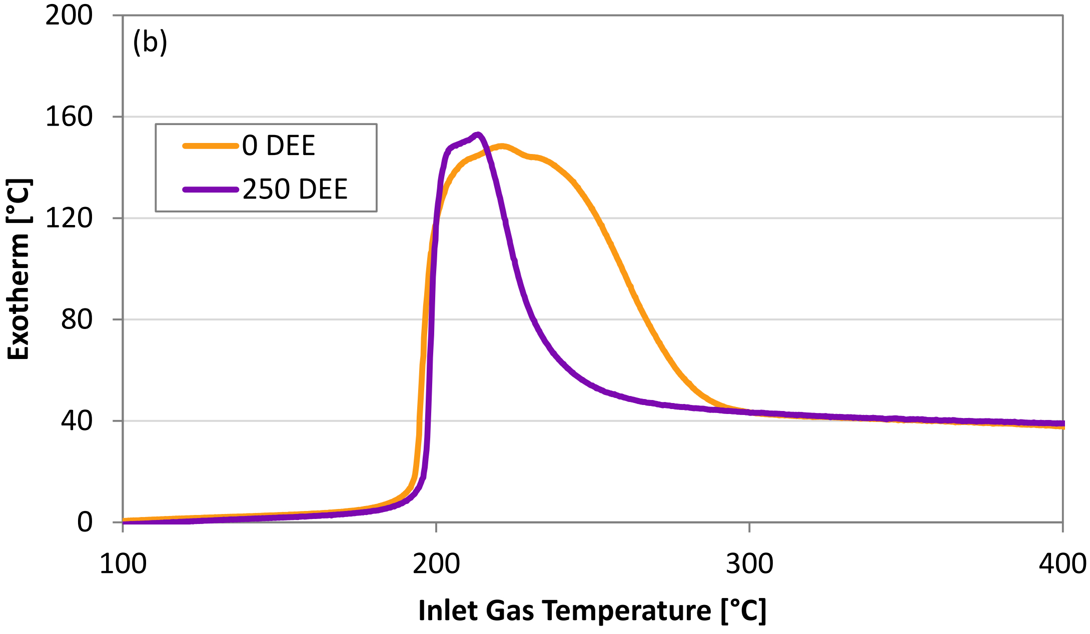

Figure 7-9 (a) NO_2 formation, (b) catalyst exotherm effect of DEE over the 1:1 Pt:Pd/Al_2O_3 catalyst. 3000 ppm CO, 1500 ppm C_3H_6, 250 ppm $C_{12}H_{26}$, 0/250 ppm $(C_2H_5)_2O$, 25 ppm NO, 5% CO_2, 5% H_2O, and 10% O_2 in balance N_2.

The inclusion of a Pt/Al_2O_3 catalyst was also examined, and results when adding CO and propylene to diethyl ether and NO in the gas mixture are shown in Figure 7-10. Over the Pt/Al_2O_3 catalyst, there was a much lower extent of NO_2 formation relative to that observed with the 1:1 Pt:Pd/Al_2O_3, Figure 7-8. "Extra" NO_2 formation was observed; for the experiment with only diethyl ether an increase in NO_2 concentration was observed at 261°C and a peak was observed at 299°C with a corresponding 98% diethyl ether conversion. DEE or DEE partial oxidation products may consume the NO_2 formed homogeneously, since the NO_2 formation onset temperature was higher than the gas-phase diethyl ether oxidation at 245°C observed in the absence of catalyst, and the total formation of NO_2 is lower. With CO or propylene addition to the reaction mixture, NO_2 is consumed resulting in significantly less NO_2 being observed, due to their acting as a NO_2 reductant. This was slightly more affected by CO, consistent with previous work showing that CO reduces NO_2 to NO more readily than propylene [73].

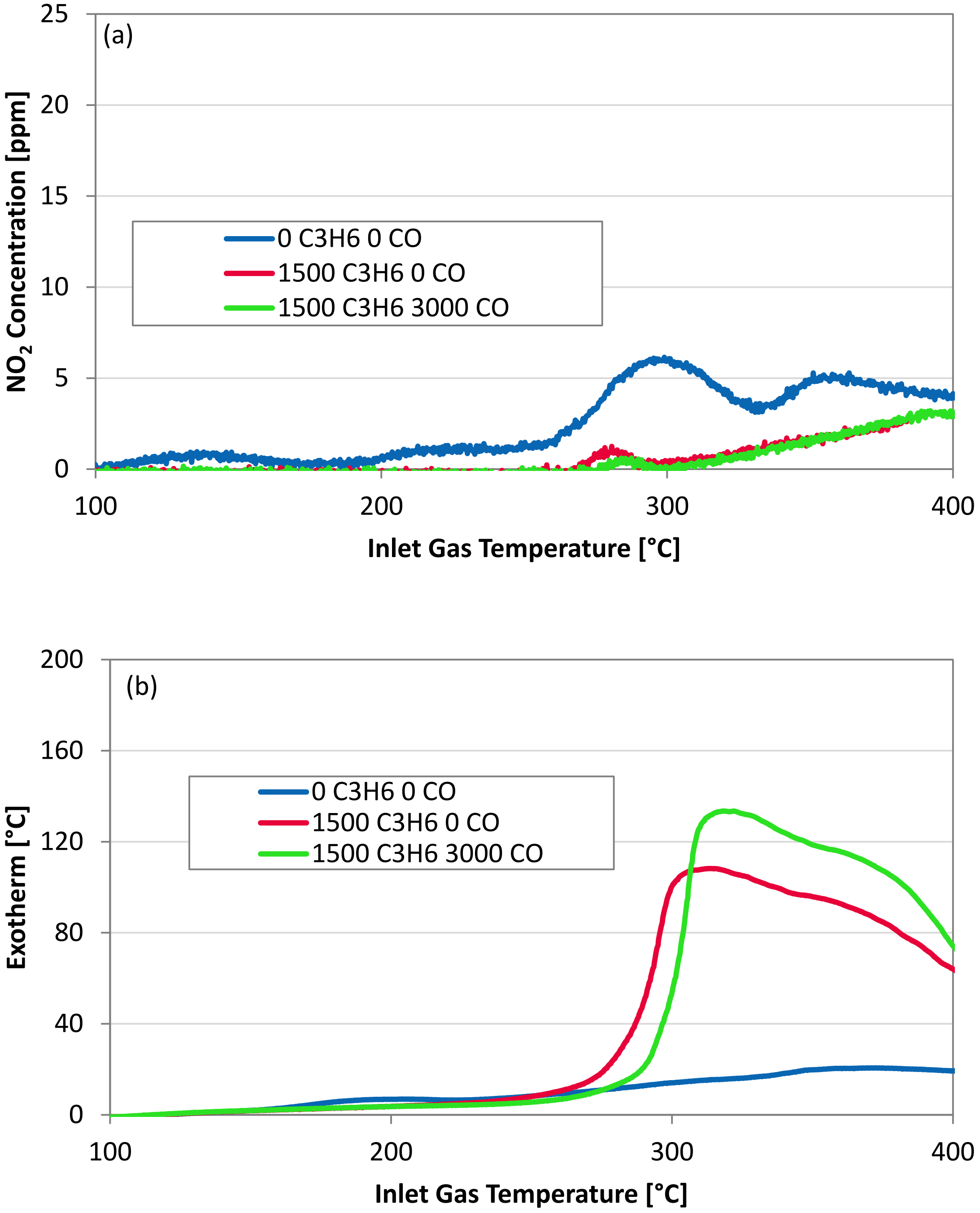

Figure 7-10 (a) NO_2 formation and (b) catalyst exotherm with and without CO or C_3H_6 over Pt/Al_2O_3 catalyst. 0/3000 ppm CO, 0/1500 ppm C_3H_6, 250 ppm $(C_2H_5)_2O$, 25 ppm NO, 5% CO_2, 5% H_2O, and 10% O_2 in balance N_2.

Once CO and hydrocarbon are completely oxidized at temperatures above 300°C, NO_2 will not be consumed as an oxidant and thus NO oxidation to NO_2 will be evident. Previous work has shown that NO_X reduction occurs more readily over Pt catalysts than Pd catalysts [161], and NO_2 reduction is expected to occur when CO is not fully reacted [162]. This suggests the Pt catalyst may intrinsically reduce NO_2 more easily than a 1:1 Pt:Pd catalyst, or it at least indicates that NO_2 isn't observed at lower temperatures on the Pt catalyst because the CO isn't completely oxidized until higher temperatures. For the 1:1 Pt:Pd/Al_2O_3 catalyst, the results demonstrated that NO_2 was not being formed upstream of the catalyst, but that the homogeneous oxidation reactions were occurring either inside the catalyst channels or downstream of the catalyst. Considering such results, the homogeneous oxidation reactions should be occurring with the monometallic Pt catalyst sample as well and yet very low NO_2 concentrations were observed, attributed to the ease of NO_2 reduction and the catalyst light-off for CO and hydrocarbons being greater than the temperature required for DEE homogeneous oxidation.

NO oxidation results from the experiment with the addition of diethyl ether into the more complex mixture, for the Pt/Al_2O_3 catalyst, are shown in Figure 7-11. NO_2 formation occurred 8°C lower when diethyl ether was present in the inlet gas; this is consistent with the improvement in CO, propylene and dodecane conversion observed which will be discussed shortly. NO oxidation at low temperature associated with homogeneous diethyl ether oxidation was not observed as it was readily oxidized on the catalyst surface. Only the higher temperature NO_2 formation feature was apparent, with and without diethyl ether, originating primarily from homogeneous oxidation of the dodecane, not the diethyl ether.

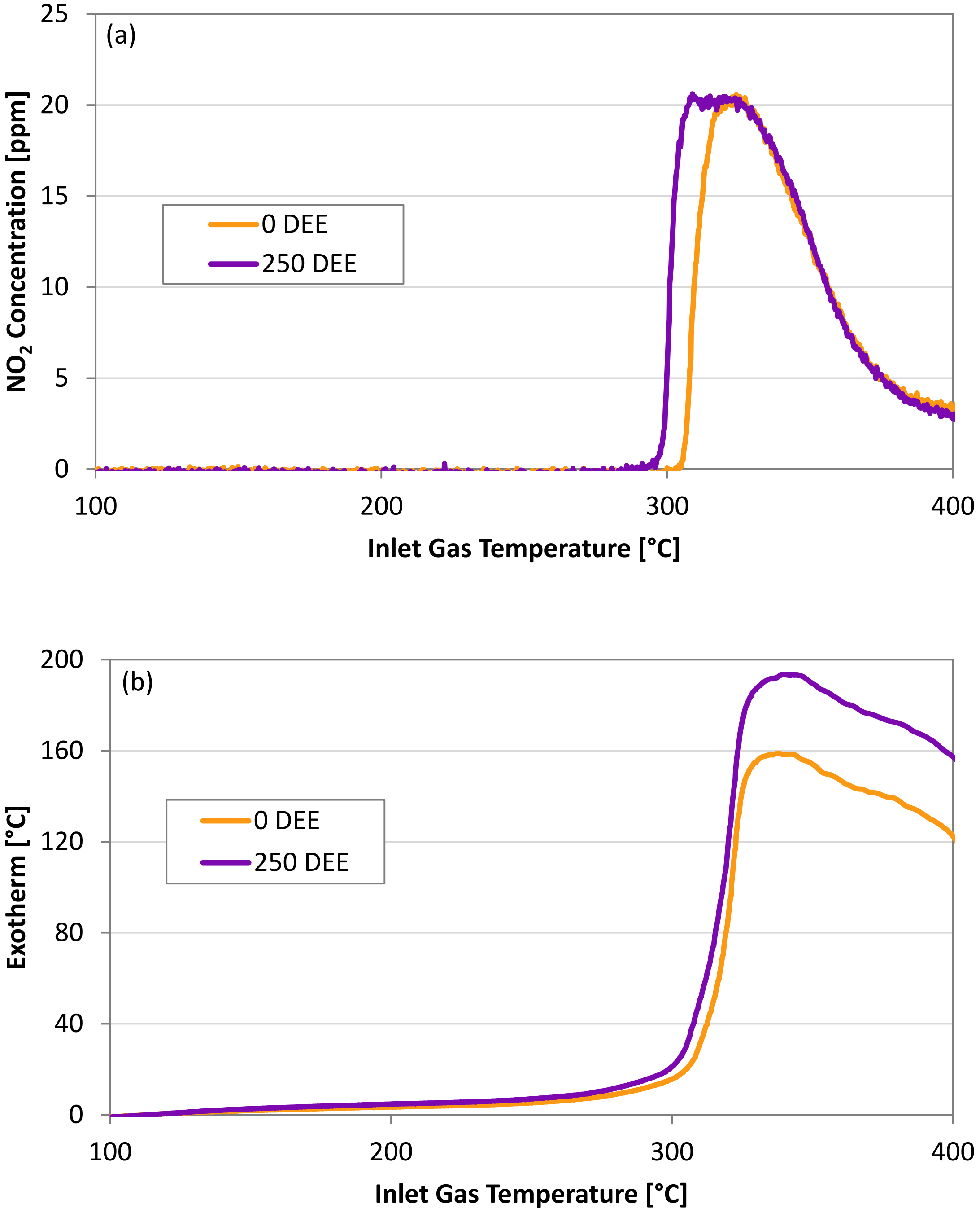

Figure 7-11 (a) NO_2 formation and (b) catalyst exotherm effect of DEE over the Pt/Al_2O_3 catalyst. 3000 ppm CO, 1500 ppm C_3H_6, 250 ppm $C_{12}H_{26}$, 0/250 ppm $(C_2H_5)_2O$, 25 ppm NO, 5% CO_2, 5% H_2O, and 10% O_2 in balance N_2.

NO_2 formation occurred when most of the CO and C_3H_6 were oxidized and therefore not available to reduce the NO_2 back to NO. For the Pt catalyst, based on T_{50} values, the diethyl ether oxidation T_{50} increased as propylene, CO, and dodecane were consecutively added to the reaction mixture. For Pt, like the Pt:Pd catalyst, adding DEE to the reaction mixture did not have a significant effect on T_{50}, nor does it have much effect on the light-off curve slope. CO, C_3H_6 and $C_{12}H_{26}$ conversions with and without diethyl ether added are shown in Figure 7-12 (a)-(c), demonstrating no impact of diethyl ether addition on their conversions and slopes.

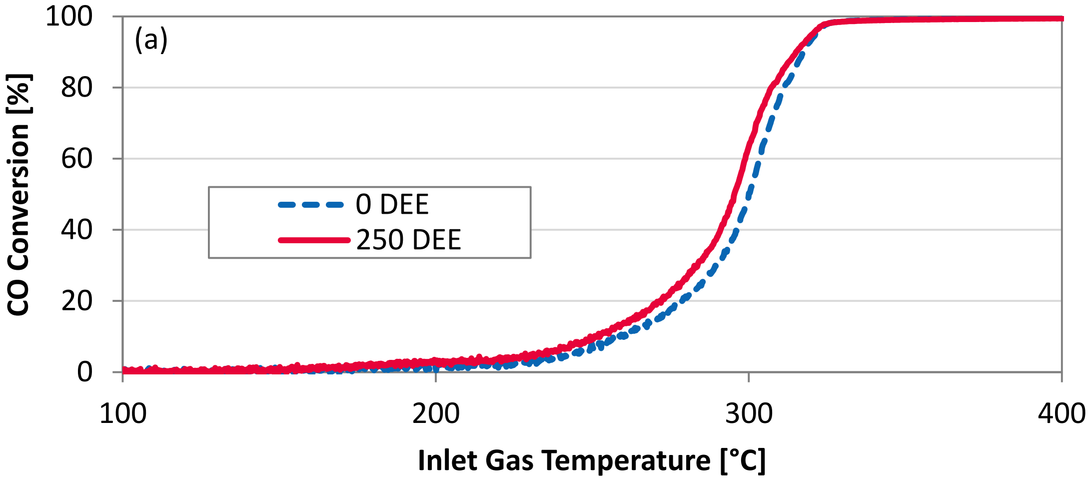

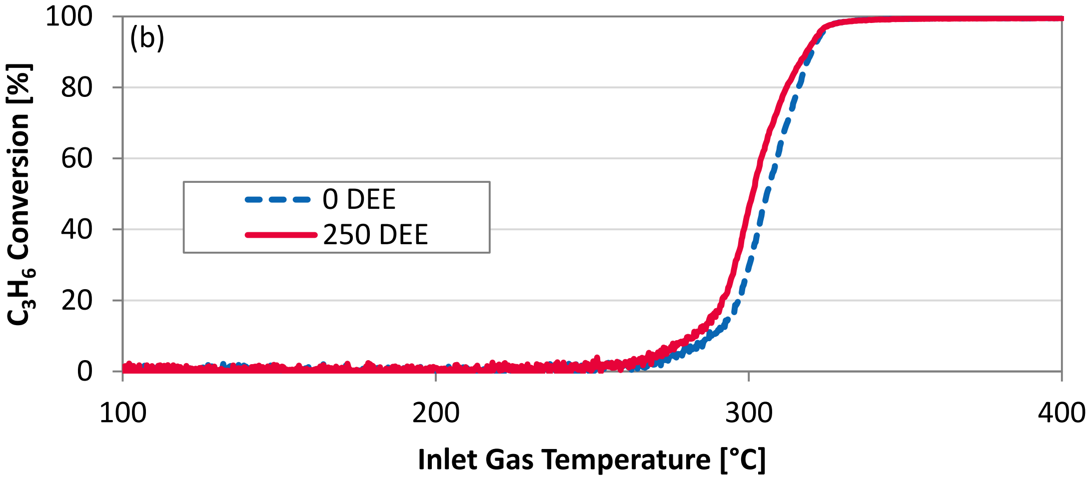

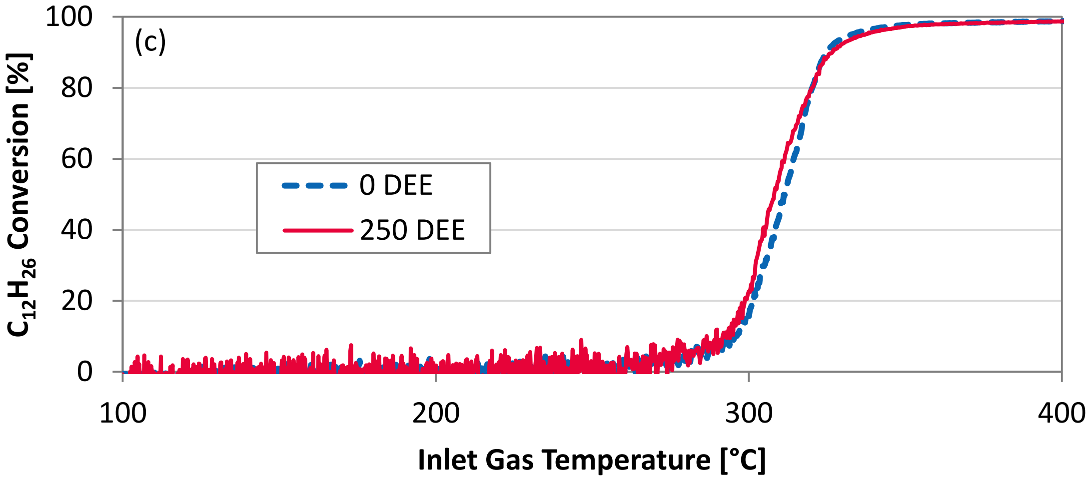

Figure 7-12 (a) CO, (b) C_3H_6 and (c) $C_{12}H_{26}$ oxidation conversion effect of DEE over Pt/Al_2O_3 catalyst. 3000 ppm CO, 1500 ppm C_3H_6, 250 ppm $C_{12}H_{26}$, 0/250 ppm $(C_2H_5)_2O$, 25 ppm NO, 5% CO_2, 5% H_2O, and 10% O_2 in balance N_2.

Diethyl ether oxidation conversion results are shown in Figure 7-13 (a). Note that both catalysts start oxidizing diethyl ether at temperatures below that observed in the quartz tube alone.

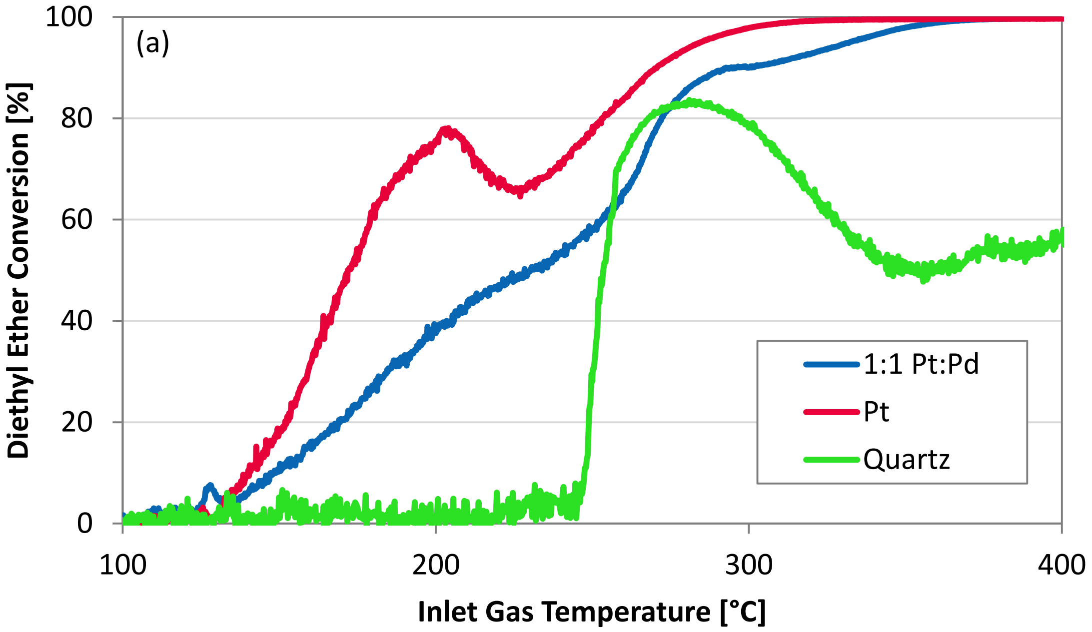

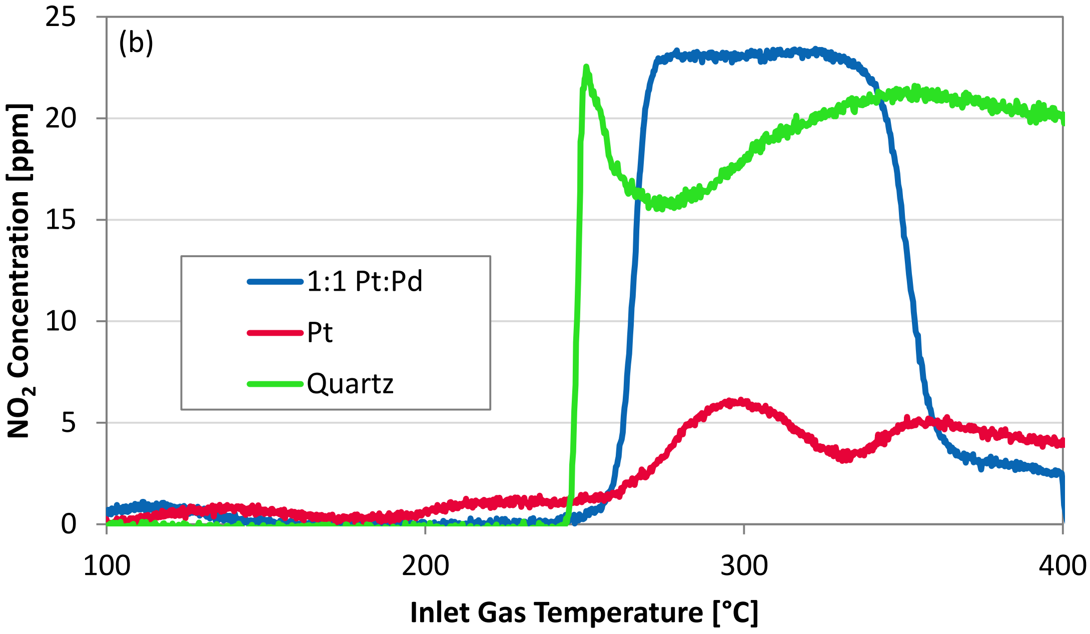

Figure 7-13 Diethyl ether oxidation in an empty quartz tube reactor, over the Pt/Al_2O_3, or over the 1:1 Pt:Pd/Al_2O_3 catalysts; (a) DEE conversion and (b) NO_2 formation. 250 ppm $(C_2H_5)_2O$, 25 ppm NO, 5% CO_2, 5% H_2O, and 10% O_2 in balance N_2.

Diethyl ether was oxidized with 80% conversion on the Pt/Al_2O_3 catalyst, at temperatures below 250°C where CO and propylene oxidation reactions also began to oxidize under the complex mixture conditions. Once CO oxidation lit off, the diethyl ether oxidized on the catalyst, resulting in less DEE to participate in the gas-phase reaction that leads to NO_2 formation. So not only is the Pt/Al_2O_3 able to reduce any NO_2 formed via the gas-phase reactions, but less of the gas-phase reactions will occur because some or all of the diethyl ether will be oxidized on the catalyst rather than in the gas-phase. Over the 1:1 Pt:Pd/Al_2O_3 catalyst, there was slightly less diethyl ether conversion compared to the Pt/Al_2O_3 sample, but the light off temperature was more similar to that of the CO and propylene oxidation reactions. This results in a window where gas-phase diethyl ether oxidation can occur leading to NO_2 formation before the onset of catalyzed diethyl ether oxidation. There was a peak in diethyl ether conversion at 204°C with the Pt/Al_2O_3 catalyst, the decrease in conversion was likely caused by diethyl ether partial oxidation intermediate inhibition, namely CO and ethylene. As Pt/Al_2O_3 is more strongly inhibited by CO compared to the bimetallic [6], this peak was observed while with the 1:1 Pt:Pd/Al_2O_3 sample only a slight inflection was observed.

The outlet NO_2 concentration results for these conditions are shown in Figure 7-13 (b). The lowest temperature where NO_2 formation occurs is in the absence of a catalyst. This implies that the diethyl ether, or the partial oxidation products thereof, react with NO_2 on the catalyst surface, particularly the Pt/Al_2O_3, as previously discussed. At temperatures above 268°C, the 1:1 Pt:Pd catalyst led to higher levels of NO_2 formation in comparison to the empty reactor test at the higher temperatures, which may be due to the catalyst reacting with excess OH that would react with NO_2 in the gas-phase to form nitric acid.

Total NO_X conversion was calculated based off of NO, NO_2, and N_2O from the equation 6-1, the results are presented in Figure 7-14. NO_X reduction in the gas phase during these conditions exceed any NO_X reduction observed during catalyst testing. Interaction between the hydrocarbons oxidation products and the nitric acid lead to difficulty, however qualitatively speaking from measuring the nitric acid concentration the majority of the NO_X reduction in the quartz tube below 350°C is due to nitric acid formation and the NO_X reduction above this temperature may be more so to N_2. Similarly for the NO_X reduction over the catalyst this is likely due to the formation of nitric acid and may not represent NO_X reduction to nitrogen.

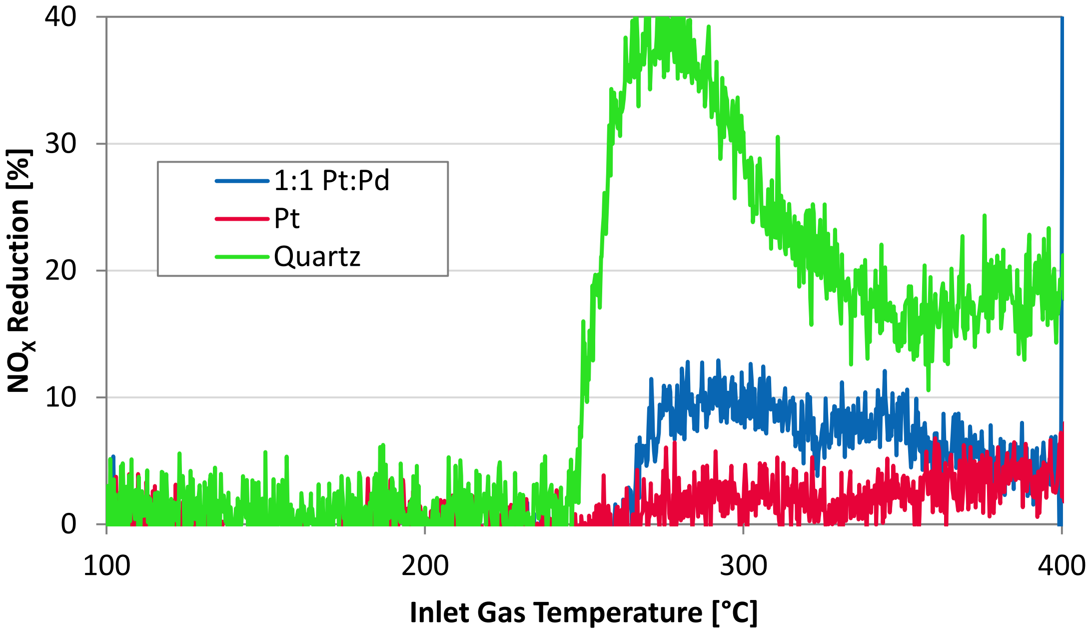

Figure 7-14 NO_X reduction during diethyl ether oxidation in an empty quartz tube reactor, over the Pt/Al_2O_3, or over the 1:1 $Pt:Pd/Al_2O_3$ catalysts. 250 ppm $(C_2H_5)_2O$, 25 ppm NO, 5% CO_2, 5% H_2O, and 10% O_2 in balance N_2.

Of the hydrocarbons examined, DEE appeared to be the better option in terms of promoting NO oxidation and not inhibiting other reactions. Prior to application some analysis of the cumulative CO_2 emissions due to addition of DEE would be needed, comparing its ability to generate NO_2 for improved DPF performance versus that of the fuel used in high temperature regeneration. In terms of tailpipe emissions, even though DEE does not reach 100% conversion over the 1:1 Pt:Pd catalyst until 350°C, the added DEE emitted is not expected to be a significant contributor. Since diethyl ether is a common cold start additive and has been proposed as an alternative fuel, its environmental impact has been investigated [163]. The air quality impacts of diethyl ether requires further study, in ambient atmosphere it is estimated to be stable for 19 hours [164]. Environmental impacts of the chemically similar dimethyl ether have also been studied and it was found to have 0.1x the global warming potential of CO_2 [158]. Though clearly further study into diethyl ethers' environmental impacts needs to be conducted, the available information is promising and warrants further investigation.

7.4 Conclusions

With high hydrocarbon and low NO_X concentrations, i.e. those encountered under LTC exhaust conditions, homogeneous hydrocarbon oxidation reactions can occur within the monolith channels. Therefore it can no longer be assumed that reactions are only occurring on the catalyst surface. With low levels of NO present, homogeneous hydrocarbon oxidation began at inlet gas temperatures as low as 300°C, depending on the hydrocarbon. With a catalyst present, large exotherms can evolve during CO and hydrocarbon oxidation, providing temperatures within the DOC that are more than sufficient for homogeneous hydrocarbon oxidation at gas inlet temperatures near 200°C. For example, using NO_2 formation as an indicator, homogeneous oxidation reactions were observed to take place within a 1:1 Pt:Pd/Al_2O_3 catalyst at inlet gas temperatures as low as 205°C. Since RCCI exhaust temperatures average around 200°C, this suggests that homogeneous hydrocarbon and NO oxidation can occur readily over the DOC due to the large catalyst exotherm. Partial oxidation products and NO_2 formation from these homogeneous oxidation reactions may impact DOC performance and the downstream DPF and SCR catalysts, and hence these reactions may need to be considered when testing and modeling catalysts under RCCI exhaust conditions with high hydrocarbon and low NO concentrations.

In exploring the possibility of adding a hydrocarbon to induce high NO oxidation conversions, diethyl ether provided low temperature NO oxidation performance. Data suggest a Pt-only DOC would not be recommended for such a case as any NO_2 formed in the gas-phase was immediately reduced on the catalyst surface by the CO and small alkenes. The results using the 1:1 Pt:Pd/Al_2O_3 catalyst were more favorable as there was a significant NO_2 yield. This addition of diethyl ether did not impact the conversion of the other exhaust species examined, and therefore seems a benign way to achieve a higher NO_2/NO ratio.

Chapter 8 Conclusions

The central theme of this dissertation is to study the CO and hydrocarbon oxidation performance characteristics of bimetallic Pt-Pd/Al_2O_3 catalysts in high CO and hydrocarbon concentrations representative of RCCI exhaust, and with this understanding to guide DOC performance optimization in the context of the DOE 150°C Challenge. The following are the main findings from this study.

8.1 Kinetic and Mechanistic Study of CO and Propylene Oxidation on Bimetallic Catalysts

8.1.1 Effect of Pt:Pd ratio

The effect of changing the Pt:Pd molar ratio in Pt-Pd/Al_2O_3 catalysts was investigated for high CO and propylene concentrations. For CO oxidation, the bimetallic catalysts with a higher Pd content led to lower temperature CO oxidation activity. From the DRIFTS results, this low temperature activity was related to how the CO bound to the bimetallic surface. CO-M-O species, M being the metal, were observed and were correlated to the most active bimetallic samples. For the Pt catalyst, CO-M-CO was observed which demonstrates high CO poisoning. On the other hand for the Pd-rich catalyst, carbonate formation appears to cause inhibition and deactivation.

For propylene oxidation there was evidence of partial oxidation product inhibition, due to at least acetone, ethylene, and CO, all observed as surface species/byproducts. On the Pd-rich catalysts, these partial oxidation products accumulate at an increased rate which coincides with poorer performance. The data suggests there may be a shift between indirect oxidation on Pt towards direct oxidation on Pd being favored as a function of Pt:Pd ratio. For the 1:1 and 3:1 Pt:Pd catalysts, both mechanisms seem to occur in parallel and a higher surface oxygen availability led to a low temperature light off than the monometallic catalysts where the surface oxygen may limit performance.

During co-oxidation of CO and propylene, the performance trends mirror those of CO oxidation by itself. The CO-M-O species was less favored, and more bridged, singly adsorbed carbonyl, and dicarbonyl were more favored. This suggests less available surface oxygen when propylene is in the reaction mixture. Higher CO poisoning on the Pt sample when propylene was in the reaction mixture was observed. During co-oxidation, deactivation of the Pd-rich catalyst becomes very drastic due to carbonate from CO oxidation as well as propylene partial oxidation products.

8.1.2 Effect of Water

The impact of adding water to the reaction and pretreatment conditions was investigated for Pd, Pt and Pt-Pd/Al_2O_3 catalysts under simulated RCCI exhaust. When water was in the reaction mixture low temperature light-off over the Pd catalyst was observed, whereas water inhibited CO oxidation. On the Pt-Pd catalyst, water helped at high temperatures and had little impact at low temperatures. The DRIFTS results showed that more CO adsorption occurred over the Pd and Pt-Pd catalysts when water was in the reaction, and less occurred over the Pt catalyst.

The DRIFTS results provided some mechanistic insights into these changes, water is important to have in the reaction mixture for the Pd and Pt-Pd catalysts as bicarbonate and carboxyl will accumulate on the surface without water. For Pt, CO desorption was rate controlling when water was present in the reaction; water appears to inhibit CO oxidation by competitive adsorption. On the Pt-Pd catalyst, carboxylate was observed as an intermediate which was not observed on either monometallic catalyst. Also the Pt-Pd catalyst showed the least accumulation of COH. The Pt-Pd catalyst has intermediate light-off performance compared to each monometallic catalyst, unlike the previous study without water. Also different surface species were observed. This could be related to the differences in particle sizes; the catalysts were severely aged during the water study but they were not aged for the other study. This may suggest changes in surface species as a function of particle sizes.

For propylene oxidation, the reaction mechanism did not appear to vary from the previous study. Adding water into the reaction mixture had trivial effects on the partial oxidation product distributions; slightly more CO is produced over the Pd and Pt-Pd catalysts when water was in the reaction mixture and slightly less is produced over the Pt catalyst. The water did effect the light-off performance. On the Pd catalyst, when water was in the reaction propylene light-off was inhibited, while water promoted propylene light-off on the Pt catalyst. For the Pt-Pd catalyst, very slight inhibition by water in the reaction and pretreatment was observed, showing intermediate performance between the monometallic catalysts. This is not surprising, in a previous study on a Pt/Al_2O_3 catalyst, the dispersion of the catalyst had a large effect on the turnover frequency for CO oxidation but had no effect on C_3H_6 oxidation [165]. This could indicate a shift in how CO adsorbs to these surfaces happens with varying particle sizes may lead to different CO oxidation performance.

8.2 Spatially Resolved Reactions in DOC for RCCI Exhaust

Spaci-FTIR experiments were conducted to investigate the reaction zones along a DOC under simulated RCCI exhaust conditions. Strong CO inhibition was observed for both NO and C_3H_6 oxidation. The high concentrations of CO led to 70% NO_X reduction at CO light off. The NO_X reduction at propylene light off was less significant, only 40% NO_X reduction occurred. When both CO and propylene are present in the feed, the NO_X reduction mirrors what was observed with propylene oxidation; inferring adsorption of propylene on the catalyst surface blocks NO_X reduction by CO.

There were two inflections in CO conversion versus temperature when propylene was part of the feed mixture, showing inhibition “steps”. Only one step was noticed when NO_X was included in the reaction feed. From DRIFTS it was shown that ethylene and formaldehyde intermediates may be causing the first step, while acetate may cause the second step. In the presence of NO_X, the reaction of NO_X and acetate may result in there only one step being observed, because ethylene does not easily react with NO_X species. Overall, these results also show that CO needs to oxidize first, then propylene can oxidize, then NO can oxidize, showing an axial sequence in reactions.

8.3 Coupled Homogeneous and Heterogeneous Hydrocarbon Oxidation

More complex hydrocarbon testing under RCCI conditions was investigated, and it was observed that using larger chain alkanes in these low NO_X concentrations led to homogeneous oxidation of the hydrocarbons and impressive NO oxidation. The hydrocarbons were found to oxidize homogeneously over the DOC at temperatures relevant for RCCI exhaust, 200°C. This has some implications for the future of testing these exhaust conditions, as the exotherm over the catalyst is very high. This may involve careful design of experiments in order to make sure these homogeneous reactions aren't taking place upstream or downstream of the catalyst in order to make sure the catalyst itself is being evaluated, however the homogeneous hydrocarbon oxidation within the DOC intrinsically cannot be eliminated. This may cause even further difficulties in deriving kinetic parameters over catalysts, and relating bench scale reactor experiments to commercial emissions.

The possibility of injecting a hydrocarbon that will homogeneously oxidize at even lower temperatures was explored. Diethyl ether was found as a possible candidate for injection in order to get NO oxidation to occur. The commercial value of this will need to be further evaluated, however it gave promising results over a Pt-Pd/Al_2O_3 catalyst. Not only did the homogeneous oxidation of diethyl ether lead to NO oxidation, the light-off of the other exhaust components were not negatively affected.

8.4 Recommendations for future work

In terms of the Pt:Pd ratios, differences in surface species of CO as a function of particle size was observed which may warrant further study. As discussed, the CO adsorbs on the metal sites as carbonyls in various configurations as follows: singly adsorbed linear carbonyls, doubly adsorbed carbonyls, doubly bridged carbonyls and triply bridged carbonyls. Through careful experimentation, observing these species for different Pt:Pd ratio catalysts and sequential aging stages could elucidate the surface segregation as a function of aging temperatures and particle size. This work would be more academic in nature than the rest of the recommendations, as catalyst sintering in automotive catalysis is ubiquitous. Actually in RCCI exhaust catalyst sintering may be even more of an issue due to large hydrocarbon concentrations generating large catalyst exotherms, and so controlling the metal particle sizes in aftertreatment catalysts is nontrivial. However, observing the adsorbed species of CO as a function of particle size may explain the observed differences between the packed bed and monolith studies. At the small particle size (Chapter 4), the bimetallic catalysts gave clearly superior light-off performance when compared to the Pd catalyst. For the larger particle sizes (Chapter 5) the Pd and Pt-Pd CO light-off performance was very comparable and the Pd catalyst was actually slightly better. This is likely to be related to the surface segregation of Pd as the particle size increases. Specifically, in the water study the CO-M-O species related to the high bimetallic CO oxidation activity was not observed and thus may explain why the bimetallic catalyst in that study does not show enhanced activity.

Future work should consider axially zoning the DOC catalysts, in terms of Pt:Pd ratio. From the spatially resolved experiments, the sequential reaction zones of CO oxidation, hydrocarbon oxidation, and NO oxidation may encourage a catalyst that has a high Pd content at the front and a high Pt content at the back. The production of acetone on the Pd-containing catalysts may suggest other oxygenated hydrocarbons, ketones specifically, may be produced in real exhaust conditions over Pd catalysts. Also the production of aldehydes during the observed homogeneous oxidation reactions is concerning. Ketones and aldehydes have toxic effects on human health, and these chemicals also have an effect on environmental ozone. This implies that it may be important for the back of the catalyst to be monometallic Pt to limit the amount of ketone and aldehyde formation, not just to promote NO oxidation. On the other hand, from the perspective of the homogeneous hydrocarbon oxidation leading to enhanced NO_2 production over the Pd-containing catalysts but not the Pt catalyst, it may also be beneficial for the back of the DOC to be bimetallic so that the DPF has more NO_2 for soot oxidation. Considering the formulation of the DPF generally contains Pt as well, perhaps the Pt on the DPF could be used to oxidize the ketones and aldehydes as well.

The added complication in simulated RCCI exhaust with large hydrocarbons leading to homogeneous reactions may require further study; in general experimental design will have to be considered for typical bench scale reactor experiments. Specifically for Spaci experiments, how the change in flow patterns inside the catalyst channel as well as inside the capillary will affect homogenous hydrocarbon reactions may need to be investigated before any results from such studies can be trusted. For instance, if the capillary collects the gases from the front of the catalyst, and the gases continue flowing through hot zones of the reactor before making it to the gas analyzer, gas-phase reactions could occur in the hot spots and distort the real concentration profiles. For RCCI exhaust then if the higher hydrocarbons such as dodecane want to be tested, a probe that is inserted at the front of the reactor may need to be used instead.

References

[1] M. Zammit, C. Dimaggio, C. Kim, C. Lambert, G. Muntean, C. Peden, J. Parks, and K. Howden, “Future Automotive Aftertreatment Solutions : The 150 ° C Challenge Workshop Report,” 2012.

[2] “Light-Duty Vehicle, Light-Duty Truck, and Medium-Duty Passenger Vehicle: Tier 2 Exhaust Emission Standards and Implementation Schedule,” 2016.

[3] V. Y. Prikhodko, S. J. Curran, T. L. Barone, S. A. Lewis, J. M. Storey, K. Cho, R. M. Wagner, and J. E. Parks, “Diesel oxidation catalyst control of hydrocarbon aerosols from reactivity controlled compression ignition combustion,” in *American Society of Mechanical Engineers International Mechanical Engineering Conference and Exposition*, 2011, pp. 273–278.

[4] V. Y. Prikhodko, S. J. Curran, J. E. Parks, and R. M. Wagner, “Effectiveness of diesel oxidation catalyst in reducing HC and CO emissions from reactivity controlled compression ignition,” *SAE Int. J. Fuels Lubr.*, vol. 6, no. 2, pp. 329–335, 2013.

[5] M. Skoglundh, L. O. Löwendahl, and J. Ottersted, “Combinations of platinum and palladium on alumina supports as oxidation catalysts,” *Appl. Catal.*, vol. 77, no. 1, pp. 9–20, 1991.

[6] B. M. Shakya, B. Sukumar, Y. M. López-De Jesús, and P. Markatou, “The Effect of Pt:Pd Ratio on Heavy-Duty Diesel Oxidation Catalyst Performance: An Experimental and Modeling Study,” *SAE Int. J. Engines*, vol. 8, no. 3, pp. 1271–1282, Apr. 2015.

[7] M. Chen and L. D. Schmidt, “Morphology and Composition of Pt-Pd Alloy

Crystallites on SiO2 in Reactive Atmospheres," *J. Catal.*, vol. 56, no. 2, pp. 198–218, 1979.

[8] A. Russell and W. S. Epling, "Diesel Oxidation Catalysts," *Catal. Rev.*, vol. 53, no. 4, pp. 337–423, 2011.

[9] T. Rades, C. Pak, M. Polisset-Thfoin, R. Ryoo, and J. Fraissard, "Characterization of bimetallic NaY-supported Pt-Pd catalyst by EXAFS, TEM and TPR," *Catal. Letters*, vol. 29, no. 1–2, pp. 91–103, 1994.

[10] T. Rades, V. Y. Borovkov, V. B. Kazansky, M. Polisset-Thfoin, and J. Fraissard, "Diffuse Reflectance IR Study of CO Adsorption on a Bimetallic Pt - Pd Catalyst Supported on NaY Zeolite. Evidence of Alloy Formation," *J. Phys. Chem. Ref. Data*, vol. 40, no. 100, pp. 16238–16241, 1996.

[11] A. Morlang, U. Neuhausen, K. V. Klementiev, F.-W. Schütze, G. Miehe, H. Fuess, and E. S. Lox, "Bimetallic Pt/Pd diesel oxidation catalysts," *Appl. Catal. B Environ.*, vol. 60, no. 3–4, pp. 191–199, Oct. 2005.

[12] Y. Yu, B. Fonfé, A. Jentys, G. L. Haller, J. a. R. van Veen, O. Y. Gutiérrez, and J. a. Lercher, "Bimetallic Pt–Pd/silica–alumina hydrotreating catalysts – Part I: Physicochemical characterization," *J. Catal.*, vol. 292, pp. 1–12, Aug. 2012.

[13] P. L. Hansen, A. M. Molenbroek, and A. V Ruban, "Alloy Formation and Surface Segregation in Zeolite-Supported Pt-Pd Bimetallic Catalysts," *J. Phys. Chem. B*, vol. 101, no. 10, pp. 1861–1868, 1997.

[14] T. Fujikawa, K. Tsuji, H. Mizuguchi, H. Godo, K. Idei, and K. Usui, "EXAFS characterization of bimetallic Pt – Pd / SiO 2 – Al 2 O 3 catalysts for hydrogenation

of aromatics in diesel fuel," *Catal. Letters*, vol. 63, no. 1–2, pp. 27–33, 1999.

[15] J. Rousset, A. J. Renouprez, and A. M. Cadrot, "Ion-scattering study and Monte Carlo simulations of surface segregation in Pd-Pt nanoclusters obtained by laser vaporization of bulk alloys," *Phys. Rev. B*, vol. 58, no. 4, pp. 2150–2156, Jul. 1998.

[16] L. C. A. van den Oetelaar, O. W. Nooij, S. Oerlemans, A. W. Denier Van Der Gon, and H. H. Brongersma, "Surface Segregation in Supported Pd-Pt Nanoclusters and Alloys," *J. Phys. Chem. B*, vol. 102, no. 18, pp. 3445–3455, 1998.

[17] T. R. Johns, J. R. Gaudet, E. J. Peterson, J. T. Miller, E. A. Stach, C. H. Kim, M. P. Balogh, and A. K. Datye, "Microstructure of Bimetallic Pt-Pd Catalysts under Oxidizing Conditions," *ChemCatChem*, vol. 5, no. 9, pp. 2636–2645, Sep. 2013.

[18] C. M. Grill, M. L. Mclaughlin, J. M. Stevenson, and D. Richard, "Characterization of Supported Using Infrared Spectroscopy Bimetallic Clusters," *J. Catal.*, vol. 69, pp. 454–464, 1981.

[19] J. C. Summers and L. L. Hegedus, "Effects of Platinum and Palladium Impregnation on the Performance and Durability of Automobile Exhaust Oxidizing Catalysts," *J. Catal.*, vol. 51, no. 2, pp. 185–192, 1978.

[20] M. Kaneeda, H. Iizuka, T. Hiratsuka, N. Shinotsuka, and M. Arai, "Improvement of thermal stability of NO oxidation Pt/Al2O3 catalyst by addition of Pd," *Appl. Catal. B Environ.*, vol. 90, no. 3–4, pp. 564–569, Aug. 2009.

[21] A. T. Delariva, T. W. Hansen, S. R. Challa, and A. K. Datye, "In situ transmission electron microscopy of catalyst sintering," *J. Catal.*, vol. 308, pp. 291–305, 2013.

[22] C. Carrillo, T. R. Johns, H. Xiong, A. DeLaRiva, S. R. Challa, R. S. Goeke, K.

Artyushkova, W. Li, C. H. Kim, and A. K. Datye, “Trapping of Mobile Pt Species by PdO Nanoparticles under Oxidizing Conditions,” *J. Phys. Chem. Lett.*, vol. 5, no. 12, pp. 2089–2093, Jun. 2014.

[23] R. J. Farrauto, J. K. Lampert, M. C. Hobson, and E. Waterman M., “Thermal decomposition and reformation of PdO catalysis; support effects,” *Appl. Catal. B Environ.*, vol. 6, no. 95, pp. 263–270, 1995.

[24] H.-R. Cho and J. R. Regalbuto, “The rational synthesis of Pt-Pd bimetallic catalysts by electrostatic adsorption,” *Catal. Today*, vol. 246, pp. 143–153, May 2015.

[25] A. P. Wong, E. A. Kyriakidou, T. J. Toops, and J. R. Regalbuto, “The catalytic behavior of precisely synthesized Pt-Pd bimetallic catalysts for use as diesel oxidation catalysts,” *Catal. Today*, vol. 267, pp. 145–156, 2016.

[26] J. R. Gaudet, A. de la Riva, E. J. Peterson, T. Bolin, and A. K. Datye, “Improved Low-Temperature CO Oxidation Performance of Pd Supported on La-Stabilized Alumina,” *ACS Catal.*, vol. 3, no. 5, pp. 846–855, May 2013.

[27] E. J. Peterson, A. T. DeLaRiva, S. Lin, R. S. Johnson, H. Guo, J. T. Miller, J. Hun Kwak, C. H. F. Peden, B. Kiefer, L. F. Allard, F. H. Ribeiro, and A. K. Datye, “Low-temperature carbon monoxide oxidation catalysed by regenerable atomically dispersed palladium on alumina.,” *Nat. Commun.*, vol. 5, p. 4885, 2014.

[28] C.-H. Lee and Y.-W. Chen, “Effect of Basic Additives on Pt/Al2O3 for CO and Propylene Oxidation under Oxygen-Deficient Conditions,” *Ind. Eng. Chem. Res.*, vol. 36, no. 5, pp. 1498–1506, 1997.

[29] K. Zorn, S. Giorgio, E. Halwax, C. R. Henry, H. Grönbeck, and G. Rupprechter, “CO

Oxidation on Technological Pd - Al 2 O 3 Catalysts : Oxidation State and Activity," *J. Phys. Chem. C*, vol. 115, no. 4, pp. 1103–1111, 2011.

[30] A. K. Datye, J. Bravo, T. R. Nelson, P. Atanasova, M. Lyubovsky, and L. Pfefferle, "Catalyst microstructure and methane oxidation reactivity during the Pd↔PdO transformation on alumina supports," *Appl. Catal. A Gen.*, vol. 198, no. 1–2, pp. 179–196, 2000.

[31] G. Lapisardi, L. Urfels, P. Gélin, M. Primet, A. Kaddouri, E. Garbowski, S. Toppi, and E. Tena, "Superior catalytic behaviour of Pt-doped Pd catalysts in the complete oxidation of methane at low temperature," *Catal. Today*, vol. 117, no. 4, pp. 564–568, 2006.

[32] C. Berthomieu and R. Hienerwadel, "Fourier transform infrared (FTIR) spectroscopy.," *Photosynth. Res.*, vol. 101, no. 2–3, pp. 157–70, 2009.

[33] J. W. Cable and R. K. Sheline, "Bond Hybridization And Structure In The Metal Carbonyls," *Chem. Rev.*, vol. 56, no. 1, pp. 1–26, 1956.

[34] M. Primet, J. M. Basset, M. V. Mathieu, and M. Prettre, "Infrared Study of CO Adsorbed on Pt/Al2O3. A method for determining metal-adsorbate interactions," *J. Catal.*, vol. 29, pp. 213–223, 1973.

[35] A. A. Davydov, *Infrared Spectroscopy of Adsorbed Species on the Surfaces of Transition Metal Oxides*. Chichester: John Wiley & Sons, 1990.

[36] A. D. Allian, K. Takanabe, K. L. Fujdala, X. Hao, T. J. Truex, J. Cai, C. Buda, M. Neurock, and E. Iglesia, "Chemisorption of CO and mechanism of CO oxidation on supported platinum nanoclusters," *J. Am. Chem. Soc.*, vol. 133, no. 12, pp. 4498–

4517, 2011.

[37] G. Djéga-Mariadassou and M. Boudart, “Classical kinetics of catalytic reactions,” *J. Catal.*, vol. 216, no. 1–2, pp. 89–97, 2003.

[38] L. Árnadóttir, E. M. Stuve, and H. Jónsson, “The effect of coadsorbed water on the stability, configuration and interconversion of formyl (HCO) and hydroxymethylidyne (COH) on platinum (111),” *Chem. Phys. Lett.*, vol. 541, pp. 32–38, Jul. 2012.

[39] F. Zaera and D. Chrysostomou, “Propylene on Pt (111) I . Characterization of surface species by infra-red spectroscopy,” *Surf. Sci.*, vol. 457, no. 1–2, pp. 71–88, 2000.

[40] A. M. Gabelnick, “Catalytic Oxidation of C3 Hydrocarbons: In Situ Mechanistic Studies on Platinum and Supported Platinum Surfaces,” The University of Michigan, 2000.

[41] R. M. Rioux, J. D. Hoefelmeyer, M. Grass, H. Song, K. Niesz, P. Yang, and G. A. Somorjai, “Adsorption and Co-adsorption of Ethylene and Carbon Monoxide on Silica-Supported Monodisperse Pt Nanoparticles : Volumetric Adsorption and Infrared Spectroscopy Studies,” *Langmuir*, vol. 24, no. 1, pp. 198–207, 2008.

[42] M. A. Vannice, W. Erley, and H. Ibach, “A RAIRS and HREELS study of acetone on Pt(111),” *Surf. Sci.*, vol. 254, pp. 1–11, 1991.

[43] N. R. Avery, “EELS identification of the adsorbed species from acetone adsorption on Pt(111),” *Surf. Sci.*, vol. 125, no. 3, pp. 771–789, 1983.

[44] O. Shakir, A. Yezerets, N. W. Currier, and W. S. Epling, “Spatially resolving

concentration and temperature gradients during the oxidation of propylene on Pt/Al2O3,” *Appl. Catal. A Gen.*, vol. 365, no. 2, pp. 301–308, Aug. 2009.

[45] K. Irani, W. S. Epling, and R. Blint, “Spatial Resolution of Reactant Species Consumption in Diesel Oxidation Catalysts,” *Top. Catal.*, vol. 52, no. 13–20, pp. 1856–1859, Jul. 2009.

[46] J.-Y. Luo, X. Hou, P. Wijayakoon, S. J. Schmieg, W. Li, and W. S. Epling, “Spatially resolving SCR reactions over a Fe/zeolite catalyst,” *Appl. Catal. B Environ.*, vol. 102, no. 1–2, pp. 110–119, Feb. 2011.

[47] M. Hettel, C. Diehm, B. Torkashvand, and O. Deutschmann, “Critical evaluation of in situ probe techniques for catalytic honeycomb monoliths,” *Catal. Today*, vol. 216, pp. 2–10, 2013.

[48] J. Sá, D. L. A. Fernandes, F. Aiouache, A. Goguet, C. Hardacre, D. Lundie, W. Naeem, W. P. Partridge, and C. Stere, “SpaciMS: spatial and temporal operando resolution of reactions within catalytic monoliths.,” *Analyst*, vol. 135, no. 9, pp. 2260–2272, 2010.

[49] W. P. Partridge, J. M. Storey, S. A. Lewis, R. W. Smithwick, G. L. DeVault, M. J. Cunningham, N. W. Currier, and T. M. Yonushonis, “Time-Resolved Measurements of Emission Transients By Mass Spectrometry,” *SAE Tech. Pap.*, no. 2000–01–2952, 2000.

[50] B. West, S. Huff, J. Parks, S. Lewis, J.-S. Choi, W. Partridge, and J. Storey, “Assessing reductant chemistry during in-cylinder regeneration of diesel lean NOx traps,” *SAE Tech. Pap.*, no. 2004–01–30, 2004.

[51] J. S. Choi, W. P. Partridge, and C. S. Daw, "Spatially resolved in situ measurements of transient species breakthrough during cyclic, low-temperature regeneration of a monolithic Pt/K/Al 2O3 NOx storage-reduction catalyst," *Appl. Catal. A Gen.*, vol. 293, no. 1–2, pp. 24–40, 2005.

[52] J. S. Choi, W. P. Partridge, W. S. Epling, N. W. Currier, and T. M. Yonushonis, "Intra-channel evolution of carbon monoxide and its implication on the regeneration of a monolithic Pt/K/Al2O3 NOx storage-reduction catalyst," *Catal. Today*, vol. 114, no. 1, pp. 102–111, 2006.

[53] J. S. Choi, W. P. Partridge, and C. S. Daw, "Sulfur impact on NOx storage, oxygen storage, and ammonia breakthrough during cyclic lean/rich operation of a commercial lean NOx trap," *Appl. Catal. B Environ.*, vol. 77, no. 1–2, pp. 145–156, 2007.

[54] J. S. Choi, W. P. Partridge, J. A. Pihl, and C. S. Daw, "Sulfur and temperature effects on the spatial distribution of reactions inside a lean NOx trap and resulting changes in global performance," *Catal. Today*, vol. 136, no. 1–2, pp. 173–182, 2008.

[55] W. P. Partridge and J. S. Choi, "NH3 formation and utilization in regeneration of Pt/Ba/Al2O3 NOx storage-reduction catalyst with H2," *Appl. Catal. B Environ.*, vol. 91, no. 1–2, pp. 144–151, 2009.

[56] R. Horn, N. J. Degenstein, K. A. Williams, and L. D. Schmidt, "Spatial and temporal profiles in millisecond partial oxidation processes," *Catal. Letters*, vol. 110, no. 3–4, pp. 169–178, 2006.

[57] A. Donazzi, B. C. Michael, and L. D. Schmidt, “Chemical and geometric effects of Ce and washcoat addition on catalytic partial oxidation of CH4 on Rh probed by spatially resolved measurements,” *J. Catal.*, vol. 260, no. 2, pp. 270–275, 2008.

[58] B. C. Michael, A. Donazzi, and L. D. Schmidt, “Effects of H2O and CO2 addition in catalytic partial oxidation of methane on Rh,” *J. Catal.*, vol. 265, no. 1, pp. 117–129, 2009.

[59] B. C. Michael, D. N. Nare, and L. D. Schmidt, “Catalytic partial oxidation of ethane to ethylene and syngas over Rh and Pt coated monoliths: Spatial profiles of temperature and composition,” *Chem. Eng. Sci.*, vol. 65, no. 12, pp. 3893–3902, 2010.

[60] R. Chakrabarti, J. S. Kruger, R. J. Hermann, S. D. Blass, and L. D. Schmidt, “Spatial profiles in partial oxidation of methane and dimethyl ether in an autothermal reactor over rhodium catalysts,” *Appl. Catal. A Gen.*, vol. 483, pp. 97–102, 2014.

[61] K. Irani, W. S. Epling, and R. Blint, “Effect of hydrocarbon species on no oxidation over diesel oxidation catalysts,” *Appl. Catal. B Environ.*, vol. 92, no. 3–4, pp. 422–428, Nov. 2009.

[62] H. Nguyen, M. P. Harold, and D. Luss, “Spatiotemporal behavior of Pt/Rh/CeO2/BaO catalyst during lean-rich cycling,” *Chem. Eng. J.*, vol. 262, pp. 464–477, 2015.

[63] M. Li, V. G. Easterling, and M. P. Harold, “Spatio-temporal features of the sequential NOx storage and reduction and selective catalytic reduction reactor system,” *Catal. Today*, vol. 267, pp. 177–191, 2016.

[64] Y. Zheng, M. Li, D. Wang, M. P. Harold, and D. Luss, “Rapid propylene pulsing for enhanced low temperature NOx conversion on combined LNT-SCR catalysts,” *Catal. Today*, vol. 267, no. 2, pp. 192–201, 2016.

[65] G. S. Bugosh, V. G. Easterling, I. A. Rusakova, and M. P. Harold, “Anomalous steady-state and spatio-temporal features of methane oxidation on Pt/Pd/Al2O3 monolith spanning lean and rich conditions,” *Appl. Catal. B Environ.*, vol. 165, pp. 68–78, 2015.

[66] J.-Y. Luo, H. Oh, C. Henry, and W. Epling, “Effect of C3H6 on selective catalytic reduction of NOx by NH3 over a Cu/zeolite catalyst: A mechanistic study,” *Appl. Catal. B Environ.*, vol. 123–124, no. 2, pp. 296–305, 2012.

[67] H. Nguyen, P. Y. Peng, D. Luss, and M. P. Harold, “Assessing intrusion by the capillary during spatially resolved mass spectrometry measurement,” *Chem. Eng. J.*, vol. 307, pp. 845–859, 2017.

[68] C. Karakaya and O. Deutschmann, “A simple method for CO chemisorption studies under continuous flow: Adsorption and desorption behavior of Pt/Al2O3 catalysts,” *Appl. Catal. A Gen.*, vol. 445–446, pp. 221–230, Nov. 2012.

[69] J. R. Anderson, *Structure of Metallic Catalysts*. London: Academic Press, 1975.

[70] *Harrick Scientific High Temperature Reaction Chamber User’s Manual*. Pleasantville: Harrick Scientific Products, Inc., 2013.

[71] R. Chen, Z. Chen, B. Ma, X. Hao, N. Kapur, J. Hyun, K. Cho, and B. Shan, “CO adsorption on Pt (111) and Pd (111) surfaces: A first-principles based lattice gas Monte-Carlo study,” *Comput. Theor. Chem.*, vol. 987, pp. 77–83, May 2012.

[72] M. Moses-Debusk, M. Yoon, L. F. Allard, D. R. Mullins, Z. Wu, X. Yang, G. Veith, G. M. Stocks, and C. K. Narula, “CO oxidation on supported single Pt atoms: Experimental and ab initio density functional studies of CO interaction with Pt atom on θ-Al 2O3(010) surface,” *J. Am. Chem. Soc.*, vol. 135, no. 34, pp. 12634–12645, 2013.

[73] M. J. Hazlett and W. S. Epling, “Spatially Resolving CO and C3H6 Oxidation Reactions in a Pt/Al2O3 Model Oxidation Catalyst,” *Catal. Today*, vol. 267, pp. 157–166, 2016.

[74] G. Busca, E. Finocchio, and V. S. Escribano, “Infrared studies of CO oxidation by oxygen and by water over Pt/Al2O3 and Pd/Al2O3 catalysts,” *Appl. Catal. B Environ.*, vol. 113–114, pp. 172–179, Feb. 2012.

[75] C. M. Grill and R. D. Gonzalez, “Infrared Study of the Adsorption of CO and NO on Silica-Supported Pd and Pt-Pd,” *J. Phys. Chem.*, vol. 84, no. 4, pp. 878–882, 1980.

[76] J. T. Yates, T. M. Duncan, S. D. Worley, and R. W. Vaughan, “Infrared spectra of chemisorbed CO on Rh,” *J. Chem. Phys.*, vol. 70, no. 3, pp. 1219–1224, 1979.

[77] J. G. Goodwin and C. Naccache, “CO Adsorption on Ion-Exchanged Ru Zeolite Catalyst,” *J. Catal.*, vol. 64, no. 2, pp. 482–486, 1980.

[78] E. V Benvenutti, L. Franken, and C. C. Moro, “FTIR Study of Hydrogen and Carbon Monoxide Adsorption on Pt / TiO 2 , Pt / ZrO 2 , and Pt / Al 2 O 3,” *Langmuir*, vol. 15, no. 23, pp. 8140–8146, 1999.

[79] M. A. Vannice, C. C. Twu, and S. H. Moon, “SMSI Effects on CO Adsorption and Hydrogenation on Pt Catalysts - I. Infrared Spectra of Adsorbed CO prior to and

during Reaction Conditions," *J. Catal.*, vol. 79, no. 1, pp. 70–80, 1983.

[80] M. Primet, "Electronic transfer and ligand effects in the infrared spectra of adsorbed carbon monoxide," *J. Catal.*, vol. 88, no. 2, pp. 273–282, 1984.

[81] H. Heyne and F. C. Tompkins, "Application of infrared spectroscopy and surface potential measurements in a study of the oxidation of carbon monoxide on platinum," *Proc. R. Soc. A*, vol. 292, no. 1431, pp. 460–478, 1966.

[82] G. Busca, J. Lamotte, J.-C. Lavalley, and V. Lorenzelli, "FT-IR Study of the Adsorption and Transformation of Formaldehyde on Oxide Surfaces," *J. Am. Chem. Soc.*, vol. 109, no. 17, pp. 5197–5202, 1987.

[83] M. I. Zaki, M. A. Hasan, and L. Pasupulety, "Surface Reactions of Acetone on Al2O3, TiO2, ZrO2, and CeO2: IR Spectroscopic Assessment of Impacts of the Surface Acid - Base Properties," *Langmuir*, vol. 17, no. 11, pp. 768–774, 2001.

[84] Y. Zhu, H. Uchida, and M. Watanabe, "Oxidation of Carbon Monoxide at a Platinum Film Electrode Studied by Fourier Transform Infrared Spectroscopy with Attenuated Total Reflection Technique," *Langmuir*, vol. 15, no. 25, pp. 8757–8764, 1999.

[85] K. I. Hadjiivanov and G. N. Vayssilov, "Characterization of oxide surfaces and zeolites by carbon monoxide as an IR probe molecule," *Adv. Catal.*, vol. 47, pp. 307–511, 2002.

[86] M. M. Schubert, H. A. Gasteiger, and R. Jürgen Behm, "Surface Formates as Side Products in the Selective CO Oxidation on Pt / γ -Al 2 O 3," *J. Catal.*, vol. 172, pp. 256–258, 1997.

[87] C. Daniel, M.-O. Clarté, S. P. Teh, O. Thinon, H. Provendier, A. C. Van Veen, B. J. Beccard, Y. Schuurman, and C. Mirodatos, “Spatially resolved catalysis in microstructured reactors by IR spectroscopy : CO oxidation over mono- and bifunctional Pt catalysts,” *J. Catal.*, vol. 272, no. 1, pp. 55–64, 2010.

[88] J. L. Robbins and E. Marucchi-Soos, “Evience for Multiple CO Hydrogenation Pathways on Pt/Al2O3,” *Am. Chem. Soc.*, vol. 2885, no. 8, pp. 2885–2888, 1989.

[89] T. Iwasita and F. C. Nart, “Identification of methanol adsorbates on platinum: An in situ FT-IR investigation,” *Electroanal. Chem.*, vol. 317, pp. 291–298, 1991.

[90] N. Cant and W. K. Hall, “Catalytic oxidation II. Silica supported noble metals for the oxidation of ethylene and propylene,” *J. Catal.*, vol. 16, no. 2, pp. 220–231, 1970.

[91] N. Cant and W. Hall, “Catalytic oxidation. IV. Ethylene and propylene oxidation over gold,” *J. Phys. Chem.*, vol. 76, no. 6, pp. 2914–2921, 1971.

[92] A. A. Davydov, V. G. Mikhaltchenko, and V. D. Sokolovskii, “Surface Complexes of Propylene and Their Role in Catalytic Oxidation,” *J. Catal.*, vol. 55, pp. 299–313, 1978.

[93] J. Datka, Z. Sarbak, and R. P. Eischens, “Infrared Study of Coke on Alumina and Zeolite,” *J. Catal.*, vol. 145, pp. 544–550, 1994.

[94] K. Shimizu, H. Kawabata, A. Satsuma, and T. Hattori, “Role of Acetate and Nitrates in the Selective Catalytic Reduction of NO by Propene over Alumina Catalyst as Investigated by FTIR,” *J. Phys. Chem. B*, vol. 103, no. 25, pp. 5240–5245, Jun. 1999.

[95] J. C. De Jesús and F. Zaera, “Adsorption and thermal chemistry of acrolein and crotonaldehyde on Pt(111) surfaces,” *Surf. Sci.*, vol. 430, no. 1–3, pp. 99–115, 1999.

[96] S. B. Mohsin, M. Trenary, and H. J. Robota, “Infrared Identification of the Low-Temperature Forms of Ethylene Adsorbed on platinum/alumina,” *J. Phys. Chem.*, vol. 92, no. 18, pp. 5229–5233, 1988.

[97] J. Raskó, T. Kecskés, and J. Kiss, “Formaldehyde formation in the interaction of HCOOH with Pt supported on TiO2,” *J. Catal.*, vol. 224, pp. 261–268, 2004.

[98] R. D. Gonzalez and C. Grill, “Infrared evidence for the segregation of silica-supported Pt-Pd bimetallic clusters in oxidizing atmospheres,” *J. Catal.*, vol. 64, no. 2, pp. 487–490, 1980.

[99] W. Yu, M. D. Porosoff, and J. G. Chen, “Review of Pt-based bimetallic catalysis: From model surfaces to supported catalysts,” *Chem. Rev.*, vol. 112, no. 11, pp. 5780–5817, 2012.

[100] P. Thormählen, M. Skoglundh, E. Fridell, and B. Andersson, “Low-Temperature CO Oxidation over Platinum and Cobalt Oxide Catalysts,” *J. Catal.*, vol. 188, no. 2, pp. 300–310, 1999.

[101] R. Burch, “Gold catalysts for pure hydrogen production in the water-gas shift reaction: activity, structure and reaction mechanism.,” *Phys. Chem. Chem. Phys.*, vol. 8, no. 47, pp. 5483–5500, Dec. 2006.

[102] A. Russell and W. S. Epling, “Diesel Oxidation Catalysts,” *Catal. Rev.*, vol. 53, no. 4, pp. 337–423, 2011.

[103] A. T. Gremminger, H. W. Pereira de Carvalho, R. Popescu, J.-D. Grunwaldt, and O. Deutschmann, “Influence of gas composition on activity and durability of bimetallic Pd-Pt/Al2O3 catalysts for total oxidation of methane,” *Catal. Today*, pp. 1–11, Mar. 2015.

[104] P. Gélin, L. Urfels, M. Primet, and E. Tena, “Complete oxidation of methane at low temperature over Pt and Pd catalysts for the abatement of lean-burn natural gas fuelled vehicles emissions: Influence of water and sulphur containing compounds,” *Catal. Today*, vol. 83, no. 1–4, pp. 45–57, 2003.

[105] D. L. Mowery, M. S. Graboski, T. R. Ohno, and R. L. McCormick, “Deactivation of PdO-Al2O3 oxidation catalyst in lean-burn natural gas engine exhaust: aged catalyst characterization and studies of poisoning by H2O and SO2,” *Appl. Catal. B Environ.*, vol. 21, pp. 157–169, 1999.

[106] H. J. Kwon, J. H. Baik, Y. T. Kwon, I.-S. Nam, and S. H. Oh, “Enhancement effect of water on oxidation reactions over commercial three-way catalyst,” *Chem. Eng. J.*, vol. 141, no. 1–3, pp. 194–203, 2008.

[107] O. Mihai, A. Fathali, X. Auvray, and L. Olsson, “DME, propane and CO: The oxidation, steam reforming and WGS over Pt/Al2O3. The effect of aging and presence of water,” *Appl. Catal. B Environ.*, vol. 160–161, pp. 480–491, 2014.

[108] R. Caporali, S. Chansai, R. Burch, J. J. Delgado, A. Goguet, C. Hardacre, L. Mantarosie, and D. Thompsett, “Critical role of water in the direct oxidation of CO and hydrocarbons in diesel exhaust after treatment catalysis,” *Appl. Catal. B Environ.*, vol. 147, pp. 764–769, 2014.

[109] F. Liang, H. Zhu, Z. Qin, H. Wang, G. Wang, and J. Wang, “Positive effect of water vapor on CO oxidation at low temperature over Pd/CeO2-TiO2 catalyst,” *Catal. Letters*, vol. 126, no. 3–4, pp. 353–360, 2008.

[110] A. B. Mhadeshwar and D. G. Vlachos, “Microkinetic modeling for water-promoted CO oxidation, water-gas shift, and preferential oxidation of CO on Pt,” *J. Phys. Chem. B*, vol. 108, no. 39, pp. 15246–15258, 2004.

[111] M. J. Hazlett, M. Moses-Debusk, J. E. Parks, L. F. Allard, and W. S. Epling, “Kinetic and Mechanistic Study of Bimetallic Pt-Pd/Al2O3 Catalysts for CO and C3H6 Oxidation,” *Appl. Catal. B Environ.*, 2016.

[112] C. M. Kalamaras, G. G. Olympiou, and A. M. Efstathiou, “The water-gas shift reaction on Pt/γ-Al2O3 catalyst: Operando SSITKA-DRIFTS-mass spectroscopy studies,” *Catal. Today*, vol. 138, no. 3–4, pp. 228–234, 2008.

[113] G. G. Olympiou, C. M. Kalamaras, C. D. Zeinalipour-Yazdi, and A. M. Efstathiou, “Mechanistic aspects of the water-gas shift reaction on alumina-supported noble metal catalysts: In situ DRIFTS and SSITKA-mass spectrometry studies,” *Catal. Today*, vol. 127, no. 1–4, pp. 304–318, 2007.

[114] G. Jacobs, U. M. Graham, E. Chenu, P. M. Patterson, A. Dozier, and B. H. Davis, “Low-temperature water-gas shift: Impact of Pt promoter loading on the partial reduction of ceria and consequences for catalyst design,” *J. Catal.*, vol. 229, no. 2, pp. 499–512, 2005.

[115] O. Pozdnyakova, D. Teschner, A. Wootsch, J. Kröhnert, B. Steinhauer, H. Sauer, L. Toth, F. C. Jentoft, A. Knop-Gericke, Z. Paál, and R. Schlögl, “Preferential CO

oxidation in hydrogen (PROX) on ceria-supported catalysts , part II: Oxidation states and surface species on Pd/CeO2 under reaction conditions, suggested reaction mechanism," *J. Catal.*, vol. 237, pp. 17–28, 2006.

[116] I. M. Hamadeh and P. R. Griffiths, "Diffuse reflectance FT-IR studies of the adsorption of CO on Rh/Al2O3 catalysts," *Appl. Spectrosc.*, vol. 41, no. 4, pp. 682–688, 1987.

[117] J. R. Rostrup-Nielsen, "Catalysis Science and Technology," in *Catalytic Steam Reforming*, J. R. Anderson and M. Boudart, Eds. Berlin: Springer-Verlag, 1984, pp. 1–118.

[118] S. E. Voltz, C. R. Morgan, D. Liederman, and S. M. Jacob, "Kinetic Study of Carbon Monoxide and Propylene Oxidation on Platinum Catalysts," *Ind. Eng. Chem. Prod. Res. Dev.*, vol. 12, no. 4, pp. 294–301, Dec. 1973.

[119] S. M. Al-Adwani, J. Soares, and W. S. Epling, "Evaluating the Effects of Precious Metal Distribution along a Monolith-Supported Catalyst for CO oxidation," *Ind. Eng. Chem. Res.*, vol. 51, no. 19, pp. 6672–6679, May 2012.

[120] R. W. Mccabe and D. F. Mccready, "Formaldehyde Oxidation on Pt: Kinetic Evidence for Adsorbed Carbon Monoxide Intermediate," *Chem. Phys. Lett.*, vol. 111, no. 1, pp. 89–93, 1984.

[121] A. Pandya, J. Mmbaga, R. E. Hayes, W. Hauptmann, and M. Votsmeier, "Global Kinetic Model and Parameter Optimization for a Diesel Oxidation Catalyst," *Top. Catal.*, vol. 52, no. 13–20, pp. 1929–1933, Jul. 2009.

[122] S. R. Katare, J. E. Patterson, and P. M. Laing, "Aged DOC is a Net Consumer of

NO2: Analyes of Vehicle, Engine-dynamometer and Reactor Data," *SAE Tech. Pap. Ser.*, 2007.

[123] S. R. Katare, J. E. Patterson, and P. M. Laing, "Diesel Aftertreatment Modeling: A Systems Approach to NO x Control," *Ind. Eng. Chem. Res.*, vol. 46, no. 8, pp. 2445–2454, 2007.

[124] P. Granger, P. Malfoy, P. Esteves, L. Leclercq, and G. Leclercq, "Kinetics of the CO+N2O Reaction over Noble Metals," *J. Catal.*, vol. 187, no. 2, pp. 321–331, Oct. 1999.

[125] P. Granger, C. Dathy, J. J. Lecomte, L. Leclercq, M. Prigent, G. Mabilon, and G. Leclercq, "Kinetics of the NO and CO Reaction over Platinum Catalysts I . Influence of the Support," *J. Catal.*, vol. 173, pp. 304–314, 1998.

[126] R. Burch and D. Ottery, "Selective catalytic reduction of NOx by hydrocarbons on Pt/Al2O3 catalysts at low temperatures without the formation of N2O," *Appl. Catal. B Environ.*, vol. 9, pp. 19–24, 1996.

[127] R. Burch, J. Sullivan, and T. Watling, "Mechanistic considerations for the reduction of NOx over Pt/Al2O3 and Al2O3 catalysts under lean-burn conditions," *Catal. Today*, vol. 42, pp. 13–23, 1998.

[128] H. Oh, J. Luo, and W. Epling, "Reduction of Surface Nitrates via C3H6 Oxidation Over a Pt/Al2O3 Catalyst," *Top. Catal.*, vol. 56, no. 1–8, pp. 114–117, Feb. 2013.

[129] H. Oh, J. Luo, and W. S. Epling, "NO Oxidation Inhibition by Hydrocarbons over a Diesel Oxidation Catalyst: Reaction Between Surface Nitrates and Hydrocarbons," *Catal. Letters*, vol. 141, no. 12, pp. 1746–1751, Oct. 2011.

[130] M. Khosravi, A. Abedi, R. E. Hayes, W. S. Epling, and M. Votsmeier, “Kinetic modelling of Pt and Pt:Pd diesel oxidation catalysts,” *Appl. Catal. B Environ.*, vol. 154–155, pp. 16–26, Jul. 2014.

[131] X. H. Xia, T. Iwasita, F. Ge, and W. Vielstich, “Structural Effects and Reactivit in Methanol Oxidation on Polycrystalline and Single Crystal Platinum,” *Electrochim. Acta*, vol. 41, no. 5, pp. 711–718, 1996.

[132] T. H. Ballinger and J. T. Yates, “IR Spectroscopic Detection of Lewis Acid Sites on A1203 Using Adsorbed CO. Correlation with AI-OH Group Removal,” *Langmuir*, vol. 7, no. 14, pp. 3041–3045, 1991.

[133] M. I. Zaki, M. A. Hasan, and L. Pasupulety, “Surface Reactions of Acetone on Al2O3, TiO2, ZrO2, and CeO2: IR Spectroscopic Assessment of Impacts of the Surface Acid - Base Properties,” *Langmuir*, vol. 17, no. 3, pp. 768–774, 2001.

[134] H. Oh, I. S. Pieta, J. Luo, and W. S. Epling, “Reaction Kinetics of C3H6 Oxidation for Various Reaction Pathways Over Diesel Oxidation Catalysts,” *Top. Catal.*, vol. 56, no. 18–20, pp. 1916–1921, Jul. 2013.

[135] S. Chansai, R. Burch, C. Hardacre, H. Oh, and W. S. Epling, “An investigation of the role of surface nitrate species in the oxidation of propene on a Pt-based diesel oxidation catalyst,” *Catal. Sci. Technol.*, vol. 3, no. 9, pp. 2349–2356, 2013.

[136] M. K. Ainsworth, M. R. S. Mccoustra, M. A. Chesters, N. Sheppard, and C. De la Cruz, “An infrared study of ethene and CO coadsorption on Pt [111] and a Pt/SiO2 catalyst : ambiguities in the interpretation of difference spectra,” *Surf. Sci.*, vol. 437, pp. 9–17, 1999.

[137] P. Chen, K. . Kung, Y. . Shen, and G. . Somorjai, “Sum frequency generation spectroscopic study of CO/ethylene coadsorption on the Pt() surface and CO poisoning of catalytic ethylene hydrogenation,” *Surf. Sci.*, vol. 494, no. 3, pp. 289–297, Dec. 2001.

[138] V. Y. Prikhodko, S. J. Curran, T. L. Barone, S. A. Lewis, J. M. Storey, K. Cho, R. M. Wagner, and J. E. Parks, “Emission Characteristics of a Diesel Engine Operating with In-Cylinder Gasoline and Diesel Fuel Blending,” *SAE Int. J. Fuels Lubr.*, vol. 3, no. 2, pp. 946–955, 2010.

[139] S. Curran, Z. Gao, and R. Wagner, “Reactivity Controlled Compression Ignition Drive Cycle Emissions and Fuel Economy Estimations Using Vehicle Systems,” *SAE Int. J. Engines*, vol. 7, no. 2, pp. 902–912, 2014.

[140] S. V Bohac, M. Han, T. J. Jacobs, A. J. López, and D. N. Assanis, “Speciated Hydrocarbon Emissions from an Automotive Diesel Engine and DOC Utilizing Conventional and PCI Combustion,” *SAE Tech. Pap. Ser.*, vol. 2006–01–02, 2006.

[141] J. M. Smith, H. C. Van Ness, and M. M. Abbott, *Indtroduction to Chemical Engineering Thermodynamics*, 7th ed. 2005.

[142] H. S. Fogler, “Elements of chemical reaction engineering,” *Chem. Eng. Sci.*, vol. 42, p. 1000, 1999.

[143] R. T. Pollard, D. J. Dixon, G. Skirrow, and J. A. Barnard, “Gas-Phase Combustion,” in *Comprehensive Chemical Kinetics*, vol. 17, C. H. Bamford and C. F. H. Tipper, Eds. Boston: Elsevier Scientific Publishing Company, 1977, pp. 249–472.

[144] M. Koebel, G. Madia, and M. Elsener, “Selective catalytic reduction of NO and

NO2 at low temperatures," *Catal. Today*, vol. 73, no. 3–4, pp. 239–247, 2002.

[145] I. P. Kandylas, O. A. Haralampous, and G. C. Koltsakis, "Diesel Soot Oxidation with NO2: Engine Experiments and Simulations," *Ind. Eng. Chem. Res.*, vol. 41, no. 22, pp. 5372–5384, 2002.

[146] M. Schejbal, J. Štěpánek, M. Marek, P. Kočí, and M. Kubíček, "Modelling of soot oxidation by NO2 in various types of diesel particulate filters," *Fuel*, vol. 89, no. 9, pp. 2365–2375, 2010.

[147] R. G. Tonkyn, S. E. Barlow, and J. W. Hoard, "Reduction of NOx in synthetic diesel exhaust via two-step plasma-catalysis treatment," *Appl. Catal. B Environ.*, vol. 40, no. 3, pp. 207–217, 2003.

[148] S. Yoon, A. G. Panov, R. G. Tonkyn, A. C. Ebeling, S. E. Barlow, and M. L. Balmer, "An examination of the role of plasma treatment for lean NOx reduction over sodium zeolite Y and gamma alumina. Part 1. Plasma assisted NOx reduction over NaY and Al2O3," *Catal. Today*, vol. 72, no. 3–4, pp. 243–250, 2002.

[149] H. Miessner, K. P. Francke, and R. Rudolph, "Plasma-enhanced HC-SCR of NOx in the presence of excess oxygen," *Appl. Catal. B Environ.*, vol. 36, no. 1, pp. 53–62, 2002.

[150] N. I. Butkovskaya, A. Kukui, N. Pouvesle, and G. Le Bras, "Formation of nitric acid in the gas-phase HO2 + NO reaction: effects of temperature and water vapor.," *J. Phys. Chem. A*, vol. 109, no. 29, pp. 6509–20, 2005.

[151] S. Tamm, H. H. Ingelsten, M. Skoglundh, and A. E. C. Palmqvist, "The influence of gas phase reactions on the design criteria for catalysts for lean NOx reduction

with dimethyl ether," *Appl. Catal. B Environ.*, vol. 91, no. 1–2, pp. 234–241, 2009.

[152] G.-M. Côme, *Gas-Phase Thermal Reactions*. Dordrecht: Kluwer Academic Publishers, 2001.

[153] J. Zádor, C. A. Taatjes, and R. X. Fernandes, "Kinetics of elementary reactions in low-temperature autoignition chemistry," *Prog. Energy Combust. Sci.*, vol. 37, no. 4, pp. 371–421, 2011.

[154] K. Otsuka, R. Takahashi, K. Amakawa, and I. Yamanaka, "Partial oxidation of light alkanes by NOx in the gas phase," *Catal. Today*, vol. 45, no. 1–4, pp. 23–28, 1998.

[155] K. Otsuka, R. Takahashi, and I. Yamanaka, "Oxygenates from Light Alkanes Catalyzed by NO x in the Gas Phase," *J. Catal.*, vol. 191, no. x, pp. 182–191, 1999.

[156] J. M. Kuchta, "Summary of Ignition Properties of Jet Fuels and Other Aircraft Combustible Fluids, Technical Report AFAPL-TR-75-70," 1975.

[157] C. F. Cullis, C. N. Hinshelwood, M. F. R. Mulcahy, and R. G. Partington, "Labile molecules in the kinetics of hydrocarbon reactions," *Discuss. Faraday Soc.*, vol. 2, no. C, p. 111, 1947.

[158] T. A. Semelsberger, R. L. Borup, and H. L. Greene, "Dimethyl ether (DME) as an alternative fuel," *J. Power Sources*, vol. 156, no. 2, pp. 497–511, 2006.

[159] Y.-F. Yu Yao, "Oxidation of Alkanes over Noble Metal Catalysts," *Ind. Eng. Chem. Prod. Res Dev.*, vol. 19, no. 3, pp. 293–298, 1980.

[160] F. Diehl, J. Barbier, D. Duprez, I. Guibard, and G. Mabilon, "Catalytic oxidation of heavy hydrocarbons over Pt/Al2O3. Influence of the structure of the molecule on its reactivity," *Appl. Catal. B Environ.*, vol. 95, no. 3–4, pp. 217–227, 2010.

[161] M. Khosravi, A. Abedi, R. E. Hayes, W. S. Epling, and M. Votsmeier, “Kinetic modelling of Pt and Pt:Pd diesel oxidation catalysts,” *Appl. Catal. B Environ.*, vol. 154–155, pp. 16–26, 2014.

[162] T. C. Watling, M. Ahmadinejad, M. Ţuţuianu, Å. Johansson, and M. a. J. Paterson, “Development and Validation of a Pt-Pd Diesel Oxidation Catalyst Model,” *SAE Int. J. Engines*, vol. 5, no. 3, pp. 1420–1442, Apr. 2012.

[163] B. Bailey, J. Eberhardt, S. Goguen, and J. Erwin, “Diethyl Ether (DEE) as a Renewable Diesel Fuel,” *SAE Tech. Pap.*, vol. 972978, 1997.

[164] T. J. Wallington, J. M. Andino, L. M. Skewes, W. O. Siegl, and S. M. Japar, “Kinetics of the reaction of OH radicals with a series of ethers under simulated atmospheric conditions at 295 K,” *Int. J. Chem. Kinet.*, vol. 21, no. 11, pp. 993–1001, 1989.

[165] M. Haneda, T. Watanabe, N. Kamiuchi, and M. Ozawa, “Effect of platinum dispersion on the catalytic activity of Pt/Al2O3 for the oxidation of carbon monoxide and propene,” *Appl. Catal. B Environ.*, vol. 142–143, pp. 8–14, 2013.

[166] A. Cudok, H. Froitzheim, and G. Hess, “Kinetics of the dissociative adsorption of O2 on Pt (lll): a TREELS study,” *Surf. Sci.*, vol. 307–309, pp. 761–767, 1994.

[167] C. M. Koeritz, “Surface stress changes resulting from molecular oxygen and carbon monoxide adsorption on platinum (111),” Arizona State University, 2007.

[168] M. P. Harold and M. E. Garske, “Kinetics and multiple rate states of CO oxidation on Pt II. Linking UHV and atmospheric pressure kinetic behavior,” *J. Catal.*, vol. 127, no. 2, pp. 553–575, 1991.

[169] G. I. Godolets, “Heterogeneous Catalytic Reactions Involving Molecular Oxygen,”

in *Studies in Surface Science and Catalysis*, vol. 15, J. R. H. Ross, Ed. New York: Elsevier Science, 1983.

[170] J. Goscianska and M. Ziolek, “Adsorption and interaction of NO, C3H6 and O2 on Pt, Zr, Nb-MCM-41—FTIR study,” *Catal. Today*, vol. 137, no. 2–4, pp. 197–202, Sep. 2008.

[171] T. Schalow, B. Brandt, M. Laurin, S. Schauermann, J. Libuda, and H. Freund, “CO oxidation on partially oxidized Pd nanoparticles,” *J. Catal.*, vol. 242, no. 1, pp. 58–70, Aug. 2006.

Appendices

Appendix 1: DRIFTS Peak Assignments

Table A-1-1: Bands used for peak assignments of carbonate, carboxylate, hydrocarbon species

Species	Vibrational Mode[a]	Wavenumber [cm^{-1}][b]	Reference
Acrolein $H_2C = C - CHO$	ν(C=O)	1700 (vs), 1622 (m)	Pt(111) [95]
	ν(C=C)	1618 (w)	
	γ(CH_2)	1427 (w)	
	$\delta_{ip}(CH)_{aldehyde}$	1367 (m)	
	$\delta_{ip}(CH)_{vinyl}$	1275 (vw)	
	ν(C-C)	1166 (m)	
	τ(CH_2)	993 (s)	
	$\delta_{oop}(CH)_{aldehyde}$	1016 (sh)	
	ρ(CH_2)	922 (m)	
Acetone $H_3C - CO - CH_3$	ν(CH_3)	3005 (m)	Pt(111) [42]
	ν(C=O)	1638 (s)	
	$\delta_a(CH_3)$	1426 (s)	
	$\delta_s(CH_3)$	1350 (m)	
	ν(CH_3-C-CH_3)	1238 (w)	
	ρ(CH_3)	1086 (m)	
π-Ethylene $H_2C = CH_2$	δ(C-H)	2955 (s), 2998, 3018 (s), 3073	Pt/Al_2O_3, Pt(111) [96]
	ν(C-C)	1200 (s)	
	γ(CH_2)	1498	
Di-σ-ethylene $H_2C - CH_2$	δ(C-H)	2912	Pt/Al_2O_3, Pt(111) [96]
	γ(CH_2)	1427, and 1050 Pt(111)	

Table A-1-1 (continued)

Ethylidyne CCH_3	δ(C-H)	2887,2947	Pt/Al_2O_3, Pt(111) [96]
	$\text{bend}_a(CH_3)$	2803	
	ν(C-C)	1128	
	$\gamma(CH_2)$, $\delta(CH_3)$	1341	
π-Propylene $H_2C = CH - CH_3$	$\nu_a(CH_2)$	3080 (s)	Pt (111) [39]
	ν(CH)	3066 (s)	
	$\nu_s(CH_2)$	2995 (w)	
	$\nu_a(CH_3)$	2978 (s)	
	$\nu_s(CH_3)$	2963 (s), 2939 (s)	
	ν(C=C)	1680 (m)	
	$\delta_a(CH_3)$	1453 (s)	
	$\gamma(CH_2)$	1435 (s)	
	$\delta_s(CH_3)$	1373 (w)	
	$\tau(CH_2)$	989 (s)	
Di-σ-propylene $H_2C - CH - CH_3$	$\nu_a(CH_2)$	2915 (s)	Pt (111) [39]
	ν(CH)	2883 (s)	
	$2\delta_a(CH_3)$, $\nu_s(CH_3)$	2860 (m)	
	$\nu_s(CH_2)$	2830 (w)	
	$\gamma(CH_2)$	1437 (m)	
	$\delta_s(CH_3)$	1375 (w)	
	δ(CH)	1309 (w)	
	$\omega(CH_2)$	1260 (w)	
	$\nu(C\text{-}CH_3)$	1088 (s)	
	$\tau(CH_2)$	1037 (s)	
	$\rho(CH_3)$	1015 (s)	
	$\nu_a(COO)$	1435,1470 or 1430	
	$\nu_s(COO)$	1304 (w) [86]	
	ν(COH)	1230	

Table A-1-1 (continued)

Propylidyne CCH_2CH_3	$\nu_a(CH_3)$	2960 (s)	Pt (111) [39]
	$\nu_s(CH_3)$	2917 (s)	
	$2\delta_a(CH_3)$	2860 (m)	
	$\delta_a(CH_3)$	1450 (m)	
	$\gamma(CH_2)$	1408 (m)	
	$\delta_s(CH_3)$	1374 (w)	
	$\nu(C\text{-}C)$	1104 (m)	
	$\rho(CH_3)$	1079 (w)	
	$\rho(CH_3)$	1041 (m)	
Formaldehyde CH_2O	$\nu(C{=}O)$	1716	Pt/TiO_2 [97]
	$\omega(CH_2)$	1509	
	$\gamma(CH_2)$	1260	
	$\tau(CH_2)$	1166	
Acetate CH_3COO^-	$\nu_a(COO^-)$	1560-1630 or 1550-1590 or 1580	[35] or [94] or [93]
	$\nu_s(COO^-)$	1350-1420 or 1465 or 1460	
	$\delta_s(CH_3)$	1390 (w)	
Formate $HCOO^-$	$\nu(C\text{-}H)$	2962	[35], [74], [82], [83]
	$\nu_a(COO^-)$	1600	
	$\nu_s(COO^-)$	1394, 1363	
Carbonate (free ion) $CO_3{}^{2-}$	$\nu_a(CO_3{}^{2-})$	1450-1420	[35], [84]
	$\nu_s(CO_3{}^{2-})$	1090-1020	
Monodentate carbonate $CO_3{}^-$	$\nu_a(COO)$	1530-1470/1455	[35]
	$\nu_s(COO)$	1300-1370/1330	
	$\nu(C\text{-}O)$	1080-1040	
	$\nu_a(COO)$	1435,1470 or 1430	
	$\nu_s(COO)$	1304 (w) [86]	
	$\nu(COH)$	1230	

Table A-1-1 (continued)

Bidentate carbonate CO_3	ν(C=O)	1530-1620/1620-1670/1540	[35]
	ν_a(COO)	1270-1250/1220-1270	
	ν_s(COO)	1030-1020/980-1020	
Bicarbonate HCO_3^-	ν(C=O)	1640 or 1650	Pt/Al_2O_3 and Pd/Al_2O_3, or Pt/Al_2O_3 [74] or [87], [88]
	ν_a(COO)	1435,1470 or 1430	
	ν_s(COO)	1304 (w) [86]	
	ν(COH)	1230	

[a] Nomenclature: ρ, rocking; τ, twisting; ν, stretching; ω, wagging; δ, deformation; γ, scissoring; subindices: s, symmetric; a, asymmetric

[b] Peak intensities: vw, very weak; w, weak; m, medium; s, strong; vs, very strong; sh, shoulder.

Appendix 2: Kinetic Modeling

A-2.1 CO and C_3H_6 Oxidation Mechanisms

The kinetic model over a Pt catalyst for CO oxidation used by Voltz can be obtained by assuming a mechanism where oxygen is adsorbed molecularly on the surface [118]; however in the literature there is evidence to support dissociative oxygen adsorption on Pt [166], [167]. In addition there is previous modeling of CO oxidation on Pt in which dissociative adsorption was found to be the rate limiting step in the CO reaction mechanism at low temperatures [168]. The mechanism for CO oxidation on Pt can then be written as [169]:

$$CO + * \leftrightarrow CO *, \tag{A-2-1}$$

$$O_2 + * \leftrightarrow O_2 *, \tag{A-2-2}$$

$$O_2 + 2 * \leftrightarrow 2O *, \tag{A-2-3}$$

$$CO * + O_2 * \leftrightarrow CO_2 * + 0 *, \tag{A-2-4}$$

$$CO * + O * \leftrightarrow CO_2 * + *, \text{ and} \tag{A-2-5}$$

$$CO_2 * \rightarrow CO_2 + *, \tag{A-2-6}$$

where * indicates a catalyst active site. Rate equations for CO oxidation are shown in equations A-2-7 and A-2-8 as

$$(-r_{CO}) = \frac{kC_{CO}C_{O2}}{[1+k_A C_{CO}]^2} \text{ and} \tag{A-2-7}$$

$$(-r_{CO}) = \frac{kC_{CO}C_{O2}^{1/2}}{[1+k_A C_{CO}]^2} \tag{A-2-8}$$

Equations A-2-2, A-2-4 and A-2-5 are used in the derivation of the molecularly adsorbed oxygen reaction rate model for CO oxidation (equation A-2-7) used by Voltz, and equations A-2-3 and A-2-5 are used for the dissociative oxygen adsorption reaction rate model (equation A-2-8) using the assumption that the surface reactions (equations A-2-4 and A-2-5 respectively) are rate determining steps, where the rates of all the other reactions are approximately zero. Additional assumptions of these models are that CO_2 desorbs very quickly (denoted by →) and that O_2 does not have significant surface coverage compared to CO.

In the paper by Voltz, a similar rate equation is used for C_3H_6 oxidation on Pt, where a similar mechanism of molecular adsorption of oxygen was likely assumed in the derivation. A reaction intermediate of the form of $C_3H_6O_2$, shown below, has been suggested on the Pt surface [169].

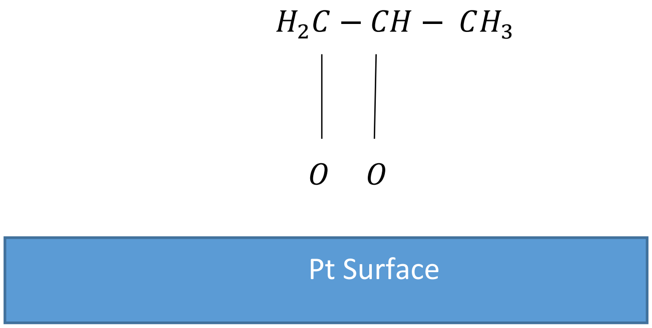

Another reaction intermediate has been suggested in the literature, where C_3H_5 has been found where the abstraction of the vinyl hydrogen occurs leaving the vinyl carbon susceptible to an oxygen attack [40]. The suggested reaction mechanism is shown in reactions A-2-9 through A-2-11 as follows:

$$C_3H_6 + * \leftrightarrow C_3H_6 *, \qquad \text{(A-2-9)}$$

$$O_2 + * \leftrightarrow O_2 *, \text{ and} \qquad \text{(A-2-10)}$$

$$C_3H_6 * + O_2 * \leftrightarrow C_3H_6O_2 ** \rightarrow 3CO_2 + 3H_2O, \qquad \text{(A-2-11)}$$

leading to the rate equation

$$(-r_{C3H6}) = \frac{kC_{C3H6}C_{O2}}{[1+k_A C_{C3H6}]^2}\,. \qquad \text{(A-2-12)}$$

Using the first suggested intermediate, Equations A-2-9 to A-2-11 can describe the beginning steps of the oxidation mechanism, with the following steps leading to complete oxidation to CO_2 and H_2O assumed to be happening instantaneously after reaction A-2-11, which is assumed to be the rate determining step, and a reaction rate identical to the Voltz reaction rate can be derived (Equation A-2-12). A study of the surface coverage of Pt during propylene oxidation shows some evidence of CH and CH_2 intermediates on the surface, however here we assume these are short lived intermediates [170].

For a Pd catalyst, the mechanism for C_3H_6 oxidation is slightly different, since under the reaction conditions used the natural oxidation state of Pd is PdO [171]. As mentioned previously once Pt is introduced in a bimetallic catalyst the oxidation state of Pd incorporated in Pt particles will change to metallic, for which we will assume the reaction mechanism will be identical to the Pt mechanisms provided earlier. For the oxidation of propylene over metal oxides a similar intermediate is on the surface; however the difference is that the oxygen is actually chemisorbed to the surface instead of molecularly adsorbed, as depicted below [169]:

.

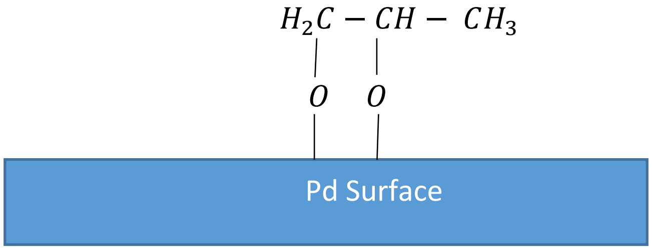

$$H_2C - CH - CH_3$$

Since oxygen adsorption occurs so readily, the oxidation of propylene by PdO occurs with zero order in oxygen, where the catalytic active site is PdO and not metallic Pd, shown as follows:

$C_3H_6 + * \leftrightarrow\ C_3H_6 *$ and (A-2-13)

$C_3H_6 * +\ * \leftrightarrow\ C_3H_6 ** \rightarrow\ 3CO_2 + 3H_2O,$ (A-2-14)

with the reaction rate

$$(-r_{C3H6}) = \frac{kC_{C3H6}}{[1+k_A C_{C3H6}]^2}, \quad \text{(A-2-15)}$$

again assuming formation of this intermediate is rate limiting and it oxidizes very quickly.

A-2.2 Kinetic Model Development

Parameter optimization for the oxidation of CO and C_3H_6 was conducted in the following manner. A plug flow model was assumed for the powder catalyst reactor, energy balances were not considered as isothermal conditions were assumed. Another assumption used in this modeling is that there is no pressure drop along the powder catalyst. The differential equation was solved to obtain model conversion, using MATLAB function ode45. The differential equation used was

$$C_{A,o} v_o \frac{dX}{dV} = (-r_A)(1-\emptyset), \quad \text{(A-2-16).}$$

where $C_{A,o}$is the initial concentration of component A in mol/L, $v_o$is the initial volumetric flow rate, V is the catalyst volume, X is the conversion, $(-r_A)$ is the reaction rate for oxidation of species A, and $\emptyset$ is catalyst porosity, assumed to be the same for all samples and identical to the porosity of Al_2O_3 as measured by the Micromeritics ASAP 2020. In this case A is either CO or C_3H_6.

The reaction rate equations used for single component kinetic testing were discussed previously, and was adapted from equations used by Voltz where both CO and C_3H_6 oxidation follow a Langmuir-Hinshelwood type mechanism [5], [118]. The generalized reaction rate is

$$(-r_A) = \frac{kC_AC_{O2}^{\gamma}}{[1+k_AC_A]^2}, \tag{A-2-17}$$

where C_A is the concentration of component A in mol/L, C_{O2} is the oxygen concentration, and γ is the power dependence of O_2. For CO oxidation on Pt $\gamma = 0.5$, for C_3H_6 oxidation on Pt $\gamma = 1$, and for Pd $\gamma = 0$, and for bimetallic cases γ is assumed to be the same as for Pt. The parameters k and k_A are the kinetic parameters defined by the Arrhenius equation shown as follows:

$$k = Ae^{-E_a/RT} \text{ and} \tag{A-2-18}$$

$$k_A = A_Ae^{-E_{a,A}/RT}, \tag{A-2-19}$$

where A is the frequency factor, E_a is the activation energy, A_A is the frequency factor for adsorption of A, and $E_{a,A}$ is the energy of adsorption of A, R is the ideal gas constant and T is the temperature in K.

Data from TPO experiments were taken from 2-20% conversion averaged over 1-3°C increments. The sum of squared differences between the experimental conversion and model conversion was used as the objective function to minimize to calculate the kinetic parameters of each reaction in question.

A-2.3 CO Oxidation

The parameter optimization results for CO oxidation on the various Pt:Pd ratios (excluding a monometallic Pd sample) are shown in Table A-2-1. Problems associated with the frequency factor are obvious, order of magnitude differences do not make much sense. We can see trends in the activation energy which make some sense compared to the data, the Pd rich sample had a lower slope in the ignition curve which is captured by a higher activation energy than the other samples. The adsorption energy increases in magnitude as the Pd content increases, which is actually not the trend expected from the data which show that Pt shows higher CO poisoning, however we do see product inhibition for the Pd rich samples which was not yet included in the model. In general the fit of the model gets worse, the sum of squared errors (SSE) increases, as the Pd content increases. This could also be related to the fact that the product inhibition of formed carbonates on the surface was not included in the model, however this does seem unlikely as we are only considering low conversion data (2-20%) for the parameter estimation where one would expect these contributions would be low.

Table A-2-1 Optimized parameters CO oxidation

Samples	**A $[(L/(mol\text{-}s^2))^{1/2}]$**	**E_a [kJ/mol]**	**A_{CO} [L/mol]**	**$\Delta H_{ads,co}$**	**SSE**
Pt	4.08×10^{12}	72	2.05×10^{3}	-15	2.20×10^{-03}
3:1 PtPd	5.54×10^{10}	60	46.8	-25	1.67×10^{-02}
1:1 PtPd	2.94×10^{12}	74	38.5	-24	2.05×10^{-02}
1:3 PtPd	6.78×10^{16}	98	12.8	-37	3.42×10^{-02}

Appendix 3: Propylene Partial Oxidation Products

The acetaldehyde, acetic acid, and methane concentration over Pd, Pt and Pt-Pd catalysts for experiments performed in the Chapter 5 study are shown below in Figures A-3-1 through A-3-3. Reaction conditions (RX) 1500 ppm C_3H_6, 10% O_2, 0 or 5% H_2O, in balance N_2 and pretreatment conditions (PT) 14% O_2, 0 or 5% H_2O, in balance N_2.

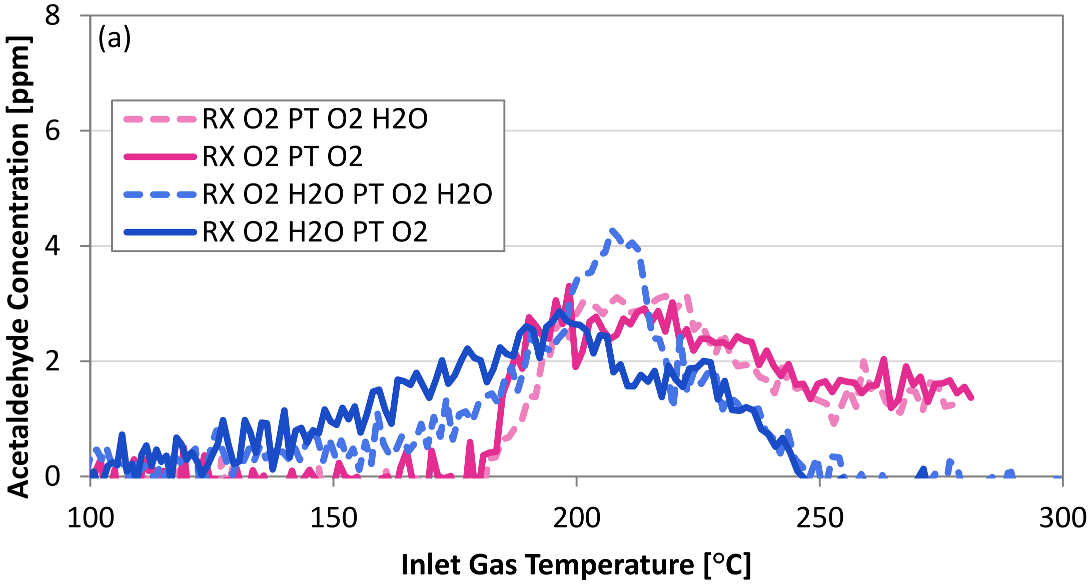

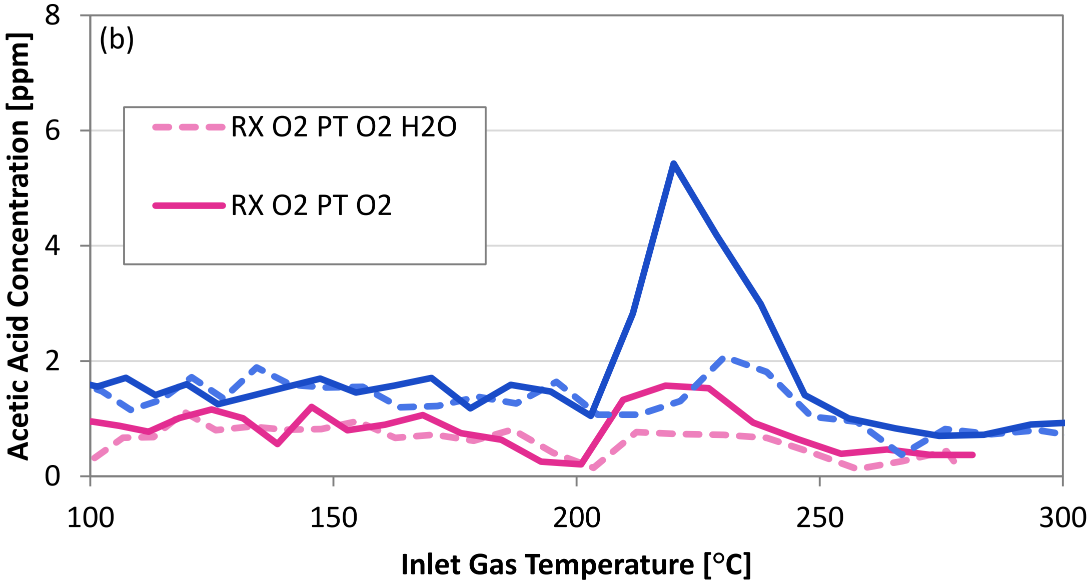

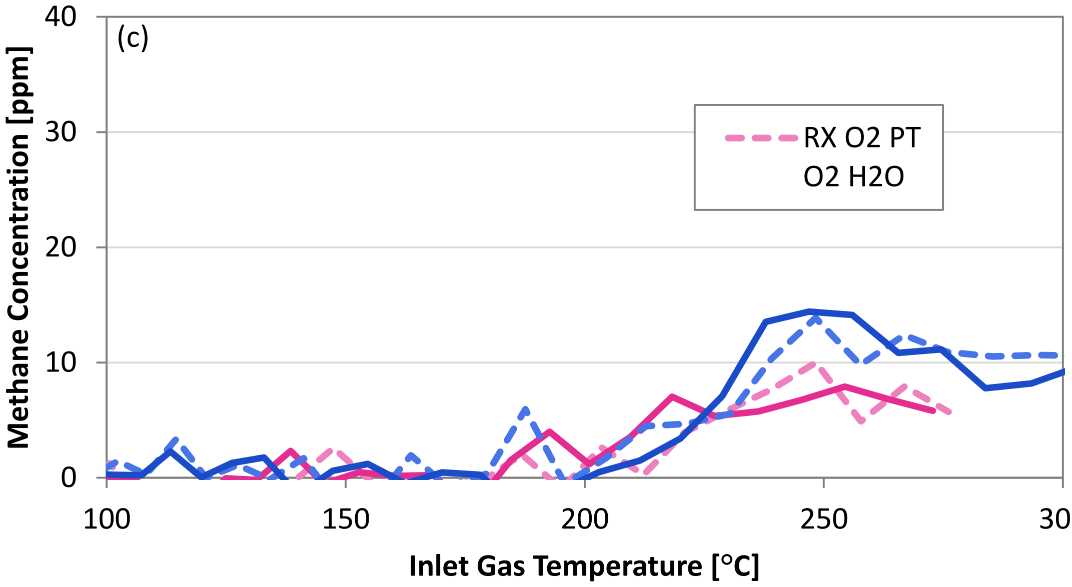

Figure A-3-1 Reactor testing Pd/Al_2O_3 catalyst, a) acetaldehyde formation, b) acetic acid formation, c) methane formation

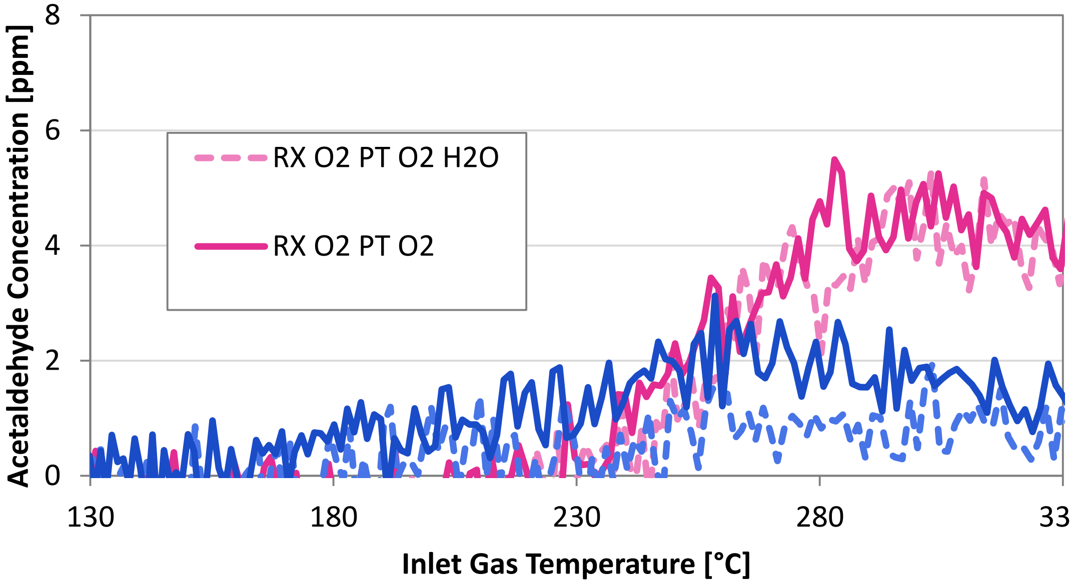

Figure A-3-2 Reactor testing Pt/Al_2O_3 catalyst, acetaldehyde formation

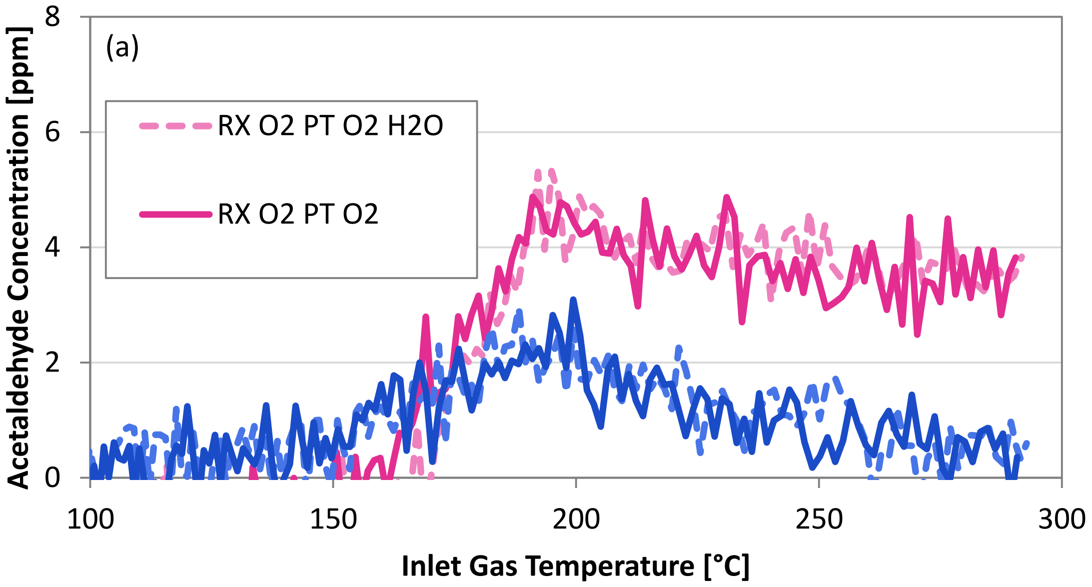
(a)
RX O2 PT O2 H2O
RX O2 PT O2
Acetaldehyde Concentration [ppm]
0
2
4
6
8
100
150
200
250
300
Inlet Gas Temperature [°C]

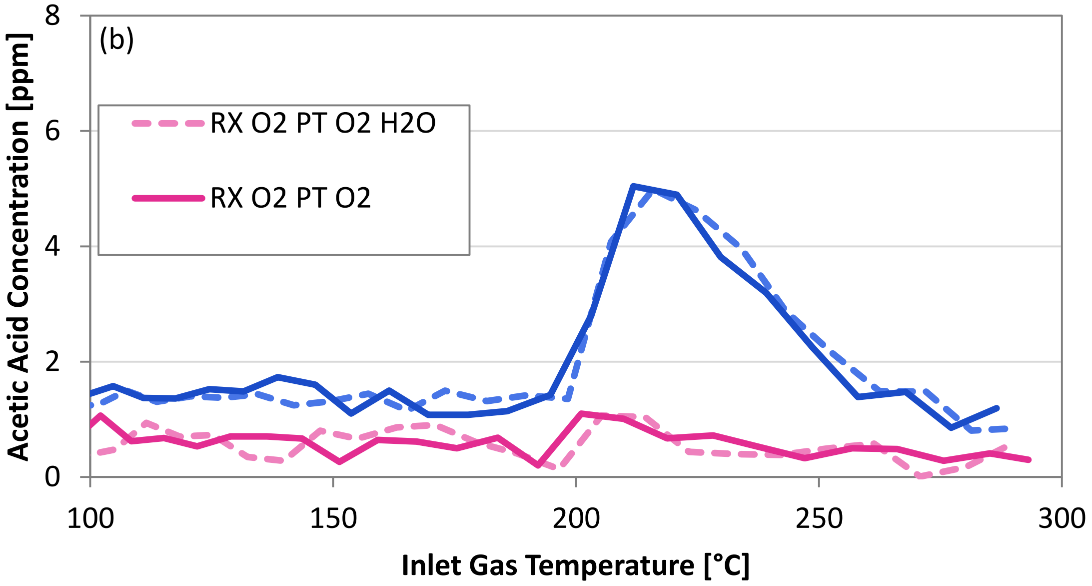
(b)
RX O2 PT O2 H2O
RX O2 PT O2
Acetic Acid Concentration [ppm]
0
2
4
6
8
100
150
200
250
300
Inlet Gas Temperature [°C]

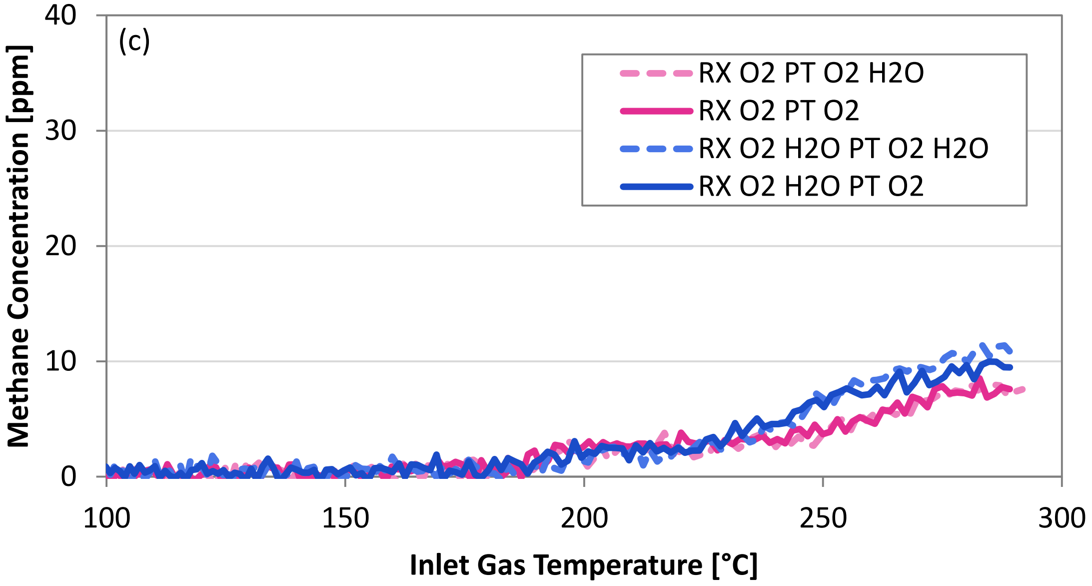

Figure A-3-3 Reactor testing Pt-Pd/Al_2O_3 catalyst, a) acetaldehyde formation, b) acetic acid formation, c) methane formation